

Springer Theses

Recognizing Outstanding Ph.D. Research

Andreas S.J.L. Bachmeier

Metalloenzymes as Inspirational Electrocatalysts for Artificial Photosynthesis

From Mechanism to Model Devices



Springer

Springer Theses

Recognizing Outstanding Ph.D. Research

Aims and Scope

The series “Springer Theses” brings together a selection of the very best Ph.D. theses from around the world and across the physical sciences. Nominated and endorsed by two recognized specialists, each published volume has been selected for its scientific excellence and the high impact of its contents for the pertinent field of research. For greater accessibility to non-specialists, the published versions include an extended introduction, as well as a foreword by the student’s supervisor explaining the special relevance of the work for the field. As a whole, the series will provide a valuable resource both for newcomers to the research fields described, and for other scientists seeking detailed background information on special questions. Finally, it provides an accredited documentation of the valuable contributions made by today’s younger generation of scientists.

Theses are accepted into the series by invited nomination only and must fulfill all of the following criteria

- They must be written in good English.
- The topic should fall within the confines of Chemistry, Physics, Earth Sciences, Engineering and related interdisciplinary fields such as Materials, Nanoscience, Chemical Engineering, Complex Systems and Biophysics.
- The work reported in the thesis must represent a significant scientific advance.
- If the thesis includes previously published material, permission to reproduce this must be gained from the respective copyright holder.
- They must have been examined and passed during the 12 months prior to nomination.
- Each thesis should include a foreword by the supervisor outlining the significance of its content.
- The theses should have a clearly defined structure including an introduction accessible to scientists not expert in that particular field.

More information about this series at <http://www.springer.com/series/8790>

Andreas S.J.L. Bachmeier

Metalloenzymes as Inspirational Electrocatalysts for Artificial Photosynthesis

From Mechanism to Model Devices

Doctoral Thesis accepted by
University of Oxford, UK

 Springer

Author

Dr. Andreas S.J.L. Bachmeier
Business Unit Catalysts
Clariant
Munich
Germany

Supervisor

Prof. Fraser A. Armstrong
Department of Chemistry
University of Oxford
Oxford
UK

ISSN 2190-5053

Springer Theses

ISBN 978-3-319-47068-9

DOI 10.1007/978-3-319-47069-6

ISSN 2190-5061 (electronic)

ISBN 978-3-319-47069-6 (eBook)

Library of Congress Control Number: 2016953207

© Springer International Publishing AG 2017

This work is subject to copyright. All rights are reserved by the Publisher, whether the whole or part of the material is concerned, specifically the rights of translation, reprinting, reuse of illustrations, recitation, broadcasting, reproduction on microfilms or in any other physical way, and transmission or information storage and retrieval, electronic adaptation, computer software, or by similar or dissimilar methodology now known or hereafter developed.

The use of general descriptive names, registered names, trademarks, service marks, etc. in this publication does not imply, even in the absence of a specific statement, that such names are exempt from the relevant protective laws and regulations and therefore free for general use.

The publisher, the authors and the editors are safe to assume that the advice and information in this book are believed to be true and accurate at the date of publication. Neither the publisher nor the authors or the editors give a warranty, express or implied, with respect to the material contained herein or for any errors or omissions that may have been made.

Printed on acid-free paper

This Springer imprint is published by Springer Nature

The registered company is Springer International Publishing AG

The registered company address is: Gewerbestrasse 11, 6330 Cham, Switzerland

Supervisor's Foreword

Artificial photosynthesis (AP) research involves designing and building physical systems that mimic natural photosynthesis by using solar energy to convert water into hydrogen and oxygen, leading also to the endothermic conversion of carbon dioxide into organic molecules. If AP could be made efficient and scalable, it would offer a way of storing solar energy as chemical bonds in a 'fuel'. Although it is well known that electricity generated by photovoltaic cells can be used to electrolyse water, it might advantageous to combine these two steps in a single device. Early research on AP focused on single materials that split water when illuminated, but later research has tried to mimic more closely the modular processes that occur in chloroplasts. Hence, photosynthesis needs a minimum of three components bolted together: (1) the excitation centre (chlorophyll in natural photosynthesis/semiconductor in AP) converts the energy of photons into a separated electron and hole; (2) the fuel-forming electrocatalyst (hydrogenase or ferredoxin NADP⁺ reductase in natural photosynthesis) uses excited electrons to split water and produce hydrogen or organic molecules; (3) the hole-quenching electrocatalyst converts water into oxygen (the oxygen-evolving MnCaO cluster in natural photosynthesis) releases electrons that are required to fill the vacancies ('holes') left in the valence orbitals (or band) when electrons are excited, thus completing a cycle.

In work leading up to 2012, prior to Andreas Bachmeier starting in Oxford as a Graduate Scholar at St John's College, my group had drawn attention to observations we had made regarding the superb efficiency of enzymes as electrocatalysts when attached to suitable electrode materials. Hence, the idea behind attaching enzymes to semiconductors was that the resulting hybrids could provide information on how efficient AP could be, were catalysts as good as enzymes to be available. Enzymes use abundant elements rather than precious metals and they excel at fast, long-range electron transfer with small reorganisation energies. We know the 3D structures of the active sites and have spectroscopic information on different states, and these active sites and surroundings can be systematically modified by genetic engineering.

In his doctoral research, Andreas studied the behaviour of hybrid modular AP systems, investigating several types of enzyme linked to various semiconductors differing in surface properties, bandgap, and energies of valence and conduction bands. His thesis thus combines the principles of structural enzymology with the physical chemistry of semiconductors. Andreas explored different enzyme/material combinations and obtained very interesting results, fostering new mechanistic ideas that resulted in five peer-reviewed publications. One line of reasoning to stem from these experiments was that enzymes are able to 'trap' catalytic electrons, using a combination of distance and low reorganisation energy to compete with destructive recombination (a model also applicable for charge separation in natural photosynthesis).

One of the most pressing problems in AP development is how to scale up economically: at present, researchers are focused on tiny bench-scale demonstrations. Owing to the huge availability of fossil resources, hydrogen and hydrocarbons have little commercial value and it is difficult to encourage any investment by the private sector. Andreas initiated studies of other systems that might give more valuable products than H₂ or C1 compounds. He looked into the possibility of using enzymes containing useful natural chromophores to monitor photo-driven catalytic electron transfer.

In a related project, Andreas worked with Dr. Will Myers to use pulsed EPR spectroscopy to study a particularly active hydrogenase to learn more about its mechanism. Formaldehyde intercepts the catalytic cycle at a highly reduced state, and he was able to propose options for the structure of a highly reduced intermediate of a [FeFe]-hydrogenase trapped by binding of formaldehyde.

Oxford, UK

Prof. Fraser A. Armstrong, FRS

Preface

Artificial photosynthesis, an important route towards future supply of renewable energy, seeks to convert sunlight into storable chemical energy such as fuels. Building upon the principles of biological solar energy conversion, artificial photosynthesis can be broken down into four essential processes: harvesting of visible light, charge (electron–hole) separation, oxidation of water to dioxygen, and fuel formation. Importantly, unlike natural photosynthesis, artificial photosynthesis is solely dedicated to efficient formation of fuels and is not restricted by the availability of arable land.

Both water oxidation and fuel formation require efficient and selective catalysts. This work utilises certain metalloenzymes, which have evolved to catalyse fuel-generating reactions such as the formation of H_2 or the reductive activation of CO_2 to carbon-based fuels with unmatched efficiencies. In contrast to most artificial catalysts, these enzymes are composed solely of abundant elements and operate efficiently at neutral pH. Thus, although not suitable for scale-up, they can be used to mimic conditions under which future devices will have to operate and provide design criteria for the components of applied technologies.

In this thesis, physico-chemical techniques are used to study the mechanism of [FeFe]-hydrogenases, the most proficient H_2 -evolving catalysts that rival platinum in activity, by investigating how reversible inhibitors intercept transient enzyme states. The interaction of fuel-forming enzymes with light-absorbing semiconductor electrodes is also explored, leading to the construction of a photoelectrochemical cell for the selective, light-driven reduction of CO_2 . Furthermore, this thesis demonstrates that metalloenzymes can be used to establish new directions in artificial photosynthesis research, driving endergonic organic reactions such as specific $C=C$ hydrogenation.

Munich, Germany

Andreas S.J.L. Bachmeier

Parts of this thesis have been published in the following journal articles:

1. How Formaldehyde Inhibits Hydrogen Evolution by [FeFe]-Hydrogenases: Determination by ^{13}C ENDOR of Direct Fe–C Coordination and Order of Electron and Proton Transfers. Andreas Bachmeier, Julian Esselborn, Suzannah V. Hexter, Tobias Krämer, Kathrin Klein, Thomas Happe, John E. McGrady, William K. Myers, and Fraser A. Armstrong, *J. Am. Chem. Soc.* **2015**, *137*, 5381.
2. Enzymes as Exploratory Catalysts in Artificial Photosynthesis. Andreas Bachmeier, Bhavin Siritanaratkul, and Fraser A. Armstrong, in ‘From Molecules to Materials – Pathways to Artificial Photosynthesis’, Eds: E. A. Rozhkova, K. Ariga, Springer **2015**, 99.
3. Solar-driven proton and carbon dioxide reduction to fuels – lessons from metalloenzymes. Andreas Bachmeier and Fraser Armstrong, *Curr. Opin. Chem. Biol.* **2015**, *25*, 141.
4. Selective Visible-Light-Driven CO_2 Reduction on a p-Type Dye-Sensitized NiO Photocathode. Andreas Bachmeier, Samuel Hall, Stephen W. Ragsdale, and Fraser A. Armstrong, *J. Am. Chem. Soc.* **2014**, *136*, 13518.
5. A Multi-Heme Flavoenzyme as a Solar Conversion Catalyst. Andreas Bachmeier, Bonnie J. Murphy, and Fraser A. Armstrong, *J. Am. Chem. Soc.* **2014**, *136*, 12876 (highlighted as ‘JACS-Spotlight’: *J. Am. Chem. Soc.* **2014**, *136*, 13469).
6. How Light-Harvesting Semiconductors Can Alter the Bias of Reversible Electrocatalysts in Favor of H_2 Production and CO_2 Reduction. Andreas Bachmeier, Vincent C. C. Wang, Thomas W. Woolerton, Sophie Bell, Juan C. Fontecilla-Camps, Mehmet Can, Stephen W. Ragsdale, Yatendra S. Chaudhary, and Fraser A. Armstrong, *J. Am. Chem. Soc.* **2013**, *135*, 15026.

Acknowledgments

First and foremost, I would like to thank Prof. Fraser A. Armstrong, for offering me a place in his group and for providing me with all the freedom I needed to pursue my own ideas, while, at the same time, being a constant source of inspiration and intellectual challenge. I thoroughly enjoyed working under his guidance.

Thanks must also go to my collaborators, without the contributions of whom this work would not have been possible. I am particularly grateful to Dr. William Myers for all his contributions to the work on [FeFe]-hydrogenases and for teaching me (or trying to, at least) a fair bit on pulsed EPR during the many long nights we shared sitting in front of the spectrometer. In this regard, Julian Esselborn is also acknowledged, not only for supplying me with copious amounts of highly concentrated enzyme ('black gold'), but also for his helpful comments regarding mechanistic aspects of [FeFe]-hydrogenases.

To my proofreaders, Dr. Rhiannon Evans, Prof. Radim Beranek, Dr. Suzannah Hexter, Dr. Thomas Esterle, and Dr. Holly Reeve: I am grateful for all the valuable and constructive feedback. Thanks to my part II students Samuel Hall and Sophie Bell for their heroic efforts; it has been great pleasure overseeing their first steps into research.

A very special thanks to my fellow leaders of the 'Solar Fuels' exhibit at the 2013 Royal Society Summer Science Exhibition: Non, Suzannah, and Alison. Not only has it been a very exciting (albeit stressful, at times) experience organising the exhibit and bringing it to success, but I also feel it has brought us closer together as friends.

Thank you to past and present members of the Armstrong group: Non, Suzannah, Philip, Bonnie, Thomas, Vincent, Maxie, Tom, Yatendra, Gopan, Edgar, Alison, Carina, Emily, and Bhavin, for all the help and support, for teaching me a great deal about science, for sharing your expertise on enzymes and electrochemistry, and, of course, for all the fun we had in- and outside the laboratory.

I am also thankful for all the help I received from the Department of Chemistry's support staff over the years, in particular from Terri Adams (glassblowing), Nenad Vranjes (electronics), Ashleigh Hewson and Jonathan Hawkins (building

management), Charlie Jones (PCTL student workshop), as well as Karl Harrison, Keith Waters, and Tom Bradshaw (IT).

St John's College Oxford is gratefully acknowledged for providing me with a Graduate Scholarship that allowed me to pursue my doctoral studies in such a vibrant and stimulating environment. Furthermore, I am grateful to St John's College and also the UK Solar Fuels Network for generous financial contributions towards the attendance of several international conferences. I would like to thank the SCG innovation fund for a six-month funding extension in form of a 'pump prime' grant.

Last but not least, special thanks go to my family, who have been a constant source of support, and to all my friends who have made my time at Oxford so memorable and enjoyable. I dedicate this work to both my late father, who is sorely missed, and Stephanie: I have been fortunate to meet the most wonderful person so early on in my life.

Collaborations

The following collaborators contributed to the work presented in this thesis. Enzyme samples were kindly provided by several laboratories: [FeFe]-hydrogenase enzymes were prepared by Julian Esselborn (laboratory of Prof. Thomas Happe, Ruhr-Universität Bochum, Germany). Carbon monoxide dehydrogenase was provided by Dr. Mehmet Can (laboratory of Prof. Stephen Ragsdale, University of Michigan, USA), and [NiFeSe]-hydrogenase was prepared by Dr. Christine Cavazza, (laboratory of Prof. Juan-Carlos Fontecilla-Camps, Institute de Biologie Structurale, Grenoble). Samples of flavocytochrome c_3 were provided by Profs. Graeme Reid (Institute of Cell and Molecular Biology, University of Edinburgh) and Stephen Chapman (Department of Chemistry, University of Edinburgh).

The pulsed EPR experiments presented in Chap. 3 were carried out together with Dr. William Myers (Centre for Advanced Electron Spin Resonance, University of Oxford), who developed the mathematical framework for data analysis, analysed the data, and prepared the figures. The DFT calculations presented in Chap. 3 were performed by Prof. John McGrady (Inorganic Chemistry Laboratory, University of Oxford).

Some of the electrochemistry experiments presented in Chap. 4 were carried out by Sophie Bell under my supervision, and some of the electrochemistry experiments shown in Chap. 5 were conducted by Samuel Hall, also under my supervision. In both cases, I devised the experiments.

The SEM images presented in Chaps. 4 and 5 were recorded by Prof. Jamie Warner (Department of Materials, University of Oxford).

Contents

1 Introduction	1
1.1 Rationale for Artificial Photosynthesis	1
1.2 Principles of Photosynthetic Energy Conversion.	3
1.2.1 Energy Flow in Biology and Photosynthetic Efficiencies	3
1.2.2 The Photosynthetic Reactions	6
1.2.3 Using Photosystem II as a Guide for Assembling an Artificial Photosynthetic System.	12
1.3 The Individual Components of Artificial Photosynthetic Systems	14
1.3.1 Light-Absorption and Charge Separation.	14
1.3.2 Water Oxidation Catalysis.	18
1.3.3 H ₂ Formation	20
1.3.4 CO ₂ Reduction	24
1.4 Strategies for Integrated Systems	30
1.4.1 Integrating the Individual Components	30
1.4.2 Photochemical versus Photoelectrochemical Water Splitting	31
1.4.3 The Combination of Photovoltaics and Electrolysis	36
1.5 The Role of Enzymes in Artificial Photosynthesis	37
1.5.1 General Considerations	37
1.5.2 Photosystem II in Artificial Systems	38
1.5.3 Fuel-Forming Enzymes for Artificial Photosynthesis.	38
1.6 The Mechanisms of Fuel-Forming Enzymes.	44
1.6.1 Common Mechanistic Principles	44
1.6.2 [FeFe]-Hydrogenases.	44
1.6.3 [NiFe]-Hydrogenases.	51
1.6.4 Carbon Monoxide Dehydrogenase	58
1.7 Aims of This Thesis	62
References.	62

2	Theory of Experimental Techniques	77
2.1	Rate and Efficiency Parameters in Artificial Photosynthesis	77
2.2	Protein Film Electrochemistry	79
2.2.1	A Brief Introduction to Protein Film Electrochemistry	79
2.2.2	The Electrochemical Setup	79
2.2.3	Non-faradaic Processes	81
2.2.4	Faradaic Current	82
2.2.5	Mass Transport and Interfacial Electron Transfer	83
2.2.6	Catalytic Voltammetry	88
2.2.7	Chronoamperometry	90
2.3	Semiconductor Electrochemistry	91
2.3.1	The Energy Band Model	91
2.3.2	The Semiconductor/Solution Interface	94
2.3.3	The Semiconductor/Electrolyte Junction Under Applied Bias	96
2.3.4	Photoeffects at the Semiconductor/Electrolyte Interface	100
2.3.5	Measurement of the Flat-Band Potential	102
2.4	Marcus Theory and Theoretical Treatment of Photoinduced Electron Transfer	108
2.4.1	The Electron Transfer Rate Constant	109
2.4.2	The Free Energy of Activation	110
2.4.3	Reorganisation	111
2.4.4	The Normal and Inverted Regions	112
2.4.5	Electronic Coupling	115
2.4.6	Electron Transfer in Biological Systems	118
2.5	Electron Paramagnetic Resonance Spectroscopy	119
2.5.1	The Electronic g Value	119
2.5.2	The g Value is Anisotropic	120
2.5.3	Multiple Magnetic Interactions	122
2.5.4	'Advanced' EPR Techniques	123
	References	124
3	The Mechanism of [FeFe]-Hydrogenases—How Aldehydes Inhibit H_2 Evolution	127
3.1	Introduction	127
3.2	Protein Film Electrochemistry Investigations	131
3.2.1	Inhibition by Formaldehyde	132
3.2.2	Inhibition by Trifluoroacetaldehyde	133
3.2.3	Inhibition by Acetaldehyde	135
3.2.4	Inhibition by Butyraldehyde	136
3.2.5	Inhibition by Isovaleraldehyde	137
3.3	Discussion	139
3.3.1	Discussion of the Different Aldehyde Reactivities	139
3.3.2	Implications from the Investigation of Formaldehyde Inhibition of the H-Cluster by Pulsed-EPR Techniques	143

3.3.3	Insight from Density Functional Theory	148
3.3.4	Comparative Analysis and Discussion.	150
3.4	Conclusions and Perspectives	153
	References.	154
4	The Direct Electrochemistry of Fuel-Forming Enzymes on Semiconducting Electrodes: How Light-Harvesting Semiconductors Can Alter the Bias of Reversible Electrocatalysts in Favour of H₂ Production and CO₂ Reduction.	157
4.1	Introduction	157
4.2	Results	159
4.2.1	Characteristics of Porous CdS and TiO ₂ Electrodes and Enzyme Immobilisation	159
4.2.2	Direct Electrochemistry of CODH and [NiFeSe]-Hydrogenase on TiO ₂ and CdS	162
4.2.3	Mott-Schottky Measurements	165
4.2.4	Photoelectrochemistry	172
4.3	Discussion	173
4.4	Conclusions and Perspectives	175
	References.	176
5	Selective Visible-Light-Driven CO₂ Reduction on a <i>p</i>-Type Dye-Sensitised NiO Photocathode.	179
5.1	Introduction	179
5.2	Results and Discussion.	181
5.2.1	Electrocatalytic Activity of Carbon Monoxide Dehydrogenase Adsorbed on a <i>p</i> -Type NiO Electrode	181
5.3	Photoelectrocatalytic CO ₂ Reduction	184
5.4	Conclusions and Perspectives	188
	References.	190
6	A Multi-haem Flavoenzyme as a Solar Conversion Catalyst	193
6.1	Introduction	193
6.2	Results and Discussion.	194
6.2.1	Protein Film Electrochemistry.	194
6.2.2	Photocatalytic Fumarate Formation	196
6.2.3	Closing the Photosynthetic Cycle	200
6.3	Conclusions and Perspectives	204
	References.	205
7	Conclusions and Perspectives	207
7.1	Conclusions	207
7.2	Perspectives	208

7.3	New Directions in Artificial Photosynthesis—Where Do We Go from Here and How Enzymes May Lead the Way.	211
	References.	212
8	Experimental Section	213
8.1	General Considerations.	213
8.2	The Mechanism of [FeFe]-Hydrogenases—How Aldehydes Inhibit H ₂ Evolution.	213
8.2.1	General Considerations	213
8.2.2	Enzyme Preparation	214
8.2.3	Protein Film Electrochemistry.	214
8.2.4	Electron Paramagnetic Resonance.	215
8.2.5	Density Functional Theory	216
8.3	The Direct Electrochemistry of Fuel-Forming Enzymes on Semiconducting Electrodes.	217
8.3.1	General Considerations	217
8.3.2	Semiconductor Electrodes.	217
8.3.3	Enzyme Preparation	219
8.3.4	Protein Film Electrochemistry.	219
8.4	Selective Visible-Light-Driven CO ₂ Reduction on a <i>p</i> -Type Dye-Sensitised NiO Photocathode	220
8.4.1	General Considerations	220
8.4.2	Fabrication of NiO Electrodes.	220
8.4.3	Enzyme Preparation	221
8.4.4	Protein Film Electrochemistry.	223
8.5	A Multi-haem Flavoenzyme as a Solar Conversion Catalyst	223
8.5.1	General Considerations	223
8.5.2	Protein Purification	224
8.5.3	Preparation of Thin Film Electrodes	224
8.5.4	Protein Film Electrochemistry Experiments.	225
8.5.5	Photocatalysis Experiments.	226
8.5.6	Photoelectrochemistry Experiments.	230
	References.	232
	Appendix A	235
	Appendix B	239
	Appendix C	243
	Appendix D	245
	Appendix E	247
	Appendix F	249
	Appendix G	251

Notation

Acronyms and Abbreviations

[2Fe] _H	Two-iron subsite of H-cluster
[Ox]	Concentration of oxidised species
[Red]	Concentration of reduced species
a_i	Activity of component i
a.c.	Alternating current
adt	Azadithiolate
aq	Aqueous
A	Area
	Hyperfine coupling constant
Acetyl-CoA	Acetyl coenzyme A
ACS	Acetyl-CoA synthase
ADP	Adenosine diphosphate
AM 1.5 G	Air mass 1.5 global standard G173
APCE	Absorbed photon-to-current efficiency
Arg	Arginine
Asp	Aspartic acid
ATP	Adenosine triphosphate
B	Magnetic field
bp	Boiling point
bpy	2,2'-bipyridine
Bu	Butyl
C	Capacitance
c	Concentration
Ca	<i>Clostridium acetobutylicum</i>
CaHydA	<i>Clostridium acetobutylicum</i> hydrogenase A
CA	Chronoamperometry
CB	Conduction band
CE	Counter electrode
Ch	<i>Carboxydotherrmus hydrogenoformans</i>

CIGS	Copper indium gallium selenide
Co-Pi	Cobalt phosphate (oxide) oxygen evolution electrocatalyst
CODH	Carbon monoxide dehydrogenase I from <i>Carboxydotherrmus hydrogenoformans</i>
<i>Cp</i>	<i>Clostridium pasteurianum</i>
CPE	Constant phase element
<i>Cr</i>	<i>Chlamydomonas reinhardtii</i>
CrHydA1	<i>Chlamydomonas reinhardtii</i> hydrogenase A1
CV	Cyclic voltammogram
CW	Continuous-wave
Cys	Cysteine
Cyt	Cytochrome
<i>D</i>	Diffusion coefficient
<i>d</i>	Separation distance between two reactants
<i>d</i> ₀	Separation distance in encounter complex
d.c.	Direct current
D1	Photosynthetic protein D1
D2	Photosynthetic protein D2
<i>Dd</i>	<i>Desulfovibrio desulfuricans</i>
DFT	Density functional theory
DSSC	Dye-sensitised solar cell
<i>e</i> ⁻	Electron
<i>e</i> ₀	Elementary charge = 1.602×10 ⁻¹⁹ C
<i>E. coli</i>	<i>Escherichia coli</i>
<i>E</i>	Electrode potential
<i>E</i> ⁰	Standard electrode potential
<i>E</i> _a	Acceptor level
<i>E</i> _{cb}	Conduction band potential
<i>E</i> _d	Donor level
<i>E</i> _F	Fermi level
<i>E</i> _{fb}	Flat-band potential
<i>E</i> _g	Band gap
<i>E</i> _{oc}	Open-circuit photopotential
<i>E</i> _{on}	Photocurrent onset potential
<i>E</i> _{vb}	Valence band potential
EIS	Electrical impedance spectroscopy
ENDOR	Electron nuclear double resonance
EPR	Electron paramagnetic resonance
EQE	External quantum efficiency
ESEEM	Electron spin echo envelope modulation
EXAFS	Extended X-ray absorption fine structure
<i>f</i>	Force constant
<i>ff</i>	Fill factor
fcc ₃	Flavocytochrome <i>c</i> ₃ from <i>Shewanella frigidimarina</i> NCIMB400
<i>F</i>	Faraday's constant = 96,485 C mol ⁻¹

FAD	Flavin adenine dinucleotide
Fd	Ferredoxin
FDH	Formate dehydrogenase
FID	Free-induction decay
FTIR	Fourier transform infrared spectroscopy
FTO	Fluorine doped tin oxide
G	Gibbs free energy
GC	Gas chromatography
Glu	Glutamic acid
h	Planck's constant = 6.626×10^{-34} J s
\hbar	Reduced Planck's constant = $h/2\pi$
H ₂ ase	Hydrogenase
H_{el}	Electronic coupling matrix element
His	Histidine
HOMO	Highest occupied molecular orbital
Hyd1	<i>E. coli</i> hydrogenase I
HYSCORE	Hyperfine sublevel correlation spectroscopy
i	Current
	Imaginary number
i_{ph}	Photocurrent
I	Nuclear spin
	Photon flux
IHP	Inner Helmholtz plane
IPCE	Incident photon-to-current efficiency
IQE	Internal quantum efficiency
IR	Infrared (spectroscopy)
ITO	Indium tin oxide
j	Current density
j_0	Exchange current density
k	Kinetic rate constant
k_B	Boltzmann constant = 1.381×10^{-23} J K ⁻¹
K	Equilibrium constant
KPi	0.1 M potassium phosphate buffer
L	Minority carrier diffusion length
LSV	Linear sweep voltammetry
LUMO	Lowest unoccupied molecular orbital
Lys	Lysine
M	Metal
m_s	Electron spin quantum number
Me	Methyl
MES	2-(<i>N</i> -morpholino)ethanesulfonic acid
MMCT	Metal-to-metal charge-transfer
MO	Molecular orbital
MPA	3-mercaptopropionic acid

n	Amount of substance Electron density, concentration
N_A	Acceptor density
N_D	Donor density
NADP(H)	Nicotinamide adenine dinucleotide phosphate
NHE	Normal hydrogen electrode
NMR	Nuclear magnetic resonance
OEC	Oxygen evolving cluster
OHP	Outer Helmholtz plane
Ox	Oxidised species
p	Hole density, concentration
P_{in}	Incident illumination power density
P1	4-[Bis(4-{5-[2,2-dicyanovinyl]-thiophene-2-yl}phenyl)amino]benzoic acid
P25	TiO ₂ nanopowder: primary particle size 21 nm, 80% anatase/20% rutile
PCET	Proton-coupled electron transfer
PDB	Protein data bank
PEC	Photoelectrochemical cell
PFE	Protein film electrochemistry
PFIRE	Protein film infrared electrochemistry
PGE	Pyrolytic graphite edge
Phe	Pheophytin <i>a</i>
Pr	Propyl
PSI	Photosystem I
PSII	Photosystem II
PV	Photovoltaics
Py	Pyridyl
PZC	Point of zero charge
q	Charge stored on capacitor
Δq	Change in equilibrium bond distance
Q_A	Plastoquinone A
Q_B	Plastoquinone B
Q_BH_2	plastoquinol B
r	Radius
rpm	Revolutions per minute
R	Ideal gas constant = 8.314 J K ⁻¹ mol ⁻¹ Resistance
RE	Reference electrode
Red	Reduced species
RHE	Reversible hydrogen electrode
RuBisCO	Ribulose-1,5-biphosphate carboxylase-oxygenase
RuBP	Ribulose-1,5-biphosphate
RuP	[Ru ^{II} (bpy) ₂ (4,4'-(PO ₃ H ₂) ₂ bpy)]Br ₂
S	Electron spin

S	State in Kok cycle
SCE	Saturated calomel electrode
SeCys	Selenocysteine
SEM	Scanning electron microscopy
Ser	Serine
SHE	Standard hydrogen electrode
SOMO	Singly occupied molecular orbital
STH	Solar-to-hydrogen
STS	Solar-to-succinate
t	Time
T	Temperature
	Dipolar component of hyperfine interaction
TEOA	Triethanolamine
TOF	Turnover frequency
TON	Turnover number
TST	Transition state theory
UV	Ultraviolet
UV/vis	Ultraviolet–visible absorption spectroscopy
ν	Scan rate
	Kinematic viscosity of the solvent
ν_i	Stoichiometric coefficient of component i
v	Volume
V	Voltage
V_{oc}	Open-circuit voltage
VB	Valence band
wt	Weight
W	Depletion layer width
WE	Working electrode
XAE	X-ray absorption and emission
XAS	X-ray absorption spectroscopy
z	Number of electrons
Z	Impedance
Z_w	Warburg impedance
α	Transfer coefficient
	Absorption coefficient
β	Attenuation factor
ϵ	Dielectric constant
ϵ_0	Permittivity of free space
ϵ_{op}	Optical dielectric constant of the solvent
ϵ_s	Static dielectric constant
ϕ	Electric potential
Φ	Quantum yield
Γ	(electroactive) coverage
η	Overpotential
	Efficiency

$\eta_{e-/h+}$	Absorptance
κ_{el}	Electronic factor
κ_n	Nuclear factor
λ	Wavelength
	Reorganisation energy
μ	Electrochemical potential
$\tilde{\mu}$	Chemical potential
μ_0	Vacuum permeability
μ_B	Bohr magneton
μ_n	Nuclear magnetic moment
ν	Frequency
Θ	Phase difference
ρ	Spin density
τ	Decay constant
	Delay time (EPR)
ω	Rotation rate
	Angular frequency

Units of Measure

‰	Per mille
Å	Ångström
atm	Atmosphere(s)
au	Atomic units
bn	Billion
C	Coulomb(s)
Da	Dalton(s)
eV	Electron volt(s)
F	Farad(s)
G	Gauss
h	Hour(s)
Hz	Hertz
J	Joule(s)
K	Kelvin
L	Litre(s)
m	Metre(s)
M	mol L ⁻¹
min	Minute(s)
Mtoe	Million tons of oil equivalent
ppm	Parts per million
rad s ⁻¹	Radian per second
s	Second(s)
scc	Standard cubic centimetre(s)
S	Siemens
T	Tesla

V	Volt(s)
W	Watt(s)
Ω	Ohm(s)

Prefices

p	Pico (10^{-12})
n	Nano (10^{-9})
μ	micro (10^{-6})
m	Milli (10^{-3})
c	Centi (10^{-2})
k	Kilo (10^3)
M	Mega (10^6)
G	Giga (10^9)
T	Tera (10^{12})
<i>i</i>	iso
<i>meso</i>	Mesoporous
<i>p</i>	Para

Common Subscripts and Superscripts

*	Excited state
‡	Transition state
0	Standard state
a	Anodic
c	Cathodic
cat	Catalytic
ct	Charge-transfer
d	Differential
	Distal
diff.	Diffuse layer
dl	Double layer
e	Electron
eq	Equilibrium
et	Electron transfer
F	Faradaic
	Fermi
H	Helmholtz layer
i	Inner-sphere
in	Incident
iso	Isotropic
lim	Limiting
m	Midpoint
	Metal
o	Outer-sphere

obs	Observed
oc	Open-circuit
ox	Oxidised
p	Pendant
	Product
	Proximal
ph	Photo
r	Reactant
red	Reduced
ref	Reference
s	Solution
sc	Short-circuit
	Space-charge layer
w	Working electrode

Chapter 1

Introduction

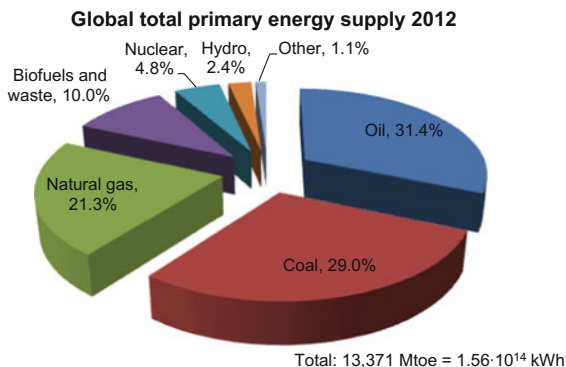
1.1 Rationale for Artificial Photosynthesis

New sources of energy have to be utilised to empower us to address the world's growing energy demand, which is projected to double by 2050 and triple by the end of the century [1–3]. The global human power requirement in 2009 was approximately 16 TW; more than 10,000 nuclear power plants would be needed to satisfy this demand [4]. In 2012, fossil fuels (oil, gas, coal) comprised more than 80% of the world's primary energy supply (Fig. 1.1), followed by biomass (10%, much of it simple deforestation [5]) and nuclear fission (4.8%)—all renewables combined only accounted for 3.5% [6].

Although fossil fuels sources are dwindling, problems and challenges do not arise from availability: projections estimate the global oil resources to 50–150 years, natural gas to 200–600 years, and coal to almost 200 years [4]. Rather, it is the effects caused by releasing ever more amounts of anthropogenic carbon dioxide into the atmosphere when fossil fuels are burned. The existence of climate change and global warming caused by increasing atmospheric CO₂ levels is now widely accepted among the scientific community [7, 8], albeit less so in the general public. According to Thomas [4], to combat global warming, it is of vital importance, amongst other things, to decrease the liberation of CO₂ into the atmosphere to a minimum, seek new ways to harvest and convert CO₂ into useful products, pursue existing and develop new ways of implementing the principles of green chemistry and clean technology including the development of a hydrogen economy, and evolve and extend new ways of utilising renewable sources of energy. Sunlight is by far the most abundant of all carbon-neutral energy sources and therefore constitutes the most viable option to address the latter challenge on a global scale. More energy from sunlight strikes the Earth in one hour (1.19×10^{14} kWh) than all the energy currently consumed on the planet in one year (1.14×10^{14} kWh) [1].

Solar electricity (photovoltaics, PV) is an established technology with commercialised silicon-cells obtaining solar conversion efficiencies > 20% [9]. Solar

Fig. 1.1 World total primary energy supply 2012, data taken from Ref. [6]. Peat and oil shale are aggregated with coal, ‘other’ includes geothermal, solar, wind, heat etc. Mtoe = million tons of oil equivalent



cells are familiar in society as artificial, engineered devices that utilise sunlight and convert its energy into electricity. Although variations of this approach are widely used nowadays, for example on house roofs, electricity generally cannot be easily stored: cost-effective and efficient large-scale energy storage systems that can buffer the intermittency of solar-electricity generation are not yet available. Moreover, solar energy could and should be converted directly into chemical energy, i.e. a portable fuel such as hydrocarbon(s) or hydrogen, that can be stored, used when needed, and is suitable for powering transport. The direct conversion of sunlight into fuels, e.g. using a photoelectrochemical cell, is known as artificial photosynthesis, because it mimics the action of green plants. Defined most loosely, artificial photosynthesis means using solar energy to make fuels in vitro, i.e. without a living organism.

Artificial photosynthesis research seeks to develop robust synthetic systems, inspired by Nature’s design principles, for the direct conversion of CO_2 and water to fuels, e.g. methanol, hydrogen, or hydrocarbons (‘solar fuels’), or valued organic chemicals (‘solar chemicals’). Whereas solar fuels have the potential to, ultimately, ‘power the planet’, solar chemicals may one day replace the myriad chemicals currently derived from petroleum (see Fig. 1.2).

However, whereas solar electricity is an established technology, artificial photosynthesis is still in its infancy. Even though the goal of artificial photosynthesis has been rigorously pursued since the first report of electrochemical photolysis of water by Fujishima and Honda [10] (using a photoelectrochemical approach based on the *n*-type semiconductor TiO_2), systems developed thus far rarely possess efficiencies above 5% (notable exceptions are given in Refs. [11–17]). The aim is to produce devices with efficiencies greater than 10%, increasing to 20% in the longer term. A vision on how a future centred on energy provision by solar fuels could look like is depicted in Fig. 1.3: provided a ‘hydrogen economy’ [18] will be established and the challenge of hydrogen storage solved [19, 20], solar hydrogen can be used as a ‘clean’ transportation fuel. Alternatively, carbon-based fuels such as methanol [21] can be used to power transport, complementing their use as feedstock in a future solar chemicals industry, where they would provide replacements for existing petrochemicals and value-added downstream products.

Products from petroleum

Tents	Toothpaste	Combs	Motorcycle helmet	Golf bags
Crayons	Gasoline	CD's & DVD's	Caulking	Life jackets
Parachutes	Heart valves	Paint brushes	Petroleum jelly	Percolators
Telephones	Candles	Detergents	Transparent tape	Rubbing alcohol
Enamel	Trash bags	Perfumes	CD player	Tennis rackets
Pillows	House paint	TV cabinets	Faucet washers	Rubber cement
Dishes	Water pipes	Shag rugs	Antiseptics	Fishing boots
Cameras	Hand lotion	Electrician's tape	Clothesline	Vaporisers
Anaesthetic	Roller skates	Tool racks	Curtains	Balloons
Artificial turf	Surf boards	Car battery cases	Food preservatives	Sun glasses
Artificial limbs	Shampoo	Epoxy	Basketballs	Solvents
Bandages	Wheels	Paint	Soap	Diesel fuel
Dentures	Paint rollers	Mops	Vitamin capsules	Motor oil
Model cars	Shower curtains	Lipstick	Antihistamines	Bearing Grease
Folding doors	Guitar strings	Denture adhesive	Purses	Ink
Hair curlers	Luggage	Linoleum	Shoes	Floor wax
Cold cream	Aspirin	Ice cube trays	Dashboards	Ballpoint pens
Movie film	Safety glasses	Synthetic rubber	Cortisone	Football cleats
Soft contact lenses	Antifreeze	Speakers	Deodorant	Upholstery
Drinking cups	Football helmets	Plastic wood	Footballs	Sweaters
Fan belts	Awnings	Electric blankets	Putty	Boats
Car enamel	Eyeglasses	Glycerine	Dyes	Insecticides
Shaving cream	Clothes	Cassettes	Panty hose	Bicycle tires
Ammonia	Toothbrushes	Dishwasher parts	Refrigerant	Sports car bodies
Refrigerators	Ice chests	Tool boxes	Dresses	Nail polish
Golf balls	Footballs	Shoe polish	Tires	Fishing lures

Fig. 1.2 A selection of the variety of products that are derived from fossil resources. Adapted from Ref. [4]

1.2 Principles of Photosynthetic Energy Conversion

1.2.1 Energy Flow in Biology and Photosynthetic Efficiencies

Biology developed the capacity to efficiently capture solar energy and use it to power the synthesis of organic molecules more than 3 billion years ago (oxygenic photosynthesis appeared on our planet approximately 2.5 bn years ago [22]); today, photosynthesis produces more than 100 billion tons of dry biomass annually [23]. All fossil fuels burned in our time, i.e. oil, gas, and coal, were provided by photosynthesis with energy originally derived from sunlight [24]. A general understanding of how Nature uses photosynthesis to convert sunlight into chemical energy is needed to identify the key components chemists have to mimic in their pursuit to devise efficient artificial photosynthetic systems.

Biological energy flow is schematically depicted in Fig. 1.4 [22, 23, 25]. The resources needed for photosynthetic energy conversion, water, sunlight, and carbon dioxide, are of almost unlimited abundance. As illustrated in Fig. 1.4, water is split into oxygen and hydrogen (equivalents) in the photosynthetic light reactions— O_2 is released into the atmosphere whereas 'hydrogen' is combined with carbon dioxide to form sugars and other organic matter [22] (the immediate end product being the

What could the production and use of solar fuels look like?

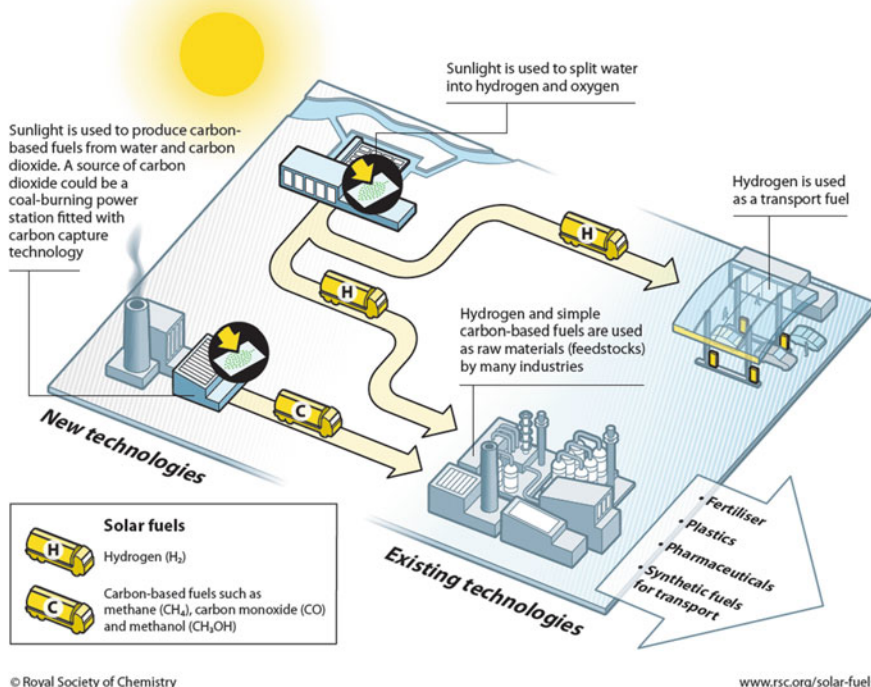


Fig. 1.3 Schematic representation of possible future energy provision by solar fuels, their use as transportation fuels, and integration into existing chemical technologies. Reprinted with permission from the Royal Society of Chemistry. Copyright The Royal Society of Chemistry 2012

monosaccharide D-glucose [26]). Combustion of biomass and fossil fuels originating from photosynthesis (or metabolism of organic molecules that constitute food by the process of respiration, i.e. *in vivo* oxidation) leads to recombination of the stored hydrogen equivalents with oxygen, thereby completing the cycle. From an energetic point of view, the synthesis of organic molecules represents a way of storing hydrogen and therefore storing solar energy in the form of chemical bonds [22].

A maximum efficiency for the conversion of light to stored chemical energy (dry carbon matter) of approximately 5% has been calculated [23, 26], a value that is rarely reached due to several loss mechanisms, illustrated in Fig. 1.5. The net efficiency of photosynthesis averaged over Earth's surface (both land and oceans) is $\sim 0.15\%$; for modern food crops energy storage efficiencies of 0.5–1.0% are typical, and only short-term yields can be as high as $\sim 4\%$ [26]. Despite these low efficiencies, about ten times the amount of the current world energy consumption is stored annually by photosynthesis and it is important to note that the imperative for any photosynthetic organism is replication, not the accretion of biomass [26]. The different loss mechanisms illustrated in Fig. 1.5 make immediately apparent that an

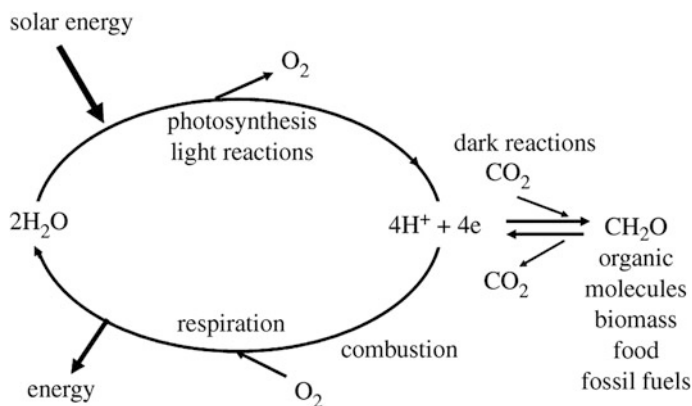


Fig. 1.4 Diagram depicting the flow of energy in biology [22, 23, 25]. Solar energy is used by photosynthesis to oxidise water to oxygen and hydrogen equivalents, which are stored in the form of organic molecules such as glucose. Upon combustion or metabolism, energy is released while oxygen is consumed. Reprinted with permission from Ref. [22]. Copyright 2009 The Royal Society of Chemistry

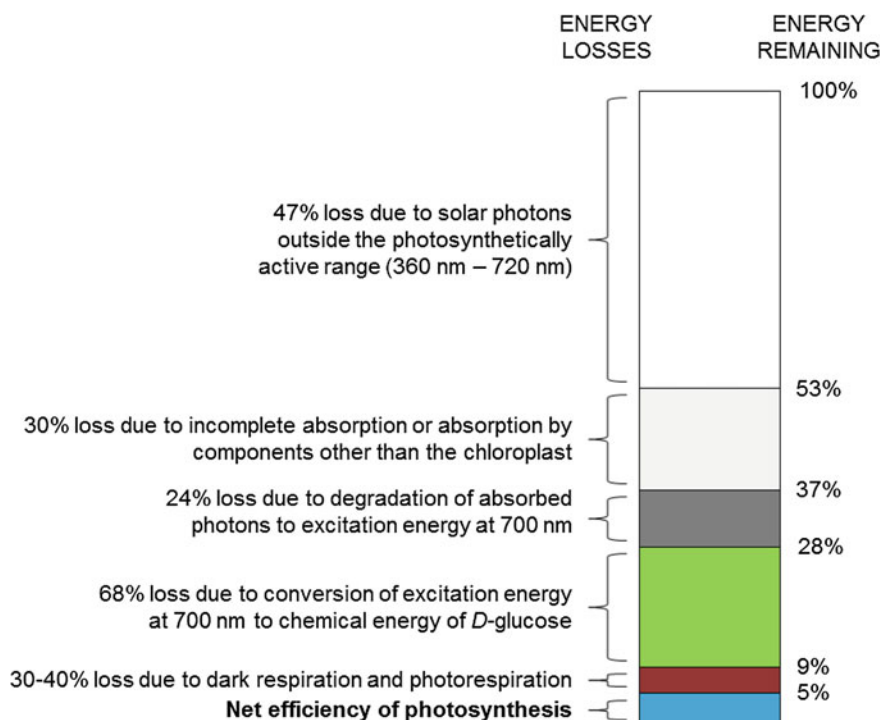


Fig. 1.5 Energy losses in photosynthesis according to Ref. [26]

intrinsically simpler synthetic device, solely dedicated to converting solar to chemical energy *and* capable of utilising the solar spectrum to a maximum extent offers possibilities for much higher conversion efficiencies.

1.2.2 The Photosynthetic Reactions

1.2.2.1 From Light-Absorption to Carbon Dioxide Fixation—A Brief Overview

In oxygenic photosynthetic organisms (plants, algae, and cyanobacteria), the photosynthetic apparatus involved in the light reactions is embedded in the thylakoid membrane [26]. Two reaction centres (protein complexes in which light energy is converted to electrochemical potential) termed Photosystem I (PSI) and Photosystem II (PSII) are coupled to provide sufficient energy to oxidise water and reduce CO_2 (Fig. 1.6). Two photons are required to drive each electron through this system, commonly termed the ‘Z-scheme’. Energy storage is accomplished by rapid separation of the initial oxidants and reductants of the primary charge separation events so as to avoid wasteful recombination reactions [26].

In all types of photosynthetic organism, light-harvesting antenna systems funnel excitation energy rapidly to the respective reaction centre [27, 28] through Förster resonance energy transfer on a sub-nanosecond time domain. The overall energy transfer rates are faster than the singlet excited state lifetimes of the pigments involved, requiring these to be located in close proximity, with typical centre-to-centre distances being 10–15 Å [26]. Approximately 250 pigments service

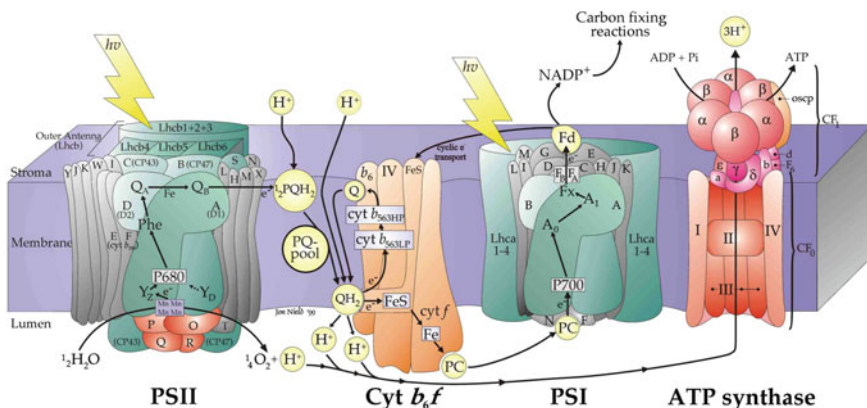


Fig. 1.6 Cartoon showing the electron-proton transport chain of oxygenic photosynthesis in the thylakoid membrane. Copyright Professor James Barber, Imperial College London. See main text for key abbreviations

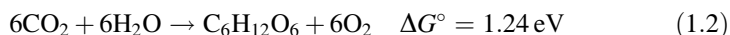
a reaction centre in plants and algae; the main molecules bound to light-harvesting proteins are chlorophyll *a*, chlorophyll *b*, and carotenoids [26].

Once excitation energy arrives at the reaction centre from the light-harvesting system, primary charge separation occurs, followed by secondary electron flow to a terminal electron acceptor, ferredoxin (Fd) in PSI and quinone (Q_B) in PSII (see Fig. 1.6) [26]. As mentioned above, in oxygenic photosynthetic organisms the two photosystems work together to oxidise water and reduce ferredoxin; two photons are needed to drive one electron from water to Fd.

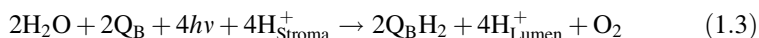
PSI and PSII are coupled by cytochrome (Cyt) *b₆f*, which acts as a plastoquinol-plastocyanin oxidoreductase and facilitates the maintenance of the electrochemical potential gradient of protons across the thylakoid membrane needed to convert ADP to ATP [26]. Reduced ferredoxin is used to convert NADP⁺ to NADPH, which, together with ATP, is required to convert CO₂ to carbohydrates.

Carbon dioxide fixation takes place separately from the light-driven reactions in the stroma or cytoplasm [26]. Photosynthetic organisms can carry out the required transformational sequences in the dark; hence, the processes of carbohydrate formation are often referred to as the ‘dark’ reactions. The most common pathway of photosynthetic carbon assimilation is the C₃ or reductive pentose cycle, which operates in algae and most plants [26]. Central to this sequence is the Calvin cycle, the complex metabolic pathway by which plants incorporate CO₂ as carbohydrates [29]. In short, carboxylation of the CO₂ acceptor ribulose-1,5-biphosphate (RuBP), catalysed by the enzyme RuBisCO (ribulose-1,5-biphosphate carboxylase-oxygenase), is followed by reduction of the primary product to a 3-carbon sugar phosphate and regeneration of RuBP [30].

When comparing the reversible potential for water splitting into hydrogen and oxygen [Eq. (1.1)] with the reversible potential for the reduction of CO₂ to carbohydrate and water [Eq. (1.2)] it becomes apparent that, from an energetic standpoint, water splitting lies at the heart of photosynthetic solar energy storage [31, 32]. Only a mere 0.01 eV more energy (on an electron equivalency basis) is stored in the production of carbohydrates:



The light-driven redox chemistry of PSII [Eq. (1.3)] closely resembles the water splitting reaction described in Eq. (1.2): water is oxidised to dioxygen and the reducing equivalents (‘hydrogen’) leave the photosystem in the form of reduced plastoquinol (Q_BH₂) [22], at an estimated [33, 34] midpoint potential ($E_m(\text{Q}_\text{B}\text{H}_2/\text{Q}_\text{B}) = -0.06 \text{ V}$ [35, 36]) similar to the thermodynamic potential for H⁺/H₂ interconversion.



The reaction described in Eq. (1.3) is coupled to acidification of the lumen and alkalinisation of the stroma [37] (see Fig. 1.6). Because of the important similarities

Fig. 1.7 **a** Cartoon representation of Photosystem II based on a recent 1.9 Å resolution crystal structure (PDB code 3ARC) [38]. The main electron transfer components and the OEC are highlighted. **b** Schematic illustration of kinetic and thermodynamic parameters of the charge separation events in PSII. Key abbreviations are defined in the main text. Reprinted with permission from Ref. [37]. Copyright 2012 Elsevier

between Eqs. (1.2) and (1.3), the next section will cover the processes occurring in PSII in more detail.

1.2.2.2 Water Splitting by Photosystem II

Figure 1.7a depicts a cartoon representation [37] of a 1.9 Å resolution crystal structure of PSII [38]. Photosystem II is a homodimeric complex [39], the reaction centre consists of two proteins, D1 and D2, with the electron transfer processes occurring mainly on the D1-side [40]. Some of the symmetrically related D2 cofactors are non-functional, whereas others are functionally active and seem to play a role in protecting PSII against photoinduced damage [22].

As illustrated in Fig. 1.7b, initial electron-hole separation occurs after excitation of the primary electron donor P680, which is composed of four chlorophylls located in close proximity (known as P_{D1} , P_{D2} , Chl_{D1} , and Chl_{D2}). In $P680^*$,¹ the excited-state electron is likely delocalised over all four chlorophyll centres, but the initial electron donation occurs from Chl_{D1} [22]. Electron transfer to the primary electron acceptor pheophytin *a* (denoted ‘Phe’ in Fig. 1.7) occurs on the ultrafast time domain with a lifetime of approximately 3 ps; subsequent electron transfer to the intermediate, bound plastoquinone Q_A occurs within 300 ps [33, 34, 37, 41]. The latter event, termed ‘stabilisation step’ [42] comes at an energetic cost in the range of 0.6 eV [43]. These two electron transfer events are followed, on the kinetic timeline, by hole injection from $P680^+$ into the redox active tyrosine Y_z , regenerating the ground state of the former [42]. This step is accompanied by proton transfer to the nearby (with respect to Y_z) D1His190, resulting in the formation of a neutral tyrosine radical [42], which then oxidises the oxygen evolving cluster OEC (as described in more detail below). Finally, electron transfer from the reduced primary quinone acceptor Q_A^- to the secondary two-electron acceptor plastoquinone Q_B occurs on the μ s to ms regime, mediated by a non-haem Fe centre that is ligated by four histidine ligands [22]. Once Q_B has accumulated two electrons and two protons [compare Eq. (1.3)] it departs from the reaction centre via the hydrophobic lipid phase of the membrane and enters the electron/proton transfer chain illustrated in Fig. 1.6 [22]; it is replaced by an oxidised plastoquinone molecule from the membrane-soluble plastoquinone pool [39].

¹The superscript ‘*’ commonly refers to the excited that of a molecule/group. This notation is used throughout this thesis.

Although the series of electron transfer events described above comes at a significant energetic cost (see Fig. 1.7b), Nature has engineered and optimised these processes, making the quantum efficiency of charge separation approach 100% [41, 44]: ‘barrierless’ forward electron transfer over great distances occurs at maximum rate, while destructive recombination is greatly retarded and rendered kinetically unfavourable. The theory that mathematically links the thermodynamics and kinetics of electron transfer events, developed first and foremost by Marcus, is discussed in Sect. 2.4.

The processes in Fig. 1.7 that govern the splitting/oxidation of water to dioxygen occur in the OEC, located off-centre towards the D1 side of the core reaction centre complex of PSII [29]. To achieve O₂ evolution, a catalyst must survive the production of very electrophilic and highly oxidising intermediates, which seems at first incompatible with organic chemistry. Biology has indeed adopted a cofactor that is ‘mineral-like’ but housed in a subunit that is regularly replaced to offset oxidative damage (vide infra). The OEC has a composition of [4MnCa–5O] (where the Mn ions are commonly designated Mn1 to Mn4 and the oxygens are referred to as O1–O5) and serves as the ‘benchmark’ catalyst for O₂ evolution: it is capable of operating at neutral or near-neutral pH under ambient conditions [31], achieving turnover frequencies (TOFs) > 100 s⁻¹ (the hypothetical maximum being *ca.* 500 s⁻¹ [39]) at a relatively modest overpotential, compared to synthetic analogues, of approximately 400 mV [36]. The [4MnCa–5O] complex self-assembles by an oxidative mechanism [45] involving the photooxidation of Mn(II) ions bound to the apo-coordination environment [46] of the PSII complex to Mn(III), with the oxidising equivalents being passed through the P680–Y_z pathway depicted in Fig. 1.7 [31].

As the water splitting reaction produces toxic reactive oxygen species, the turnover number (TON) of the OEC is limited to approximately 10⁶; subunit D1, which supplies most of the ligands to the [4MnCa–5O] cluster, is replaced as frequently as every 30 min [31, 47], being damaged by the intense photocatalytic activity. This process is accompanied by the disassembly of the OEC, which reassembles upon re-insertion of D1 [31].

The crystallographic model of PSII resolved to 1.9 Å resolution firmly established the cubane motif of the OEC depicted in Fig. 1.8a, proposed by Barber (apart from the position of Mn4 [40]), Dau et al. [48], and Siegbahn [49, 50], even though photoreduction of the electrophilic Mn-complex upon X-ray exposure caused significant Mn–O/N and Mn–Mn/Ca distance elongations (reviewed in Ref. [37]).

As established by Kok [52], the OEC undergoes a series of five different redox states known as S₀ to S₄ (see Fig. 1.8b), which represent successively more oxidised forms [29]. According to this model, the system advances through the cycle by single electron/proton transfer steps, each following excitation of P680, until O₂ is spontaneously, i.e. within 1 ms [53], released upon formation of the transient S₄ state. In the dark, S₂ and S₃ decay back to the dark-stable S₁ state, meaning approximately three-fourths of the OEC appear to be in the S₁ state, with one-fourth being in state S₀ (S₄ is unstable and occurs only transiently) [29].

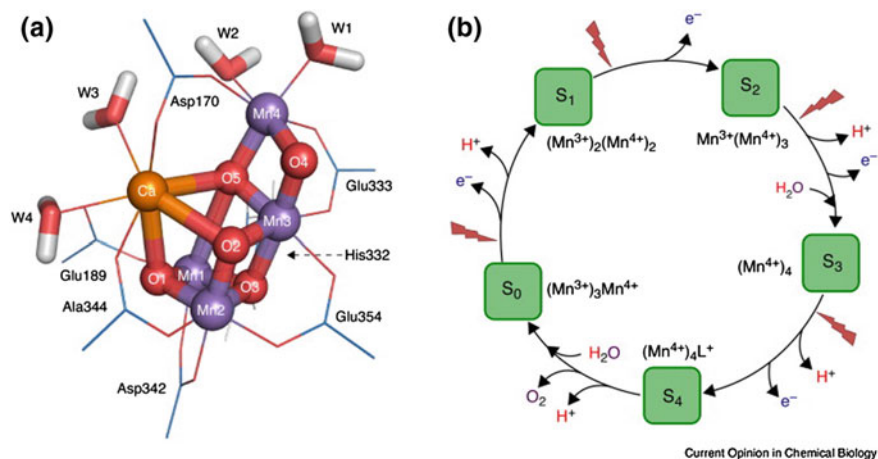


Fig. 1.8 **a** Structural representation of the OEC and coordinating residues according to the crystal structure presented by Shen et al. [38], computationally optimised for the dark-stable S₁ state [51]. All labelled side chains apart from Glu354 belong to the D1 protein. Abbreviations are defined in the main text. **b** Sequential steps leading to O₂ formation according to Kok [52]: electrons and protons are released in an alternating pattern, starting from the S₁ state, until O₂ release spontaneously occurs in the S₄ state. Reprinted with permission from Ref. [39]. Copyright 2015 Elsevier

Whilst the Kok cycle formally explains the observed pattern for O₂ release, it does not provide mechanistic details on how O–O bond formation occurs. Although the precise mechanism is still under debate [36, 37, 39, 54, 55], a more detailed picture is emerging thanks to recent progress from both experimentalists and theoreticians. Two main, competing mechanistic proposals have evolved over the last one and a half decades: Brudvig and co-workers put forward a mechanism in which O₂ formation occurs by nucleophilic attack of a Ca-bound water molecule on a highly electrophilic Mn(V)-oxo species at Mn4 [56, 57]. In contrast, a radical coupling mechanism, in which dioxygen is formed between an oxyl radical in the centre of the cluster and a Mn-bridging μ -oxo ligand, has been championed by Siegbahn [49, 50, 58–60].

Recently, multifrequency, multidimensional magnetic resonance spectroscopy revealed a detailed picture of the electronic configuration of the S₃ state [61], meaning that all S-states prior to O₂ release in the transiently occurring S₄ state have now been trapped at low temperatures and characterised [54, 62]. As indicated in Fig. 1.8b, the [4MnCa–5O] cofactor is assigned to an all-octahedral (Mn(IV))₄ complex, with all Mn ions being coordinatively saturated through six-fold coordination. Hence, all S-state transitions before S₄ represent Mn-centred oxidations.

Lubitz and co-workers established that this all-octahedral coordination geometry is achieved through inclusion of an additional, water-derived hydroxyl ligand at Mn1 (along the Mn4–Mn1 axis) upon one electron oxidation of S₂ [61]. However, it remains to be determined whether this second, late binding substrate represents an

additional water molecule binding from bulk solvent or a repositioned terminal oxygen ligand of Mn4 (W2 in Fig. 1.8a) or Ca (W3 in Fig. 1.8a). Conversely, the early binding substrate water is incorporated into the cluster via Ca(II) at the start of the Kok cycle, i.e. at S_0 [54]. Presumably, the structural flexibility the OEC shows in the S_2 state ('open' vs. 'closed' geometry) makes the inclusion of this additional, late binding water ligand possible. The S_3 state characterised by Lubitz et al. is similar to recent S_3 models proposed by Siegbahn [60], the calculations of whom suggest that the flexibility of the S_2 state is lost upon formation of the S_3 state [63], with the cluster then adopting an 'open' geometry.

Regardless of the precise identity and origin of the additional hydroxyl ligand at Mn1 in S_3 , O–O bond formation most likely proceeds by coupling of the two proximal oxygens ligated to Mn1 and Mn4 [61], in contrast to the reaction of an Mn4-oxo species with a Ca-bound water/hydroxide ligand. The final oxidation towards S_4 can then either be substrate-centred [64], generating the Mn(IV)-oxyl radical proposed by Siegbahn [50, 58, 60], or metal-centred, resulting in the formation of a Mn(V)-oxo species proposed by Brudvig et al. [56]. While such high-spin Mn(V)-O species are unknown in other biological contexts [53], a metalorganic variant has been synthesised [65]. The fact that the Mn4 and Mn1 ions carry opposite spin in S_3 [61] would, in a radical-coupling mechanism, lead to the development of opposite spin on the two substrate oxygens in the S_4 state, decreasing the barrier for O–O bond formation [50, 58, 60] such that it is significantly lower than for the nucleophilic attack mechanisms preferred by Brudvig and colleagues [36]. An oxo/oxyl radical coupling mechanism is also supported by substrate water exchange studies, reviewed in Refs. [54, 55, 62].

Although we cannot *yet* discriminate between the two putative pathways, the scientific community is rapidly advancing to close the remaining gaps in the mechanism of photosynthetic dioxygen formation. Emerging experimental techniques such as time-resolved X-ray spectroscopy and diffraction [66, 67], which allow studying the structural and chemical dynamics of the OEC under functional conditions, could soon provide concluding evidence.

1.2.3 Using Photosystem II as a Guide for Assembling an Artificial Photosynthetic System

The highly engineered processes of natural photosynthesis, 'perfected' by evolution, are highlighted in Sect. 1.2.2. Understanding the Natural system allows identification of the essential components chemists have to mimic for assembling artificial photosynthetic systems and, moreover, the processes that Nature does not carry out with sufficient efficiency. Hence, there is room for improvement, as discussed below.

First, despite the complexity and intricacy of photosynthetic organisms, biology has no difficulty in constructing these in rapid and reliable stages by

‘polymerisation’ and *self-assembly* processes that follow a blueprint. Hence, the problem of short-lived activities can be compensated by the replacement of worn-out parts, such as *catalyst repair* of the OEC described in Sect. 1.2.2.2. Herein lies a lesson for artificial photosynthesis, because outside biology there is no automatic repair mechanism for oxidative damage: a useful synthetic oxygen evolution catalyst must therefore be stabilised under oxidising conditions and avoid organic ligands.

Second, the photosynthetic reaction centres are not only able to efficiently generate free charge carriers (by utilisation of low-energy near-infrared photons), but, crucially, can achieve *spatial electron-hole separation across long-distances*, with carefully tuned redox potentials so as to minimise energy loss as heat.

Third, even a reaction as thermodynamically demanding as water oxidation [compare Eq. (1.1)] is catalysed *with high turnover frequencies under environmental conditions*, i.e. by *proton-coupled electron transfer catalysis* using earth-abundant elements at (near) neutral pH, ambient pressure and temperature, and with minimal driving force (overpotential). An important feature, identified by Lubitz et al. [61], could be the ability of the OEC to incorporate the second substrate water late in the catalytic cycle in a concerted process coupled to S₂ oxidation, to avoid slow, two-electron reactivity. Replicating these features constitutes a grand challenge for the synthetic community.

However, the natural photosynthetic apparatus (Fig. 1.6) imposes certain limitations an artificial system needs to address and overcome. First and foremost, these are the complexity of the photosynthetic organism and the resulting efficiency limitations. An engineered device has to be intrinsically simpler in design, with its sole purpose being the conversion of solar energy to chemical molecules. Further, even a process as highly optimised as photosynthesis suffers from some form of energy-mismatch, i.e. the limited ability to reconcile single-photon charge-generation with two types of multi-electron catalysis—the four-electron chemistry of water oxidation and two-electron ‘hydrogen’ formation. While the OEC has a hypothetical maximum TOF of approximately 500 s⁻¹, the observed turnover rate of PSII is 25–88 O₂ s⁻¹, with kinetic limitations arising mainly from slow plastoquinol (H₂Q_B) exchange [39].

To summarise, a future artificial system has to be made from robust materials comprising earth-abundant elements, using inexpensive and scalable processes. Independent of its design architecture, it must contain light-absorbers that can utilise the electromagnetic spectrum to a maximum extent, even 1000 nm infrared light contains enough energy to effect water splitting. Further essential components include charge-separators such as membranes that prevent recombination and back reactions, and multi-electron catalysts for both water oxidation and fuel-formation that can keep up with the solar-flux, have the ability to synchronise proton and electron transfer to avoid high-energy intermediates, operate at the limit of reversibility and do not kinetically limit the overall process, and, last but not least, work under benign conditions.

These restrictions make apparent that an artificial photosynthetic system will have to *functionally* mimic natural photosynthesis, not *structurally*. One ought to

remember that, as Blankenship puts it [29], “although both airplanes and birds are devices that fly, they work in very different ways. Yet, they must obey the same laws of physics. If birds and other flying creatures did not exist, it is unlikely that people would have ever invented airplanes, as the idea would simply have been too far outside of the realm of possibility. The existence of natural photosynthetic systems provides the inspiration and the conceptual framework for artificial photosynthetic devices, even if the details of the implementation are entirely different in the two systems.”

1.3 The Individual Components of Artificial Photosynthetic Systems

1.3.1 Light-Absorption and Charge Separation

1.3.1.1 General Considerations

Independent of the type of light-harvester employed (e.g. molecular dye or semiconductor), optimal electronic coupling to the respective, ideally reversible and highly efficient multi-electron catalyst for oxygen evolution and fuel-formation needs to be ensured. Properties to be enhanced are, amongst other things, wavelength and absorption efficiency, exciton propagation and charge separation, and the lifetime(s) of the charge-separated state(s).

1.3.1.2 Molecular Dyes

Building on the principles of photosynthetic light-absorption and charge separation, much effort has been put into mimicking naturally occurring antenna systems. Many organic or organometallic pigment architectures have been designed over the past decades, examples include tris(bipyridine)ruthenium(II) derivatives [68] or supramolecular porphyrin based systems [69, 70] including the recently developed ‘high-potential’ porphyrins [71]. A distinct advantage of these types of molecular light-absorber is that their (excited-state) energy levels can be precisely tailored through synthetic modifications. Further, their photochemistry, particularly the kinetics of charge separation and recombination, is well established: in addition to having large extinction coefficients in the visible region, these types of dye possess long-lived charge-separated (triplet) states, allowing for electron/hole injection into a catalyst before recombination occurs [68, 72, 73]. Yet, their lack of robustness and durability, especially under the harsh conditions of water oxidation, makes molecular dyes unsuitable for incorporation into tightly integrated systems.

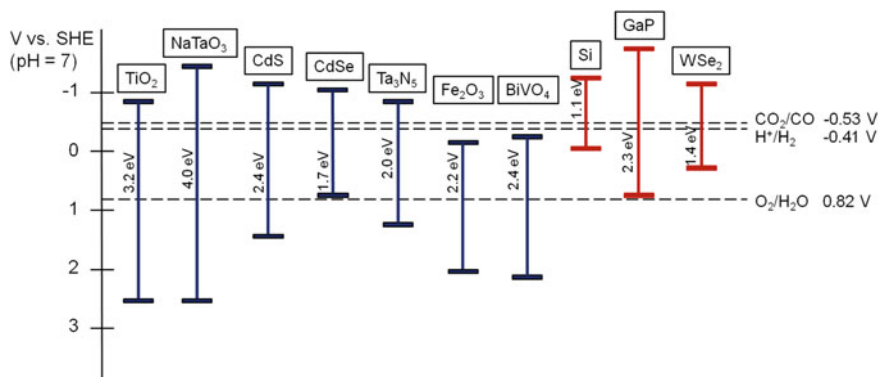


Fig. 1.9 Electronic band structures of selected *n*-type (blue) and *p*-type (red) semiconductors at neutral pH, as well as reduction potentials for O₂ evolution, CO₂ reduction, and H₂ formation from water. Reprinted with permission from Ref. [83]. Copyright 2015 Springer

1.3.1.3 Metal-to-Metal-Charge-Transfer Units

An interesting approach toward visible-light capture and electron-hole separation has been developed by Frei: all-inorganic oxo-bridged binuclear metal-to-metal charge-transfer (MMCT) units [74] combine the advantage of broad absorption well into the visible region, known for molecular dyes, with the robustness of metal oxides. Integration of MMCT units into silica scaffolds allows scalability and provides opportunities for separating reduction and oxidation sites, while the redox potentials can be tailored through the use of different abundant first row transition metal centres [75]. These units, some of which show remarkable charge-separated state lifetimes (μs -regime) [76], have been employed to drive water oxidation [77, 78], as well as CO₂ reduction [79, 80]. Recently, MMCT units have been incorporated into an integrated system capable of reductively activating CO₂ using water as the electron source [81].

1.3.1.4 Semiconductors

Natural photosynthetic light-harvesting pigments can also be mimicked by semiconductors, e.g. in the form of particles (nano, micro) or (porous) electrodes. A guide to optical and electronic properties of some important semiconducting materials is shown in Fig. 1.9, alongside electrochemical data (reduction potentials) for fuel- and O₂-forming reactions under neutral conditions. The investigator needs to consider both *n*- and *p*-type conductivity of materials, their carrier mobilities and band gaps, and how the conduction and valence band potentials are suited, respectively, for fuel formation or O₂ evolution. The values shown are for the bulk materials, but they still provide a good guide as to what is expected for the respective nanoparticles and highly porous structures. Attachment of external,

visible-light-absorbing sensitisers such as the pigments described in Sect. 1.3.1.2 can greatly enhance the absorptive abilities of wide-band gap materials that would otherwise be transparent in the visible region of the electromagnetic spectrum; this approach is based on the advent of dye-sensitised solar cells (DSSCs) [82], which commonly use n -TiO₂ as large band gap semiconductor, modified with ruthenium polypyridyl sensitisers. The surface chemistry of the material becomes important when considering strategies for attaching sensitisers and catalysts.

In Fig. 1.9 the electronic band structures of selected n -type and p -type semiconductors are represented by blue and red lines, respectively. To be useful for artificial photosynthesis, the conduction band minimum must be more negative than the reduction potential of the fuel-forming reaction (H₂ evolution or CO₂ reduction), and the valence band maximum must be more positive than the reduction potential of the oxidation reaction (ideally O₂ evolution from water). Metal oxides such as TiO₂ satisfy these conditions, but at the cost of a wide band gap, resulting in lower utilisation of the solar spectrum. Some non-oxide materials, e.g. chalcogenides and nitrides, can have a smaller band gap due to the contribution of less electronegative S and N atoms to the valence band. The stability of the semiconductors in water must also be considered, as chalcogenides, among other materials, can undergo self-decomposition in water under irradiation [84].

Some materials are only suitable for half of the overall reaction, due to insufficient positioning of either the conduction band or valence band. For example, BiVO₄, an n -type material that has been used in conjunction with a variety of water oxidation electrocatalysts [85, 86], is only useful for O₂ evolution due to its conduction band minimum lying more positive than the H₂ evolution potential [87]. To construct an overall water splitting system, such materials can be used with an applied bias in a photoelectrochemical set-up or in conjunction with another light-absorbing material that is able to evolve H₂ or reduce CO₂ (see Sect. 1.4).

1.3.1.5 Photovoltaics

Due to rapid progress of the photovoltaic community [9], especially in emerging PV technologies (see Fig. 1.10), the ‘brute force’ approach of directly using solar cells to power ‘dark’ electrocatalysis can also be considered. Whereas the multi-junction cells that have previously been deployed in artificial photosynthetic systems [11–15] were too intricate and costly to allow for scale-up, new technologies are on the horizon that have the potential to overcome the Shockley–Queisser efficiency limit for single band gap cells of approximately 34% [88]. These include third generation cells [89–91] and strategies such as multiple-exciton generation [92] and singlet-fission [93, 94].

Of particular interest are organometal trihalide perovskite-based solar cells [95–97], most commonly using methylammonium lead triiodide as the light-absorber [98] (see Fig. 1.11 for a structural representation). Originally employed as visible-light sensitisers for liquid-electrolyte TiO₂-based DSSCs [99], a paradigm shift occurred when Snaith established, using mesoporous Al₂O₃

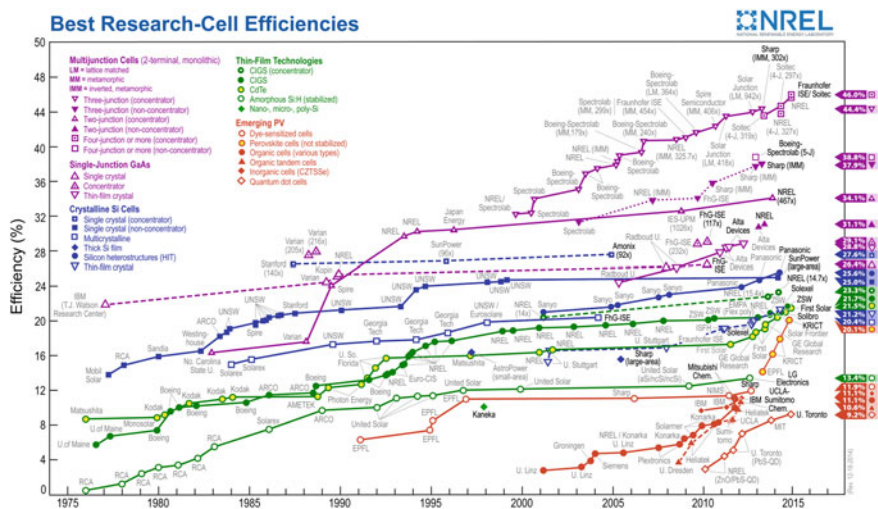


Fig. 1.10 Compilation of the highest confirmed conversion efficiencies for research cells of different photovoltaic technologies, confirmed by independent, recognised test laboratories. This plot is courtesy of the National Renewable Energy Laboratory, Golden, CO, USA

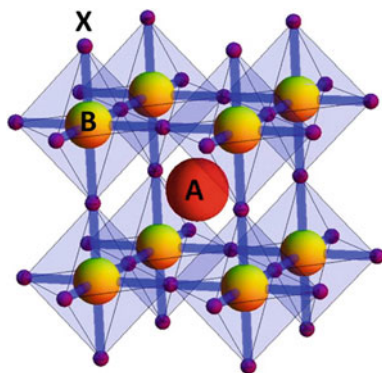


Fig. 1.11 Ideal cubic structure of perovskite, with the general formula ABX_3 , consisting of corner-sharing octahedra (BX_6) with the A-cation occupying a 12-fold coordination site. In $CH_3NH_3PbI_3$, A is the monovalent cation $CH_3NH_3^+$, B represents the divalent cation Pb^{2+} , and X corresponds to the monovalent halide anion I^- . Reprinted with permission from Ref. [106]. Copyright 2015 American Chemical Society

instead of TiO_2 (the former being unable to accept electrons from the sensitizer), that the perovskite itself acts as the charge-transporter and must therefore have a high charge-carrier mobility [100]. Indeed, the effective diffusion length is relatively large in $CH_3NH_3PbI_3$ [101, 102]; values exceeding $1 \mu m$ have been reported for a mixed halide (iodide-chloride) variant [101]. With a reported efficiency of 10.9%, this new, unoptimised type of cell already rivalled highly optimised DSSCs

[103]. Subsequent to this seminal discovery, it was established that complex nanostructures are not vital to cell performance and thin films created by vapour deposition offer even higher efficiencies [104]. Values as high as 20% [105] have been realised only two years after the initial report by Snaith.

Although few stability studies have been performed so far [107, 108] and it is yet unclear whether these perovskite-based cells can meet the stringent norms for outdoor photovoltaic applications [97], a reported efficiency decrease of less than 20% after 500 h of operation [107] can certainly be regarded as encouraging [98]. The toxicity of lead also needs to be addressed, as $\text{CH}_3\text{NH}_3\text{PbI}_3$ converts to the known carcinogen PbI_2 under humid conditions [97]. However, less than 10,000 tons of lead would be needed for a production capacity of 1000 GW per year compared to 4 million tons used per year for lead-acid batteries [98]. The spectacular rise of perovskite cells prompted their integration into artificial photosynthetic systems and, indeed, Grätzel and colleagues realised a device with a solar-to-hydrogen (STH) efficiency of 12.3% [16], using two perovskite cells connected in electrical series. Their approach takes advantage of the high photovoltage offered by $\text{CH}_3\text{NH}_3\text{PbI}_3$; a related study using silicon photovoltaics relies on four cells connected in series [17].

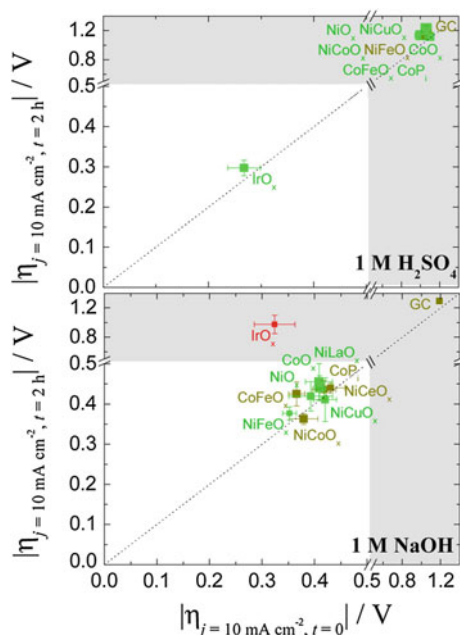
1.3.2 Water Oxidation Catalysis

As outlined in Sect. 1.2.2.2, the four-electron/hole chemistry of water oxidation is thermodynamically and kinetically challenging. Following billions of years of evolution, Nature has evolved the mineral-like OEC that serves as the benchmark, both in terms of achieved turnover frequencies at low driving force and its composition of earth-abundant elements.

In the synthetic world, the best contenders are transition metal oxides, apart from a few transition metal complexes that are, most notably, based on Ru (originally developed by Meyer [109, 110]) or Ir (pioneered by Crabtree [111–113]). Furthermore, a bipyridine-isoquinoline ruthenium complex co-developed by Llobet and Sun exhibits a water oxidation TOF of 300 s^{-1} under acidic conditions, which is comparable to the rates of PSII *in vivo* ($100\text{--}400 \text{ s}^{-1}$) [114]. Although the TON of 8400 might indicate chemical stability, the compound degrades within a minute. Furthermore, these performance measures were achieved under the large driving force provided by the highly oxidising Ce(IV) ion ($E^0 = +1.76 \text{ V}$ vs. the standard hydrogen electrode, SHE) [115]. The development of other molecular water oxidation electrocatalysts has recently been reviewed by Åkermark and colleagues [116]. Several groups have achieved photocatalytic O_2 evolution catalysed by molecular catalysts interacting with/coupled to different types of light-absorber such as tris(bipyridine)ruthenium(II) sensitisers [117–119], perylene diimide derivatives [120], dye-sensitised TiO_2 [110, 121–125], WO_3 [126], and BiVO_4 [127].

The catalytic activity and stability of several heterogeneous oxygen evolution catalysts has recently been ‘benchmarked’ by Jaramillo and co-workers, at a current

Fig. 1.12 Comparison of catalytic activity, stability, and electroactive surface area for heterogeneous water oxidation catalysts in acidic and basic media. The overpotential requirement for operation at 10 mA cm^{-2} of a given catalyst after $t = 2 \text{ h}$ is plotted against the overpotential requirement at $t = 0$. Hence, the dashed line indicates a stable catalyst. Only catalysts with activity and stability parameters falling into the non-shaded area of the plot have sufficient activity to be considered benchmarks. Adapted with permission from Ref. [128]. Copyright 2013 American Chemical Society



density of 10 mA cm^{-2} that corresponds to a 10% solar-to-fuel conversion efficiency (Fig. 1.12) [128]. In alkaline solution, every non-noble metal system achieved this current density at similar operating overpotentials between 0.35 and 0.43 V. However, only iridium oxide (IrO_x) is stable under oxidative conditions in acidic solutions. It is important to note that although benchmarking experiments are easiest to carry out in acidic or basic media, a future artificial photosynthetic system will have to operate at neutral pH, ideally using waste or sea water. Iridium oxide closely approaches the efficiency and stability required for the ultimate use in integrated artificial photosynthetic systems, demonstrated both under electro- (see Fig. 1.12) and photocatalytic conditions—for example, a TOF of 40 s^{-1} has been demonstrated for colloidal IrO_2 particles under a modest overpotential of 370 mV [129]. Iridium oxide has also been deposited onto semiconductor surfaces such as hematite [130] and TiO_2 [131, 132] for light-driven photoelectrocatalytic water oxidation. However, iridium oxide is not a viable catalyst for future large-scale systems as it is the least abundant stable element in the upper continental earth crust [133].

The good news, however, is that in the context of the ability to operate efficiently at neutral pH, first-row transition elements do feature well: even the *isolated* OEC is predicted to be a good O_2 -evolving catalyst [83]. To be efficient, the catalyst must be able to store four oxidising equivalents at the right potential and/or stabilise intermediates just sufficiently so that they are not too tightly bound. Further, as described in Sect. 1.2.3, the water oxidation catalyst must either be durable and

robust, or have the ability to undergo self-repair. The Co ('Co-Pi') and Ni oxide catalysts developed by Nocera and co-workers are good examples of heeding this latter requirement [134, 135]. Interestingly, the amorphous cobaltate films in Co-Pi, as established by X-ray absorption spectroscopy [136, 137], are nearly identical structural congeners of the PSII-OEC: both systems are of partial cubane structure with identical metal-metal ($d = 2.82 \text{ \AA}$) and metal-oxo ($d = 1.89 \text{ \AA}$) distances [31]. The discovery of this type of catalyst sparked intense research activity across the scientific community. Several groups have achieved photoelectrocatalytic water oxidation by interfacing cobalt oxide electrocatalysts with semiconductor electrodes made of ZnO [138], Si [139, 140], TiO₂ [141], Fe₂O₃ [142, 143], WO₃ [144], and BiVO₄ [145–149].

Another class of emerging heterogeneous electrocatalysts for water oxidation are metal oxyhydroxides such as FeOOH and NiOOH [150, 151], recently interfaced with photoanodes made of TiO₂ [152] and BiVO₄ [153, 154]. Choi et al. serially applied dual layers of both FeOOH and NiOOH on a nanoporous BiVO₄ photoanode, with the former reducing interface recombination at the BiVO₄/OEC junction and the latter creating a more favourable Helmholtz layer potential drop at the OEC/electrolyte junction (NiOOH) [155]. The resulting BiVO₄/FeOOH/NiOOH photoanode achieves a photocurrent density of 2.73 mA cm^{-2} square at a potential as low as 0.6 V vs. the reversible hydrogen electrode (RHE), even without doping the underlying BiVO₄ semiconductor layer.

Yet, despite progress being made in the area of water oxidation catalyst development, new materials will have to be developed to collectively address efficiency, durability, and abundance of materials. Novel experimental techniques such as pulsed-laser ablation [156, 157] or photochemical metal-organic deposition [158], in combination with high throughput screening techniques [159–162], may greatly accelerate this search.

1.3.3 *H₂ Formation*

1.3.3.1 Molecular Catalysts

Platinum is well established as a reversible catalyst for hydrogen production, but it is too rare to allow it to be scaled up for global artificial photosynthesis and there is much interest in finding alternatives. Hence, extensive research activities are being carried out, most promisingly in the areas of organometallic and solid-state chemistry. Well-known contenders from the organometallic world are cobalt tetraazamacrocycles [163–167] such as cobaloximes [168, 169]. Originally developed as model compounds for vitamin B₁₂ [170], these species have been explored extensively as catalysts for the hydrogen evolution reaction over the past three decades. Mechanistically, Gray and colleagues established that a transiently

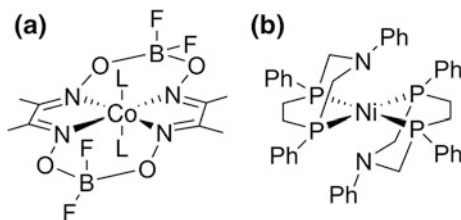


Fig. 1.13 Well-known molecular hydrogen evolution catalysts. **a** Cobaloxime complex (L is typically H_2O or CH_3CN) [169]. **b** Nickel bisdiphosphine catalyst developed by DuBois [173]

generated Co(III)-hydride is reduced to the Co(II) hydrido complex, which, upon protonation, yields molecular hydrogen [171]. Theoretical calculations from Hammes-Schiffer [172] showed that in addition to this monometallic pathway, favoured at high acid concentrations, these complexes can also undergo bimetallic reactions in which both two Co(III)-H or two Co(II)-H complexes can react to produce H_2 . It is worth noting that despite the great deal of mechanistic insight these complexes offer, there is still much room for improvement, particularly in terms of stability (TON), TOF, overpotential requirement, and solubility in water (Fig. 1.13).

More recently, a family of nickel bisdiphosphine electrocatalysts has been pioneered by DuBois [174, 175]. These molecules are based on a nickel (II) redox platform and feature a pendant amine base in close proximity to the metal. Mechanistically, dihydrogen formation occurs by reaction of a Ni(II)-hydrido complex with a protonated amine-N. The Ni(II) hydride is proposed to be generated by initial reduction of a Ni(II) species to Ni(I) followed by protonation of the pendant amine, transfer of a second electron leading to a monoprotonated Ni(0) complex and eventual hydride formation after protonation of a second pendant amine-N [176]. Alternatively, two consecutive reductions can occur prior to the first protonation step, leading to an unprotonated Ni(0) intermediate [177].

Both turnover frequencies and overpotential requirements of this family of catalysts can be tailored through ligand modification. Through rational design, turnover frequencies of $106,000\text{ s}^{-1}$ have been achieved in a mixture of acetonitrile and water [173]. Derivatives modified with amino acids have been shown to catalyse H_2 production/oxidation fully reversibly at elevated temperatures in aqueous suspension, highlighting the importance of the outer coordination sphere [178]. This study, where an arginine-modified variant emerged as particularly proficient catalyst, addresses the lack of water solubility most of the DuBois-type complexes suffer from [166], albeit at the cost of synthetic complexity.

Both cobaloximes and DuBois-type catalysts have been ‘heterogenised’ through immobilisation on a variety of materials, including carbon nanotubes [179–181], and, for light-driven H_2 evolution, semiconducting materials such as TiO_2 [182–185], CdSe [186], Si [187], NiO [188], and GaP [189], as well as ‘soft’

materials including self-assembling hydrogel scaffolds [190]. Advances in the development of hybrid photocatalysts for solar-fuel production are reviewed by Loo et al. [191].

1.3.3.2 Solid-State Catalysts

The activities of a variety of heterogeneous hydrogen evolution catalysts have been evaluated under standardised conditions, showing that most catalysts exhibit much lower specific activity than Pt, which still serves as benchmark in both acidic and alkaline solutions [192]. However, progress is being made and several new non-precious metal electrocatalyst materials, sulphide and phosphide derivatives in particular, have emerged as promising contenders for electrochemical hydrogen evolution under harsh acidic conditions, offering nearly platinum-like catalytic performance [193].

The isostructural materials molybdenum sulphide (MoS_2) and tungsten sulphide (WS_2) [194–196] (the latter being slightly less active [166]), both well established catalysts for hydrodesulphurisation [197], are considered promising due to their high electrocatalytic activities and stabilities over a wide pH range [166]. Although the precise mechanism of H_2 formation by these layered S–M–S ($\text{M} = \text{Mo}$ or W) materials is still unclear, Jano and colleagues recently established that terminal disulphide units are involved in the reduction of protons by amorphous molybdenum sulphide [198]. Light-driven H_2 evolution has been demonstrated with molybdenum sulphide catalysts deposited on light-absorbing *p*- Cu_2O cathodes [197, 199], Si photoelectrodes protected by thin Ti [200] and MoS_2 layers [201], Si nanowire photoelectrodes [202], an organic photovoltaic cell [203], and CdSe-seeded CdS nanorods [204].

Cobalt phosphide (CoP) is another well established hydrodesulphurisation material that was recently rediscovered as an efficient HER catalyst. Being of the MnP structure, electrodes constructed from CoP nanoparticles display high stability² in acid, i.e. no significant degradation occurs over 24 h of continuous operation at -20 mA cm^{-2} , and show an overpotential requirement of -85 mV at this cathodic current density, compared to -25 mV for the Pt control electrode [205]. An estimated per active site TOF of 0.046 s^{-1} has been reported.

Nickel-based materials have also received much attention as hydrogen evolution electrocatalysts, with Ni being a significantly more abundant element than molybdenum (which is part of MoS_2 catalysts) [206]. Most Ni-alloys are unstable in acidic solution, in contrast to two recently explored nickel phosphide phases, Ni_2P [206], another well-known hydrodesulphurisation catalyst, and Ni_5P_4 [207]. Nanostructured Ni_2P , which adopts the hexagonal Fe_2P structure, has been predicted to be a highly efficient HER catalyst by density functional theory already in 2005 [208]. Of particular interest is its (001) surface, which has exposed Ni and P

²From a basic research perspective.

sites and exhibits an ‘ensemble’ effect, whereby proton acceptor and hydride acceptor centres are both present to facilitate catalysis. The overpotential requirements of Ni₂P compare favourably with other non-Pt HER electrocatalysts in acidic solutions [206]. However, the catalyst electrodes are not stable in base; Ni₂P quickly degrades to Ni in 1.0 M KOH under rapidly declining HER performance. This stands in contrast to Ni₅P₄, which is stable in both acid and base. This nickel phosphide phase shows geometric activities on par with bulk platinum catalysts and superior catalytic efficiency compared to Ni₂P [207], with estimated turnover frequencies per surface atom being 200 times greater in both acidic and basic media (3.5 and 0.8 s⁻¹ at $\eta = 0.1$ V, respectively). However, on a per active site basis, Pt-foil still displays a two orders of magnitude higher TOF in acid (assuming an atomically flat surface). Apart from one report dealing with iron phosphide nanoparticles immobilised on TiO₂ particles [209], light-driven hydrogen evolution using recently established transition metal phosphide materials has yet to be demonstrated.

1.3.3.3 Hydrogenases

Looking at nature for inspiration, hydrogenase enzymes are exceptional catalysts for H₂ production and oxidation. With turnover frequencies exceeding 10³ s⁻¹ [210], their active sites rival Pt in performance [211, 212]. Both main classes of enzyme, [FeFe]- and [NiFe]-hydrogenases [210, 213] (see Fig. 1.14 for structural representations of the respective active sites), catalyse the two-electron interconversion of protons and dihydrogen in mechanisms involving a metal-bound hydride and a proton (bound to a nearby base), similar to the type of mechanism favoured for the molecular electrocatalysts synthesised and investigated by DuBois

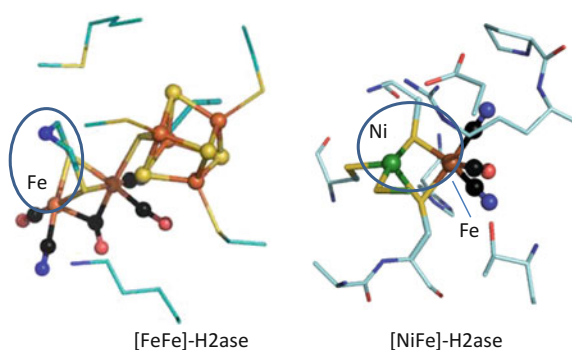


Fig. 1.14 Active sites of [FeFe]-hydrogenase from *Clostridium pasteurianum* (left, PDB code 3C8Y) and [NiFe]-hydrogenase from *E. coli* (right, PDB code 3USC). Regions considered to be the focus of the catalytic transformation are indicated by ovals. Note the structural similarity between the [FeFe]-Hydrogenase active site and the functional analogue depicted in Fig. 1.13b, i.e. a pendant amine base placed above the reactive metal centre

(described in Sect. 1.3.3.1), which can thus be considered functional analogues of the enzymes. Yet, these molecular catalysts show inferior performance on a per catalyst active site basis when compared to hydrogenases incorporated into artificial photosynthetic systems [214].

Although [FeFe]-hydrogenases are more active H_2 producers than the [NiFe] analogues, they are inactivated irreversibly by trace O_2 [213]. The [NiFe]-hydrogenases are less sensitive to O_2 and some even function in air, but they are less active H_2 producers, partly because H_2 binds tightly and is a strong inhibitor. One exception is the subclass known as [NiFeSe]-hydrogenases: these enzymes, in which one cysteine ligand to Ni is replaced by selenocysteine, are excellent H_2 producers that retain some activity in the presence of O_2 [215]. The respective mechanisms of the two classes of hydrogenases are described in more detail in Sect. 1.6.

1.3.4 CO_2 Reduction

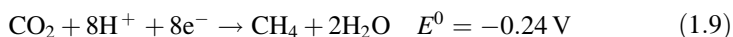
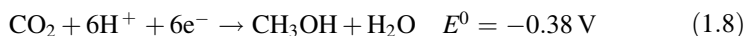
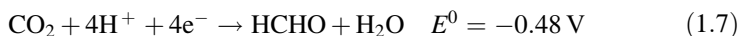
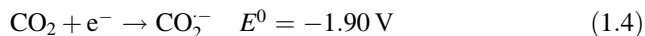
1.3.4.1 General Considerations on the Reduction of Carbon Dioxide to Fuels and Chemicals

We established in Sect. 1.2.2.1 that it is the water splitting chemistry of PSII that accounts for virtually all of photosynthetic energy storage; fixation of CO_2 in the photosynthetic dark reactions does not store additional energy [Eqs. (1.1)–(1.2)]. However, from a practical perspective, transforming CO_2 in the reduction half-reaction can be beneficial. Carbon dioxide can be reduced to liquid fuels such as methanol, which offer much higher *volumetric* energy densities than hydrogen. Such an approach would obviate the need to develop a hydrogen storage infrastructure for later use as transportation fuel [75]. Further, CO_2 could form the basis of a future solar-chemicals industry, in which drop-in replacements for existing petrochemicals and other value-added products derived from petroleum (compare Fig. 1.2) will be made by artificial photosynthesis, for example via formation of methanol as a C1 intermediate [216].

Multi-electron catalysts are required to achieve the reduction of CO_2 to liquid fuels/chemicals. Carbon dioxide is a difficult molecule to activate: the HOMO is localised on the two O-atoms and the linear molecule must bend and convert to a C-bonded carbonyl. The large reorganisation energy required to form this bent 1-electron reduced radical anion CO_2^- is reflected in its thermodynamic potential of -1.9 V [Eq. (1.4)] [217].

From a thermodynamic perspective, the most demanding step in multi-electron reduction of CO_2 is its initial two-electron reduction to CO or formate intermediates [218, 219] [Eqs. (1.5)–(1.6)]. Indeed, provided upon the availability of suitable reversible catalysts, the thermodynamic potentials for HCHO, CH_3OH and CH_4 formation [218, 219] from CO_2 given in Eqs. (1.7)–(1.9) suggest that coupled multi-electron, multi-proton steps can be performed at less cathodic potentials [220]

(the standard potentials summarised in Eqs. (1.4)–(1.9) are referenced to pH 7 under aqueous conditions, 1 atm gas pressure, 25 °C, and 1 M solutes).



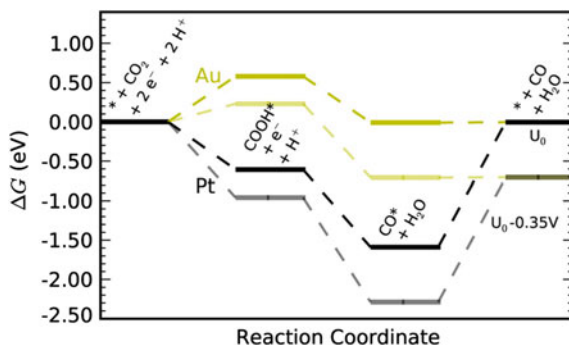
Numerous synthetic homogeneous and heterogeneous electrocatalysts have been developed and interfaced with light-absorbers to achieve photodriven reduction of CO_2 [219, 221]. However, progress in this field has been quite limited compared to other areas of artificial photosynthesis research [222] and most synthetic catalysts do not afford reactivity beyond the two-electron reduction of CO_2 to CO or formate. Nonetheless, it is important to note that although an ultimate goal of artificial photosynthesis is to produce liquid fuels (such as methanol) directly, both CO and HCOOH are valuable feedstock in industrial processes, e.g. the Fischer-Tropsch process that converts carbon monoxide and hydrogen into hydrocarbons [223].

1.3.4.2 Heterogeneous Electrocatalysts for CO_2 Reduction

Most heterogeneous electrocatalysts for CO_2 reduction suffer from high overpotential requirements and low faradaic efficiencies that result in product mixtures [224, 225], a direct consequence of the multiple reduction pathways illustrated in Eqs. (1.4)–(1.9).

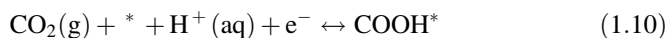
Much research has focused on using transition metals as catalysts, which have been shown to produce a variety of CO_2 reduction products [222]. However, evolution of H_2 is the preferred pathway at most of them [226]. Copper, for which CO_2 reduction has been first demonstrated in 1985 [227], has been extensively investigated [228–231]. Even so, large overpotentials are typically required and up to 16 different CO_2 reduction products (C1–C3) have been identified [232]. Yet, despite its lack of specificity, Cu is the only known transition metal capable of reducing CO_2 in multiple reducing steps to yield carbon-based chemicals such as methane, ethylene, etc. [222, 232]. Other transition metal electrodes and nanostructures [233] that show activity towards CO_2 activation, with varying selectivity, are Au [234–236] and Ag [237–239], both selective and active for CO [236], as well as Sn, which shows pronounced activity towards the formation of formate

Fig. 1.15 Free energy diagrams for CO₂ electroreduction to CO on Au (211) and Pt(211) at the reversible potential, denoted U_0 , and at an overpotential of 0.35 V. Reprinted with permission from Ref. [236]. Copyright 2013 American Chemical Society



[226, 240, 241]. However, all of these examples suffer from significant overpotential requirements.

In a density functional theory study, Nørskov examined the mechanism of CO₂ reduction on metal surfaces, considering the following steps for the two electron reduction to CO [236]:



In Eqs. (1.10)–(1.12), COOH* and CO* denote adsorbed intermediates and * refers to a free step site. Figure 1.15 shows the calculated free energy diagram for CO₂ reduction through this scheme on Au(211) and Pt(211) surfaces. On Au(211), the free energies of the initial and final states are the same and the standard free energy of CO desorption is close to zero, but initial formation of adsorbed COOH* is associated with a high increase in free energy at the reversible potential. Therefore, increasing the driving force makes COOH formation easier and results in increased CO production. In contrast, for Pt(211), COOH* is very stable and CO₂ activation will be exergonic. However, desorption of CO is associated with a large change in free energy, but this ‘non-electrochemical’ step does not affect the free energy directly. Comparing the reaction pathways at the two different metals, Nørskov et al. suggest accordingly that improved CO evolution activity could be obtained by finding a catalyst where the binding of COOH is stronger than on Au (211) or where the binding of CO is weaker than on Pt(211) [236].

In an interesting recent development, Koper and co-workers devised a system capable of *reversibly* interconverting CO₂ and formate (Fig. 1.16) [242] by electrodepositing palladium onto a polycrystalline platinum substrate. The authors hypothesised that a Pd-Pt alloy electrode is formed, which slows down CO poisoning compared to bare Pd. Further, it is assumed that the alloy is covered by a thin layer of Pd, the effect of which is to suppress hydrogen adsorption. However, the activity decreases significantly over the course of the 20 voltammograms

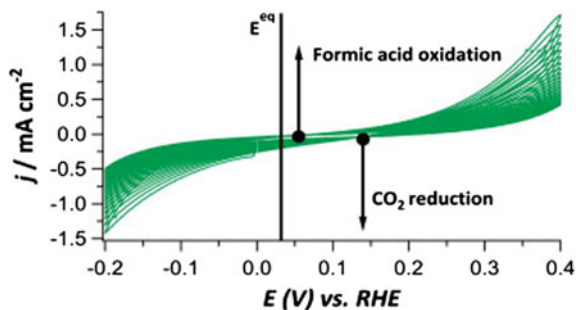


Fig. 1.16 Cyclic voltammograms (20 consecutive cycles) showing reversible formic acid oxidation and CO₂ reduction by a Pd–Pt electrode. Experimental conditions: scan rate = 50 mV s⁻¹, 0.2 M NaH₂PO₄/0.2 M Na₂HPO₄ buffer (pH 6.7, saturated with CO₂), 25 mM NaHCOO. Reprinted with permission from Ref. [242]. Copyright 2015 Elsevier

depicted in Fig. 1.16; this decay is attributed to electrode-poisoning by CO, which is also formed in the potential window around the reversible potential for HCOOH formation/oxidation. Simultaneous evolution of hydrogen during CO₂ reduction is also detected. Hence, despite the important demonstration of reversible behaviour for CO₂/CO interconversion, the system is severely limited by both lack of stability and selectivity.

Over the past decade, the transition metal catalysts described above have been interfaced with light absorbing materials for photoinduced CO₂ reduction. Notable examples include Cu-sensitised *p*-Si nanowires [243], photocatalytic CO₂ reduction by Cu–Au nanoalloys supported on TiO₂ [244], as well as Cu-nanoparticle decorated graphene oxide [245]. Several recent review articles [219, 246–248] provide comprehensive overviews on approaches towards photocatalytic CO₂ reduction by heterogeneous transition metal catalyst/semiconductor light-absorber composites.

1.3.4.3 Molecular CO₂ Reduction Catalysts

Notable organometallic CO₂ reduction electrocatalysts include Ni(II)-cyclam systems originally devised by Sauvage and co-workers [249], and Lehn's Re(bpy)(CO)₃X catalysts, with X being Cl⁻ or Br⁻ [250, 251]. Both classes of catalyst have been intensively studied and developed further by many research groups [218]. However, rhenium is among the least-abundant elements on Earth. A recent advance is the incorporation of an earth-abundant manganese ion as the metal centre into the bipyridyl-tricarbonyl ligand environment, which lowers the overpotential for CO₂ reduction by 0.4 V while maintaining selectivities and Faradaic efficiencies that are comparable to the rhenium analogues [252]. Both cyclam [253] and bipyridyl-carbonyl (Re and Ru) complexes have been used in systems for light-driven CO₂ reduction [254–256].

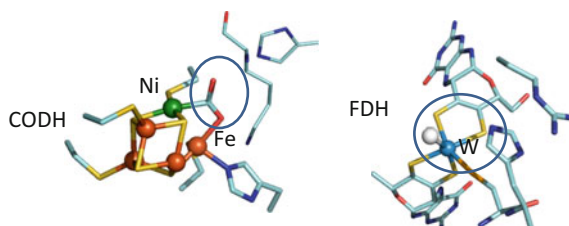


Fig. 1.17 Active sites of CO dehydrogenase II (CODH) from *Carboxydotherrnus hydrogeniformans* (left, PDB code 3B52) and tungsten containing formate dehydrogenase from *Desulfovibrio gigas* (right, PDB code 1H0H). Regions considered to be at the focus of the catalytic transformation are indicated by ovals

Iron tetraphenylporphyrins developed by Savéant and colleagues represent another class of molecular electrocatalysts for the conversion of CO_2 –CO that are based on earth-abundant metal ions [257]. Modification of the porphyrin-framework with *ortho*-phenol moieties results in a high local concentration of protons being available, which significantly enhances catalysis by the transiently generated iron (0) complex. Reduction of CO_2 is catalysed with an average TOF of 3500 s^{-1} over 4 h at an overpotential requirement of approximately 0.5 V, which represents a significant advance for synthetic catalysts, but still constitutes a substantial energetic cost. This catalyst has been employed to effect photocatalytic CO_2 reduction in acetonitrile (but not water), using the organic photosensitiser 9-cyanoanthracene and trimethylamine as electron donor [258].

A further, interesting approach developed by the group of Bocarsly constitutes the utilisation of the pyridinium ion as homogeneous catalyst for the six-electron reduction of CO_2 to methanol, with comparatively modest overpotentials of 200 mV being sufficient to drive the reaction [259]. Photoreduction of CO_2 using the pyridinium ion in conjunction with a *p*-GaP photocathode has also been demonstrated [260], and initial mechanistic studies suggested that the one-electron reduced pyridyl radical PyH^\bullet acts as electron shuttle and activates CO_2 [261, 262]. However, this proposal has been questioned in a recent mechanistic study conducted by Savéant [263], who calls for a more careful examination of the actual role of the pyridinium ion, as the reduction of this species in conjunction with a platinum electrode did not involve the pyridyl radical and neither methanol nor formate could be detected in preparative-scale electrolyses.

Approaches toward photo- and photoelectrocatalytic reduction of CO_2 using the molecular catalysts described in this section have recently been reviewed by the groups of Fujita [264], Loo [191], Kubiak [219], and Perutz [265].

1.3.4.4 CO_2 Reduction in Biology

Although they are not suitable for large-scale applications, enzymes lead the way as CO_2 reduction catalysts, meeting the criteria of minimal driving force requirement,

high stability, as well as high selectivity, i.e. the ability to form *specific* products with high Faradaic efficiencies [222]. Similar to hydrogenases that are able to reversibly catalyse the hydrogen evolution reaction (Sect. 1.3.3.3), certain enzymes act as reversible CO₂ reduction catalysts with unprecedented efficiency and specificity: in biology, two-electron reduction of CO₂ is catalysed by two very different types of enzyme, formate dehydrogenases and carbon monoxide dehydrogenases (Fig. 1.17). Both are electroactive on conducting electrodes and set excellent benchmarks for the performance that must be possible with small molecular or surface catalysts. Through proton-coupled electron transfer (PCET), these enzymes are capable of avoiding the high energy CO₂^{•-} radical intermediate in favour of the two-electron reduced species CO or HCOOH.

Formate dehydrogenase (FDH) was among the first enzymes to be studied in the context of artificial photosynthesis. A paper published by Parkinson and Weaver in 1984 describes how electrons from a photoexcited *p*-InP photocathode are transferred via methyl viologen to the enzyme, which carries out CO₂ reduction to formic acid [266]. Photogenerated electrons in the semiconductor can be produced with wavelengths of up to 900 nm. More recent work has shown that both tungsten- [267] and molybdenum-containing [268] FDH are reversible electrocatalysts when adsorbed directly on graphite electrodes, although immobilisation on semiconductor materials for photodriven CO₂ reduction has yet to be demonstrated.

Carbon monoxide dehydrogenases (CODHs) fall into two main types, aerobic and anaerobic, but it is the latter class, containing a [Ni₄Fe-4S] cluster, that were established to be excellent electrocatalysts for CO₂ reduction to CO [269]. The anaerobic enzymes operate virtually reversibly, contrasting markedly with the situation for small molecular and heterogeneous catalysts described in the previous two sections. As is the case with hydrogenases, the surrounding outer-shell environment probably holds the secret to the very high activity. Evidence suggests that a bond forms between the C-atom and the Ni subsite, which is very nucleophilic in the reduced enzyme: an O-atom is then removed (as oxide/hydroxide) by the pendant Fe in a PCET process that is exquisitely organised by the side chains of appropriately positioned residues [269, 270]. Considerations regarding the mechanism of CO₂ reduction by CODH will be presented in more detail in Sect. 1.6.

The supremacy of CODH over metal electrocatalysts inspired an interesting comparison by Nørskov and co-workers [236], who argued the importance of the active site of CODH being able to attack CO₂ at *two* atoms (Ni-C and Fe-*departing* O) simultaneously, stabilising a bound intermediate without also stabilising bound CO, in contrast to metallic surfaces. Figure 1.18 compares the calculated electrocatalytic activity towards CO₂ reduction, i.e. the TOF per site vs. applied potential, for CODH and Au(211), showing reversible behaviour for CODH and significant overpotential requirements in either direction for the Au surface.

To summarise, major scientific breakthroughs are needed to make each of the different components described in Sect. 1.3 efficient, robust, scalable, and, last but not least, composed of inexpensive and abundant materials. All these are necessary requirements for artificial photosynthesis to achieve scalability and, ultimately, commercial viability.

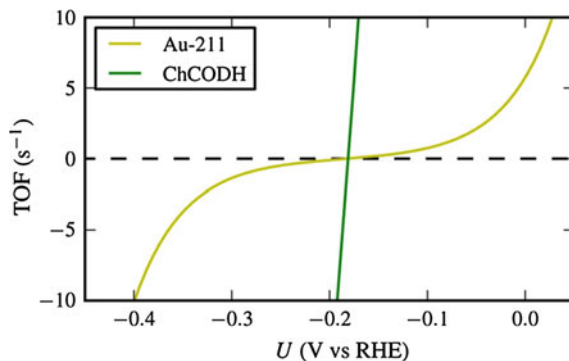


Fig. 1.18 Comparison of electrocatalytic activity for CO_2/CO interconversion as a function of applied potential at a metal surface [Au(211)] and an enzyme (CODH). On CODH, the turnover changes sharply through the equilibrium potential, suggesting a reversible interconversion of CO_2 and CO, while a significant overpotential is required on Au(211). Reprinted with permission from Ref. [236]. Copyright 2013 American Chemical Society

1.4 Strategies for Integrated Systems

1.4.1 Integrating the Individual Components

As described in Sect. 1.3, the essential components of a solar-fuels device are a light-absorber, multi-electron electrocatalysts for water oxidation and fuel-formation, a conducting electrolyte, and a means of product separation, such as a proton conducting but gas impermeable membrane. A major challenge in integrating these different components, independent of the actual design architecture, is to achieve efficient charge transport between the different components, without losing large fractions of transient carriers in side or back reactions, or being trapped at defect sites [75]. A further inherent difficulty is the need to reconcile single-photon, charge generation events with multi-electron catalysis.

The individual components can be assembled to form integrated systems of varying intricacy. The two limiting cases, categorised by Gray according to their complexity, technological maturity, and projected manufacturing cost [271], are aqueous photocatalyst colloids and commercial photovoltaic modules connected to discrete electrolyzers, with various integrated photoelectrochemical design architectures lying somewhere in-between (Fig. 1.19). Some of these approaches have recently been evaluated in terms of efficiency criteria and resulting design implications [272], and from a technical and economic feasibility perspective [273–275].

It is important to remember that even though individual components might be efficient, robust, and scalable, this does not imply that they can be arbitrarily combined to form viable integrated systems [271], they must be *compatible* with each other. Moreover, new challenges arise when reactions are being driven under real operating conditions by transiently generated carriers instead of half systems

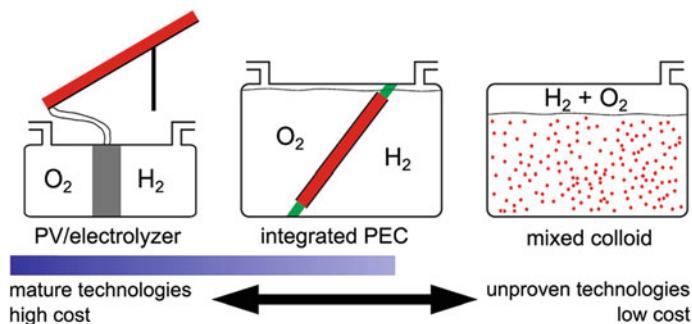


Fig. 1.19 Schematic of three device architectures available for solar-driven water splitting, ordered according to their relative technological maturity and projected costs to manufacture. Reprinted with permission from Ref. [271]. Copyright 2013 American Chemical Society

relying on sacrificial reagents or externally applied bias: it is now becoming a recurring theme that the electrocatalytic activities of catalysts for artificial photosynthesis observed in standard, ‘dark’ electrochemistry experiments are often orders of magnitude higher than the turnover frequencies observed under photo- and photoelectrochemical conditions. Although this is yet to be firmly established, it seems that the major reason for the lower rates observed in light-driven experiments is that the charge carriers are transient and there is unfavourable competition with destructive charge carrier recombination, which is thermodynamically preferred—a formidable challenge that needs to be addressed.

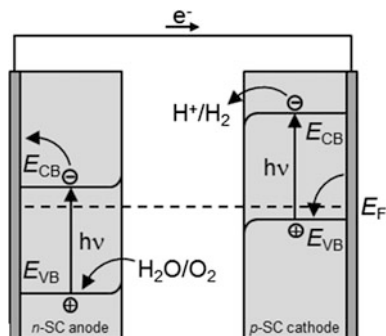
1.4.2 Photochemical versus Photoelectrochemical Water Splitting

1.4.2.1 Photoelectrochemical Cells

The first proof-of-concept example of photoinduced water splitting was a photoelectrochemical cell (PEC) developed in 1972 by Fujishima and Honda [10]. In this system, the reactions are driven by UV light absorbed by a TiO_2 photoanode. The electrons excited into the TiO_2 conduction band are transferred through an external circuit to a ‘dark’ platinum cathode, where the H_2 evolution reaction takes place. Water is oxidised by high-energy holes in the TiO_2 valence band, the latter reaction being energetically costly as it proceeds via high-energy intermediates such as hydroxyl radicals [276].

Photoelectrochemical cells can be constructed from single *p*-type or *n*-type semiconductor materials to give single band gap devices (where the second half-reaction takes place at a dark electrode similar to the Fujishima–Honda system above) or from two semiconductors connected in series, i.e. forming a dual band

Fig. 1.20 Schematic representation of a dual band gap photoelectrochemical cell for water splitting with water oxidation taking place at the n -type photoanode and proton reduction at the p -type photocathode. Reprinted with permission from Ref. [83]. Copyright 2015 Springer



gap device [277]. In dual band gap photoelectrochemical cells, combinations of semiconductor materials with different band gaps and complementary absorption characteristics should be employed to utilise the solar spectrum to its maximum extent, particularly to harvest low-energy photons in the near-infrared region. A dual band gap photoelectrochemical cell is depicted schematically in Fig. 1.20.

In Fig. 1.20, the minority carriers generated in the photoelectrodes carry out the electrochemical reactions, with charge separation being assisted by the electric fields that arise at the semiconductor/electrolyte (or semiconductor/catalyst) interface. In the case of an n -type semiconducting photoanode, a depletion layer prevents oxidative currents in the dark (see Sect. 2.3 for a general description of the underlying principles). Upon illumination, the electron-hole pair is separated by the electric field of the space-charge region, resulting in a photooxidation current: electrons, the majority carriers, move through the conduction band into the bulk of the material (and to the counter electrode for fuel-formation). In the valence band the minority carriers, holes, move to the semiconductor/electrolyte interface where they drive the water oxidation reaction. p -Type materials show analogous behaviour, but with holes as majority carriers; they are dark anodes and photocathodes.

One of the inherent advantages of a ‘wired’ photoelectrochemical cell is that this design utilises fast electronic conductivities: an electronic conductor completes the circuit between the anode and the cathode by a relatively long path, but with the ionic path being as short as possible [278]. Placing the two electrodes in close proximity limits ‘bottleneck’ effects of the intrinsically lower ionic conductivities. Progress made on photoelectrochemical cells for artificial photosynthesis has been reviewed by several authors [277, 279–284] and notable examples of recently developed photoelectrochemical cells for artificial photosynthesis are given in Refs. [11, 12, 131, 243, 285–300].

In ground-breaking work from 1998, Khaselev and Turner established the proof-of-principle for efficient photoelectrocatalytic water splitting using visible-light, achieving a solar-to-hydrogen efficiency of 12.4% [12]. The reported cell structure consists of a top layer of p -GaInP₂, connected in series, via a tunnel junction, to a GaAs p/n bottom photovoltaic cell on a GaAs substrate. In this

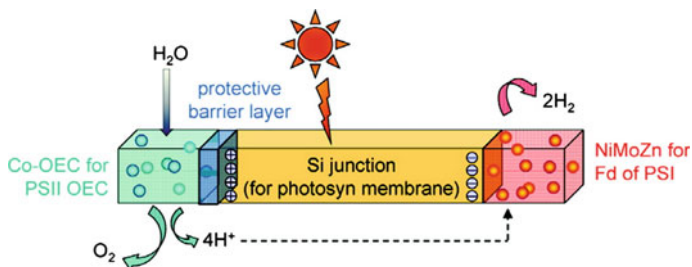


Fig. 1.21 Wireless solar-fuel generator (‘artificial leaf’) developed by Nocera and co-workers, comprising a Co–Pi oxygen evolving catalyst (Sect. 1.3.2) and a NiMoZn alloy for H₂ evolution. Reprinted with permission from Ref. [31]. Copyright 2012 American Chemical Society

‘D4’-configuration (‘dual-absorber—four-photons’), two-photons are required to produce one electron in the external circuit and four-photons are required for the formation of H₂. Hydrogen is produced at the semiconductor electrode and the water oxidation reaction takes place at the Pt counter electrode. However, despite proving that STH efficiencies > 10% are possible using a single integrated device, the instability of the materials (degradation under use within days) and the use of non-abundant materials make this device unsuitable for manufacturing on the scale needed for global fuel generation [75].

‘Wireless’ PEC architectures, in contrast to the wired cell designs described above, provide a direct connection between anode and cathode with the ionic conductor taking a much longer path. The ‘wireless’ *p/n*-PEC device configurations, first developed by Nozik and referred to as ‘photochemical diodes’ [301], are intrinsically simpler in structure and are thus projected to be more suited for a low-cost, manufactured device [277]. The intimate integration of the light-harvesting, charge separation and chemical bond-forming functions into one single structure is advantageous compared to a multi-component process in which electricity is a tangible intermediary: integration avoids the cost and system constraints associated with electrical contacts, wires, and inverters [3]. Consequently, several ‘wireless’ integrated architectures for artificial photosynthesis have been designed and evaluated both theoretically [302–305] and experimentally [15, 306–309] in recent years; an example of an artificial leaf is depicted in Fig. 1.21 [31]. Notably, a ‘free-standing’ monolithic device developed by Jacobsson et al. [15], consisting of three series interconnected copper indium gallium selenide (CIGS) PV light-absorbers coupled with two platinum catalysts for water oxidation and hydrogen evolution, achieves a STH efficiency of 10% (the US Department of Energy target [11] and threshold for economic and technological compatibility [15]), rivalling the efficiency achieved by Turner. Although the use of non-cost effective precious metal catalysts prevents further scale-up, the device has important value from a proof-of-principle viewpoint.

1.4.2.2 Photochemical Systems

To study the mechanistic interplay between catalysts and light-absorbing components, it is advantageous to examine the water oxidation or fuel-forming ‘half-systems’ separately through photochemical experiments in (ideally homogeneous) solution: equilibria can be shifted in the desired direction and reaction rates can be controlled through the use of sacrificial reactants (in very large excess). Mechanisms can be elucidated through a variety of spectroscopic tools (e.g. steady-state UV/Vis or time-resolved optical spectroscopy), most of which are easiest to perform in solution.

Aside from the difficulty of product separation in a colloidal approach, it is extremely unlikely that light-driven overall water splitting, i.e. simultaneous water oxidation and fuel production could occur efficiently at a single nanoparticle site. Reasons include the lack of spatial charge separation to suppress recombination and destructive back reactions, as well as the difficulty in dealing with two sets of highly reactive intermediates during a four-photon cycle. Nevertheless, colloidal semiconductor nanocrystals are excellent light-harvesting elements for artificial photosynthetic model systems because they are strong light-absorbers with tuneable particle size, shape, electronic structure, absorption spectra, and surface chemistry [310–317].

Figure 1.22 schematically illustrates the principle for a system catalysing fuel-formation driven by a sacrificial electron donor [184]. Domen pioneered the approach of using semiconductor powders for photocatalytic water splitting, such as in his laboratory’s elegant study from 2006: using a solid solution of $(\text{Ga}_{1-x}\text{Zn}_x)(\text{N}_{1-x}\text{O}_x)$, impregnated with nanoparticles of rhodium-chromium mixed oxide [318], hydrogen and oxygen have been shown to evolve stoichiometrically in the expected 2:1 ratio under visible-light irradiation ($\lambda > 400$ nm), with an external quantum efficiency of approximately 2.5% at 420–440 nm. The system shows remarkable stability, no noticeable degradation was observed after repeated runs for 35 h. Following Domen’s seminal work, a variety of fuel-forming catalysts have

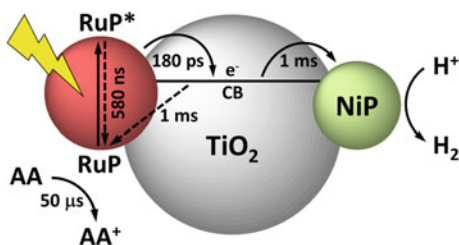


Fig. 1.22 Cartoon representation of a semiconductor nanoparticle-based ‘half’-system for hydrogen evolution in colloidal solution [184]. A molecular DuBois-type hydrogen evolution catalyst (NiP) is immobilised on a TiO_2 semiconductor particle, co-sensitised with a visible-light-absorbing tris(bipyridine)ruthenium(II) dye (RuP). Ascorbic acid (AA) acts as sacrificial electron donor and respective carrier dynamics are indicated. Reprinted with permission from Ref. [83]. Copyright 2015 Springer

been coupled with nanoparticulate, colloidal semiconductor materials (both for CO₂ reduction and H₂ evolution), either through directed immobilisation or non-specific ‘bimolecular’ interactions, and integrated ‘colloidal’ systems have also been devised [319–337].

Many of the semiconductor/molecular catalyst systems developed thus far focus on dye-sensitised TiO₂ nanoparticles and Cd-chalcogenide nanostructures of various geometries. Both types of material offer several advantages: their photochemistry and excited-state kinetics are well established [338, 339] and the conduction band edges (see Fig. 1.9 for a guide) provide enough driving force to effect the fuel-forming reactions.

Both TiO₂ and CdS are *n*-type semiconductors that normally form a depletion layer at open circuit potential. A positive charge is associated with the space-charge region (Sect. 2.3.3), which is reflected in an upward bending of the band edges at the semiconductor/electrolyte interface [340]. Size becomes crucial: at the *macro-scale*, excited electrons in the conduction band migrate from the surface into the interior and render the material unsuitable for light-harvesting applications for the fuel-generating half-reaction. However, at the *nanoscale*, formation of a space-charge layer is improbable due to the tiny dimensions. Semiconductor nanocrystals with very small particle diameters do not contain enough electrons to support an effective space-charge layer. In practice, this lack of space-charge effects applies to both nanoparticle suspensions and highly porous electrodes [341]. Hence, on the nanometre scale, both TiO₂ and CdS are useful light absorbers for light-driven fuel formation.

Commercially available TiO₂ nanoparticles (such as ‘P25’, an 80:20 mixture of rutile and anatase) are widely used in self-cleaning wall paint (exploiting hydroxyl radicals generated by UV radiation). The disadvantage for artificial photosynthesis is their transparency towards visible light, with band gaps of 3.03 eV for rutile and 3.20 eV for anatase, respectively [342]. To overcome this issue, TiO₂ is commonly sensitised with molecular dyes, most commonly tris(bipyridine)ruthenium(II) derivatives [68, 82] and high-potential porphyrins [71]. These types of sensitiser have large extinction coefficients in the visible region and long-lived charge-separated (triplet-) states, leading to efficient charge injection from the chromophore to the semiconductor [73, 338]. Due to the position of its conduction band potential (Fig. 1.9), TiO₂ provides only a marginal driving force for fuel formation, especially for CO₂ reduction. This disadvantage however will pose little problem for a reversible electrocatalyst. Owing to a combination of advantages that include low cost, TiO₂ has been widely used in research on DSSCs and is one of the best-characterised semiconductor materials.

In contrast to TiO₂, CdS, which has a band gap of 2.3 eV, absorbs visible light below a wavelength of about 540 nm. The conduction band edge of bulk CdS lies at a significantly more negative potential than for TiO₂: with $E_{cb} = -0.87$ V vs. SHE (pH 6.0) [343], a much larger driving force is available for fuel-forming reactions (consider for example the reduction of CO₂ to CO, which has a reduction potential of -0.46 V vs. SHE, at pH 6.0).

1.4.3 *The Combination of Photovoltaics and Electrolysis*

Despite the additional complexities, constraints, and potential costs imposed by the need for electrical contacts, wires, inverters, etc. [3], an approach in which light absorption by photovoltaic devices is physically separated from ‘dark’ electrocatalysis has several distinct advantages: firstly, the rapid advancement of photovoltaic cell development (Sect. 1.3.1.5) offers the potential for solar-conversion efficiencies much higher than what is achievable with conventional semiconductor photoelectrodes. Further, there is no need to precisely match the light-absorber with the catalysts in order to make them compatible for device integration. Instead, the type of light-harvester is irrelevant for catalysis as long as sufficient voltage is (steadily) supplied to drive the water oxidation and fuel-forming reactions. To overcome restrictions imposed by the intermittency of solar irradiation, other sources of renewable electricity such as wind power could also be utilised. Professor Stephen Chu, former US Secretary of Energy, for example proposed to use cheap night-time electricity to split water and produce liquid hydrocarbons through the concomitant reduction of CO_2 [344].

Many non-oxide semiconductor electrodes undergo decomposition by photo-corrosion or photopassivation when in contact with aqueous electrolytes in solution [84]. Attempts at protection have been undertaken and, among others, amorphous TiO_2 [345–347] and NiO_x [348] coatings have been demonstrated to stabilise and protect Si, GaAs, GaP, and CdTe photoanodes. However, it remains to be seen whether such an approach will be viable in the long-term. Conversely, there is no need to protect intricate and fragile semiconductor surfaces from aqueous environments when catalysis is separated from the light-harvesting events. Recently, two papers established the general feasibility of this approach on a bench-scale level. Nocera and Grätzel respectively achieved solar-to-hydrogen efficiencies greater 10% using photovoltaic cells based upon silicon (10% STH [17]) and $\text{CH}_3\text{NH}_3\text{PbI}_3$ (12.3% STH [16]) connected in series to dark electrocatalysts. Importantly, both architectures consist of earth-abundant materials.

Grätzel’s example is particularly elegant: the simplistic design features the same catalyst material for both the OER and the HER, a bi-functional Ni–Fe layered double hydroxide material that is grown on a Ni foam surface. The high photovoltage of the perovskite absorber permits the use of only two PV cells connected in series, as opposed to the system devised by Nocera, which relies on four cells connected in series. Further, the operating point of the water-splitting cell lies very close to the maximum power-point of the perovskite photovoltaic tandem cell. A photovoltaic efficiency of 15.7% is converted into 12.3% STH efficiency, i.e. minimal energy is lost in converting electrical to chemical energy. Currently, the system is limited by the instability of the perovskite solar cell, which degrades within hours [349].³

³Use of a single band gap material in a tandem configuration is also not ideal: combining a perovskite cell with a different semiconductor of similar band gap could further enhance the solar conversion efficiency [349].

Further, there is still room for catalyst improvement: more proficient catalysts with lower overpotential requirements are needed to keep up with the development of future photovoltaic cells of even higher efficiency, or to compensate for some loss in available photovoltage by substitution of one of the PV components by a lower-voltage silicon cell.

1.5 The Role of Enzymes in Artificial Photosynthesis

1.5.1 General Considerations

Enzymes set the benchmark for water oxidation, hydrogen production, and CO₂ reduction catalysis (see Sects. 1.3.2–1.3.4). Thus, the obvious question arises if enzymes can add value to artificial photosynthesis, not for technology development and scale-up, but to gain mechanistic insight at a fundamental level and establish design criteria for future all-inorganic devices.

Enzymes make possible the design and construction of bench-scale test systems that are instructive because the chemical reactions of solar-fuel production are rendered so fast and efficient that they are expected not to limit the overall performance of a device. If attached to light-absorbers so that interfacial electron transfers are fast, metalloenzymes can serve as smooth, proficient depolarisers to allow electron flow. Exploitation of enzymes in this way makes possible the evaluation of semiconducting materials for artificial photosynthesis development in cases where those materials may be highly suited for light harvesting but very poor catalysts.

There is an interesting connection between redox catalysis that occurs on the surface of a photoexcited semiconductor and electrocatalysis that occurs at electrodes [343]. Extensive investigations using a suite of techniques called protein film electrochemistry (PFE, Sect. 2.2), have established that many redox enzymes catalysing artificial photosynthetic transformations are extremely fast and efficient, despite their giant size [213, 350]. This information is implicit in numerous observations: fuel-forming electrocatalytic reactions such as H₂ evolution and CO₂ reduction are reversible when catalysed by the appropriate enzyme and require only a minimal overpotential to operate in either direction. Given the crucial importance, for scaling up artificial photosynthesis, of having catalysts based upon inexpensive, abundant materials, it is highly significant that these investigations have proved that solar-fuel production *does not* require precious metal catalysts like Pt, Ru, or Ir. Indeed, experiments with enzymes show instead that in the right atomic environments, the 3d elements Mn, Fe, Ni, and Cu perform excellently. Importantly also, these inexpensive, ‘dressed-up’ catalysts perform under ambient, neutral conditions. Studies with enzymes provide hints at other advantages, such as the ability of an enzyme to trap and accumulate all the charge carriers (electrons or holes) required for the reaction (e.g. two for H₂ evolution, four for water oxidation).

1.5.2 *Photosystem II in Artificial Systems*

Highly electrophilic intermediates have to be stabilised under the harsh conditions of water oxidation, prohibiting the use of any soft material. Nonetheless, PSII has been incorporated and studied in a variety of artificial photosynthetic systems. The enzyme displays *photoelectrocatalysis* when interfaced with different light-absorbing nanomaterials—the light-harvesting and catalytic components being inseparable parts of the same super-molecule.

Using the technique of protein film photoelectrochemistry [351], cyanobacterial PSII has been shown to be electroactive on mesoporous indium tin oxide (*meso*-ITO) electrodes, and catalytic water oxidation was observed under red light irradiation [352]. Orientation-controlled adsorption of PSII on *meso*-ITO through electrostatic or covalent interaction with self-assembled monolayers of organic linker molecules on the ITO surface improved interfacial electron transfer and substantially enhanced the turnover frequencies for light-driven oxygen evolution [353]. Other recent reports include O₂ evolution by His-tagged PSII immobilised on Au-nanoparticles [354] and incorporation into redox-active polymers [355–357]. Enzyme-based photovoltaic cells have also been devised [35, 358].

However, it has to be re-emphasised that there is no repair mechanism outside biology and artificial photosynthetic systems using PSII *in vitro* are prone to quick degradation [210], limiting the value such systems can bring about.

1.5.3 *Fuel-Forming Enzymes for Artificial Photosynthesis*

1.5.3.1 Configurations

In contrast to water oxidation, the reducing chemistry of fuel-formation relies on nucleophilic attacks and insight from molecular and/or biological components incorporated into artificial photosynthetic systems can be very useful: enzymes can remove the related burden of poor catalytic activity and high overpotential requirement.

Following seminal demonstrations of photochemical reduction of CO₂ and H⁺ by metalloenzymes in 1984 [266, 359], various strategies have been used to link redox enzymes to light-harvesters. Tight electronic integration between enzymes and light-absorbers can be achieved through four main strategies (Fig. 1.23): (a) non-specific interaction with light-absorbing components, (b) specific covalent-linkage, (c) immobilisation on porous semiconductor nanoparticles, and (d) photoelectrodes. (Much less advantageous in this respect are multi-component ‘cascade’ systems, which depend on regenerating freely diffusing components such as NAD(P)H, as devised for light-driven, FDH-catalysed CO₂ reduction [360–362].)

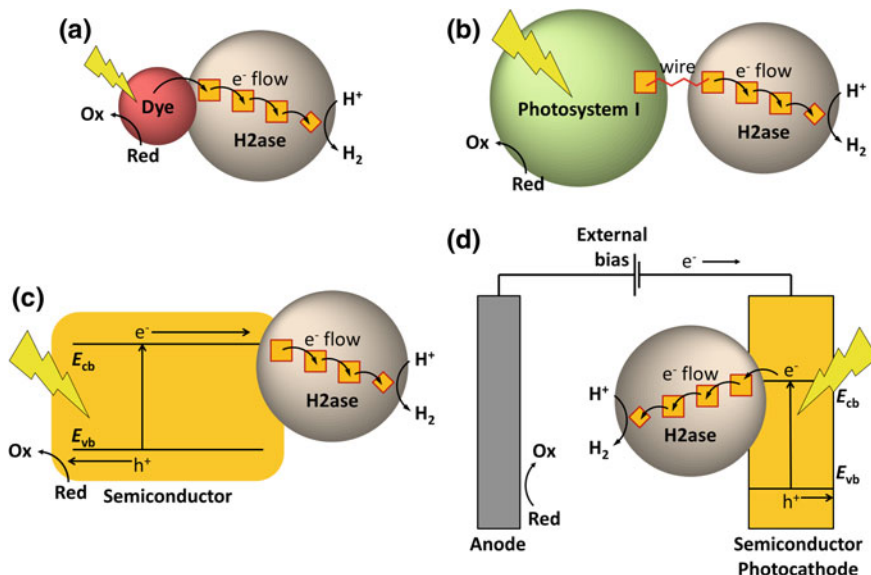


Fig. 1.23 Cartoons depicting different strategies for enzyme-light-absorber interaction, exemplified with a hydrogenase enzyme. **a** 'Photoenzyme', **b** 'fusion protein' comprising hydrogenase wired to Photosystem I, **c** hydrogenase immobilised on a semiconductor nanoparticle, **d** photoelectrochemical cell with hydrogenase attached to a semiconductor photocathode. Reprinted with permission from Ref. [363]. Copyright 2015 Elsevier

1.5.3.2 Photoenzymes

'Photoenzymes' can be formed as short-lived encounter-complexes between sensitizer and protein in bimolecular reactions, or by covalent dye-attachment on selected protein sites (created by introducing specific anchoring groups via site-directed mutagenesis). A photoenzyme formed by covalently attaching a polypyridine Ru(II) photosensitizer to a [NiFe]-hydrogenase was reported by Peters and co-workers [364]. The authors used an amine functionality on one of the Ru-ligands to form amide bonds with various carboxylates on the protein surface. Visible-light-driven H₂ production was observed (even in the presence of O₂) using ethylenediaminetetraacetic acid as a sacrificial electron donor, but the system still relied on a soluble mediator (methyl viologen), reflecting the poor electron transfer rates resulting from nonspecific coupling. Reisner and co-workers used Eosin Y, a polyaromatic photosensitizer that drives H₂ evolution by [NiFeSe]-hydrogenase through efficient bimolecular electron transfer, without the need for a redox mediator, using triethanolamine (TEOA) as sacrificial donor [365]. The powerfully reducing nature of excited Eosin ($E = -0.91$ V vs. NHE) also ensured adequate O₂ tolerance.

1.5.3.3 From Photoenzymes to Fusion-Complexes: The Limiting Case of Stoichiometric Architectures

Lacking specific linkages, the aforementioned photoenzymes depend on a proportion of orientations being productive, as well as bimolecular reactions. An alternative approach is to attach enzymes stoichiometrically to light-harvesting components using specific linkages. Photocatalytic activity of nitrogenase, for example, has been achieved in this manner [366]: a variant of the molybdenum-iron-protein, specifically derivatised with a Ru-photosensitiser, reduces protons to H_2 and acetylene to ethylene when illuminated.

Photosystem I can be fused with hydrogenases [367], such as in the intricate example from Golbeck and co-workers, where a fusion complex is produced by tethering PSI to the [FeFe]-Hydrogenase *CaHydA* from *Clostridium acetobutylicum* through an alkane-dithiol molecular wire [368]. The dithiol tether connects the two enzymes by binding at their respective solvent-exposed [4Fe-4S] clusters. Overcoming the diffusion limit, the nanoconstruct is, under illumination, twice as active as natural cyanobacterial photosynthesis in terms of electrons per second per PSI.

1.5.3.4 Enzymes on Semiconductor Nanoparticles

Overall rates of 1:1 fusion systems, comparable to synthetic molecular ‘dyads’ [120, 369], will always be controlled by the slower component, a limitation that need not apply if enzymes are attached to nanoparticles. The amount of immobilised catalyst (and, if necessary, molecular sensitiser) can be varied, allowing control over the reaction rates of the different components. The band gap determines the spectral region that can be utilised, while valence and conduction band potentials determine, respectively, the oxidising and reducing ability of the photoexcited material. The challenge is to find materials that present these fundamental properties to greatest advantage for specific enzymes: several successful systems have been described, each assembled using electrostatic interactions or small linker molecules.

Obtaining stable and efficient linkages between catalysts and semiconductor surfaces is crucial but far from being a simple task. The linkage can be a deciding factor in terms of charge transport yields and chemical robustness under reaction conditions. A large fraction of electrons or holes is typically diverted by destructive side or back reactions, or trapped at defect sites, resulting in low photochemical quantum yields. Ideally, enzymes should be attached such that the electron entry/exit point, usually lying close to the protein surface, comes into close contact with the semiconductor surface, thus minimising the interfacial electron tunnelling barrier. Due to their relatively large dimensions, this problem is far greater for enzymes than for molecular catalysts. A covalent linker improves stability but need not improve interfacial electron transfer rates. Efficient charge transport is crucial at every stage of the catalytic cycle, but for efficient catalysts that operate close to

reversibility, charge injection from the excited semiconductor to the catalyst is most critical. This step is always in direct competition with several destructive decay processes in the semiconductor such as photoemission, non-radiative decay, and intersystem crossing.

Several strategies for linking enzymes to semiconductor materials are in use. Electrostatic interactions can be exploited, using variations in pH and ionic composition, and utilising favourable charge distributions on the enzyme surface. For example, the surface of TiO_2 is covered with hydroxyl groups that are in acid–base equilibrium with H_2O , and the enzyme’s electrostatic surface can be computed from a crystal structure. Electrostatic interactions alone usually result in a wide distribution of enzyme orientations on the semiconductor and may limit experiments to certain narrow pH regimes in which semiconductor and the optimal contact region on the enzyme have opposite charges.

Semiconductor surfaces can be modified with small linker molecules to give more specific enzyme attachment. The [FeFe]-hydrogenase *CaHydA*, for example, has a positively charged region of surface close to the ‘distal’ [4Fe–4S] cluster lying at the end of the relay system [370]. This is the site at which electrons enter or leave the enzyme and, *in vivo*, engages in a dynamic ET complex with its natural redox partner ferredoxin. Exploiting this knowledge, *CaHydA* was attached to CdS nanorods capped with a monolayer of negatively charged 3-mercaptopropionic acid (MPA) [310, 371].

Enzymes can be immobilised on carbon nanotubes, resulting in excellent electron transfer kinetics—usually measured by electrochemical methods. By attaching *CaHydA* directly to single-walled carbon nanotubes [372], King and co-workers obtained an order-of-magnitude increase in catalytic rates for both H^+ reduction and H_2 oxidation [373]. Another example has been developed in the course of electrochemical studies where the aim has been to maximise coverage and stability for a membraneless H_2/O_2 fuel cell [374]: first, a graphite electrode is pre-coated with multi-walled carbon nanotubes, modified by binding of 1-pyrenebutyric acid (through π – π interactions), producing a dense, permeable conducting layer. Second, a [NiFe]-hydrogenase (Hyd1) from *E. coli* is introduced to the modified electrode surface, where it becomes covalently linked to the 1-pyrenebutyric acid units via peptide coupling to surface lysines. This modification leads to an order-of-magnitude enhancement of an enzymatic hydrogen–air fuel cell compared to analogous cells in which the enzymes are conventionally adsorbed on graphite [375].⁴

Another strategy to link hydrogenases covalently to graphite electrodes is via amide coupling to graphite surfaces pre-functionalised with a layer of either 4-aminophenyl or 4-carboxyphenyl moieties, depending on the surface charge of

⁴The powerful π – π -stacking capability of pyrene moieties has also been exploited to attach small *molecular* fuel-forming catalysts to electrodes: Gray and co-workers attached small organometallic H_2 evolving and CO_2 reducing catalysts to a graphite electrode via pyrene-appended bipyridine ligands; even so, the resulting electrocatalytic rates were much lower than observed with enzymes as catalysts.

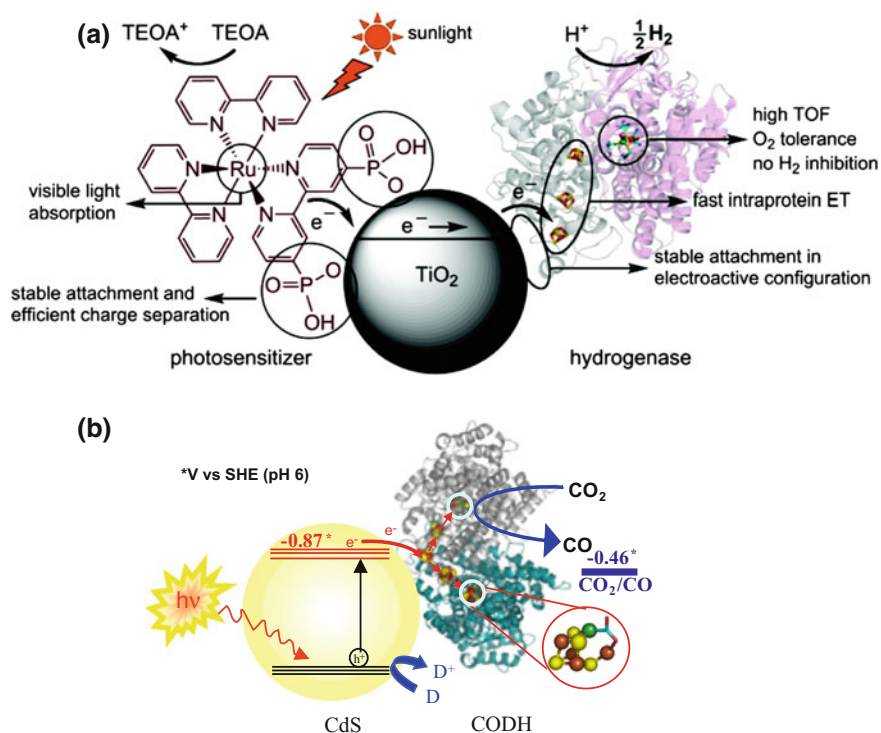


Fig. 1.24 Cartoons depicting visible-light-driven photocatalytic fuel formation catalysed by hydrogenase and CODH enzymes immobilised on semiconductor nanoparticles. **a** [NiFeSe]-hydrogenase adsorbed on dye-sensitised TiO_2 particles. Reprinted with permission from Ref. [378]. Copyright 2009 American Chemical Society. **b** CODH attached to visible-light-responsive CdS nanocrystals. Reprinted with permission from Ref. [381]. Copyright 2012 The Royal Society of Chemistry

the respective enzyme [376]. Covalent bond formation is again achieved through peptide coupling (with *N*-hydroxysuccinimide).

Figure 1.24 depicts H^+ and CO_2 photoreduction by semiconductor-enzyme systems. The prototype was established by immobilising hydrogenases on TiO_2 nanoparticles co-modified with the visible-light sensitizer RuP (Fig. 1.24a) [377]. A [NiFeSe]-hydrogenase was identified as a particularly proficient catalyst, the optimised system (enzyme-RuP- TiO_2 with TEOA as donor) achieving a reproducible TOF of 50 s^{-1} (total) enzyme $^{-1}$ under ambient conditions, thus providing a benchmark for subsequent systems [378]. Similar dye-sensitised metal oxide systems have been devised for CODH-catalysed conversion of CO_2 to CO, and one based on RuP-sensitised TiO_2 -P25 (a rutile-anatase mixture) emerged as clear winner among several metal oxides, including ZnO and SrTiO_3 [379, 380]. A simpler construct, which uses band gap excitation, was assembled using CdS nanocrystals (Fig. 1.24b) that absorb visible light [381]. Both quantum-dots and

Table 1.1 Overview of enzyme-semiconductor systems for photochemical solar-fuel generation

Semiconductor	Enzyme	Evolved gas	TOF ($\text{s}^{-1} \text{enzyme}^{-1}$)	Φ (%)	Reference
RuP/TiO ₂	NiFeSe	H ₂	50	N/A	[378]
RuP/TiO ₂	CODH	CO	0.14	0.07 at 420 nm	[380]
CdS	CODH	CO	1.23	N/A	[381]
CdTe	<i>CaHydA</i>	H ₂	25	9 at 532 nm	[382]
CdS	<i>CaHydA</i>	H ₂	380–900	20 at 405 nm	[371]

nanorods were investigated, the CODH-nanorod assemblies proving superior, with an average TOF of $1.23 \text{ s}^{-1} \text{enzyme}^{-1}$. Semiconductor nanocrystals have also been utilised for solar H₂ production with the [FeFe]-hydrogenase *CaHydA*, which is more active than [NiFeSe]-hydrogenase [310, 371, 382]. Using CdTe nanoparticles (and ascorbic acid as donor), a STH efficiency of 1.8% was achieved under simulated sunlight with a TOF of $25 \text{ s}^{-1} \text{enzyme}^{-1}$ [382]. In a major step forward, a per-enzyme TOF in excess of 380 s^{-1} has recently been achieved for *CaHydA* adsorbed on CdS nanorods [371].

Performances of the aforementioned systems for photocatalytic hydrogen evolution and CO₂ reduction are summarised in Table 1.1.

1.5.3.5 Photoelectrode Assemblies for Fuel-Formation

With regard to closing the photosynthetic cycle and creating an integrated photoelectrochemical device, linking enzymes to semiconductor *photoelectrodes* would constitute a further evolutionary step compared to the approaches described thus far. Enzyme-photoelectrode assemblies do not depend on sacrificial reactants and an external bias can be applied to supply additional driving force if needed. Product separation is possible by compartmentalisation of the electrochemical cell using a porous membrane.

A notable example of this approach, using a molecular cobalt cobaloxime catalyst, comes from Sun and co-workers who achieved light-driven H₂ evolution by co-adsorbing the organic pigment P1, developed as organic photosensitiser for *p*-type DSSCs [383], and the metalorganic catalyst on NiO [188]. Few other systems using molecular catalysts anchored on *p*-type semiconductors exist [189, 253, 255, 291, 384, 385] and no such system building upon a fuel-forming enzyme has been devised yet. Chapter 5 will address this issue on a proof-of-concept level.

1.6 The Mechanisms of Fuel-Forming Enzymes

1.6.1 Common Mechanistic Principles

This section will examine in detail the mechanisms and important structural features of the three classes of fuel-forming enzymes that are of central relevance to this thesis, [NiFe]-hydrogenases, [FeFe]-hydrogenases, and CODH. The active sites of these enzymes have evolved to optimise selectivity and reaction rates by tuning reduction potentials, coupling proton and electron transfers so they are synchronous, and stabilising intermediates by just the right degree (i.e. avoiding high-energy states). Most attempts to mimic enzymes have focused on the active site, but it is important to consider how and why the inner coordination complex is held in such a special environment (the outer shell). Away from the active site, which is buried and shielded from bulk solvent, electron relay centres have evolved to have small reorganisation energies, optimal reduction potentials, and separation distances just short enough to allow fast and efficient electron transfer. The complete enzyme has the capacity to store all the charge carriers (electrons or holes) that are required to perform a complete half-cell reaction—a property that contrasts with most small metal-complex catalysts. The charge carriers may be ‘trapped’ within the enzyme, thus impeding recombination within the semiconductor. How important then is the outer shell, with its special environment—a factor distinguishing redox enzymes from small-molecule electrocatalysts? In enzymes, the outer shell can be engineered to produce bespoke variants, with atoms and their positions altered precisely. All this is achieved with earth-abundant elements—demonstrating what is possible *without* rare or expensive elements.

Crucially, the active sites shown in Figs. 1.14 and 1.17 are two-centre catalysts, i.e. they possess acid and base functionalities, located at precise distances apart (a prime example is the active site of [FeFe]-hydrogenases, where an amine-moiety is placed right above the Fe-coordination site). Inorganic surfaces can mimic some of these principles at defects or bimetallic interfaces—but can chemists realise all of these necessary requirements?

1.6.2 [FeFe]-Hydrogenases

1.6.2.1 Structural Features

Most of the [FeFe]-hydrogenases that have been studied are from green algae, *Clostridia*, and *Desulfovibrio* species [210]. Three enzymes have been crystallised: the hydrogenase HydA1 from the green alga *Chlamydomonas reinhardtii* (*Cr*) has been crystallised in its apo-form, i.e. lacking a di-iron subdomain that is part of the active site [386]. Structures of the complete holo-enzymes were determined for the periplasmic hydrogenase from *Desulfovibrio desulfuricans* (*DdH*) [387] and the

cytoplasmic Hydrogenase I from *Clostridium pasteurianum* (*CpI*) [388], depicted in Fig. 1.25. The active site, known as the H-cluster, is structurally conserved among the different types of [FeFe]-hydrogenase. In prokaryotic hydrogenases, it is buried inside the protein and pathways associated with substrate/product transport such as gas channels exist, as well as components for electron and proton transfer [210].

Many of the [FeFe]-hydrogenases contain additional FeS clusters ('F-clusters'), which are typically spaced within 11 Å [210] and act as an electron relay chain, providing efficient electron transport between the active site and external redox partners at the protein surface [389, 390]. The [FeFe]-hydrogenase from *Dd* consists of two subunits, with the active site and the two additional [4Fe-4S] relay centres being housed in the large subunit [387]. Its monomeric congener *CpI* contains four F-clusters, three [4Fe-4S] and one [2Fe-2S] centre (Fig. 1.25) [388]. Theoretical calculations on this enzyme found the electron-transport process to activate a water channel, suggesting a coupled mechanism for proton and electron transport to the active site [391]. The algal enzyme *CrHydA1* is unique in that it does not contain any further FeS clusters in addition to the one that is part of the active site [386].

Substrate and inhibitors access the active site through hydrophobic gas-access channels, which are, according to the crystal structures obtained so far, much shorter than the channels in [NiFe]-hydrogenase enzymes [210]. Three putative pathways

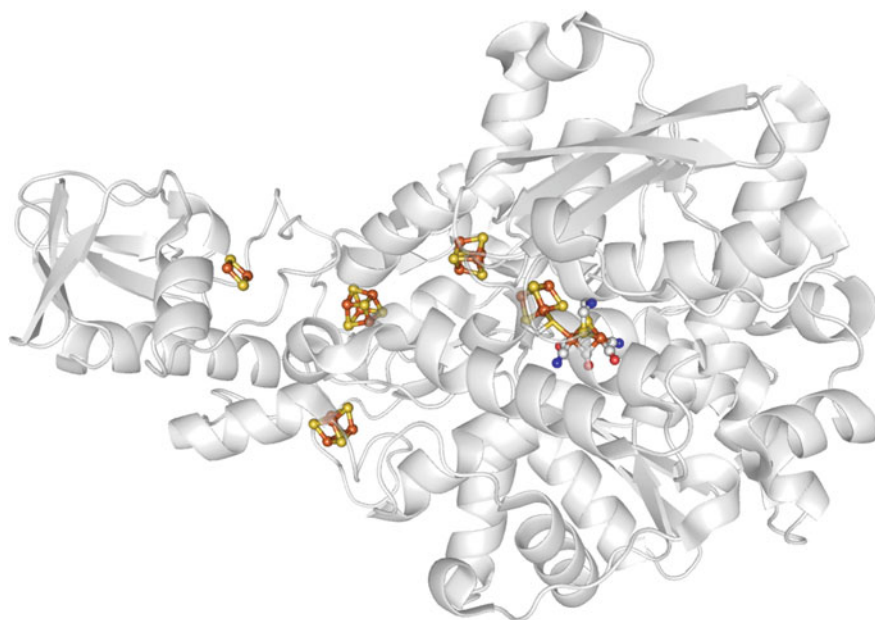


Fig. 1.25 X-ray crystal structure of the [FeFe]-hydrogenase I from *Clostridium pasteurianum* (*CpI*, PDB structure 3C8Y). The active site and the FeS centres are represented as spheres and sticks. Colour coding: iron, orange; sulphur, yellow; carbon, grey; nitrogen, blue; oxygen, red

that extend from the solvent to the H-cluster and the so-called central ‘C’ cavity (which leads to the active site) have been suggested [210, 392]. The static ‘A’ channel comprises an elongated cavity, connecting the protein surface to the central C cavity [387]. A recent computational study suggested O₂ diffusion into the protein proceeds via this channel [392]. A ‘dynamic’ channel, ‘B’, which extends from the protein to the central cavity, was identified by molecular dynamics simulations: it was previously suggested to be the dominant route for oxygen transport [393]. A third channel (‘W’) is lined by hydrophilic amino acids that stabilise water molecules [392].

Putative proton pathways in both *Dd* and *CpI* have been investigated in silico [394, 395]. In both enzymes, proton transfer to the active site takes place via three Glu residues, one Ser, one water molecule and one Cys, the latter being located close to the azadithiolate bridgehead atom of the active site (Fig. 1.26). Genetic modification of any of the highly conserved residues leads to a drastic reduction in activity [396], corroborating the computational results. A molecular dynamics study suggests the same pathway [397].

1.6.2.2 Active Site and Redox States

The ‘H-cluster’ (Fig. 1.26) consists of two components: a binuclear iron subcluster [2Fe]_H that is connected, via a cysteine sulphur ligand, to a cubane [4Fe–4S]_H cluster [210]. The Fe atoms in [2Fe]_H, designated ‘distal’ (Fe_d) or proximal (Fe_p) according to their position with respect to the [4Fe–4S]_H domain, are each coordinated by CO and CN[−] ligands and are bridged by an unusual azadithiolate (adt) ligand that positions a pendant amine–N above Fe_d.

Aside from an inactive oxidised form known as H_{ox}^{inact} [where both Fe atoms of [2Fe]_H are Fe(II) and the [4Fe–4S]_H domain is oxidised (2+)] and the non-catalytic one-electron reduced form referred to as H_{trans} ([4Fe–4S]_H¹⁺ [Fe(II)Fe(II)]), three active oxidation levels of the H-cluster have been identified by spectroscopy—H_{ox}, H_{red}, and a ‘super-reduced’ state known as H_{red}²⁺ [210]. The H_{ox} state ([4Fe–4S]_H²⁺ [Fe(I)Fe(II)]), which is found in all known [FeFe]-hydrogenases, has the same overall electron count as H_{trans}, but contains a mixed valence binuclear subdomain. One-electron reduction of H_{ox} leads to the formation of H_{red} ([4Fe–4S]_H²⁺ [Fe(I)Fe(I)]), in which the H-cluster is EPR-silent. Addition of a further electron yields the

Fig. 1.26 The active site of [FeFe]-hydrogenases, known as the H-cluster. The overall charge of [4Fe–4S]_H is 2+, but individual charges on Fe_p and Fe_d are still under debate [398]—both Fe_p(II)–Fe_d(I) and Fe_p(I)–Fe_d(II) are possible combinations

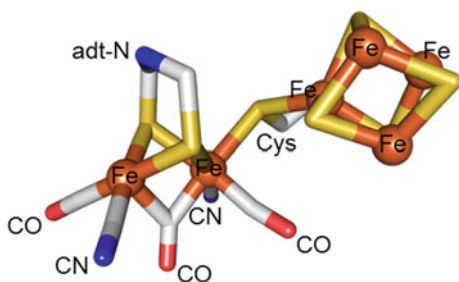
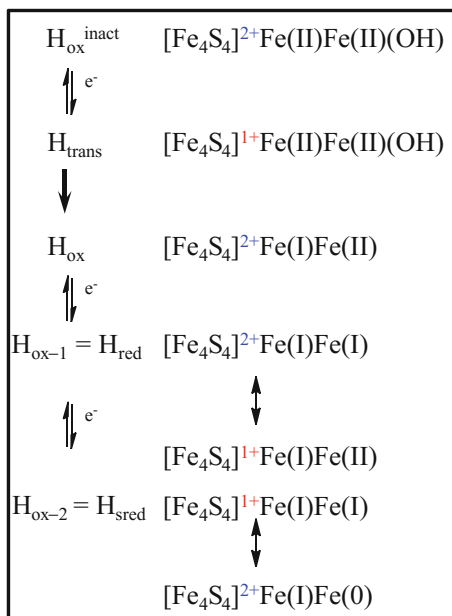


Fig. 1.27 Overview of the redox levels and corresponding spectroscopic states of the H-cluster in [FeFe]-hydrogenases



‘super-reduced’ state, which has been characterised by EPR and FTIR spectroscopy in the algal hydrogenase *CrHydA1*, where no F-clusters that would interfere with the EPR spectrum of the active site are present [376]. In the spectroscopically accessible resting-form of H_{sred} , the EPR spectrum is typical for a reduced FeS cluster, $[4Fe-4S]^{1+}$, implicating that both the proximal and distal iron are Fe(I). Lubitz and colleagues proposed that this resting state cannot be stabilised in other [FeFe]-hydrogenases, as the additional F-clusters present in these enzymes are expected to quickly reoxidise the reduced cubane subdomain of the H-cluster [376].

A detailed EPR and FTIR study by King and co-workers, also carried out using *CrHydA1*, corroborates the characterisation of H_{sred} by Lubitz, but suggests that the overall picture is more complex [399]. Further states in which an electron is transiently housed on the H-cluster cubane (i.e. $[4Fe-4S]_{H}^{1+}$ -moieties) have been identified. Armstrong and co-workers introduced a nomenclature in which the steady-state redox levels of the H-cluster dominating at different potentials are distinguished as H_{ox} , H_{ox-1} , and H_{ox-2} , rather than using the spectroscopic labels H_{red} and H_{sred} [400]. This nomenclature allows for discrimination between catalytic oxidation levels that have clear overall electronation states, but may have different protonation states and the oxidation numbers of the individual iron centres are still vague. The different redox levels of the H-cluster are summarised in Fig. 1.27.

Carbon monoxide, a potent inhibitor of [FeFe]-hydrogenases, binds strongly to H_{ox} and X-ray crystallography shows CO to bind to Fe_d [401]. The extrinsic CO ligand is photolabile and reactivation of the inactivated H-cluster is greatly

enhanced under illumination [402]. From CO inhibition, it follows that Fe_d is most likely the site at which H_2 binds. Carbon monoxide binds less strongly to H_{red} (it destabilises the H-cluster [403]) and does not bind to H_{sred} [400]. The fact that CO protects against irreversible inactivation by O_2 has been interpreted in terms of O_2 also binding, initially, at Fe_d [402, 404], leaving an inactive $[\text{4Fe-4S}]_{\text{H}}$ domain that can be reactivated in vitro [405].

1.6.2.3 Artificial Maturation

An excellent example of the special nature of the active sites of metalloenzymes is provided by a recent discovery made during investigations of the biosynthesis of $[\text{FeFe}]$ -hydrogenases. Two papers which appeared in 2013 showed how the Fe-carbonyl precursor of $[\text{2Fe}]_{\text{H}}$ (which shows little catalytic activity in vitro) becomes extremely active when inserted into the $[\text{2Fe}]_{\text{H}}$ binding cavity of the preformed ‘apo-enzyme’ that is already equipped with the $[\text{4Fe-4S}]$ cluster [406, 407]. The conversion is shown pictorially in Fig. 1.28a. All that occurs in terms of the inner-sphere coordination chemistry is that one CO is replaced by the cysteine-S ligand to link the two components together. The structures of the $[\text{2Fe}]_{\text{H}}$ precursor, the apo-enzyme, and the active site of the assembled H-cluster within the binding cavity are depicted in Fig. 1.28b.

Significant catalytic activity is *only* achieved upon completion of the insertion reaction, i.e. *formation of the ‘holo’-enzyme*, as visualised in an elegant electrochemical study by Dr. Suzannah Hexter [408] (Department of Chemistry, University of Oxford). Figure 1.29a shows cyclic voltammograms of the CrHydA1 apo-protein adsorbed on a pyrolytic graphite electrode, catalytic activity only commences upon injection of the $[\text{2Fe}]_{\text{H}}$ precursor complex and increases until the voltammograms are virtually indistinguishable from native enzyme. Artificially matured CrHydA1 displays reversible electrocatalysis and the voltammetric scans cross the zero-current axis sharply at precisely the thermodynamic equilibrium potential for H^+/H_2 interconversion. The kinetics of the insertion reaction/enzyme activation are depicted in Fig. 1.29b. These experiments demonstrate that the integrity of the whole enzyme is essential for catalytic activity.

One important possibility is that only the complete H-cluster is able to delocalise, or accommodate more easily, a second electron. A recent experiment by Rauchfuss et al. showed that attaching a ferrocene unit to an Fe-carbonyl analogue of $[\text{2Fe}]_{\text{H}}$ conferred catalytic activity for H_2 oxidation that was previously absent [409]. However, the activity remained orders of magnitude lower than for the enzyme. The discovery outlined above further establishes the importance of optimising the *total* environment (i.e. the second- and outer-shell atoms, not just the first coordination shell). Despite the much longer distance that is required to transfer electrons to and from the buried active site of the enzyme compared to the small complex, the enzyme is the clear winner. A buried active site poses no problem if

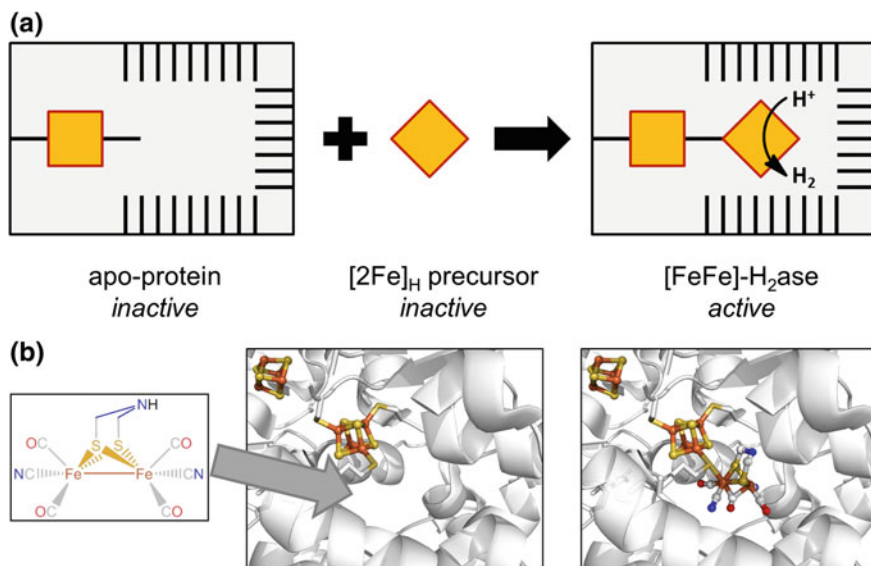


Fig. 1.28 **a** Cartoon showing the insertion of the $[2\text{Fe}]_{\text{H}}$ precursor into the hydrogenase apo-protein to give active enzyme. Binding of $[2\text{Fe}]_{\text{H}}$ to the $[4\text{Fe-4S}]_{\text{H}}$ domain via a cysteine-S ligand occurs after loss of one CO ligand. The grey box represents the binding cavity, with amino acids surrounding the active site depicted as black lines. The $[4\text{Fe-4S}]_{\text{H}}$ fragment is shown as an orange square, and $[2\text{Fe}]_{\text{H}}$ is depicted as an orange rhombus. **b** Structural representation of the insertion reaction. Depictions of the active site and the surrounding cavity were generated in PyMOL using the PDB structure 3C8Y. Some amino acids are omitted to provide an unobstructed view of the active site and the surrounding environment. Colour coding: iron, orange; sulphur, yellow; carbon, grey; nitrogen, blue; oxygen, red

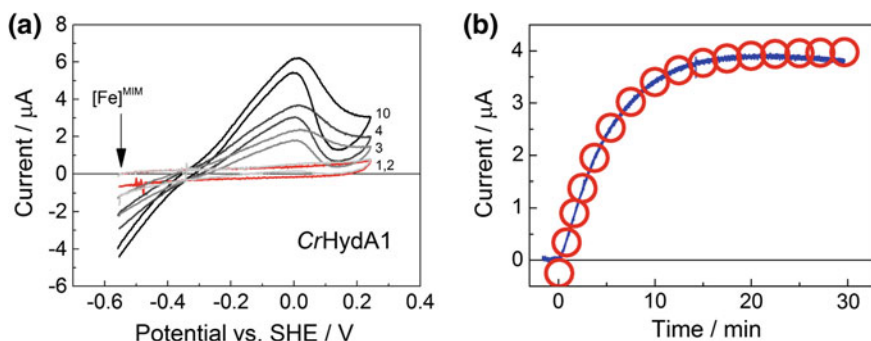


Fig. 1.29 Insertion of the $[2\text{Fe}]_{\text{H}}$ H-cluster precursor ($[\text{Fe}]^{\text{MIM}}$) into the apo-hydrogenase *CrHydA1*, monitored by protein film electrochemistry. **a** Set of cyclic voltammograms, in which apo-*CrHydA1* is adsorbed on a pyrolytic graphite electrode (PGE). $[\text{Fe}]^{\text{MIM}}$ is introduced into the electrochemical cell solution (final concentration 230 nM) at -560 mV after the first scan (shown in red). Consecutive scans are depicted in shades of grey. Conditions: pH 6.1; 5°C ; scan rate = 30 mV s^{-1} ; $\omega = 1000\text{ rpm}$; 100% H_2 . **b** Current response (blue line) observed upon injection of $[\text{Fe}]^{\text{MIM}}$ ($c_{\text{final}} = 230\text{ nM}$) at $t = 0$. A single-exponential fit of the kinetics of enzyme activation is depicted as red circles ($k_{\text{obs}} = 3.3 \times 10^{-3}\text{ s}^{-1}$). Conditions: $E = -40\text{ mV}$; pH 6.1; 15°C ; $\omega = 1000\text{ rpm}$; 100% H_2 . Adapted with permission from Ref. [408]

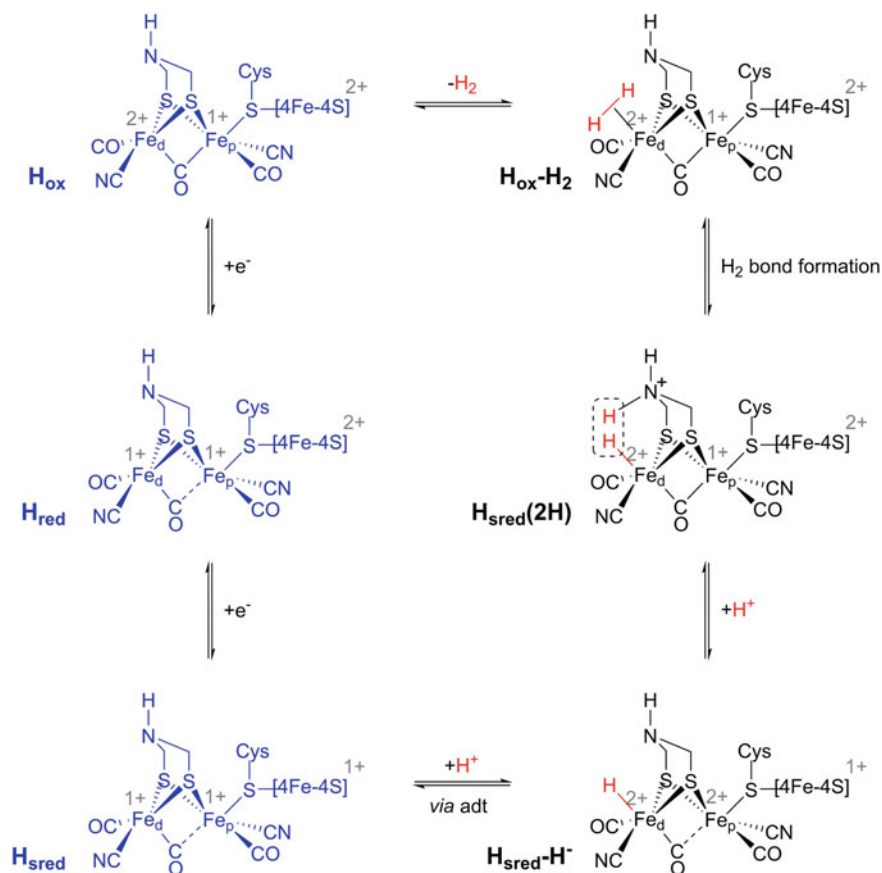
electron relay centres are present. In addition to providing a fast ‘wire’, these relay centres, noted as having small reorganisation energies, can trap and store electrons (or ‘holes’) within the macromolecule.

1.6.2.4 Mechanism

In principle, H_2 molecules are formed by the reaction of a metal-hydride (Fe-H^-) with a nearby, protonated base, most likely the bridgehead adt-N (a H^+NHR_2 moiety). However, due to the high activity of [FeFe]-hydrogenases, it is very difficult to trap intermediates in the catalytic cycle. During catalytic turnover, the H-cluster is thought to interchange between three one-electron separated redox states that have been spectroscopically characterised and identified as/proposed to be part of the catalytic cycle: H_{ox} , H_{red} , and H_{sred} (compare Fig. 1.27) [210, 376, 399]. Starting from H_{ox} , two electrons and two protons are needed to evolve H_2 . However, it has not yet been established, experimentally and in a kinetic study, in which order these events occur.

Scheme 1.1 shows a proposed mechanism, which takes into account recent observations from both experiment and theory. Therein, formation of a terminal [410] Fe_d -hydride and subsequent creation of the dihydrogen-bond is hypothesised to take place when the enzyme is in the super-reduced electronation level. Recent experimental evidence for Fe_d being unprotonated in the reduced H_{red} state stems from X-ray absorption and emission (XAE) spectroscopy [411]. Lubitz et al. [376] conclude from combined EPR/FTIR studies that Fe_d is also unprotonated in the spectroscopically accessible resting-form of H_{sred} [210]. A terminal hydride at Fe_d ($^{\text{H}_{\text{sred}}}\text{Fe}_d\text{-H}^-$) is proposed to be formed in a rapid, exothermic process following the first protonation of the adt-bridge in H_{sred} [210]. Theoretical calculations suggest that the unpaired electron in $^{\text{H}_{\text{sred}}}\text{Fe}_d\text{-H}^-$ still resides on the cubane subcluster and only the second protonation of the adt-ligand triggers electron transfer to the $[\text{2Fe}]_{\text{H}}$ moiety, which in turn leads to facile H_2 formation [412] in a mechanism similar to the functional DuBois-type analogues discussed in Sect. 1.3.3.1.

Investigations into the mechanism of H_2 -formation by [FeFe]-hydrogenases and the sequential order of protonation and electronation steps are presented in Chap. 3; [FeFe]-hydrogenase electrochemistry studies presented therein utilise the hydrogenase *CaHydA* from the strictly anaerobic bacterium *Clostridium acetobutylicum*. As depicted in Fig. 1.30, this enzyme shows little inactivation at high potentials, in contrast to other [FeFe]-hydrogenases, and can therefore be characterised within a relatively large potential window [213]. Also containing a series of three [4Fe-4S] clusters and one [2Fe-2S] cluster, monomeric *CaHydA* (64.3 kDa) [413] is very similar to the crystallographically characterised hydrogenase *CpI* (Fig. 1.25)—both enzymes share 71% sequence identity [414]. EPR-spectroscopy experiments presented in Chap. 3 were undertaken using the [FeFe]-hydrogenase *CrHydA1* from the green alga *Chlamydomonas reinhardtii*, due to its lack of F-clusters (vide supra).



Scheme 1.1 Proposed catalytic mechanism for hydrogen formation at the H-cluster based on recent spectroscopic observations and theoretical investigations [210, 376, 399, 412]. The three previously characterised redox states H_{ox} , H_{red} , and H_{sred} are depicted in blue. Note that due to lack of conclusive experimental evidence the Fe oxidation states in the $[2Fe]_H$ subsite can only be tentatively assigned to the two individual Fe centres

1.6.3 [NiFe]-Hydrogenases

1.6.3.1 Structural Features

[NiFe]-hydrogenase enzymes can be broadly categorised into three main subclasses: (i) ‘standard’, oxygen-sensitive [NiFe]-hydrogenases, (ii) O_2 -tolerant [NiFe]-hydrogenases, and (iii) [NiFeSe]-hydrogenases. The [NiFeSe]-hydrogenase from *Desulfomicrobium baculatum* (Fig. 1.31) [415] (henceforth simply [NiFeSe]-hydrogenase) was used in semiconductor protein film electrochemistry experiments described in Chap. 4. Forming a subclass of [NiFe]-hydrogenases in which one

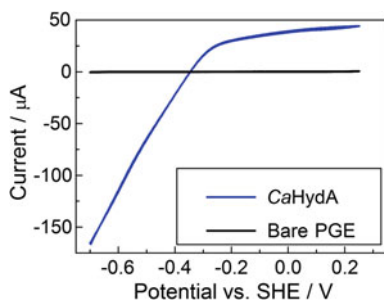


Fig. 1.30 Typical cyclic voltammogram of the [FeFe]-hydrogenase CaHydA adsorbed on a pyrolytic graphite electrode, recorded under a H_2 atmosphere at pH 6.0. The voltammogram illustrates the relative stability of this enzyme under oxidising conditions, as well as the reversibility of catalysis. The zero-current axis is cut sharply at the thermodynamic equilibrium potential for H^+/H_2 conversion

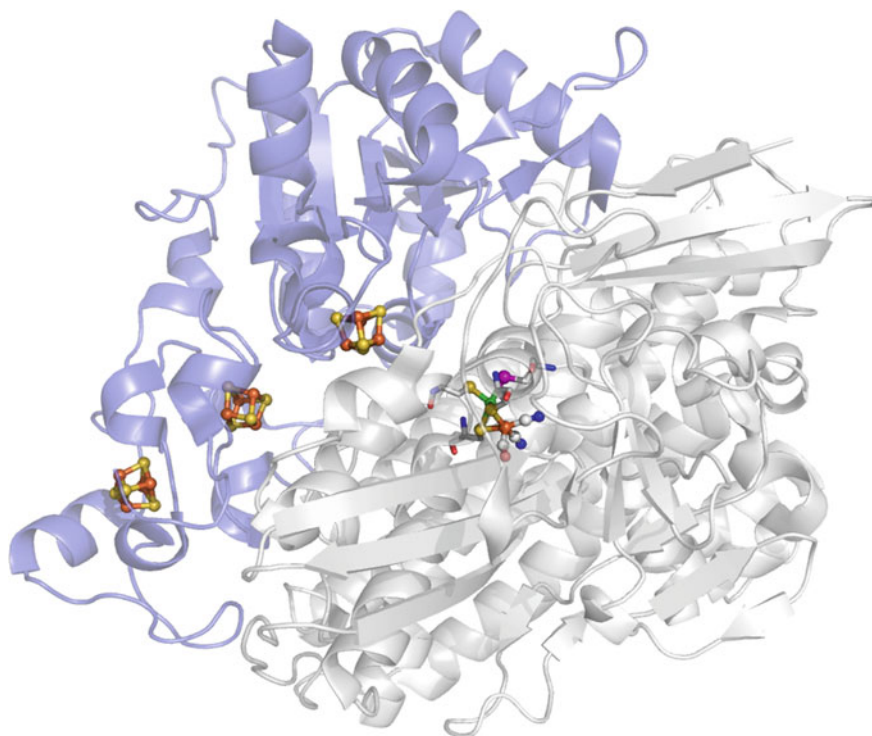


Fig. 1.31 X-ray crystal structure representation of the [NiFeSe]-hydrogenase from *Desulfomicrobium baculatum* (PDB code 1CC1). The large and small subunits are depicted in grey and blue, respectively. FeS clusters and the active site are shown as sticks and spheres. Colour coding: iron, orange; sulphur, yellow; carbon, grey; nitrogen, blue; oxygen, red; nickel, green; selenium, purple

cysteine ligand to Ni is replaced by a selenocysteine, [NiFeSe]-hydrogenases are excellent H₂ producers that retain some activity in the presence of O₂ [215].

The overall structures of the [NiFe]-hydrogenases show a great deal of similarity across the three above-mentioned subclasses and most of the enzymes are purified as heterodimers, with the small subunit containing an FeS electron transport chain, ‘wired’ to the deeply buried catalytic centre that is housed in the large subunit, as for example in Fig. 1.31 [210]. A substrate/inhibitor pathway and a putative proton pathway have also been found [210].

Similar to the [FeFe]-hydrogenases, [NiFe]-hydrogenases contain additional FeS clusters. The electron transfer chain in all three subclasses consists of three FeS clusters—termed ‘proximal’, ‘medial’, and ‘distal’ with respect to the active site—located in an almost linear fashion in the small subunit with intercluster distances of approximately 12 Å [210]. In O₂-sensitive [NiFe]-hydrogenases the proximal and distal cluster are [4Fe–4S] clusters, and the medial cluster is [3Fe–4S]. Conversely, [NiFeSe]-hydrogenases contain a [4Fe–4S] medial cluster. Oxygen-tolerant [NiFe]-hydrogenases in turn have a modified proximal cluster, [4Fe–3S], ligated by two additional cysteine residues compared to the standard [NiFe]-hydrogenases. One of the thiolates of the cysteine residues substitutes a sulphide ligand in this FeS centre [210].

The hydrophobic gas channels through which the known gaseous reactants H₂, O₂, and CO transfer to the active site in standard [NiFe]-hydrogenases have been probed experimentally through crystallisation under a xenon-atmosphere [416]. Although the cavities derived from these xenon-bound structures are static models, they reveal several hydrophobic channels on the molecular surface, which combine close to the active site [210]. In the [NiFeSe]-hydrogenase, a computational study identified a hydrogen diffusion pathway in addition to the gas channel found in the crystal structure [417]; it has been suggested that the existence of such alternative pathways is required to yield higher amounts of H₂ accumulation near the active site, compared to standard [NiFe]-hydrogenases [210]. Although it has been suggested that one of the origins of the O₂-tolerance displayed by certain [NiFe]-hydrogenases lies in the substrate transfer channels, and a site-directed mutagenic study [418] created a bottleneck in the hydrophobic gas channel, leading to a lower gas-diffusion rate, enhanced CO inhibition, and increased O₂ sensitivity, it is not considered essential for O₂ tolerance [210]. In order to sustain catalytic activity in the presence of O₂, oxygen is reduced quickly and efficiently to water [419, 420], which is thought to leave the enzyme via hydrophilic water-filled cavities near the active site that lead to the molecular surface [421].

Despite several investigations, both experimentally and computationally, a definitive proton pathway has yet to be established [210]. One model suggests a pathway wherein a structurally conserved Arg residue positioned opposite the μ -hydrido ligand at the active site acts as initial proton acceptor [422], further transfer away from the active site is thought to take place (with increasing distance) via Asp, His, and Glu residues. Substitutions of the conserved amino acids of this

presumed transfer route impaired the activity of the hydrogenase. A different model suggests a terminal cysteine at the active site as initial proton acceptor [423], followed by transfer to a nearby glutamate [424]. It is entirely conceivable that both pathways play a role in the heterolytic splitting of H_2 by [NiFe]-hydrogenases, one acting as a shuttle for H^+ , the other one transferring the proton that originally stems from the hydrido ligand, the other immediate product of H_2 cleavage.

1.6.3.2 Active Site and Redox States

Similar to the H-cluster, the active site of [NiFe]-hydrogenases (Fig. 1.32a) also contains CO and CN^- ligands, unusual for biological systems. Four sulphurs from four strictly conserved cysteine residues are coordinated to the Ni, two of which are bridging to the adjacent Fe centre and the other two being bound to the Ni in a terminal fashion [210]. The low-spin Fe(II) ion is coordinated by one CO ligand and two CN^- ligands, strong σ -donors that form hydrogen bonds to amino acids surrounding the active site. A third bridging ligand (not shown in Fig. 1.32), the nature of which changes depending upon the redox state of the enzyme (vide infra), is ligated to both the Ni and the Fe centres [210]. Figure 1.32b depicts the active site of [NiFeSe]-hydrogenase, the only structural difference being the replacement of one of the terminal cysteine residues by a selenocysteine (SeCys) [415].

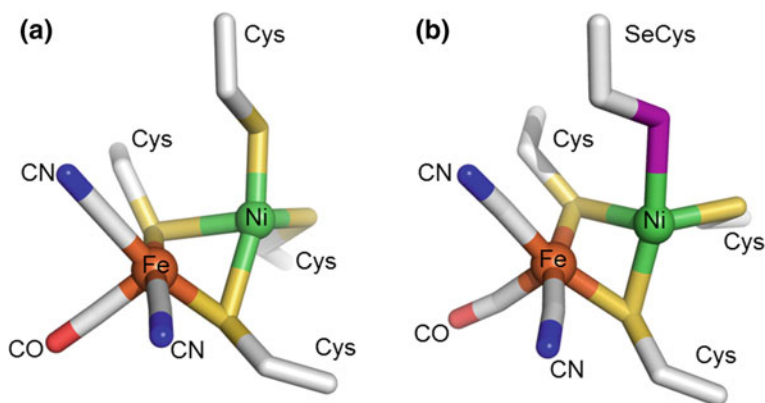


Fig. 1.32 Structural representations of the active sites of **a** [NiFe]-hydrogenase from *Desulfovibrio gigas* (inactive, oxidised ‘unready’ form, bridging ligand not shown, and PDB code 1YQ9) and **b** [NiFeSe]-hydrogenase from *Desulfomicrobium baculatum* (reduced, active form, PDB structure 1CC1)

The most oxidised states of [NiFe]-hydrogenases are known as Ni–A (commonly termed ‘unready’) and Ni–B (‘ready’). Both states are catalytically inactive and assigned as [Ni(III)Fe(II)], they can be obtained upon exposure to oxygen or through anaerobic inactivation at high potentials [210]. In Ni–B the bridging ligand was assigned as hydroxide [425–427], whereas the exact nature of this ligand in Ni–A is still under debate (a hydroperoxide species was postulated [425, 426]). Whereas Ni–B is quickly reactivated by H₂ (typically within one min), Ni–A requires a much longer reactivation time (> 1 h) [210].

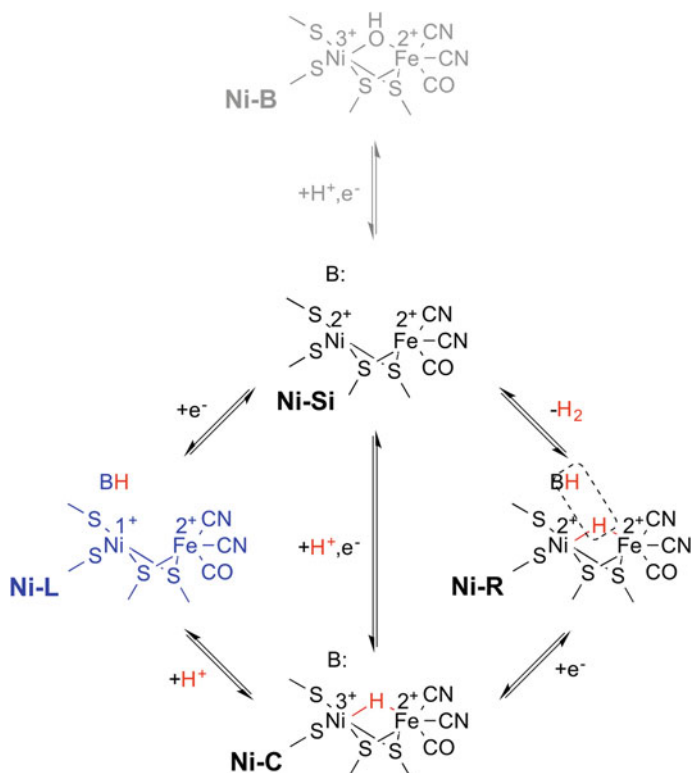
One-electron reduction of the inactive oxidised states leads to the formation of different EPR-silent states, which are all in the [Ni(II)Fe(II)] electronation level. Ni–A reduction yields Ni–SU (‘silent unready’), one-electron reduction of Ni–B results give the Ni–SI_r state (‘silent ready’). The latter is in acid/base equilibrium with Ni–SI_a [428], the most oxidised catalytically active state. Protonation and dissociation of the bridging OH[−] ligand is thought to be responsible for conversion of Ni–SI_r to Ni–SI_a.

Further reduction by one-electron converts the Ni–SI_a state into the active, reduced Ni–C state. Here, H[−] is the third bridging ligand and the nickel centre is formally assigned as Ni(III). Photolysis of Ni–C at cryogenic temperatures yields distinctive EPR-active states, collectively termed NivL [210], in which the bridging hydride has migrated as a proton to a nearby basic ligand such as a terminal cysteine sulphur, leaving behind a [Ni(I)Fe(II)] bimetallic core. The conversion is reversible; Ni–C can be recovered at elevated temperatures. Ni–L has mainly been regarded as an artefact of no mechanistic relevance, however, Hidalgo et al. demonstrated that Ni–L can be generated reversibly in the dark at ambient temperature under turnover conditions and that it is present under all potentials during turnover under H₂ [429]. More recently, Murphy et al. showed that the interconversion (in *E. coli* Hyd1) is a pH-dependent process that proceeds readily in the dark, suggesting that NivL is a true catalytic intermediate of [NiFe]-hydrogenases [430].

Additional one-electron reduction of Ni–C leads to the formation of Ni–R, the most reduced catalytically active state, which has recently been crystallised to a resolution of 0.89 Å [423]. NivR is EPR-silent and is characterised by a bridging hydrido ligand bound to the [Ni(II)Fe(II)] binuclear site.

1.6.3.3 Catalytic Mechanism

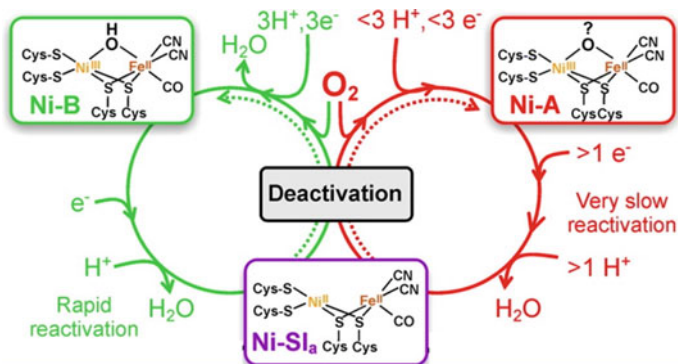
Although more [NiFe]-hydrogenase states have been characterised by spectroscopy than for the [FeFe] analogues, the catalytic mechanism of the former is less clear. A general consensus exists that, following addition of H₂ to the open-bridge Ni–SI_a state, heterolytic H–H bond cleavage leads to formation of Ni–R (Scheme 1.2). As indicated in Sect. 1.6.3.1, two residues are currently favoured to act as base for initial proton removal, a terminal cysteine ligated to Ni [423], or a strictly conserved



Scheme 1.2 Proposed catalytic cycle of hydrogen formation by [NiFe]-hydrogenases, taking into account recent findings by that suggest Ni-L (blue) is a true catalytic intermediate [429, 430]. Anaerobic inactivation (Ni-B) is shown in grey

arginine residue positioned opposite the Ni-Fe site, at a distance of approximately 4.5 Å to the Ni [422]. Recently, a variant of hydrogenase 1 from *E. coli* has been crystallised (PDB structure 4UE3), in which this arginine has been exchanged for a lysine by site-directed mutagenesis. The resulting enzyme is stable and fully assembled, but shows a 100-fold decreased activity [431], indicating that this arginine has indeed mechanistic relevance and might serve as initial proton acceptor in a frustrated Lewis pair mechanism, similar to the adt-N bridgehead in [FeFe]-hydrogenases.

Oxidation of Ni-R yields Ni-C, which is, upon loss of a further electron and proton from the μ -hydrido ligand, converted back into the Ni-SI₃ state. It is conceivable that this second proton leaves the active site through a different pathway, e.g. via one of the terminal cysteine ligands. As suggested in Sect. 1.6.3.2, conversion of Ni-R into Ni-SI₃ can also proceed via Ni-L as catalytic intermediate, if electron transfer is sufficiently slower than proton transfer [429, 430].



Scheme 1.3 The reaction of [NiFe]-hydrogenases with oxygen. O_2 -tolerant hydrogenases form Ni-B, which can be rapidly reactivated (*green* pathway). In ‘standard’ hydrogenases Ni-A is formed accumulatively (*red* pathway), a state that requires low potentials and long reactivation times to restore activity. Anaerobic inactivation is represented by dotted lines. Adapted with permission from Ref. [210]. Copyright 2014 American Chemical Society

1.6.3.4 Oxygen Tolerance

The two oxidised states Ni-A and Ni-B are involved in inactivation by O_2 . In oxygen tolerant [NiFe]-hydrogenases, Ni-B is formed almost exclusively, and O_2 is split into H_2O [419, 420] and OH^- in a four-electron, three-proton process [210] (Scheme 1.3). Of special importance in this reactivation mechanism is the unique proximal [4Fe-3S] cluster [432], which provides two electrons through its ability to undergo two redox transitions at high potentials: the first electron in the four-electron Ni-B reactivation is provided by the active site, the second and third electrons come from the proximal cluster’s [4Fe-3S] $^{3+/4+}$ and [4Fe-3S] $^{4+/5+}$ transitions, respectively, and the fourth electron is provided by the [3Fe-4S] $^{0/1+}$ couple of the medial cluster [210, 421, 433–435]. The precise mechanism of Ni-B reactivation, i.e. the elementary steps, is still under debate and it has yet to be established that the oxygen species in the bridge originates from complete O_2 reduction [210].

Neither Ni-A nor Ni-B have been observed in [NiFeSe]-hydrogenases [436], which form EPR-silent oxidised states and can only sustain activity in the presence of O_2 when low potentials are applied, i.e. in the hydrogen production regime [215]. Their inability to form the [Fe(II)-O(X)-Ni(III)] inactive states found in other [NiFe]-hydrogenases suggests a different pathway exists for oxygen inhibition [436]: the medial [4Fe-4S] cluster, ligated by three Cys and one Ser might play a role [210], coordination by the more electronegative serine should perturb the redox potential of the cluster and impact the electronic structure [436]. Further, oxygen exposure converts the selenocysteine ligated to Ni into oxidised seleninate [437] or selenate [438] species. Compared to sulphur-oxygen bonds, selenium-oxygen bonds are more labile [439], a potential reason why the inactivated protein is readily reactivated and thus exhibits little oxygen sensitivity [215, 440] at low potentials.

1.6.4 Carbon Monoxide Dehydrogenase

1.6.4.1 Structural Features and Active Site

Carbon monoxide dehydrogenases can be classified according to two main categories: the aerobic Mo-CODHs with a Cu-S-Mo(pyranopterin) centre [441] and the anaerobic Ni-CODHs, which contain a [Ni₄Fe-4S] cluster as their active site [442]. Both classes are monofunctional enzymes. Ni-CODHs are frequently associated with acetyl coenzyme A synthase (ACS), forming a bifunctional enzyme which couples CO₂ reduction with formation of acetyl-CoA [442].

This work utilises the Ni carbon monoxide dehydrogenase CODH I from the thermophilic eubacterium *Carboxydothemus hydrogenoformans* (*Ch*), a chemolithoautotroph that is able to grow with CO as its only source of carbon and energy [269]. This bacterium expresses five different Ni-CODH enzymes [443], two monofunctional proteins (CODH I and CODH II) which reversibly catalyse the oxidation of CO [444], the bifunctional CODH III, which is found in a stable complex with ACS and supports autotrophic carbon assimilation [445], CODH IV, which based on genomic analysis is suggested to be associated with a multisubunit enzyme complex for oxidative stress response [270], and CODH V, the role of which remains unclear.

The crystal structure of CODH II has been determined (Fig. 1.33) [446]. The homodimeric enzyme contains five metal clusters, three [4Fe-4S] cubanes (two

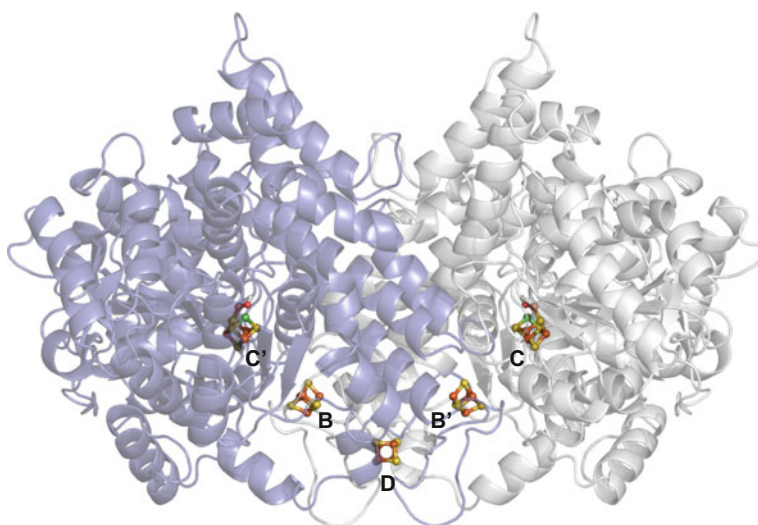


Fig. 1.33 X-ray crystal structure of CODH II from *Carboxydothemus hydrogenoformans* (PDB code 1SU7). The two subunits of the homodimeric enzyme are depicted in grey and blue, respectively. The FeS conduit and the active site are shown as sticks and spheres. Colour coding: iron, orange; nickel, green; sulphur, yellow; oxygen, red; hydrogen, white

B-clusters and one known as D-cluster), as well as two active site clusters, known as C-clusters. The D-cluster, which lies close to the protein surface, covalently links both monomers; it is coordinated by two cysteines of each monomer at the dimer interface [443]. Although it is not yet established if it is part of the electron transfer chain, the D-cluster is ideally positioned to serve as electron entry/exit point. However, it is not reducible at potentials as low as -530 mV, indicating that it may serve a structural, rather than an electron-transfer role [447]. The two B-clusters, each coordinated by the *other* subunit, are positioned about 10 Å away from cluster D and approximately 10 Å from the respective active site, i.e. within typical biological electron transfer distances [389, 448]. In short, the electron transfer chain may encompass $D \leftrightarrow B' \leftrightarrow C$. The active site itself comprises a $[\text{Ni}_4\text{Fe}-4\text{S}]$ cluster [449] (Fig. 1.34), which can be described as $[\text{Ni}_3\text{Fe}-4\text{S}]$ cubane cluster with an extra-cuboidal ‘pendant’ or ‘dangling’ Fe [270].

Ni-CODHs employ two sets of gas channels [443]. One channel is unique to the monofunctional enzymes and, as revealed by a recent X-ray crystallisation study in the presence of the inhibitor *n*-butyl isocyanide, directed to the solvent, allowing CO and CO₂ to rapidly transfer to/escape from the active site [450]. This channel is blocked by several residues in bifunctional Ni-CODHs, most likely to avoid escape of the substrates [269]. A second channel coincides with the tunnel that connects the C-cluster and the active site of ACS (A-cluster) in bifunctional Ni-CODHs [443]. A recent molecular dynamics and DFT study provides evidence for a further, dynamically formed gas channel in bifunctional CODH/ACS, through which CO₂ might diffuse from the solvent to the C-cluster: Blumberger and colleagues proposed that this channel is formed by two cavities that are transiently created by protein fluctuations and are thus not apparent in the X-ray crystal structures [451].

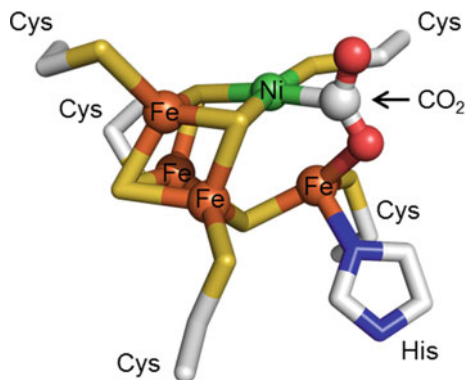
A network of hydrophilic, charged residues is responsible for water transfer from the surface to the C-cluster; protons leave the active site through a chain of four consecutive histidine residues (His93, 96, 99, and 102), the last of which is in contact with the solvent [443].

1.6.4.2 Redox States and Catalytic Mechanism

Four redox states have been identified by spectroscopy, they are referred to as C_{ox} , C_{red1} , C_{int} , and C_{red2} , in order of decreasing oxidation level [452, 453]. The most oxidised state, C_{ox} , is EPR-silent and catalytically inactive, but can be reductively activated at potentials below -200 mV [454]. Using Mössbauer spectroscopy, C_{ox} was assigned as $[\text{Ni}(\text{II})\text{Fe}_{\text{pendant}}(\text{III})]:[3\text{Fe}-4\text{S}]^{1-}$ [452]. One-electron reduction of C_{ox} yields the paramagnetic ($S = 1/2$) C_{red1} state. Here, the pendant iron is coordinated by an aquo or hydroxyl ligand (OH_x) and Mössbauer spectroscopy suggests $[\text{Ni}(\text{II})\text{Fe}_{\text{pendant}}(\text{II})]:[3\text{Fe}-4\text{S}]^{1-}$ [452].

C_{red2} is obtained upon transfer of two electrons from CO oxidation; its operational midpoint potential of -530 mV [269] coincides with the redox potential of the CO₂/CO couple [Eq. (1.5)]. An X-ray crystal structure with CO₂ bound to the active site (Fig. 1.34) [455], obtained by incubating crystals of CODH II in a bicarbonate

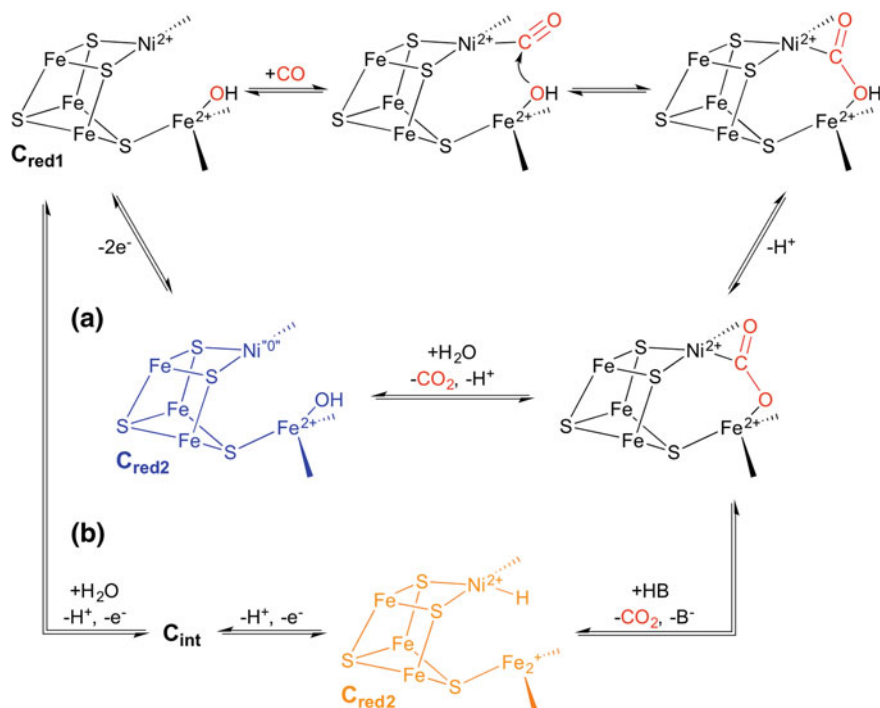
Fig. 1.34 Active site of CODH II from *Carboxydotherrmus hydrogenoformans* in its reduced, CO₂-bound form (PDB structure: 3B52)



solution adjusted to -600 mV (where $C_{\text{red}2}$ prevails) using Ti(III)-citrate, reveals structural insight into CO₂ activation by CODH. A carboxylate bridges Ni and the pendant Fe as a μ_2 - η^2 ligand, C-bound to square planar Ni. One of the oxygens of CO₂ replaces the hydroxo/aquo ligand at the extra-cuboidal Fe. An O–C–O angle of 133° shows that CO₂, which is further stabilised through hydrogen bonding to Lys and His residues, is in an activated state.

It is still unclear where the two additional electrons in $C_{\text{red}2}$ reside, involvement of Ni(0) [452], a Ni(II)-hydride [456], and a Ni–Fe bond (dative metal–metal bond) [457] have been proposed. EPR spectroscopy suggests that the [3Fe–4S] core fragment remains unchanged in the two reduced states $C_{\text{red}1}$ and $C_{\text{red}2}$ [270]. Hence, at least one electron must be transferred to the Ni subsite, as it is unclear as to how a two-electron change could be accommodated by the pendant Fe, which is also coordinated by sulphide, histidine–N, and cysteine–S [270]. Studies using X-ray absorption spectroscopy, carried out on two different CODH enzymes subjected to different oxidation states [458–460], all suggest the Ni subsite is present as Ni(II), irrespective of the redox state of the enzyme [270]. Results, which seem to disfavour formation of a transient Ni(0) state. Half-cycle regeneration to restore the CO–reactive $C_{\text{red}1}$ state proceeds via the transient, EPR-silent C_{int} state, formed by intramolecular one-electron transfer to the B-cluster.

Regarding the mechanism of CO₂/CO interconversion by CODH, crystallographic and spectroscopic observations, in particular the CO₂-bound X-ray structure, suggest a mode of CO₂ activation in which the pendant Fe atom abstracts an O-atom from the C-coordinated CO₂ via a proton-coupled two-electron process, leaving CO bound to Ni with OH[−] on the pendant Fe [270] (Scheme 1.4). In the direction of CO oxidation, CO binding to the $C_{\text{red}1}$ state of the C-cluster is diffusion controlled and not rate-limiting [461, 462], the rate of reduction of the B-cluster in turn is only slightly higher than the steady-state k_{cat} [269, 461], indicating that this step is partly rate-limiting. CO₂ release has also been proposed to be partly rate-limiting [462]. CO is bound to the Ni in a bent fashion at an angle of 103° , which could contribute to the high turnover numbers of the enzyme by destabilising



Scheme 1.4 Possible mechanisms for catalytic CO₂/CO interconversion by Ni-CODHs, adapted from Ref. [270]. **a** Pathway proposed by Dobbek [455] and Lindahl [453]; the Ni centre is formally assigned as Ni(0) in the C_{red2} state. **b** Pathway suggested by Fontecilla-Camps et al.; in C_{red2} a proton is coordinated to Ni in the form of a Ni(II)-hydrido species [456]. His or Lys residues are possible proton donating/accepting amino acids

the ground state of the Ni-CO intermediate [269]. When Ni-bound CO is attacked by the Fe_{pendant}-hydroxide, a metal carboxylate (vide supra) is formed and the nickel coordination geometry changes from tetrahedral to square planar. This step is followed by the generation and release of CO₂ and a proton, and the reduction of the C-cluster from C_{red1} to the C_{red2} state. Scheme 1.4 depicts two possible pathways: formation of a Ni(0) species (A) and formation of a nickel-hydrido intermediate (B).

Since only CODH I was used in this thesis, it will henceforth be abbreviated simply as CODH. This enzyme shows great similarity with CODH II: the two isozymes share 58.3% sequence identity and 73.9% sequence similarity, and show similar patterns of behaviour with regard to selective inhibition by small molecule inhibitors [444]. Unprecedented turnover frequencies of 31,000 s⁻¹ for CO oxidation have been reported for CODH, with CO₂ reduction occurring around one order of magnitude slower [463].

1.7 Aims of This Thesis

One central aim of this thesis is to study and understand the mechanism of [FeFe]-hydrogenases, Nature's most proficient fuel-forming catalysts, specifically by introducing aldehyde molecules as reversible inhibitors (Chap. 3). These can intercept and trap reactive intermediates such as the elusive super-reduced state H_{sred} , making them amenable to spectroscopic characterisation. Insights into the mechanism of enzymatic H_2 evolution can provide design principles for future all-inorganic systems.

Another objective of this thesis is to study fuel-forming enzymes in the context of artificial photosynthetic systems, in particular their interaction with semiconducting materials. Chapter 4 deals with the direct electrochemistry of [NiFeSe]-hydrogenase and CODH adsorbed on TiO_2 and CdS electrodes, with the aim of shedding some light on the marked efficiency discrepancies these enzymes display under photo- vs. electrocatalytic conditions.

The topic of Chap. 5 is the development of a proof-of-concept system for photoelectrocatalytic CO_2 reduction based on the principles outlined in Sect. 1.5.3.5. The aim is to achieve CODH catalysed CO_2 reduction on a *p*-type dye-sensitised NiO photocathode.

Current artificial photosynthesis research is focused on H_2 production or reduction of CO_2 , but the low-value products have little immediate opportunity to compete with fossil fuels. Chapter 6 aims at establishing new directions for artificial photosynthesis research, in particular for solar-energy-driven synthesis of organic chemicals. The catalytic conversion of fumarate to succinate (essentially a catalytic hydrogenation reaction) catalysed by the enzyme flavocytochrome c_3 (fcc_3) is studied in two artificial photosynthetic systems. The objective is to achieve and investigate, mechanistically, both photo- and photoelectrocatalytic solar-to-chemical conversion, and draw implications for future systems capable of effecting solar-driven transformations more elaborate than the production of simple fuel molecules.

In short, using enzymes in model systems for artificial photosynthesis, this thesis asks 'what can we learn from biology?'

References

1. Lewis N, Crabtree G, Nozik A, Wasielewski M, Alivisatos P (2005) Basic research needs for solar energy utilization. US Department of Energy, Washington, DC
2. Hoffert MI, Caldeira K, Jain AK, Haites EF, Harvey LDD, Potter SD, Schlesinger ME, Schneider SH, Watts RG, Wigley TML, Wuebbles DJ (1998) Nature 395:881
3. Lewis NS, Nocera DG (2006) Proc Natl Acad Sci U S A 103:15729
4. Thomas JM (2014) ChemSusChem 7:1801
5. May RM (2007) Phil Trans R Soc A 365:879
6. International Energy Agency: Key World Energy Statistics 2014. Paris, 2014
7. Oreskes N (2004) Science 306:1686

8. John C, Dana N, Sarah AG, Mark R, Bärbel W, Rob P, Robert W, Peter J, Andrew S (2013) *Environ Res Lett* 8:024024
9. Green MA, Emery K, Hishikawa Y, Warta W, Dunlop ED (2014) *Prog Photovolt Res Appl* 22:701
10. Fujishima A, Honda K (1972) *Nature* 238:37
11. Rocheleau RE, Miller EL, Misra A (1998) *Energy & Fuels* 12:3
12. Khaselev O, Turner JA (1998) *Science* 280:425
13. Khaselev O, Bansal A, Turner JA (2001) *Int J Hydrogen Energy* 26:127
14. Peharz G, Dimroth F, Wittstadt U (2007) *Int J Hydrogen Energy* 32:3248
15. Jacobsson TJ, Fjällström V, Sahlberg M, Edoff M, Edvinsson T (2013) *Energy Environ Sci* 6:3676
16. Luo J, Im J-H, Mayer MT, Schreier M, Nazeeruddin MK, Park N-G, Tilley SD, Fan HJ, Grätzel M (2014) *Science* 345:1593
17. Cox CR, Lee JZ, Nocera DG, Buonassisi T (2014) *Proc Natl Acad Sci U S A* 111:14057
18. Bockris JO (1972) *Science* 176:1323
19. Edwards PP, Kuznetsov VL, David WIF, Brandon NP (2008) *Energy Policy* 36:4356
20. Wells SA, Sartbaeva A, Kuznetsov VL, Edwards PP (2006) In: *Encyclopedia of Inorganic Chemistry*. John Wiley & Sons, Ltd
21. Olah GA, Goepfert A, Prakash GKS (2009) *Beyond Oil and Gas: The Methanol Economy*, 2 ed. Wiley-VCH
22. Barber J (2009) *Chem Soc Rev* 38:185
23. Barber J (2007) *Phil Trans R Soc A* 365:1007
24. Janssen PJD, Lambreva MD, Plumeré N, Bartolucci C, Antonacci A, Buonasera K, Frese RN, Scognamiglio V, Rea G (2014) *Front. Chem* 2
25. Barber J (2007) In: Armstrong F, Blundell K (eds) *Energy: Beyond Oil*. Oxford University Press, Oxford, p 137
26. Archer MD, Barber J (2004) In: Archer MD, Barber J (eds). *Molecular to Global Photosynthesis*. Imperial College Press, London, p 1
27. Fleming GR, Schlau-Cohen GS, Amarnath K, Zaks J (2012) *Farad Discuss* 155:27
28. Herek JL, Wohlleben W, Cogdell RJ, Zeidler D, Motzkus M (2002) *Nature* 417:533
29. Blankenship RE (2014) *Molecular Mechanisms of Photosynthesis*, 2 ed. Wiley-Blackwell
30. Edwards GE, Walker DA (2004) In: Archer MD, Barber J (eds) *Molecular to Global Photosynthesis*. Imperial College Press, London, p 189
31. Nocera DG (2012) *Acc Chem Res* 45:767
32. Blankenship RE, Tiede DM, Barber J, Brudvig GW, Fleming G, Ghirardi M, Gunner MR, Junge W, Kramer DM, Melis A, Moore TA, Moser CC, Nocera DG, Nozik AJ, Ort DR, Parson WW, Prince RC, Sayre RT (2011) *Science* 332:805
33. Rappaport F, Diner BA (2008) *Coord Chem Rev* 252:259
34. Dau H, Zaharieva I (2009) *Acc Chem Res* 42:1861
35. Kothe T, Plumeré N, Badura A, Nowaczyk MM, Guschin DA, Rögner M, Schuhmann W (2013) *Angew Chem Int Ed* 52:14233
36. Vinyard DJ, Ananyev GM, Dismukes GC (2013) *Annu Rev Biochem* 82:577
37. Dau H, Zaharieva I, Haumann M (2012) *Curr Opin Chem Biol* 16:3
38. Umena Y, Kawakami K, Shen J-R, Kamiya N (2011) *Nature* 473:55
39. Vogt L, Vinyard DJ, Khan S, Brudvig GW (2015) *Curr Opin Chem Biol* 25:152
40. Ferreira KN, Iverson TM, Maghlaoui K, Barber J, Iwata S (2004) *Science* 303:1831
41. Kavarnos GJ (1993) *Fundamentals of Photoinduced Electron Transfer*. Wiley-VCH, Weinheim
42. Cardona T, Sedoud A, Cox N, Rutherford AW (2012) *BBA-Bioenergetics* 1817:26
43. Woodbury NW, Allen JP (1995) *Adv Photosynth* 2:527
44. Tachibana Y, Vayssieres L, Durrant JR (2012) *Nat Photon* 6:511
45. Burnap RL (2004) *Phys Chem Chem Phys* 6:4803
46. Ananyev GM, Zaltsman L, Vasko C, Dismukes GC (2001) *BBA-Bioenergetics* 1503:52
47. Takahashi S, Badger MR (2011) *Trends Plant Sci* 16:53

48. Dau H, Grundmeier A, Loja P, Haumann M (2008) *Philos Trans R Soc B* 363:1237
49. Siegbahn PEM (2008) *Chem Eur J* 14:8290
50. Siegbahn PEM (2009) *Acc Chem Res* 42:1871
51. Pal R, Negre CFA, Vogt L, Pokhrel R, Ertem MZ, Brudvig GW, Batista VS (2013) *Biochemistry* 52:7703
52. Kok B, Forbush B, McGloin M (1970) *Photochem Photobiol* 11:457
53. Britt RD, Oyala PH (2014) *Science* 345:736
54. Cox N, Pantazis DA, Neese F, Lubitz W (2013) *Acc Chem Res* 46:1588
55. Cox N, Messinger J (2013) *BBA-Bioenergetics* 1827:1020
56. Limburg J, Szalai VA, Brudvig GW (1999) *J Chem Soc Dalton Trans* 1353
57. McEvoy JP, Brudvig GW (2006) *Chem Rev* 106:4455
58. Siegbahn PEM (2006) *Chem Eur J* 12:9217
59. Siegbahn PEM (2011) *J Photochem Photobiol B* 104:94
60. Siegbahn PEM (2013) *BBA-Bioenergetics* 1827:1003
61. Cox N, Retegan M, Neese F, Pantazis DA, Boussac A, Lubitz W (2014) *Science* 345:804
62. Yano J, Yachandra V (2014) *Chem Rev* 114:4175
63. Pantazis DA, Ames W, Cox N, Lubitz W, Neese F (2012) *Angew Chem Int Ed* 51:9935
64. Haumann M, Liebisch P, Müller C, Barra M, Grabolle M, Dau H (2005) *Science* 310:1019
65. Taguchi T, Gupta R, Lassalle-Kaiser B, Boyce DW, Yachandra VK, Tolman WB, Yano J, Hendrich MP, Borovik AS (2012) *J Am Chem Soc* 134:1996
66. Kern J, Alonso-Mori R, Tran R, Hattne J, Gildea RJ, Echols N, Glöckner C, Hellmich J, Laksmono H, Sierra RG, Lassalle-Kaiser B, Koroidov S, Lampe A, Han G, Gul S, DiFiore D, Milathianaki D, Fry AR, Miahnahri A, Schafer DW, Messerschmidt M, Seibert MM, Koglin JE, Sokaras D, Weng T-C, Sellberg J, Latimer MJ, Grosse-Kunstleve RW, Zwart PH, White WE, Glatzel P, Adams PD, Bogan MJ, Williams GJ, Boutet S, Messinger J, Zouni A, Sauter NK, Yachandra VK, Bergmann U, Yano J (2013) *Science* 340:491
67. Kupitz C, Basu S, Grotjohann I, Fromme R, Zatsepin NA, Rendek KN, Hunter MS, Shoeman RL, White TA, Wang D, James D, Yang J-H, Cobb DE, Reeder B, Sierra RG, Liu H, Barty A, Aquila AL, Deponte D, Kirian RA, Bari S, Bergkamp JJ, Beyerlein KR, Bogan MJ, Caleman C, Chao T-C, Conrad CE, Davis KM, Fleckenstein H, Galli L, Hau-Riege SP, Kassemeyer S, Laksmono H, Liang M, Lomb L, Marchesini S, Martin AV, Messerschmidt M, Milathianaki D, Nass K, Ros A, Roy-Chowdhury S, Schmidt K, Seibert M, Steinbrener J, Stellato F, Yan L, Yoon C, Moore TA, Moore AL, Pushkar Y, Williams GJ, Boutet S, Doak RB, Weierstall U, Frank M, Chapman HN, Spence JCH, Fromme P (2014) *Nature* 513:261
68. Kalyanasundaram K (1982) *Coord Chem Rev* 46:159
69. Moore TA, Gust D, Mathis P, Mialocq J-C, Chachaty C, Bensasson RV, Land EJ, Doizi D, Liddell PA, Lehman WR, Nemeth GA, Moore AL (1984) *Nature* 307:630
70. Wasielewski MR (1992) *Chem Rev* 92:435
71. Moore GF, Konezny SJ, Song H-e, Milot RL, Blakemore JD, Lee ML, Batista VS, Schmuttenmaer CA, Crabtree RH, Brudvig GW (2012) *J Phys Chem C* 116:4892
72. White HS, Becker WG, Bard AJ (1984) *J Phys Chem* 88:1840
73. Milot RL, Moore GF, Crabtree RH, Brudvig GW, Schmuttenmaer CA (2013) *J Phys Chem C* 117:21662
74. Frei H (2009) *Chimia* 63:721
75. Bachmeier A (2010) Diploma Thesis, University of Erlangen-Nuremberg
76. Cuk T, Weare WW, Frei H (2010) *J Phys Chem C* 114:9167
77. Han H, Frei H (2008) *J Phys Chem C* 112:16156
78. Nakamura R, Frei H (2006) *J Am Chem Soc* 128:10668
79. Lin W, Frei H (2005) *J Am Chem Soc* 127:1610
80. Macnaughtan ML, Soo HS, Frei H (2014) *J Phys Chem C* 118:7874
81. Kim W, Yuan G, McClure BA, Frei H (2014) *J Am Chem Soc* 136:11034
82. O'Regan B, Grätzel M (1991) *Nature* 353:737

83. Bachmeier A, Siritanaratkul B, Armstrong FA (2015) In: Rozhkova EA, Ariga K (eds) *From Molecules to Materials - Pathways to Artificial Photosynthesis*. Springer International Publishing, Switzerland, p 99
84. Chen S, Wang L-W (2012) *Chem Mater* 24:3659
85. Ye H, Park HS, Bard AJ (2011) *J Phys Chem C* 115:12464
86. Park Y, McDonald KJ, Choi K-S (2013) *Chem Soc Rev* 42:2321
87. Hong SJ, Lee S, Jang JS, Lee JS (2011) *Energy Environ Sci* 4:1781
88. Shockley W, Queisser HJ (1961) *J Appl Phys* 32:510
89. Green MA (2005) *Third Generation Photovoltaics: Advanced Solar Energy Conversion*, 2nd edn. Springer, Berlin
90. Conibeer G (2007) *Mater Today* 10:42
91. Brown GF, Wu J (2009) *Laser Photon Rev* 3:394
92. Sambur JB, Novet T, Parkinson BA (2010) *Science* 330:63
93. Smith MB, Michl J (2010) *Chem Rev* 110:6891
94. Smith MB, Michl J (2013) *Annu Rev Phys Chem* 64:361
95. Park N-G (2015) *Mater Today* 18:65
96. Jung HS, Park N-G (2015) *Small* 11:10
97. Grätzel M (2014) *Nat Mater* 13:838
98. Hodes G (2013) *Science* 342:317
99. Kojima A, Teshima K, Shirai Y, Miyasaka T (2009) *J Am Chem Soc* 131:6050
100. Lee MM, Teuscher J, Miyasaka T, Murakami TN, Snaith HJ (2012) *Science* 338:643
101. Stranks SD, Eperon GE, Grancini G, Menelaou C, Alcocer MJP, Leijtens T, Herz LM, Petrozza A, Snaith HJ (2013) *Science* 342:341
102. Xing G, Mathews N, Sun S, Lim SS, Lam YM, Grätzel M, Mhaisalkar S, Sum TC (2013) *Science* 342:344
103. Yella A, Lee H-W, Tsao HN, Yi C, Chandiran AK, Nazeeruddin MK, Diao EW-G, Yeh C-Y, Zakeeruddin SM, Grätzel M (2011) *Science* 334:629
104. Liu M, Johnston MB, Snaith HJ (2013) *Nature* 501:395
105. Zhou H, Chen Q, Li G, Luo S, Song T-b, Duan H-S, Hong Z, You J, Liu Y, Yang Y (2014) *Science* 345:542
106. Patwardhan S, Cao DH, Hatch S, Farha OK, Hupp JT, Kanatzidis MG, Schatz GC (2015) *J Phys Chem Lett* 6:251
107. Burschka J, Pellet N, Moon S-J, Humphry-Baker R, Gao P, Nazeeruddin MK, Grätzel M (2013) *Nature* 499:316
108. Mei A, Li X, Liu L, Ku Z, Liu T, Rong Y, Xu M, Hu M, Chen J, Yang Y, Grätzel M, Han H (2014) *Science* 345:295
109. Gersten SW, Samuels GJ, Meyer TJ (1982) *J Am Chem Soc* 104:4029
110. Concepcion JJ, Jurss JW, Brennaman MK, Hoertz PG, Patrocinio AOT, Murakami Iha NY, Templeton JL, Meyer T (2009) *J Acc Chem Res* 42:1954
111. Hull JF, Balcells D, Blakemore JD, Incarvito CD, Eisenstein O, Brudvig GW, Crabtree RH (2009) *J Am Chem Soc* 131:8730
112. Blakemore JD, Schley ND, Balcells D, Hull JF, Olack GW, Incarvito CD, Eisenstein O, Brudvig GW, Crabtree RH (2010) *J Am Chem Soc* 132:16017
113. Schley ND, Blakemore JD, Subbaiyan NK, Incarvito CD, D'Souza F, Crabtree RH, Brudvig GW (2011) *J Am Chem Soc* 133:10473
114. Duan L, Bozoglian F, Mandal S, Stewart B, Privalov T, Llobet A, Sun L (2012) *Nat Chem* 4:418
115. Weller M, Overton T, Rourke J, Armstrong F (2014) *Inorganic Chemistry*, 6th edn. Oxford University Press, Oxford
116. Kärkäs MD, Verho O, Johnston EV, Åkermark B (2014) *Chem Rev* 114:11863
117. Berardi S, La Ganga G, Natali M, Bazzan I, Puntoriero F, Sartorel A, Scandola F, Campagna S, Bonchio M (2012) *J Am Chem Soc* 134:11104
118. Kaveevivitchai N, Chitta R, Zong R, El Ojaimi M, Thummel RP (2012) *J Am Chem Soc* 134:10721

119. Al-Oweini R, Sartorel A, Bassil BS, Natali M, Berardi S, Scandola F, Kortz U, Bonchio M (2014) *Angew Chem Int Ed* 53:11182
120. Vagnini MT, Smeigh AL, Blakemore JD, Eaton SW, Schley ND, D'Souza F, Crabtree RH, Brudvig GW, Co DT, Wasielewski MR (2012) *Proc Natl Acad Sci U S A* 109:15651
121. Brimblecombe R, Dismukes GC, Swiegers GF, Spiccia L (2009) *Dalton Trans* 9374
122. Young KJ, Martini LA, Milot RL, Snoeberger RC, Batista VS, Schmuttenmaer CA, Crabtree RH, Brudvig GW (2012) *Coord Chem Rev* 256:2503
123. Swierk JR, Mallouk TE (2013) *Chem Soc Rev* 42:2357
124. Sartorel A, Bonchio M, Campagna S, Scandola F (2013) *Chem Soc Rev* 42:2262
125. Ashford DL, Lapidus AM, Vannucci AK, Hanson K, Torelli DA, Harrison DP, Templeton JL, Meyer TJ (2014) *J Am Chem Soc* 136:6578
126. Klepser BM, Bartlett BM (2014) *J Am Chem Soc* 136:1694
127. Jeon TH, Choi W, Park H (2011) *Phys Chem Chem Phys* 13:21392
128. McCrory CCL, Jung S, Peters JC, Jaramillo TF (2013) *J Am Chem Soc* 135:16977
129. Hara M, Waraksa CC, Lean JT, Lewis BA, Mallouk TE (2000) *J Phys Chem A* 104:5275
130. Tilley SD, Cornuz M, Sivula K, Grätzel M (2010) *Angew Chem Int Ed* 49:6405
131. Youngblood WJ, Lee S-HA, Kobayashi Y, Hernandez-Pagan EA, Hoertz PG, Moore TA, Moore AL, Gust D, Mallouk TE (2009) *J Am Chem Soc* 131:926
132. Bledowski M, Wang L, Neubert S, Mitoraj D, Beranek R (2014) *J Phys Chem C* 118:18951
133. Greenwood NN, Earnshaw A (1997) *Chemistry of the Elements*, 2nd edn. Butterworth-Heinemann Ltd, Oxford
134. Kanan MW, Nocera DG (2008) *Science* 321:1072
135. Dincă M, Surendranath Y, Nocera DG (2010) *Proc Natl Acad Sci U S A* 107:10337
136. Risch M, Khare V, Zaharieva I, Gerencser L, Chernev P, Dau H (2009) *J Am Chem Soc* 131:6936
137. Kanan MW, Yano J, Surendranath Y, Dincă M, Yachandra VK, Nocera DG (2010) *J Am Chem Soc* 132:13692
138. Steimiller EMP, Choi K-S (2009) *Proc Natl Acad Sci U S A* 106:20633
139. Pijpers JHH, Winkler MT, Surendranath Y, Buonassisi T, Nocera DG (2011) *Proc Natl Acad Sci U S A* 108:10056
140. Yang J, Walczak K, Anzenberg E, Toma FM, Yuan G, Beeman J, Schwartzberg A, Lin Y, Hettick M, Javey A, Ager JW, Yano J, Frei H, Sharp ID (2014) *J Am Chem Soc* 136:6191
141. Bledowski M, Wang L, Ramakrishnan A, Bétard A, Khavryuchenko OV, Beranek R (2012) *ChemPhysChem* 13:3018
142. Zhong DK, Gamelin DR (2010) *J Am Chem Soc* 132:4202
143. Zhong DK, Cornuz M, Sivula K, Gratzel M, Gamelin DR (2011) *Energy Environ Sci* 4:1759
144. Seabold JA, Choi K-S (2011) *Chem Mater* 23:1105
145. Pilli SK, Furtak TE, Brown LD, Deutsch TG, Turner JA, Herring AM (2011) *Energy Environ Sci* 4:5028
146. Zhong DK, Choi S, Gamelin DR (2011) *J Am Chem Soc* 133:18370
147. Zhou M, Bao J, Bi W, Zeng Y, Zhu R, Tao M, Xie Y (2012) *ChemSusChem* 5:1420
148. Abdi FF, Firet N, van de Krol R (2013) *ChemCatChem* 5:490
149. Moniz SJA, Zhu J, Tang J (2014) *Adv Energy Mater* 4
150. Trotochaud L, Ranney JK, Williams KN, Boettcher SW (2012) *J Am Chem Soc* 134:17253
151. Louie MW, Bell AT (2013) *J Am Chem Soc* 135:12329
152. Lin F, Boettcher SW (2014) *Nat Mater* 13:81
153. Seabold JA, Choi K-S (2012) *J Am Chem Soc* 134:2186
154. McDonald KJ, Choi K-S (2012) *Energy Environ Sci* 5:8553
155. Kim TW, Choi K-S (2014) *Science* 343:990
156. Blakemore JD, Gray HB, Winkler JR, Müller AM (2013) *ACS Catal* 3:2497
157. Hunter BM, Blakemore JD, Deimund M, Gray HB, Winkler JR, Müller AM (2014) *J Am Chem Soc* 136:13118
158. Smith RDL, Prévot MS, Fagan RD, Zhang Z, Sedach PA, Siu MKJ, Trudel S, Berlinguette CP (2013) *Science* 340:60

159. Gregoire JM, Xiang C, Mitrovic S, Liu X, Marcin M, Cornell EW, Fan J, Jin J (2013) *J Electrochem Soc* 160:F337
160. Xiang C, Suram SK, Haber JA, Guevarra DW, Soedarmadji E, Jin J, Gregoire JM (2013) *ACS Comb Sci* 16:47
161. Haber JA, Xiang C, Guevarra D, Jung S, Jin J, Gregoire JM (2014) *ChemElectroChem* 1:524
162. Haber JA, Cai Y, Jung S, Xiang C, Mitrovic S, Jin J, Bell AT, Gregoire JM (2014) *Energy Environ Sci* 7:682
163. Jacques P-A, Artero V, Pécaut J, Fontecave M (2009) *Proc Natl Acad Sci U S A* 106:20627
164. Artero V, Chavarot-Kerlidou M, Fontecave M (2011) *Angew Chem Int Ed* 50:7238
165. McCrory CCL, Uyeda C, Peters JC (2012) *J Am Chem Soc* 134:3164
166. Tran PD, Barber J (2012) *Phys Chem Chem Phys* 14:13772
167. Thoi VS, Sun Y, Long JR, Chang CJ (2013) *Chem Soc Rev* 42:2388
168. Connolly P, Espenson JH (1986) *Inorg Chem* 25:2684
169. Dempsey JL, Brunschwig BS, Winkler JR, Gray HB (2009) *Acc Chem Res* 42:1995
170. Schrauzer GN (1968) *Acc Chem Res* 1:97
171. Dempsey JL, Winkler JR, Gray HB (2010) *J Am Chem Soc* 132:16774
172. Solis BH, Hammes-Schiffer S (2011) *Inorg Chem* 50:11252
173. Helm ML, Stewart MP, Bullock RM, DuBois MR, DuBois DL (2011) *Science* 333:863
174. Rakowski Dubois M, DuBois DL (2009) *Acc Chem Res* 42:1974
175. Rakowski DuBois M, DuBois DL (2009) *Chem Soc Rev* 38:62
176. Shaw WJ, Helm ML, DuBois DL (2013) *BBA-Bioenergetics* 1827:1123
177. Wiese S, Kilgore UJ, Ho M-H, Raugei S, DuBois DL, Bullock RM, Helm ML (2013) *ACS Catal* 3:2527
178. Dutta A, DuBois DL, Roberts JAS, Shaw WJ (2014) *Proc Natl Acad Sci U S A* 111:16286
179. Goff AL, Artero V, Joussetme B, Tran P, Guillet N (2009) *Science* 326:1384
180. Tran PD, Le Goff A, Heidkamp J, Joussetme B, Guillet N, Palacin S, Dau H, Fontecave M, Artero V (2011) *Angew Chem Int Ed* 50:1371
181. Andreiadis ES, Jacques P-A, Tran PD, Leyris A, Chavarot-Kerlidou M, Joussetme B, Matheron M, Pécaut J, Palacin S, Fontecave M, Artero V (2013) *Nat Chem* 5:48
182. Lakadamyali F, Reynal A, Kato M, Durrant JR, Reisner E (2012) *Chem Eur J* 18:15464
183. Reynal A, Lakadamyali F, Gross MA, Reisner E, Durrant JR (2013) *Energy Environ Sci* 6:3291
184. Gross MA, Reynal A, Durrant JR, Reisner E (2014) *J Am Chem Soc* 136:356
185. Reynal A, Willkomm J, Muresan NM, Lakadamyali F, Planells M, Reisner E, Durrant JR (2014) *Chem Commun* 50:12768
186. Huang J, Mulfort KL, Du P, Chen LX (2012) *J Am Chem Soc* 134:16472
187. Moore GF, Sharp ID (2013) *J Phys Chem Lett* 4:568
188. Li L, Duan L, Wen F, Li C, Wang M, Hagfeldt A, Sun L (2012) *Chem Commun* 48:988
189. Krawicz A, Yang J, Anzenberg E, Yano J, Sharp ID, Moore GF (2013) *J Am Chem Soc* 135:11861
190. Weingarten AS, Kazantsev RV, Palmer LC, McClendon M, Koltonow AR, SamuelAmanda PS, Kiebalá DJ, Wasielewski MR, Stupp SI (2014) *Nat Chem* 6:964
191. Tran PD, Wong LH, Barber J, Loo JSC (2012) *Energy Environ Sci* 5:5902
192. McCrory CCL, Jung S, Ferrer IM, Chatman S, Peters JC, Jaramillo TF (2015) *J Am Chem Soc*
193. Vesborg PCK, Seger B, Chorkendorff I (2015) *J Phys Chem Lett* 951
194. Merki D, Fierro S, Vrubel H, Hu X (2011) *Chem Sci* 2:1262
195. Laursen AB, Kegnaes S, Dahl S, Chorkendorff I (2012) *Energy Environ Sci* 5:5577
196. Morales-Guio CG, Hu X (2014) *Acc Chem Res* 47:2671
197. Morales-Guio CG, Stern L-A, Hu X (2014) *Chem Soc Rev* 43:6555
198. Lassalle-Kaiser B, Merki D, Vrubel H, Gul S, Yachandra VK, Hu X, Yano J (2015) *J Am Chem Soc* 137:314

199. Morales-Guio CG, Liardet L, Mayer MT, Tilley SD, Grätzel M, Hu X (2015) *Angew Chem Int Ed* 54:664
200. Seger B, Laursen AB, Vesborg PCK, Pedersen T, Hansen O, Dahl S, Chorkendorff I (2012) *Angew Chem Int Ed* 51:9128
201. Laursen AB, Pedersen T, Malacrida P, Seger B, Hansen O, Vesborg PCK, Chorkendorff I (2013) *Phys Chem Chem Phys* 15:20000
202. Tran PD, Pramana SS, Kale VS, Nguyen M, Chiam SY, Batabyal SK, Wong LH, Barber J, Loo J (2012) *Chem Eur J* 18:13994
203. Bourgeteau T, Tondelier D, Geffroy B, Brisse R, Laberty-Robert C, Campidelli S, de Bettignies R, Artero V, Palacin S, Jusselme B (2013) *Energy Environ Sci* 6:2706
204. Tang ML, Grauer DC, Lassalle-Kaiser B, Yachandra VK, Amirav L, Long JR, Yano J, Alivisatos AP (2011) *Angew Chem Int Ed* 50:10203
205. Popczun EJ, Read CG, Roske CW, Lewis NS, Schaak RE (2014) *Angew Chem Int Ed* 53:5427
206. Popczun EJ, McKone JR, Read CG, Biacchi AJ, Wiltrout AM, Lewis NS, Schaak RE (2013) *J Am Chem Soc* 135:9267
207. Laursen AB, Patraju KR, Whitaker MJ, Retuerto M, Sarkar T, Yao N, Ramanujachary KV, Greenblatt M, Dismukes GC (2015) *Energy Environ Sci* 2015:8
208. Liu P, Rodriguez JA (2005) *J Am Chem Soc* 127:14871
209. Callejas JF, McEnaney JM, Read CG, Crompton JC, Biacchi AJ, Popczun EJ, Gordon TR, Lewis NS, Schaak RE (2014) *ACS Nano* 8:11101
210. Lubitz W, Ogata H, Rüdiger O, Reijerse E (2014) *Chem Rev* 114:4081
211. Jones AK, Sillery E, Albracht SPJ, Armstrong FA (2002) *Chem Commun* 866
212. Woolerton TW, Vincent KA (2009) *Electrochim Acta* 54:5011
213. Hexter SV, Grey F, Happe T, Climent V, Armstrong FA (2012) *Proc Natl Acad Sci U S A* 109:11516
214. Caputo CA, Gross MA, Lau VW, Cavazza C, Lotsch BV, Reisner E (2014) *Angew Chem Int Ed* 53:11538
215. Parkin A, Goldet G, Cavazza C, Fontecilla-Camps JC, Armstrong FA (2008) *J Am Chem Soc* 130:13410
216. Chang CD (1983) *Cat Rev Sci Eng* 25:1
217. Koppenol WH, Rush JD (1987) *J Phys Chem* 91:4429
218. Benson EE, Kubiak CP, Sathrum AJ, Smieja JM (2009) *Chem Soc Rev* 38:89
219. Kumar B, Llorente M, Froehlich J, Dang T, Sathrum A, Kubiak CP (2012) *Annu Rev Phys Chem* 63:541
220. Fenwick AQ, Gregoire JM, Luca OR (2015) *J Photochem Photobiol B* 152:47
221. Appel AM, Bercaw JE, Bocarsly AB, Dobbek H, DuBois DL, Dupuis M, Ferry JG, Fujita E, Hille R, Kenis PJA, Kerfeld CA, Morris RH, Peden CHF, Portis AR, Ragsdale SW, Rauchfuss TB, Reek JNH, Seefeldt LC, Thauer RK, Waldrop GL (2013) *Chem Rev* 113:6621
222. Kim D, Sakimoto KK, Hong D, Yang P (2015) *Angew Chem Int Ed* 54:3259
223. Elschenbroich C, Salzer A (1991) *Organometallics, A Concise Introduction*, 2nd edn. Wiley VCH, Weinheim
224. Wenzhen L (2010) In: *Advances in CO₂ Conversion and Utilization*, vol 1056. American Chemical Society, p 55
225. Jhong H-RM, Ma S, Kenis PJA (2013) *Curr Opin Chem Eng* 2:191
226. Hori Y (2008) In: Vayenas C, White R, Gamboa-Aldeco M (eds) *Modern Aspects of Electrochemistry*, vol 42. Springer, New York, p 89
227. Hori Y, Kikuchi K, Suzuki S (1985) *Chem Lett* 14:1695
228. Gattrell M, Gupta N, Co A (2006) *J Electroanal Chem* 594:1
229. Li CW, Kanan MW (2012) *J Am Chem Soc* 134:7231
230. Tang W, Peterson AA, Varela AS, Jovanov ZP, Bech L, Durand WJ, Dahl S, Norskov JK, Chorkendorff I (2012) *Phys Chem Chem Phys* 14:76

231. Reske R, Mistry H, Behafarid F, Roldan Cuenya B, Strasser P (2014) *J Am Chem Soc* 136:6978
232. Kuhl KP, Cave ER, Abram DN, Jaramillo TF (2012) *Energy Environ Sci* 5:7050
233. Lu Q, Rosen J, Jiao F (2015) *ChemCatChem* 7:38
234. Chen Y, Li CW, Kanan MW (2012) *J Am Chem Soc* 134:19969
235. Zhu W, Michalsky R, Metin Ö, Lv H, Guo S, Wright CJ, Sun X, Peterson AA, Sun S (2013) *J Am Chem Soc* 135:16833
236. Hansen HA, Varley JB, Peterson AA, Nørskov JK (2013) *J Phys Chem Lett* 4:388
237. Rosen BA, Salehi-Khojin A, Thorson MR, Zhu W, Whipple DT, Kenis PJA, Masel RI (2011) *Science* 334:643
238. Salehi-Khojin A, Jhong H-RM, Rosen BA, Zhu W, Ma S, Kenis PJA, Masel RI (2013) *J Phys Chem C* 117:1627
239. Lu Q, Rosen J, Zhou Y, Hutchings GS, Kimmel YC, Chen JG, Jiao F (2014) *Nat Commun* 5:3242
240. Chen Y, Kanan MW (2012) *J Am Chem Soc* 134:1986
241. Zhang S, Kang P, Meyer TJ (2014) *J Am Chem Soc* 136:1734
242. Kortlever R, Balemans C, Kwon Y, Koper MTM (2015) *Catal Today* 244:58
243. LaTempa TJ, Rani S, Bao N, Grimes CA (2012) *Nanoscale* 4:2245
244. Neațu Ș, Maciá-Agulló JA, Concepción P, García H (2014) *J Am Chem Soc* 136:15969
245. Shown I, Hsu H-C, Chang Y-C, Lin C-H, Roy PK, Ganguly A, Wang C-H, Chang J-K, Wu C-I, Chen L-C, Chen K-H (2014) *Nano Lett* 14:6097
246. Habisreutinger SN, Schmidt-Mende L, Stolarczyk JK (2013) *Angew Chem Int Ed* 52:7372
247. Mao J, Li K, Peng T (2013) *Catal Sci Tech* 3:2481
248. Kondratenko EV, Mul G, Baltrusaitis J, Larrazabal GO, Perez-Ramirez J (2013) *Energy Environ Sci* 6:3112
249. Beley M, Collin J-P, Ruppert R, Sauvage J-P (1984) *J Chem Soc Chem Commun* 1315
250. Hawecker J, Lehn J-M, Ziessel R (1983) *J Chem Soc Chem Commun* 536
251. Hawecker J, Lehn J-M, Ziessel R (1986) *Helv Chim Acta* 69:1990
252. Bourrez M, Molton F, Chardon-Noblat S, Deronzier A (2011) *Angew Chem Int Ed* 50:9903
253. Neri G, Walsh JJ, Wilson C, Reynal A, Lim JYC, Li X, White AJP, Long NJ, Durrant JR, Cowan AJ (2015) *Phys Chem Chem Phys* 17:1562
254. Kou Y, Nabetani Y, Masui D, Shimada T, Takagi S, Tachibana H, Inoue H (2014) *J Am Chem Soc* 136:6021
255. Kou Y, Nakatani S, Sunagawa G, Tachikawa Y, Masui D, Shimada T, Takagi S, Tryk DA, Nabetani Y, Tachibana H, Inoue H (2014) *J Catal* 310:57
256. Kobayashi K, Kikuchi T, Kitagawa S, Tanaka K (2014) *Angew Chem Int Ed* 53:11813
257. Costentin C, Drouot S, Robert M, Savéant J-M (2012) *Science* 338:90
258. Bonin J, Robert M, Routier M (2014) *J Am Chem Soc* 136:16768
259. Seshadri G, Lin C, Bocarsly AB (1994) *J Electroanal Chem* 372:145
260. Barton EE, Rampulla DM, Bocarsly AB (2008) *J Am Chem Soc* 130:6342
261. Barton Cole E, Lakkaraju PS, Rampulla DM, Morris AJ, Abelev E, Bocarsly AB (2010) *J Am Chem Soc* 132:11539
262. Morris AJ, McGibbon RT, Bocarsly AB (2011) *ChemSusChem* 4:191
263. Costentin C, Canales JC, Haddou B, Savéant J-M (2013) *J Am Chem Soc* 135:17671
264. Morris AJ, Meyer GJ, Fujita E (2009) *Acc Chem Res* 42:1983
265. Windle CD, Perutz RN (2012) *Coord Chem Rev* 256:2562
266. Parkinson BA, Weaver PF (1984) *Nature* 309:148
267. Reda T, Plugge CM, Abram NJ, Hirst J (2008) *Proc Natl Acad Sci U S A* 105:10654
268. Bassegoda A, Madden C, Wakerley DW, Reisner E, Hirst J (2014) *J Am Chem Soc* 136:15473
269. Can M, Armstrong FA, Ragsdale SW (2014) *Chem Rev* 114:4149
270. Wang VC-C, Ragsdale SW, Armstrong FA (2014) In: Kroneck PMH, Torres MES (eds) *The Metal-Driven Biogeochemistry of Gaseous Compounds in the Environment*, vol 14. Springer, The Netherlands, p 71

271. McKone JR, Lewis NS, Gray HB (2013) *Chem Mater* 26:407
272. Döscher H, Geisz JF, Deutsch TG, Turner JA (2014) *Energy Environ Sci* 7:2951
273. Newman J, Hoertz PG, Bonino CA, Trainham JA (2012) *J Electrochem Soc* 159:A1722
274. Pinaud BA, Benck JD, Seitz LC, Forman AJ, Chen Z, Deutsch TG, James BD, Baum KN, Baum GN, Ardo S, Wang H, Miller E, Jaramillo TF (2013) *Energy Environ Sci* 6:1983
275. Herron JA, Kim J, Upadhye AA, Huber GW, Maravelias CT (2015) *Energy Environ Sci* 8:126
276. Linsebigler AL, Lu G, Yates JT (1995) *Chem Rev* 95:735
277. Walter MG, Warren EL, McKone JR, Boettcher SW, Mi Q, Santori EA, Lewis NS (2010) *Chem Rev* 110:6446
278. Newman J (2013) *J Electrochem Soc* 160:F309
279. Grätzel M (2001) *Nature* 414:338
280. Minggu LJ, Wan Daud WR, Kassim MB (2010) *Int J Hydrogen Energy* 35:5233
281. Li Z, Luo W, Zhang M, Feng J, Zou Z (2013) *Energy Environ Sci* 6:347
282. Prévot MS, Sivula K (2013) *J Phys Chem C* 117:17879
283. Yang X, Liu R, He Y, Thorne J, Zheng Z, Wang D (2015) *Nano Res.* 8:56
284. Li J, Wu N (2015) *Catal Sci Tech* 5:1360
285. Kelly NA, Gibson TL (2006) *Int J Hydrogen Energy* 31:1658
286. Park JH, Bard AJ (2006) *Electrochem Solid-State Lett* 9:E5
287. Yamane S, Kato N, Kojima S, Imanishi A, Ogawa S, Yoshida N, Nonomura S, Nakato Y (2009) *J Phys Chem C* 113:14575
288. Li L, Duan L, Xu Y, Gorlov M, Hagfeldt A, Sun L (2010) *Chem Commun* 46:7307
289. Brilllet J, Cornuz M, Formal FL, Yum J-H, Grätzel M, Sivula K (2010) *J Mater Res* 25:17
290. Brilllet J, Yum J-H, Cornuz M, Hisatomi T, Solarska R, Augustynski J, Graetzel M, Sivula K (2012) *Nat Photon* 6:824
291. Tong L, Iwase A, Nattestad A, Bach U, Weidelener M, Gotz G, Mishra A, Bauerle P, Amal R, Wallace GG, Mozer AJ (2012) *Energy Environ Sci* 5:9472
292. Zhao Y, Swierk JR, Megiatto JD, Sherman B, Youngblood WJ, Qin D, Lentz DM, Moore AL, Moore TA, Gust D, Mallouk TE (2012) *Proc Natl Acad Sci U S A* 109:15612
293. Lin C-Y, Lai Y-H, Mersch D, Reisner E (2012) *Chem Sci* 3:3482
294. Alibabaei L, Brennaman MK, Norris MR, Kalanyan B, Song W, Losego MD, Concepcion JJ, Binstead RA, Parsons GN, Meyer TJ (2013) *Proc Natl Acad Sci U S A* 110:20008
295. Abdi FF, Han L, Smets AHM, Zeman M, Dam B, van de Krol R (2013) *Nat Commun* 4:2195
296. Han L, Abdi FF, van de Krol R, Liu R, Huang Z, Lewerenz H-J, Dam B, Zeman M, Smets AHM (2014) *ChemSusChem* 7:2832
297. Modestino MA, Walczak KA, Berger A, Evans CM, Haussener S, Koval C, Newman JS, Ager JW, Segalman RA (2014) *Energy Environ Sci* 7:297
298. Bornoz P, Abdi FF, Tilley SD, Dam B, van de Krol R, Grätzel M, Sivula K (2014) *J Phys Chem C* 118:16959
299. Ding C, Qin W, Wang N, Liu G, Wang Z, Yan P, Shi J, Li C (2014) *Phys Chem Chem Phys* 16:15608
300. Chen Y-S, Manser JS, Kamat PV (2015) *J Am Chem Soc* 137:974
301. Nozik AJ (1977) *Appl Phys Lett* 30:567
302. Haussener S, Xiang C, Spurgeon JM, Ardo S, Lewis NS, Weber AZ (2012) *Energy Environ Sci* 5:9922
303. Haussener S, Hu S, Xiang C, Weber AZ, Lewis NS (2013) *Energy Environ Sci* 6:3605
304. Seger B, Castelli IE, Vesborg PCK, Jacobsen KW, Hansen O, Chorkendorff I (2014) *Energy Environ Sci* 7:2397
305. Singh MR, Stevens JC, Weber AZ (2014) *J Electrochem Soc* 161:E3283
306. Reece SY, Hamel JA, Sung K, Jarvi TD, Esswein AJ, Pijpers JJH, Nocera DG (2011) *Science* 334:645
307. Liu C, Tang J, Chen HM, Liu B, Yang P (2013) *Nano Lett* 13:2989

308. Liu B, Wu C-H, Miao J, Yang P (2014) *ACS Nano* 8:11739
309. Walczak K, Chen Y, Karp C, Beeman JW, Shaner M, Spurgeon J, Sharp ID, Amashukeli X, West W, Jin J, Lewis NS, Xiang C (2015) *ChemSusChem* 8:544
310. Wilker MB, Shinopoulos KE, Brown KA, Mulder DW, King PW, Dukovic G (2014) *J Am Chem Soc* 136:4316
311. Yin Y, Alivisatos AP (2005) *Nature* 437:664
312. Burda C, Chen X, Narayanan R, El-Sayed MA (2005) *Chem Rev* 105:1025
313. Bawendi MG, Steigerwald ML, Brus LE (1990) *Annu Rev Phys Chem* 41:477
314. Cozzoli PD, Pellegrino T, Manna L (2006) *Chem Soc Rev* 35:1195
315. Brus L (1986) *J Phys Chem* 90:2555
316. Talapin DV, Lee J-S, Kovalenko MV, Shevchenko EV (2009) *Chem Rev* 110:389
317. Wilker MB, Schnitzenbaumer KJ, Dukovic G (2012) *Isr J Chem* 52:1002
318. Maeda K, Teramura K, Lu D, Takata T, Saito N, Inoue Y, Domen K (2006) *Nature* 440:295
319. Osterloh FE (2008) *Chem Mater* 20:35
320. Kudo A, Miseki Y (2009) *Chem Soc Rev* 38:253
321. Maeda K, Domen K (2010) *J Phys Chem Lett* 1:2655
322. Maeda K, Xiong A, Yoshinaga T, Ikeda T, Sakamoto N, Hisatomi T, Takashima M, Lu D, Kanehara M, Setoyama T, Teranishi T, Domen K (2010) *Angew Chem Int Ed* 49:4096
323. Maeda K, Abe R, Domen K (2011) *J Phys Chem C* 115:3057
324. Maeda K, Domen K (2011) *MRS Bull* 36:25
325. Sato S, Arai T, Morikawa T, Uemura K, Suzuki TM, Tanaka H, Kajino T (2011) *J Am Chem Soc* 133:15240
326. Sasaki Y, Kato H, Kudo A (2013) *J Am Chem Soc* 135:5441
327. Moriya Y, Takata T, Domen K (2013) *Coord Chem Rev* 257:1957
328. Sekizawa K, Maeda K, Domen K, Koike K, Ishitani O (2013) *J Am Chem Soc* 135:4596
329. Abe R, Shinmei K, Koumura N, Hara K, Ohtani B (2013) *J Am Chem Soc* 135:16872
330. Wang D, Hisatomi T, Takata T, Pan C, Katayama M, Kubota J, Domen K (2013) *Angew Chem Int Ed* 52:11252
331. Martin DJ, Reardon PJT, Moniz SJA, Tang J (2014) *J Am Chem Soc* 136:12568
332. Yang M-Q, Zhang N, Pagliaro M, Xu Y-J (2014) *Chem Soc Rev* 43:8240
333. Yang L, Zhou H, Fan T, Zhang D (2014) *Phys Chem Chem Phys* 16:6810
334. Li R, Han H, Zhang F, Wang D, Li C (2014) *Energy Environ Sci* 7:1369
335. Wang Q, Hisatomi T, Ma SSK, Li Y, Domen K (2014) *Chem Mater* 26:4144
336. Li P, Zhou Y, Li H, Xu Q, Meng X, Wang X, Xiao M, Zou Z (2015) *Chem Commun* 51:800
337. Iwashina K, Iwase A, Ng YH, Amal R, Kudo A (2015) *J Am Chem Soc* 137:604
338. Tachibana Y, Moser JE, Grätzel M, Klug DR, Durrant JR (1996) *J Phys Chem* 100:20056
339. Tseng H-W, Wilker MB, Damrauer NH, Dukovic G (2013) *J Am Chem Soc* 135:3383
340. Bott A (1998) *Curr Sep* 3:87
341. Beranek R (2011) *Adv Phys Chem* 786759
342. Scanlon DO, Dunnill CW, Buckeridge J, Shevlin SA, Logsdail AJ, Woodley SM, Catlow CRA, Powell MJ, Palgrave RG, Parkin IP, Watson GW, Keal TW, Sherwood P, Walsh A, Sokol AA (2013) *Nat Mater* 12:798
343. Woolerton TW, Sheard S, Chaudhary YS, Armstrong FA (2012) *Energy Environ Sci* 5:7470
344. Chu S (2014) In: *University of Oxford Romanes Lecture*. Oxford
345. Hu S, Shaner MR, Beardslee JA, Lichterman M, Brunschwig BS, Lewis NS (2014) *Science* 344:1005
346. Shaner MR, Hu S, Sun K, Lewis NS (2015) *Energy Environ Sci* 8:203
347. Lichterman MF, Carim AI, McDowell MT, Hu S, Gray HB, Brunschwig BS, Lewis NS (2014) *Energy Environ Sci* 7:3334
348. Sun K, Saadi FH, Lichterman MF, Hale WG, Wang H-P, Zhou X, Plymale NT, Omelchenko ST, He J-H, Papadantonakis KM, Brunschwig BS, Lewis NS (2015) *Proc Natl Acad Sci U S A* 112:3612
349. Hamann T (2014) *Science* 345:1566
350. Armstrong FA, Hirst J (2011) *Proc Natl Acad Sci U S A* 108:14049

351. Kato M, Zhang JZ, Paul N, Reisner E (2014) *Chem Soc Rev* 43:6485
352. Kato M, Cardona T, Rutherford AW, Reisner E (2012) *J Am Chem Soc* 134:8332
353. Kato M, Cardona T, Rutherford AW, Reisner E (2013) *J Am Chem Soc* 135:10610
354. Noji T, Suzuki H, Gotoh T, Iwai M, Ikeuchi M, Tomo T, Noguchi T (2011) *J Phys Chem Lett* 2:2448
355. Badura A, Kothe T, Schuhmann W, Rögner M (2011) *Energy Environ Sci* 4:3263
356. Wang F, Liu X, Willner I (2013) *Adv Mater* 25:349
357. Yehezkeili O, Tel-Vered R, Michaeli D, Willner I, Nechushtai R (2014) *Photosynth Res* 120:71
358. Yehezkeili O, Tel-Vered R, Wasserman J, Trifonov A, Michaeli D, Nechushtai R, Willner I (2012) *Nat Commun* 3:742
359. Cuendet P, Grätzel M, Pelaprat ML (1984) *J Electroanal Chem* 181:173
360. Yadav RK, Baeg J-O, Oh GH, Park N-J, Kong K-J, Kim J, Hwang DW, Biswas SK (2012) *J Am Chem Soc* 134:11455
361. Yadav RK, Baeg J-O, Kumar A, Kong K-J, Oh GH, Park N-JJ (2014) *Mater Chem A* 2:5068
362. Liu J, Cazelles R, Chen ZP, Zhou H, Galarneau A, Antonietti M (2014) *Phys Chem Chem Phys* 16:14699
363. Bachmeier A, Armstrong F (2015) *Curr Opin Chem Biol* 25:141
364. Zadornyy OA, Lucon JE, Gerlach R, Zorin NA, Douglas T, Elgren TE, Peters JW (2012) *J Inorg Biochem* 106:151
365. Sakai T, Mersch D, Reisner E (2013) *Angew Chem Int Ed* 52:12313
366. Roth LE, Nguyen JC, Tezcan FA (2010) *J Am Chem Soc* 132:13672
367. Krassen H, Schwarze A, Friedrich B, Ataka K, Lenz O, Heberle J (2009) *ACS Nano* 3:4055
368. Lubner CE, Applegate AM, Knörzer P, Ganago A, Bryant DA, Happe T, Golbeck JH (2011) *Proc Natl Acad Sci U S A* 108:20988
369. Samuël APS, Co DT, Stern CL, Wasielewski MR (2010) *J Am Chem Soc* 132:8813
370. King PW (2013) *BBA-Bioenergetics* 1827:949
371. Brown KA, Wilker MB, Boehm M, Dukovic G, King PW (2012) *J Am Chem Soc* 134:5627
372. McDonald TJ, Svedruzic D, Kim Y-H, Blackburn JL, Zhang SB, King PW, Heben MJ (2007) *Nano Lett* 7:3528
373. Svedružić D, Blackburn JL, Tenent RC, Rocha J-DR, Vinzant TB, Heben MJ, King PW (2011) *J Am Chem Soc* 133:4299
374. Krishnan S, Armstrong FA (2012) *Chem Sci* 3:1015
375. Blakemore JD, Gupta A, Warren JJ, Brunschwig BS, Gray HB (2013) *J Am Chem Soc* 135:18288
376. Adamska A, Silakov A, Lambert C, Rüdiger O, Happe T, Reijerse E, Lubitz W (2012) *Angew Chem Int Ed* 51:11458
377. Reisner E, Fontecilla-Camps JC, Armstrong FA (2009) *Chem Commun* 550
378. Reisner E, Powell DJ, Cavazza C, Fontecilla-Camps JC, Armstrong FA (2009) *J Am Chem Soc* 131:18457
379. Woolerton TW, Sheard S, Reisner E, Pierce E, Ragsdale SW, Armstrong FA (2010) *J Am Chem Soc* 132:2132
380. Woolerton TW, Sheard S, Pierce E, Ragsdale SW, Armstrong FA (2011) *Energy Environ Sci* 4:2393
381. Chaudhary YS, Woolerton TW, Allen CS, Warner JH, Pierce E, Ragsdale SW, Armstrong FA (2012) *Chem Commun* 48:58
382. Brown KA, Dayal S, Ai X, Rumbles G, King PW (2010) *J Am Chem Soc* 132:9672
383. Qin P, Zhu H, Edvinsson T, Boschloo G, Hagfeldt A, Sun L (2008) *J Am Chem Soc* 130:8570
384. Gardner JM, Beyler M, Karnahl M, Tschierlei S, Ott S, Hammarström L (2012) *J Am Chem Soc* 134:19322
385. Ji Z, He M, Huang Z, Ozkan U, Wu Y (2013) *J Am Chem Soc* 135:11696
386. Mulder DW, Boyd ES, Sarma R, Lange RK, Endrizzi JA, Broderick JB, Peters JW (2010) *Nature* 465:248

387. Nicolet Y, Piras C, Legrand P, Hatchikian EC, Fontecilla-Camps JC (1999) *Structure* 7:13
388. Peters JW, Lanzilotta WN, Lemon BJ, Seefeldt LC (1998) *Science* 282:1853
389. Page CC, Moser CC, Chen X, Dutton PL (1999) *Nature* 402:47
390. Moser CC, Keske JM, Warncke K, Farid RS, Dutton PL (1992) *Nature* 355:796
391. Topoglidis E, Discher BM, Moser CC, Dutton PL, Durrant JR (2003) *ChemBioChem* 4:1332
392. Hong G, Pachter R (2012) *ACS Chem Biol* 7:1268
393. Cohen J, Kim K, King P, Seibert M, Schulten K (2005) *Structure* 13:1321
394. Hong G, Cornish AJ, Hegg EL, Pachter R (2011) *BBA-Bioenergetics* 1807:510
395. Long H, King PW, Chang CH (2014) *J Phys Chem B* 118:890
396. Cornish AJ, Gärtner K, Yang H, Peters JW, Hegg EL (2011) *J Biol Chem* 286:38341
397. Ginovska-Pangovska B, Ho M-H, Linehan JC, Cheng Y, Dupuis M, Raugei S, Shaw WJ (2014) *BBA-Bioenergetics* 1837:131
398. Myers WK, Stich TA, Suess DLM, Kuchenreuther JM, Swartz JR, Britt RD (2014) *J Am Chem Soc* 136:12237
399. Mulder DW, Ratzloff MW, Shepard EM, Byer AS, Noone SM, Peters JW, Broderick JB, King PW (2013) *J Am Chem Soc* 135:6921
400. Foster CE, Krämer T, Wait AF, Parkin A, Jennings DP, Happe T, McGrady JE, Armstrong FA (2012) *J Am Chem Soc* 134:7553
401. Lemon BJ, Peters JW (1999) *Biochemistry* 38:12969
402. Goldet G, Brandmayr C, Stripp ST, Happe T, Cavazza C, Fontecilla-Camps JC, Armstrong FA (2009) *J Am Chem Soc* 131:14979
403. Baffert C, Bertini L, Lautier T, Greco C, Sybirna K, Ezanno P, Etienne E, Soucaille P, Bertrand P, Bottin H, Meynial-Salles I, De Gioia L, Léger C (2011) *J Am Chem Soc* 133:2096
404. Stripp ST, Goldet G, Brandmayr C, Sanganas O, Vincent KA, Haumann M, Armstrong FA, Happe T (2009) *Proc Natl Acad Sci U S A* 106:17331
405. Swanson KD, Ratzloff MW, Mulder DW, Artz JH, Ghose S, Hoffman A, White S, Zadvorny OA, Broderick JB, Bothner B, King PW, Peters JW (2015) *J Am Chem Soc* 137:1809
406. Berggren G, Adamska A, Lambertz C, Simmons TR, Esselborn J, Atta M, Gambarelli S, Mouesca JM, Reijerse E, Lubitz W, Happe T, Artero V, Fontecave M (2013) *Nature* 499:66
407. Esselborn J, Lambertz C, Adamska-Venkatesh A, Simmons T, Berggren G, Noth J, Siebel J, Hemschemeier A, Artero V, Reijerse E, Fontecave M, Lubitz W, Happe T (2013) *Nat Chem Biol* 9:607
408. Hexter SV (2014) D Phil Thesis, University of Oxford
409. Camara JM, Rauchfuss TB (2012) *Nat Chem* 4:26
410. Finkelman AR, Stiebritz MT, Reiher M (2014) *Chem Sci* 5:215
411. Lambertz C, Chernev P, Klingan K, Leidel N, Sigfridsson KGV, Happe T, Haumann M (2014) *Chem Sci* 5:1187
412. Bruschi M, Greco C, Kaukonen M, Fantucci P, Ryde U, De Gioia L (2009) *Angew Chem Int Ed* 48:3503
413. von Abendroth G, Stripp ST, Silakov A, Croux C, Soucaille P, Girbal L, Happe T (2008) *Int J Hydrogen Energy* 33:6076
414. Gorwa MF, Croux C, Soucaille P (1996) *J Bacteriol* 178:2668
415. Garcin E, Vernede X, Hatchikian EC, Volbeda A, Frey M, Fontecilla-Camps JC (1999) *Structure* 7:557
416. Montet Y, Amara P, Volbeda A, Vernede X, Hatchikian EC, Field MJ, Frey M, Fontecilla-Camps JC (1997) *Nat Struct Mol Biol* 4:523
417. Baltazar CA, Teixeira V, Soares C (2012) *J Biol Inorg Chem* 17:543
418. Bührke T, Lenz O, Krauss N, Friedrich B (2005) *J Biol Chem* 280:23791
419. Lauterbach L, Lenz O (2013) *J Am Chem Soc* 135:17897
420. Wulff P, Day CC, Sargent F, Armstrong FA (2014) *Proc Natl Acad Sci U S A* 111:6606
421. Fritsch J, Lenz O, Friedrich B (2013) *Nat Rev Micro* 11:106

422. Szóri-Dorogházi E, Maróti G, Szóri M, Nyilasi A, Rákhely G, Kovács KL (2012) *PLoS ONE* 7:e34666
423. Ogata H, Nishikawa K, Lubitz W (2015) *Nature* 520:571
424. Dementin S, Burlat B, De Lacey AL, Pardo A, Adryanczyk-Perrier G, Guigliarelli B, Fernandez VM, Rousset M (2004) *J Biol Chem* 279:10508
425. Ogata H, Hirota S, Nakahara A, Komori H, Shibata N, Kato T, Kano K, Higuchi Y (2005) *Structure* 13:1635
426. Volbeda A, Martin L, Cavazza C, Matho M, Faber B, Roseboom W, Albracht SJ, Garcin E, Rousset M, Fontecilla-Camps J (2005) *J Biol Inorg Chem* 10:239
427. van Gastel M, Stein M, Brecht M, Schröder O, Lenzian F, Bittl R, Ogata H, Higuchi Y, Lubitz W (2006) *J Biol Inorg Chem* 11:41
428. Bleijlevens B, van Broekhuizen F, De Lacey A, Roseboom W, Fernandez V, Albracht SJ (2004) *J Biol Inorg Chem* 9:743
429. Hidalgo R, Ash PA, Healy AJ, Vincent KA (2015) *Angew Chem Int Ed* 54:7110
430. Murphy BJ, Hidalgo R, Roessler MM, Evans RM, Ash PA, Myers WK, Vincent KA, Armstrong FA (2015) *J Am Chem Soc* 137:8484
431. Evans RM (2015) Mechanism of hydrogen activation by [NiFe]-hydrogenases, personal communication
432. Goris T, Wait AF, Saggiu M, Fritsch J, Heidary N, Stein M, Zebger I, Lenzian F, Armstrong FA, Friedrich B, Lenz O (2011) *Nat Chem Biol* 7:310
433. Pandelia M-E, Nitschke W, Infossi P, Giudici-Orticoni M-T, Bill E, Lubitz W (2011) *Proc Natl Acad Sci U S A* 108:6097
434. Parkin A, Sargent F (2012) *Curr Opin Chem Biol* 16:26
435. Evans RM, Parkin A, Roessler MM, Murphy BJ, Adamson H, Lukey MJ, Sargent F, Volbeda A, Fontecilla-Camps JC, Armstrong FA (2013) *J Am Chem Soc* 135:2694
436. Riethausen J, Rüdiger O, Gärtner W, Lubitz W, Shafaat HS (2013) *ChemBioChem* 14:1714
437. Volbeda A, Amara P, Iannello M, De Lacey AL, Cavazza C, Fontecilla-Camps JC (2013) *Chem Commun* 49:7061
438. Marques MC, Coelho R, De Lacey AL, Pereira IAC, Matias PM (2010) *J Mol Biol* 396:893
439. Medina M, Claude Hatchikian E, Cammack R (1996) *BBA-Bioenergetics* 1275:227
440. Darenbourg MY, Weigand W (2011) *Eur J Inorg Chem* 2011:994
441. Dobbek H, Gremer L, Kiefersauer R, Huber R, Meyer O (2002) *Proc Natl Acad Sci U S A* 99:15971
442. Ragsdale S (2004) *Crit Rev Biochem Mol Biol* 39:165
443. Jeoung J-H, Fessler J, Goetzl S, Dobbek H (2014) In: Kroneck PMH, Torres MES (eds) *The Metal-Driven Biogeochemistry of Gaseous Compounds in the Environment*, vol 14. Springer, The Netherlands, p 37
444. Wang VC-C, Ragsdale SW, Armstrong FA (2013) *ChemBioChem* 14:1845
445. Svetlitchnyi V, Dobbek H, Meyer-Klaucke W, Meins T, Thiele B, Römer P, Huber R, Meyer O (2004) *Proc Natl Acad Sci U S A* 101:446
446. Dobbek H, Svetlitchnyi V, Gremer L, Huber R, Meyer O (2001) *Science* 293:1281
447. Craft JL, Ludden PW, Brunold TC (2002) *Biochemistry* 41:1681
448. Gray HB, Winkler JR (2005) *Proc Natl Acad Sci U S A* 102:3534
449. Wu M, Ren Q, Durkin AS, Daugherty SC, Brinkac LM, Dodson RJ, Madupu R, Sullivan SA, Kolonay JF, Nelson WC, Tallon LJ, Jones KM, Ulrich LE, Gonzalez JM, Zhulin IB, Robb FT, Eisen JA (2005) *PLoS Genet* 1:e65
450. Jeoung J-H, Dobbek H (2012) *J Biol Inorg Chem* 17:167
451. Craft P-h, Bruschi M, De Gioia L, Blumberger J (2013) *J Am Chem Soc* 135:9493
452. Lindahl PA (2002) *Biochemistry* 41:2097
453. Lindahl PA (2008) *Angew Chem Int Ed* 47:4054
454. Feng J, Lindahl PA (2004) *Biochemistry* 43:1552
455. Jeoung J-H, Dobbek H (2007) *Science* 318:1461
456. Amara P, Mouessa J-M, Volbeda A, Fontecilla-Camps JC (2011) *Inorg Chem* 50:1868
457. Lindahl PA (2012) *J Inorg Biochem* 106:172

458. Tan GO, Ensign SA, Ciurli S, Scott MJ, Hedman B, Holm RH, Ludden PW, Korszun ZR, Stephens PJ, Hodgson KO (1992) *Proc Natl Acad Sci U S A* 89:4427
459. Ralston CY, Wang H, Ragsdale SW, Kumar M, Spangler NJ, Ludden PW, Gu W, Jones RM, Patil DS, Cramer SP (2000) *J Am Chem Soc* 122:10553
460. Gu W, Seravalli J, Ragsdale SW, Cramer SP (2004) *Biochemistry* 43:9029
461. Kumar M, Lu WP, Liu L, Ragsdale SW (1993) *J Am Chem Soc* 115:11646
462. Seravalli J, Ragsdale SW (2008) *Biochemistry* 47:6770
463. Svetlitchnyi V, Peschel C, Acker G, Meyer O (2001) *J Bacteriol* 183:5134

Chapter 2

Theory of Experimental Techniques

2.1 Rate and Efficiency Parameters in Artificial Photosynthesis

Several spectroscopic and mechanistic tools can be employed to study the intricate mechanisms of interaction between light-absorbing semiconductors and fuel-forming enzymes. First, the efficiencies of the fuel-forming reactions have to be determined, usually via monitoring of product formation by gas chromatography (GC). The solar-to-hydrogen (STH) efficiency can then be calculated, according to the following equation [1]:

$$\eta_{\text{STH}} = \left[\frac{(\text{mmol H}_2\text{s}^{-1}) \times (237,000 \text{ Jmol}^{-1})}{P_{\text{in}}(\text{mW cm}^{-2}) \times \text{Area}(\text{cm}^2)} \right]_{\text{AM1.5 G}} \quad (2.1)$$

Here, the directly measured rate of H₂ production (mmol H₂ s⁻¹) is multiplied by the change in Gibbs free energy per mole of H₂ ($\Delta G^\circ = 237 \text{ kJ mol}^{-1}$ at 25 °C). In the denominator of Eq. (2.1), the incident illumination power density P_{in} is multiplied by the illuminated (geometric) electrode area. The illumination source should closely match the shape and intensity of the air mass 1.5 global standard G173 (AM 1.5 G) [1].

From the amount of enzyme used, the TON and TOF values on a per enzyme basis can be determined. In photoelectrochemical cells, solar energy conversion efficiencies can also be calculated from catalytic current densities, provided the Faradaic efficiencies η_{F} for product formation are known. For solar hydrogen formation, Eq. (2.1) then translates to [1]:

$$\eta_{\text{STH}} = \left[\frac{j_{\text{sc}} (\text{mA cm}^{-2}) \times (1.23 \text{ V}) \times \eta_{\text{F}}}{P_{\text{in}} (\text{mW cm}^{-2})} \right]_{\text{AM1.5G}} \quad (2.2)$$

In Eq. (2.2), j_{sc} is the short-circuit photocurrent density normalised to the illuminated (geometric) electrode area and the voltage corresponds to the thermodynamic water splitting potential (based on ΔG°). Similar equations can be formulated for the reduction of CO_2 .

Enzymes offer much more selectivity than heterogeneous surface electrocatalysts, which often give complex mixtures of products, particularly in the case of CO_2 reduction (see Sect. 1.3.4.2). Therefore, in enzymes, Faradaic efficiencies are often close to 100%. Enzymes are also sensitive to selective inhibitors, which can help to confirm whether or not a product or current arises from catalytic conversion. However, direct product detection is always highly desirable, where possible.

It is important to note that only STH efficiencies (or solar-to- CO_2 reduction efficiencies) measured without the use of sacrificial reagents or applied bias can serve as benchmark values to compare against other materials/systems. ‘Half-cell’ efficiencies can inflate the apparent performance of a system and cannot be converted into a meaningful device performance metric [1]. Yet, although not suitable for standardisation, the other efficiency parameters described below can still give important information about mechanistic details and are valuable for understanding and improving materials and system performance.

The external quantum efficiency (EQE), equivalent to the incident photon-to-current efficiency (IPCE), is an important characteristic of a solar-fuel system (for a primary photochemical process, quantum efficiency (QE) is identical to quantum yield, Φ). The EQE describes the fraction of catalytic current generated per incoming photon flux (‘electrons out per photons in’), taking into account the spectral variation of incident photons at each energy [1]. The IPCEs are usually measured by chronoamperometry experiments (see Sect. 2.2.7) under varying monochromatic light exposure. The internal quantum efficiency (IQE) or absorbed photon-to-current efficiency (APCE) characterises the inherent performance of a material/solar-to-fuel system, since losses from reflected or transmitted photons are subtracted. The APCE can be determined by dividing the IPCE by the absorbance, η_{e^-/h^+} , which is defined as the fraction of electron-hole pairs generated per incident photon flux and can be estimated from Beer’s law [1].

The aforementioned quantities are important characteristics of solar-fuel systems, but do not give detailed information about the *mechanisms* of light-driven fuel-formation. To characterise the catalytic performances in enzyme/semiconductor systems, TOF, TON, and rates of electron injection and charge transport under catalytic conditions (i.e. light exposure and presence of substrate) are the most valuable parameters.

2.2 Protein Film Electrochemistry

2.2.1 A Brief Introduction to Protein Film Electrochemistry

Protein film electrochemistry comprises a suite of dynamic electrochemical techniques that reveal intricate mechanistic details of redox enzymes under turnover conditions. Minuscule samples of protein are adsorbed directly on electrodes to give mono- or submonolayer films [2]. Enzymes maintain their native function [3] and their catalytic properties are fully expressed: facile, reversible electron transfer occurs with the electrode, the potential of which now controls the catalytic activity, which is monitored through the observed current that acts as a direct measure of the catalytic turnover rate at any given electrode potential [2].

Carbon is the most common electrode material in protein film electrochemistry. Particularly the ‘edge’ plane of pyrolytic graphite (PGE) is used, rather than the hydrophobic basal cut, due to the former’s diversity of aromatic and oxo species present on the surface and the similarity to a protein’s natural environment [3]. Direct enzyme immobilisation obviates the need for redox mediators, diffusion of which is known to kinetically limit the superbly fast rates of electron transfer and catalysis achieved by metalloenzymes such as hydrogenase and CODH.

2.2.2 The Electrochemical Setup

Typically, a standard three-electrode setup is employed in protein film electrochemistry experiments [4] (Fig. 2.1).

Apart from PGE as most commonly used working electrode (WE) material, gold surfaces modified with self-assembled monolayers of alkanethiolate are also used [4]. Different strategies for enzyme-surface immobilisation are described in Sect. 1.5.3.4. Counter electrodes (CE) are typically made of platinum (wire or gauze) and, as the real standard hydrogen electrode (SHE) is rarely practical [5], secondary electrodes such as the saturated calomel electrode (SCE) or the Ag/AgCl electrode are commonly used as reference electrodes (RE). The RE should be placed as closely as possible to the working electrode to limit the effect of electrolyte resistance R_s [1] (vide infra). As depicted in Fig. 2.1, it can be housed in a separate compartment connected to the cell via a Luggin-Haber capillary. Electrode rotation at high frequencies ensures rapid delivery (removal) of substrate (product) to and from the enzyme active site and minimises limiting effects of mass transport. Use of a water jacket allows precise control of the temperature throughout the experiment. Specific gas mixtures can be introduced through the headspace of a gastight cell and the electrochemical setup can be illuminated if necessary.

When a potential is applied between a working electrode and a reference electrode, assuming a finite current i is flowing between the two electrodes, then [6, 7]

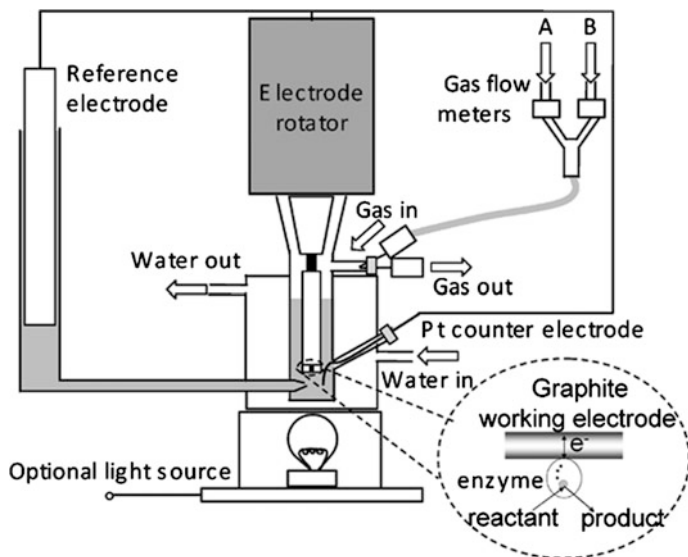


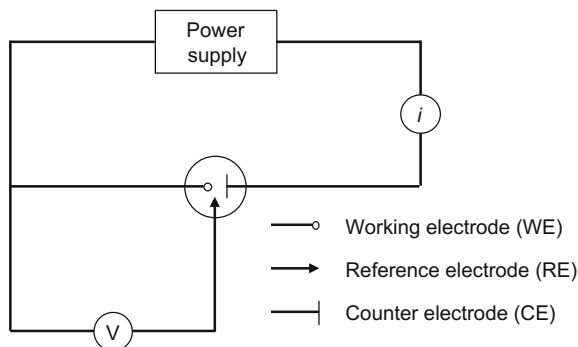
Fig. 2.1 Schematic diagram of a typical experimental setup employed in protein film electrochemistry experiments. The electrochemical cell fits tightly against an electrode rotator and is equipped with gas flow controllers for providing accurate mixtures of gases. Reprinted with permission from Ref. [2]. Copyright 2009 The Royal Society of Chemistry

$$E = (\phi_w - \phi_s^w) + iR_s + (\phi_s^{\text{ref}} - \phi_{\text{ref}}), \quad (2.3)$$

where ϕ_w and ϕ_{ref} represent the electric potentials of the working and reference electrodes, respectively.¹ ϕ_s^w and ϕ_s^{ref} represent the potential of the solution very close to the working and reference electrodes. With R_s being the electrical resistance of the solution between the electrodes, iR_s represents the voltage drop in solution due to passage of current i between the two electrodes; it is characteristic of the bulk solution and not the electrode reaction [6]. The term $(\phi_s^{\text{ref}} - \phi_{\text{ref}})$ is the potential drop at the reference electrode, which is fixed by its chemical composition [7]. Under conditions when iR_s is small ($< 1\text{--}2$ mV [6]) such as in microelectrode experiments, a two-electrode cell can be used to determine the i - E curve, i.e. the current i as a function of changes in the potential difference at the working electrode/solution interface ($\phi_w - \phi_s^w$, the driving force for electrolysis) [7]. In case of large electrodes or more resistive solutions, however, iR_s is no longer negligible, and changes in applied potential are no longer confined to changes in $(\phi_w - \phi_s^w)$. In addition to the iR_s term being altered, the passage of large currents through the

¹Throughout this thesis, electrode potentials (strictly speaking, potential differences) are denoted ' E ' and electric potentials are referred to as ' ϕ ', in agreement with Eq. (2.3).

Fig. 2.2 Schematic representation of a three-electrode circuit diagram and notation for the different electrodes, adapted from Ref. [6]



reference electrode can change its chemical composition, meaning $(\phi_s^{\text{ref}} - \phi_{\text{ref}})$ may no longer be constant [7].

A *three-electrode* system (the circuit of which is schematically depicted in Fig. 2.2), where the current is passed between the working electrode and the counter electrode only, and the potential of the working electrode is held constant (a high input impedance ensures that little current is drawn through the RE [6]) circumvents this problem [7].

Except when specifically mentioned, e.g. in photoelectrochemistry experiments under no external bias described in Chap. 6 of this thesis, PFE experiments in this work were carried out using a three-electrode system. Two main types of PFE experiment are presented in this thesis: voltammetry (cyclic voltammetry, CV, and linear sweep voltammetry, LSV) and chronoamperometry. In voltammetry, the current is measured as a function of the applied potential, which is swept between two values. In chronoamperometry, the potential is held constant and the enzymatic current is measured as a function of time.

2.2.3 Non-faradaic Processes

In protein film electrochemistry experiments, the observed current is usually the combination of a Faradaic process (which reveals redox transformations of molecules that come sufficiently close to the electrode, i.e. electrons are transferred across the electrode/solution interface) [5] and a non-Faradaic process, where no charge transfer occurs across the electrode/solution interface takes place. The latter process resembles a capacitor:

$$C = \frac{q}{E}, \quad (2.4)$$

where q is the charge stored on the capacitor (in Coulombs, C), E is the potential across the capacitor (in Volts, V), and C is the capacitance (in Farads, F) [6]. Hence,

non-Faradaic currents are often termed ‘capacitive’ or ‘charging’ currents. When the working electrode potential is swept across a potential range (such as in voltammetry experiments), charge will accumulate on its surface; an effect that has to be counterbalanced by an excess of oppositely charged ions. The result is the formation of an *electrical double layer*. This double layer itself consists of several ‘sublayers’ [6]: closest to the electrode surface, at the so-called inner Helmholtz plane (IHP), ions are specifically adsorbed to the electrode, stripped off their solvation shell. Solvated ions in turn can approach the electrode only up to a distance that marks the outer Helmholtz plane (OHP). Here, the interaction of these non-specifically adsorbed ions with the electrode is essentially independent of the chemical properties of these ions, because only long-range electrostatic forces are involved [6]. Thermal motion causes the non-specifically adsorbed ions to be distributed in a three-dimensional region called the diffuse layer, which extends from the OHP into the bulk of the solution.

In a voltammetric experiment, the current i that is produced upon modulation of the applied potential equals the change in charge with time:

$$i = \frac{dq}{dt}. \quad (2.5)$$

Combining Eqs. (2.4) and (2.5), the capacitive current i_c can be formulated as

$$i_c = C \frac{dE}{dt} = Cv. \quad (2.6)$$

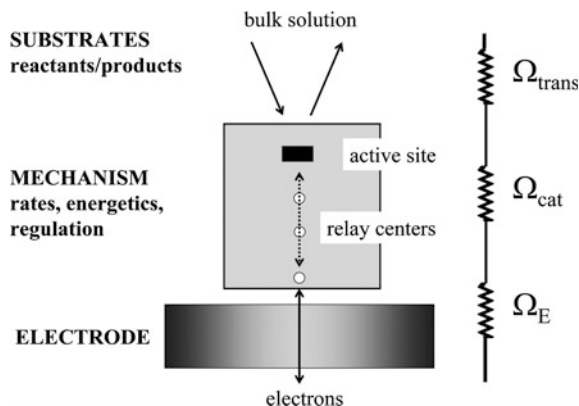
Equation (2.6) shows that i_c is proportional to the scan rate v (dE/dt). The magnitude of i_c also depends on the resistance in the circuit and, via the capacitance, on the electrode area and the applied potential [6].

In chronoamperometry experiments where the potential is held constant, capacitive currents are only observed after potential steps. They occur as exponentially decaying transients (‘spikes’), typically decaying within seconds [5]. In general, the non-Faradaic contributions arising in PFE experiments can be measured separately in ‘blank’ experiments where no enzyme is adsorbed on the bare working electrode surface. Subtraction from the total enzymatic current then allows determination of the Faradaic contribution.

2.2.4 Faradaic Current

Faradaic currents arise upon electrode transfer at the electrode, i.e. they correspond to redox processes and are governed by Faraday’s law, meaning the amount of chemical reaction caused by the flow of current is proportional to the amount of electricity passed [6]. Under equilibrium conditions, there is no net flow of electrons and the Nernst equation (derived in Appendix A) gives the ratio of the

Fig. 2.3 Catalytic electron flow through an enzyme immobilised on an electrode in which the possible rate-determining stages are represented by resistors in series. The electron entry/exit site is the lower one of the relay centres indicated as circles. Reprinted with permission from Ref. [4]. Copyright 2007 American Chemical Society



activities of oxidised and reduced species, often simplified to concentrations ($[Ox]/[Red]$) for solutions that show sufficiently ideal behaviour:

$$E_{\text{eq}} = E^0 + \frac{RT}{zF} \ln \frac{[Ox]}{[Red]}. \quad (2.7)$$

In Eq. (2.7), E_{eq} is the equilibrium potential, E^0 is the standard reduction potential for the redox couple Ox/Red, R is the ideal gas constant, T is the temperature, z is the number of electrons transferred in the process, and F is Faraday's constant.

In dynamic electrochemistry experiments, a potential is applied that induces a current flow. In PFE experiments where a redox enzyme is adsorbed on an electrode surface, this current provides a direct measure of the catalytic activity of the enzyme. However, it is important to note that the inherent activity of the catalytic centre is not the only factor contributing to the observed current at the enzyme-modified electrode. Conceptually, an enzyme adsorbed on an electrode can be visualised as a series of resistors (Fig. 2.3) [4]. In this model, catalytic electron flow is divided into three stages that express the inherent barriers of (i) interfacial electron transfer (Ω_E), (ii) enzyme catalysis (Ω_{cat}), and (iii) substrate mass transport (Ω_{trans}). To be able to study the intrinsic mechanisms of enzyme action, interfacial electron transfer and substrate mass transport must not be limiting, i.e. Ω_E and Ω_{trans} should be as small as possible.

2.2.5 Mass Transport and Interfacial Electron Transfer

In order to minimise Ω_{trans} , hydrodynamic control over substrate delivery to the active site (and product dispersion away from the catalytic centre) can be exploited

by rotating the working electrode at high frequencies. At a planar rotating disc electrode, the current is given by the Levich equation [4]:

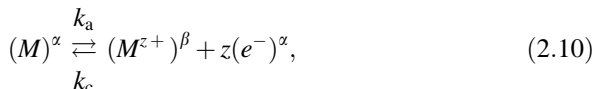
$$i_{(\omega)} = 0.62zFAD^{2/3}\nu^{-1/6}\omega^{1/2}c. \quad (2.8)$$

Here, A refers to the electrode area, D is the diffusion coefficient of the substrate, ν is the kinematic viscosity of the solvent, ω is the electrode rotation rate, and c is the concentration of the substrate. According to Eq. (2.8), the current increases as the square root of the electrode rotation rate. Eventually, the resistance component Ω_{trans} will cease to control the current and, depending on the activity of the enzyme, the linear relationship between the current and $\omega^{1/2}$ breaks down as the rotation rate continues to increase and control passes to the enzyme [4]. Then, the Koutecky-Levich equation

$$\frac{1}{i_{\text{lim}(\omega)}} = \frac{1}{i_{\text{lim}}} + \frac{1}{0.62zFAD^{2/3}\nu^{-1/6}\omega^{1/2}c}, \quad (2.9)$$

where $i_{\text{lim}(\omega)}$ is the limiting plateau current at rotation rate ω and i_{lim} is the maximum limiting current achieved at infinite rotation, describes the relationship between current and rotation rate. Whereas i_{lim} is normally obtained from the intercept of plotting $1/i_{\text{lim}(\omega)}$ vs. $1/\omega^{1/2}$, an approximation can often be obtained by using a rotation rate above which the current and waveform no longer change significantly upon increasing ω [4]. Alternatively, albeit in a more primitive way, the electrolyte solution can be sparged with gas close to the working electrode surface to assist rapid substrate delivery and product removal.

In regards to interfacial electron transfer (Ω_E in Fig. 2.3), the relationship between Faradaic current and applied potential is governed by the Butler-Volmer equation, which can be derived as follows [8]. Consider the reversible charge-transfer reaction occurring at the interface between a metal electrode (M , phase α) and the solution phase (β)



where k_a and k_c are the rate constants for the anodic (oxidation) and cathodic (reduction) reaction, respectively. At equilibrium, there is no net current flow and the anodic current density (i.e. current per unit of geometric electrode area) j_a , which, per definition, carries a positive sign, is equal to the absolute value of the cathodic current density j_c :

$$j_a = |j_c| = j_0. \quad (2.11)$$

In Eq. (2.11), j_0 is defined as the exchange current density, which represents the balanced Faradaic oxidation and reduction currents contributing to the net zero

current. In order to drive reaction (2.10) and induce a current, a potential different to E_{eq} needs to be applied. The *overpotential* η is defined as the difference between the applied potential E and the reversible equilibrium potential:

$$\eta = E - E_{\text{eq}}. \quad (2.12)$$

The resulting current that flows through the system is characterised by the current density j , which is the sum of j_a and j_c :

$$j = j_a + j_c = j_a - |j_c|. \quad (2.13)$$

Transition State Theory (TST) [9] can be used to derive the rate constants k_a and k_c in Eq. (2.10). TST assumes that an activated complex (transition state) is formed prior to formation of the products in a chemical reaction, and that this transition state is in equilibrium with the reagents. The free energy of activation ΔG^\ddagger is described by

$$\Delta G^\ddagger = -RT \ln K^\ddagger, \quad (2.14)$$

where K^\ddagger denotes the equilibrium constant for formation of the activated complex, and

$$k = A_p e^{\frac{-\Delta G^\ddagger}{RT}}. \quad (2.15)$$

Here, k is the rate of the reaction and A_p is a constant pre-exponential factor. Using TST and assuming no potential difference between metal and solution in Eq. (2.10) (see Fig. 2.4, black curve), the following rate constants are obtained:

$$k_a^0 = k'_a e^{\frac{-\Delta G_a^0}{RT}} \quad (2.16)$$

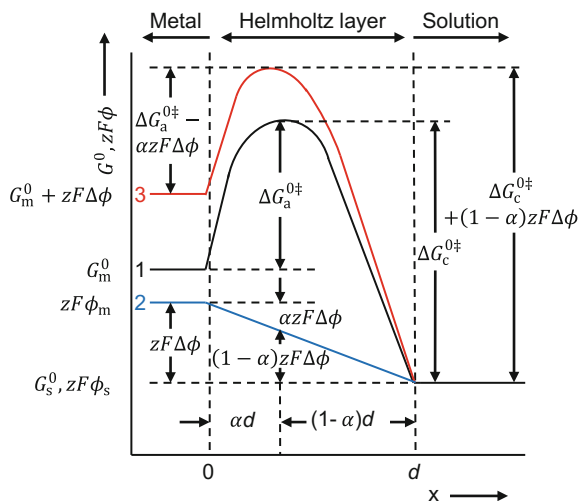
and

$$k_c^0 = k'_c e^{\frac{-\Delta G_c^0}{RT}}. \quad (2.17)$$

However, it is important to remember that if, as in Eq. (2.10), charged species migrate from one phase into another by overcoming a potential difference, one has to explicitly consider the term $zF\Delta\phi^\ddagger$ that describes the electrical work. In Fig. 2.4, the gradient of $zF\phi$ between electrode and solution is depicted in blue, using the simplest model of a rigid Helmholtz layer. The sum $G^0 + zF\phi$ is depicted in red.

Inspection of Fig. 2.4 shows that the value of $\Delta G^0 + zF\phi^\ddagger$ greatly depends on the location of the activated complex within the Helmholtz layer: at positions close to the outer Helmholtz plane the electric potential has a large influence on the

Fig. 2.4 Schematic illustration of the activation energies of anodic and cathodic processes in charge-transfer reactions. Figure adapted from Ref. [8]



anodic process and only marginally affects the cathodic reaction, and vice versa for positions close to the electrode surface. The symmetry of the barrier to electron transfer is reflected in the transfer coefficient α , which can range from 0 to 1. A value close to 0 implies that the transition state closely resembles the reactants, whereas a value close to 1 represents a transition state similar to the products. In Fig. 2.4, α shows after which fraction of the Helmholtz layer the transition state is found, coming from the IHP. For many reactions, α is found to equal 0.5, suggesting that the transition state has intermediate behaviour [7]. Taking into account the electrical term of the activation energy and, as in the derivation of the Nernst equation in Appendix A, expressing the potential difference between metal and solution as $E = \phi_m - \phi_s$, Eqs. (2.16) and (2.17) can be rewritten as

$$k_a = k'_a e^{\frac{-(\Delta G_a^{0‡} - \alpha zFE)}{RT}} = k_a^0 e^{\frac{\alpha zFE}{RT}} \quad (2.18)$$

and

$$k_c = k'_c e^{\frac{-(\Delta G_c^{0‡} + (1-\alpha)zFE)}{RT}} = k_c^0 e^{\frac{(\alpha-1)zFE}{RT}}. \quad (2.19)$$

The total current density j , defined in Eq. (2.13), can be expressed as

$$j = kzF\Gamma. \quad (2.20)$$

Here, Γ refers to the coverage ('area concentration') of the reduced (Red) and oxidised (Ox) species at the inner and outer Helmholtz plane, respectively. Thus, $zF\Gamma$ corresponds to 'charge per area'. Combining Eq. (2.20) with Eqs. (2.18) and (2.19), the anodic and cathodic current densities are [7]

$$j_a = k_a z F \Gamma_{\text{red}} = k_a^0 z F \Gamma_{\text{red}} e^{\frac{zFE}{RT}} \quad (2.21)$$

and

$$j_c = -k_c z F \Gamma_{\text{ox}} = -k_c^0 z F \Gamma_{\text{ox}} e^{\frac{(x-1)zFE}{RT}}. \quad (2.22)$$

Using the state of electrochemical equilibrium as reference point, Eq. (2.11) can be rewritten using Eqs. (2.21) and (2.22):

$$j_0 = k_a^0 z F \Gamma_{\text{red}} e^{\frac{zFE_{\text{eq}}}{RT}} = k_c^0 z F \Gamma_{\text{ox}} e^{\frac{(x-1)zFE_{\text{eq}}}{RT}}. \quad (2.23)$$

Combining Eqs. (2.21) and (2.22), respectively, with Eq. (2.23), and substituting in the overpotential η [defined in Eq. (2.12)] leads to

$$j_a = j_0 e^{\frac{zF\eta}{RT}} \quad (2.24)$$

and

$$j_c = -j_0 e^{\frac{(x-1)zF\eta}{RT}}. \quad (2.25)$$

Substitution of Eqs. (2.24) and (2.25) into Eq. (2.13) gives the Butler-Volmer equation, which describes the current density as a function of overpotential, and lies at the heart of electrochemical kinetics:

$$j = j_0 \left[e^{\frac{zF\eta}{RT}} - e^{\frac{(x-1)zF\eta}{RT}} \right]. \quad (2.26)$$

Consider again the state of electrochemical equilibrium. Solving Eq. (2.23) for the equilibrium potential E_{eq} yields

$$E_{\text{eq}} = -\frac{RT}{zF} \ln \frac{k_a^0}{k_c^0} - \frac{RT}{zF} \ln \frac{\Gamma_{\text{red}}}{\Gamma_{\text{ox}}} \quad (2.27)$$

With $\frac{k_c^0}{k_a^0} = K$ and $\Delta G^0 = -RT \ln K$ [compare Eq. (2.14)], conversion of ΔG^0 into E^0 [see eq. (A.15)] leads to

$$E_{\text{eq}} = E^0 + \frac{RT}{zF} \ln \frac{\Gamma_{\text{ox}}}{\Gamma_{\text{red}}}. \quad (2.28)$$

Equation (2.28) becomes identical to the Nernst equation [Eq. (2.7)] by substituting the area concentrations Γ_{red} and Γ_{ox} for the concentrations [Ox] and [Red].

Figure 2.5 depicts the current-voltage behaviour predicted by the Butler-Volmer equation [6]. The solid curve reflects the total current, which is the sum of the anodic and cathodic components [compare Eq. (2.13)], represented by dashed lines.

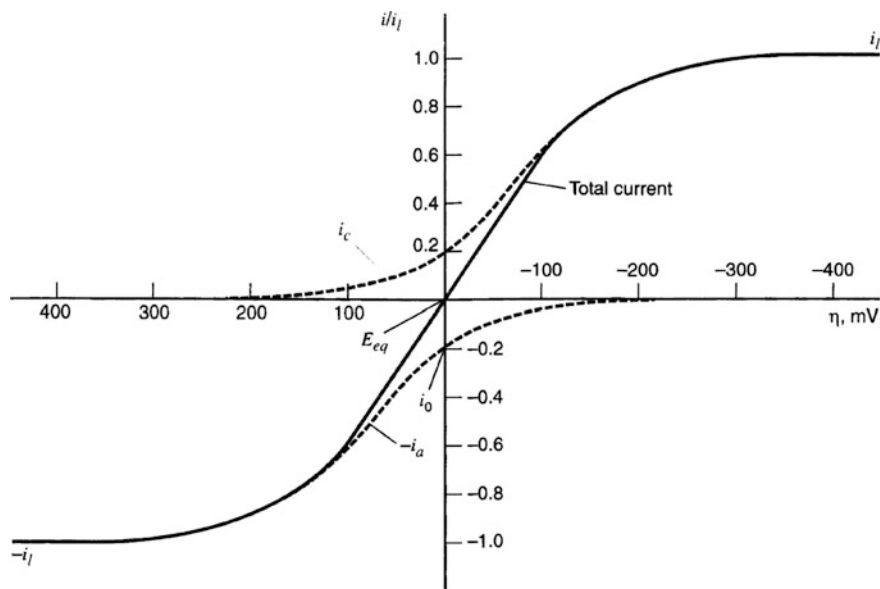


Fig. 2.5 Illustration of the Butler-Volmer relationship. The *solid curve* shows the total current for a system $[\text{Ox}] + e^- \rightleftharpoons [\text{Red}]$ with $\alpha = 0.5$, $T = 298 \text{ K}$, $i_{l,c} = -i_{l,a} = i_l$ and $i_0/i_l = 0.2$. The anodic and cathodic component currents are shown as *dashed lines*. Note that cathodic currents carry a positive sign in this figure. Reprinted with permission from Ref. [6]. Copyright 2001 John Wiley & Sons, Inc.

For large negative overpotentials, the anodic current i_a is negligible and the total current equals the cathodic current i_c , and vice versa for large positive overpotentials. At extreme overpotentials (in either direction), the current levels off, becoming limited by potential-independent steps, i.e. mass-transfer limitations or by the maximum turnover frequency according to Eqs. (2.20)–(2.22).

2.2.6 Catalytic Voltammetry

The reversible catalytic processes displayed by the redox enzymes studied in this thesis (see Sect. 1.6) are characterised, in terms of Butler-Volmer kinetics, by large exchange current densities j_0 , meaning that only small overpotentials are required to induce current flow. Their voltammograms generally adhere to the sigmoidal wave shapes predicted by Eq. (2.26), in contrast to most synthetic catalysts (see Figs. 1.17 and 1.19 for the case of CO_2 reduction). This discrepancy is illustrated in Fig. 2.6, where reversible behaviour, displayed by hydrogenases and CODH, is shown in blue and irreversible reactions are depicted in red.

In protein film voltammetry experiments, deviations from the ideal wave shape depicted in Fig. 2.6 can arise for example from a distribution of enzyme

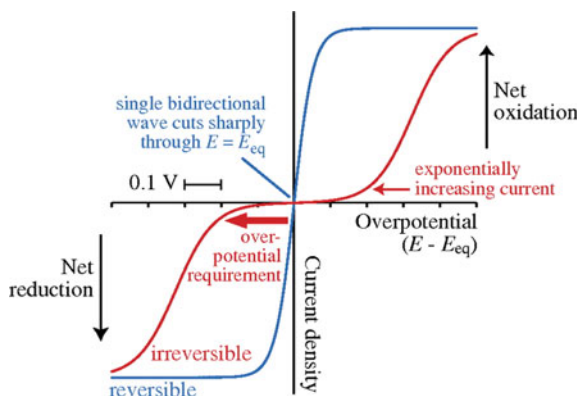


Fig. 2.6 Steady-state electrochemical kinetics visualised by cyclic voltammetry. A reversible electrochemical reaction (characterised by a large exchange current density) produces a single sigmoidal wave (*blue*) that cuts (without inflection) through the zero-current axis at the equilibrium potential (E_{eq}) and achieves a potential-independent limiting current in either direction at relatively low overpotential. If the exchange current density is low, as in most synthetic energy transducing catalysts, the current is negligible around E_{eq} and two sigmoidal waves (*red*), one for either direction, are separated in potential, emerging from the baseline with an exponential dependence on potential: a substantial overpotential is required to match the current produced by the reversible system. Reprinted with permission from Ref. [10]

orientations on the electrode surface [10], resulting in a dispersion of interfacial electron transfer rates. This effect is resembled by a residual slope in the current-voltage curve even at high driving force [11], characteristic for an electron transfer-limited process. The voltammogram of [NiFeSe]-hydrogenase adsorbed on a PGE electrode depicted in Fig. 4.3b constitutes an example of catalytic voltammetry limited by interfacial electron transfer. Potential dependent inactivation steps such as the formation of the H_{ox}^{inact} state in [FeFe]-hydrogenase at oxidising potentials can also alter the predicted waveform.

In the absence of such non-idealities and when mass transport is not limiting, the inherent enzyme activity is directly related to the maximum catalytic current, as outlined in the previous section:

$$k_{cat} = i_{lim}/zFA\Gamma. \quad (2.29)$$

Equation (2.29) is a variation of Eq. (2.20), where k_{cat} denotes the maximum turnover frequency at the limiting current i_{lim} . In order to ascertain k_{cat} , the electroactive coverage Γ needs to be determined. Γ is different to the gross coverage (which is based on how much enzyme is applied to the surface) due to, among other things, the above-mentioned dispersion phenomena [4]. However, in PFE it is rarely possible to ascertain the electroactive coverage of an enzyme as this requires, under non-turnover conditions, the detection and integration of reversible signals (for example, due to FeS redox couples), which are usually vanishingly small. It is

the high activity of enzymes that amplifies the current and PFE provides precise and continuous measurement of the *relative* catalytic rates in either direction.

Because of the porosity of the electrode materials used in this thesis and the resulting variation in actual surface area between different experiments, currents i are generally reported instead of current densities j , in conjunction with voltammograms of the respective bare electrode (as is common in PFE).

2.2.7 Chronoamperometry

Among its many different applications, chronoamperometry (CA) is primarily used in this thesis to study and determine the kinetics of enzyme inhibition processes, predominantly in Chap. 3. The black trace in Fig. 2.7a illustrates the principle: the current is measured as a function of time at a given potential. The potential and time domains are deconvoluted, in contrast to voltammetry experiments. In the particular case of Fig. 2.7a, the applied potential is held constant throughout the experiment, but this need not be the case: potential steps can be introduced to induce changes in catalytic activity. However, as described in Sect. 2.2.3, these cause transient non-Faradaic currents that have to be accounted for. In the example of Fig. 2.7a, an inhibitor is introduced into the electrochemical cell at $t = 0$, followed by a decrease in enzyme activity, kinetic analysis of which yields the rate constant of inhibition k_{obs} .

In the example above, the red curve represents a slow, underlying decay of enzymatic activity that occurs even in the absence of any inhibitor. This process, occurring in every PFE experiment, is commonly known as ‘film loss’ and arises due to several phenomena including desorption of enzyme from the electrode surface, reorientation of enzyme molecules that results in loss of electronic contact,

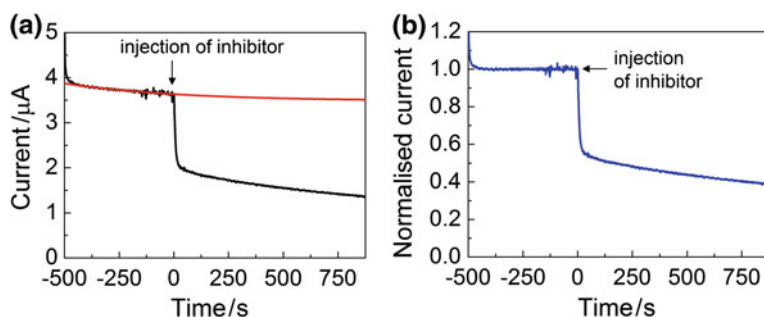


Fig. 2.7 **a** Example of a chronoamperometry experiment (H_2 oxidation by CaHydA adsorbed on PGE at 0.05 V vs. SHE, pH 6.0), in which an inhibitor (acetaldehyde) is introduced at $t = 0$ (*black curve*). Underlying film loss is depicted in *red*. The *red curve* is obtained by least square analysis of the experimental data using Eq. (2.30). **b** Current-time curve obtained after normalisation by dividing the raw data displayed in (a) by the exponential fit

and denaturation of adsorbed enzyme. The effect of film loss is all the more pronounced when the enzyme-modified electrode is subjected to high overpotentials, high temperatures, and, in rotating disk experiments, high rotation rates. To be able to determine accurate kinetics from chronoamperometry experiments, the experimentalist needs to correct for film loss, which generally follows mono-exponential kinetics:

$$i(t) = (i_0 - i_\infty)e^{\left(\frac{i_0 - t}{\tau}\right)} + i_0. \quad (2.30)$$

In Eq. (2.30), the time dependence of the current (i_t) is defined in terms of the current at the start (t_0) of the data to be fitted (i_0), the time constant of film loss (τ), and the limiting current of the exponential (i_∞) [12]. Figure 2.7b depicts a normalised current vs. time trace, obtained by dividing the experimental data displayed in Fig. 2.7a by the exponential fit according to Eq. (2.30) (i.e. dividing the black curve in Fig. 2.7a by the red curve).

To obtain meaningful data from chronoamperometry experiments, the investigator needs to ensure that mass transport and interfacial electron transfer are not limiting (vide supra).

2.3 Semiconductor Electrochemistry

The modern era of semiconductor electrochemistry started in 1955 with Brattain and Garrett's investigations of the interface between germanium and an aqueous electrolyte [13]. The field emerged rapidly over the following decades, spurred in particular by the 1973 oil crisis and the resulting need to establish ways to convert and utilise renewable sources of energy such as sunlight. Following a decline in the 1980s, triggered, in the U.S., by funding cuts for research into alternative energy sources by the Reagan administration [14], the field came to life again in the 1990s, driven especially by the advent of the dye-sensitised solar cell. Throughout the last decade, research into artificial photosynthesis has been contributing increasingly more. To name but a few, seminal contributions include Fujishima and Honda's demonstration of photoelectrochemical water splitting using TiO_2 [15], Grätzel and O'Regan's DSSC [16], and the Turner water splitting cell, capable of achieving STH efficiencies $> 10\%$ [17].

2.3.1 The Energy Band Model

The electronic structure of solids is typically discussed in terms of energy bands, due to the essentially infinite number of atoms that must be considered [18]. Extending the concept of molecular orbitals (MOs), the difference in energy

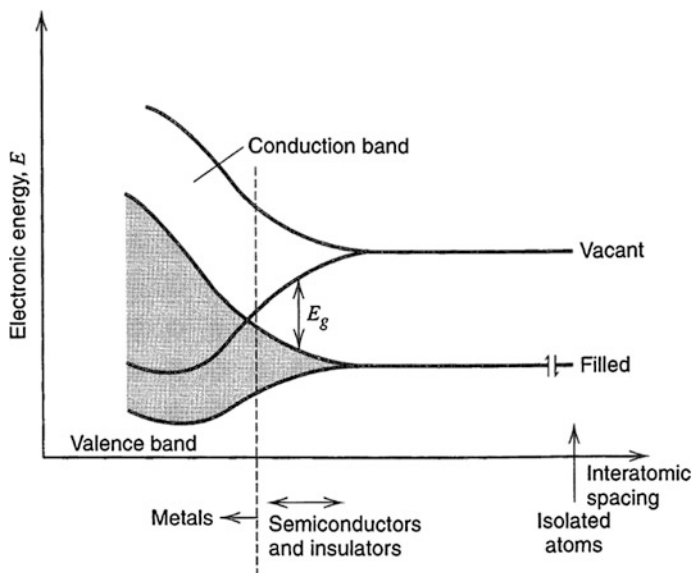


Fig. 2.8 Band formation in solids (at the *left of the image*) by assembly of isolated atoms (characterised by orbitals at the far *right*) into a lattice. Reprinted with permission from Ref. [6]. Copyright 2001 John Wiley & Sons, Inc.

between adjacent MOs is, because of the large number of orbitals, so small that the band can be effectively considered a continuum of energy levels. The highest and lowest energy levels of a band are termed ‘band edges’ [18].

In contrast to metals, semiconductors have energy gaps between the highest occupied electron band (valence band) and the lowest unoccupied energy band (conduction band) (Fig. 2.8). The size of the band gap E_g strongly influences the electrical and optical properties of the material. As illustrated in Fig. 2.8, a material is a good conductor of electricity if E_g is small ($E_g \ll k_B T$) or when the valence and conduction band overlap [6]: filled and vacant electronic energy levels then exist at virtually the same energy and electrons can move freely from one level to another with only small activation energies being required. Conversely, electrons in a completely filled band have no means for redistributing themselves in response to a field [6].

If $E_g > 1.5$ eV, a material is considered an electrical insulator at room temperature [6], but thermal or optical excitation can promote electrons from the valence band to the conduction band, where they can transfer freely among vacant levels within the band, i.e. they have electrical mobility. Left behind in the valence band are vacancies, or holes, that also possess mobility, since the valence band electrons can rearrange themselves to shift the spatial location and energy of a vacancy [6]. Electrons and holes exist in a dynamic equilibrium. In an *intrinsic* semiconductor (Fig. 2.9a), the carrier densities n_i for conduction band electrons and p_i for valence band holes are equal and can be approximated by the following equation [6, 19]:

$$n_i = p_i \approx 2.5 \times 10^{19} e^{\left(\frac{-E_g}{2kT}\right)} \text{cm}^{-3} \text{ (near } 25^\circ \text{C)}. \quad (2.31)$$

Extrinsic semiconductors are created by doping, i.e. substitution of acceptor or donor atoms into the semiconductor lattice. Doping with donor atoms (e.g. the introduction of a group V element (e.g. phosphorus) into a group IV element semiconductor such as Si) produces *n*-type semiconductors (Fig. 2.9b) by creating an energy level E_d just below the conduction band. Most of the donor atoms are ionised at room temperature, each producing a conduction band electron and leaving behind an isolated positive site at the donor atom. Hence, most of the electrical conductivity is due to the conduction band electrons, which are termed majority carriers. Holes are the minority carriers and account for only a small contribution to the conductivity. The opposite situation arises for *p*-type materials (Fig. 2.9c) (created by doping with acceptor atoms, e.g. introduction of a group III element such as Al into Si), where acceptor levels E_a just above the valence band are created. This results in the formation of mobile holes in the valence band and isolated, negatively charged acceptor sites. In this case holes are majority carriers and electrons are minority carriers.

Apart from impurity insertion as a means of doping, non-stoichiometric compound semiconductors also give rise to *n*- or *p*-type behaviour [20]. This phenomenon is exemplified in Sect. 2.3.3.3 using TiO_2 and NiO electrodes.

The Fermi level E_F is defined as the energy at which the probability of electron occupation is 1/2 [20]. In an intrinsic semiconductor at room temperature, E_F lies at the midpoint of the band gap (Fig. 2.9a). Conversely, in extrinsic semiconductors the location of E_F is dependent on the doping level [6]: for moderately to heavily doped *n*-type solids E_F lies slightly below the conduction band edge, and for moderately to heavily doped *p*-type materials the Fermi level is located just above the valence band edge. Thermodynamically, the Fermi level of a phase α can be interpreted as the electrochemical potential of an electron in α [6] [compare Eq. (A.2)], i.e. the Fermi level corresponds to the electrochemical potential of the electron in the solid [21]:

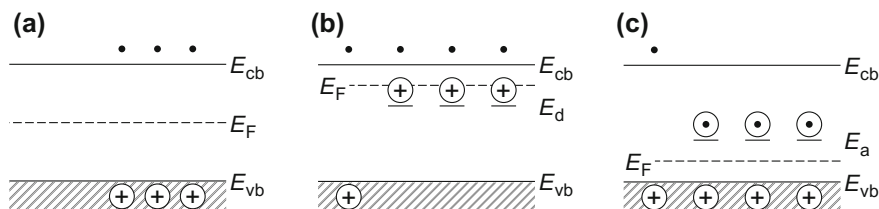


Fig. 2.9 Schematic depictions of the energy levels (bands) in **a** intrinsic, **b** *n*-type, and **c** *p*-type semiconductor materials. Adapted from Refs. [6, 18]

$$E_F^\alpha = \tilde{\mu}_e^\alpha = \mu_e^\alpha - e\phi^\alpha (\text{in eV}). \quad (2.32)$$

The absolute value of E_F depends on the reference state: using zero for a free electron in vacuum, Fermi levels in semiconductors and metals can be determined by measuring the work function (conduction band edge energies can be determined from the electron affinity) [6]. As in metal electrodes, the Fermi level in semiconductors changes upon application of a potential [18].

2.3.2 The Semiconductor/Solution Interface

Consider the formation of a junction that forms between a(n idealised) semiconductor surface and a solution containing a redox-couple Ox/Red upon immersion of the semiconductor into the liquid redox-electrolyte. When thermodynamic equilibrium is attained, the electrochemical potentials $\tilde{\mu}_e$ must be equal in both phases. The redox potential of the electrolyte solution, given by the Nernst equation Eq. (2.7), can be identified with the Fermi level in the electrolyte [20].² In other words, the Fermi levels equilibrate under transfer of charges between the semiconductor and the solution phase [6]. If E_F lies above the solution potential, as is typically the case for *n*-type materials at open-circuit [18], electrons will transfer from the semiconductor to the solution, with the former becoming positively charged (depleted) and the latter carrying a negative charge (Fig. 2.10a). Charge-transfer equilibration in a doped semiconductor removes carriers from the most easily ionisable sites, i.e. dopant atoms [22]. In principle, it could also be the electrochemical potential of the solution that shifts during equilibration. However, in accordance with double layer theory, the side of the interface containing the lower concentration of charge carriers experiences the greater change in potential upon a potential modulation [21], and even with dilute concentrations of redox species (< 10 μM), the number of available states per unit energy in the solution far exceeds the number present in a semiconductor [23]. Hence, there is little negative movement of the electrochemical potential of the solution during equilibration upon formation of a semiconductor/liquid junction, and the Fermi level for both phases in the equilibrium is principally equal to the initial value of the solution redox potential [23].

Unlike in metals, the excess charge in the semiconductor after equilibration does not reside on the surface; it is instead distributed across the so-called *space-charge* region. This region is comparable to the diffuse double layer found at the electrode interface in solution (see Sect. 2.2.3) and extends well into the material, with nominal dimensions of the so-called depletion layer width W typically being in the

²In electrochemistry the standard hydrogen electrode is traditionally used as reference scale, whereas it is common in solid-state physics to use the electron energy in vacuum. The SHE electrode lies at approximately -4.5 eV vs. the vacuum level [20].

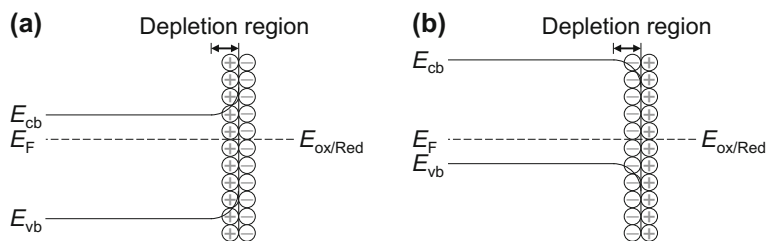


Fig. 2.10 The semiconductor solution interface at open-circuit for **a** an *n*-type semiconductor and **b** a *p*-type semiconductor. Adapted from Ref. [18]

range of 10–1000 nm [20]. The corresponding, adjacent Helmholtz layer width, in contrast, is normally in the range of 0.4–0.6 nm. Therefore, assuming a simple model in which the space-charge region and the Helmholtz layer comprise two capacitors in series, the space-charge region usually determines the total capacity of the interface (in a metal, in contrast, the high electronic conductivity cannot support an electric field within the material; almost all the potential drop at the interface occurs within the Helmholtz layer) [20].

The electric field in the space-charge region affects the electrochemical potentials of electrons, i.e. their local energy, and the band energies are different to the field free semiconductor bulk [6]. The band positions at the interface do not change, as almost the entire potential drop between bulk semiconductor and solution occurs across the space-charge region, rather than at the semiconductor/solution interface. The number of charges that need to be transferred is generally far larger than the number of dopant atoms that are present in one atomic layer of the solid [22] (the implication being that the above-mentioned depletion width W is a function of the donor density, N_D).

A positive charge in the space-charge region causes the band energies to become more negative with increasing distance from the surface, until they remain flat in the field free bulk. This effect is termed *band-bending*. In the example of Fig. 2.10a, the bands bend upward with respect to the energy levels in the bulk semiconductor. The space-charge region in this case is also referred to as depletion layer, as the majority charge carriers of the semiconductor have been removed from this region [18]. Consistent with the electric field in the depletion layer, excess electrons would move into the semiconductor bulk and holes would migrate towards the surface. The opposite situation arises for *p*-type materials (Fig. 2.10b), where, at open-circuit, the Fermi level is generally lower than the redox potential of the electrolyte [18]. Hence, a negative charge is associated with the space-charge region and the bands bend downward, again forming a depletion layer.

If the Fermi level of the semiconductor and the redox potential of the solution have the same energy even *before* equilibration, there is no net transfer of charge and hence no band-bending [18]. The corresponding potential is termed the flat-band potential E_{fb} . No electric field and no space-charge region exist at E_{fb} . It is worth noting that electrostatic adjustments analogous to the band-bending

phenomena at the semiconductor/electrolyte interface described in this section occur whenever two dissimilar phases are in contact, e.g. in the case of semiconductor/metal or semiconductor/gas junctions [20].

2.3.3 *The Semiconductor/Electrolyte Junction Under Applied Bias*

2.3.3.1 **Qualitative Description of the Semiconductor/Liquid Interface Under Applied Bias**

Further to the properties of semiconductor/electrolyte junctions at open circuit, interesting effects arise upon application of an electrostatic potential. As mentioned in the previous section, applying a potential shifts the Fermi level of the semiconductor electrode, similarly to metallic electrodes. The band edges in the interior of the semiconductor (i.e. the bulk, away from the space-charge region) undergo a concomitant change in energy [18].

Assuming that all of the applied bias drops across the space-charge region (compare Sect. 2.3.2), only the majority carrier population within the semiconductor at the surface is modulated, not the potential drop across the Helmholtz layer [20]. This means that the band edge positions at the interface (not the Fermi level) are pinned and thus *not* affected by changes in band energies occurring in the field free semiconductor bulk and the space-charge region upon application of a potential. Consequently, the magnitude and direction of band-bending change with applied potential [18].

One can now distinguish between three different scenarios that are all depicted, schematically, in Fig. 2.11.³ In case of an *n*-type semiconductor: (i) the applied potential E is equal to the flat-band potential E_{fb} . In this case, band-bending does not occur, as outlined in the previous section, because there is no net transfer of charge at equilibrium and no space-charge region exists. (ii) Formation of an *accumulation* layer. Applying a potential $E < E_{fb}$ to an *n*-type semiconductor shifts its Fermi level upwards, causing the bands to bend downward, since the band edge positions at the interface remain fixed (Fig. 2.11b). An excess of majority carriers in the space charge region exists and the material becomes increasingly conductive [18]. The surface becomes degenerate when the Fermi level contacts the conduction band edge and the semiconductor then exhibits metal-like electrochemistry [24]. Making the potential even more negative will cause a potential difference to develop across the Helmholtz layer instead of the electrode. (iii) When $E > E_{fb}$ (Fig. 2.11c), a depletion layer is formed, having properties described in Sect. 2.3.2. *p*-Type materials show equivalent behaviour (Fig. 2.11d-f): with holes being the

³Formation of ‘deep depletion’ and ‘inversion’ layers is not discussed herein as these are not relevant to this thesis.

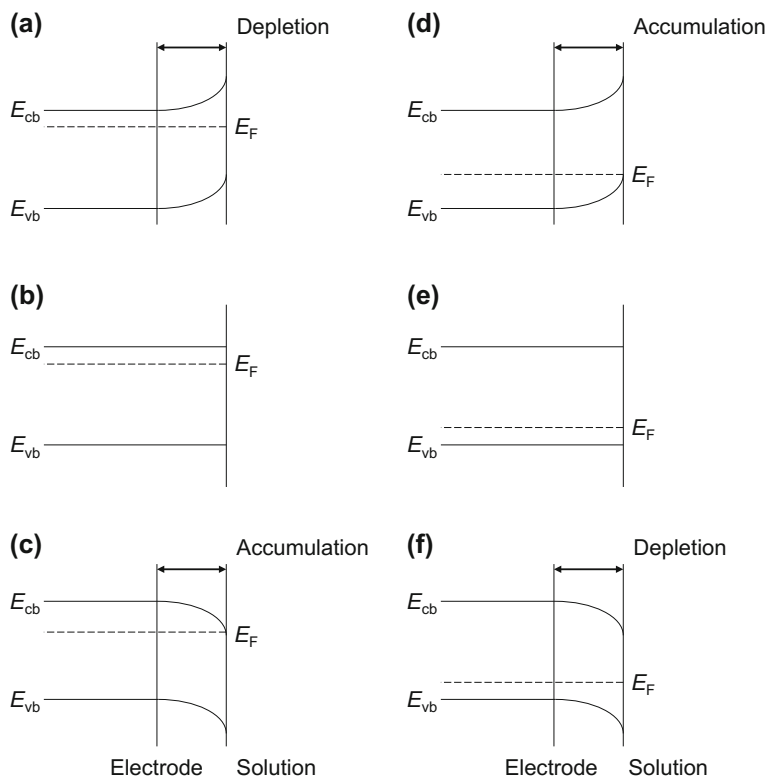


Fig. 2.11 Schematic illustration of the semiconductor/electrolyte interface under applied bias, in the case of *n*-type semiconductors (a–c), and for *p*-type materials (d–f). $E > E_{fb}$ (a), (d); $E = E_{fb}$ (b), (e); $E < E_{fb}$ (c), (f). Adapted from Ref. [18]

majority carriers and the Fermi level located close to the valence band, a depletion region arises at potentials negative of E_{fb} and accumulation occurs when the potential is increased with respect to the flat-band potential.

2.3.3.2 Current Potential Curves of Semiconductor Electrodes in the Dark

In contrast to conducting electrodes such as PGE, electron transfer processes at the semiconductor/electrolyte interface strongly depend on the density of available carriers at the semiconductor surface. In the dark, electron transfer is usually dominated by the majority carriers. Moderately doped *n*-type materials, for instance, can effect reduction reactions but not oxidations [6]. In analogy to Eq. (2.20), the cathodic current corresponding to the reduction of a species Ox by an *n*-type semiconductor is given by the following equation:

$$i_c = -zFAk'_c n_{sc} [\text{Ox}], \quad (2.33)$$

where n_{sc} (cm^{-3}) is the concentration of electrons at the interface and k'_c represents the heterogeneous electron transfer rate constant, the units of which are $\text{cm}^4 \text{s}^{-1}$, different from a metal electrode, where the high carrier density is included in the rate constant (k_c in $\text{cm} \text{s}^{-1}$) [6]. In other words, the second order kinetics stemming from the two multiplied concentration terms in Eq. (2.33), n_{sc} and $[\text{Ox}]$ (each comprising a cm^{-3} term), require the $\text{cm}^4 \text{s}^{-1}$ dimensions of k'_c [20].

p -Type materials, in turn, generally able to effect oxidation processes in the dark but not reductions, show the following anodic current for the oxidation of a species Red in the redox electrolyte:

$$i_a = zFAk'_a p_{sc} [\text{red}], \quad (2.34)$$

where k'_a is the heterogeneous rate constant for oxidation (of the same dimensions as k'_c) and p_{sc} represents the concentration of holes at the surface (cm^{-3}) [6]. In contrast to conducting electrodes, both the rate constants k'_c and k'_a in Eqs. (2.33) and (2.34), and the surface concentrations (n_{sc} and p_{sc} , respectively) depend on the applied potential. The concentrations of majority carriers on the surface respond to potential changes by

$$n_{sc} = N_D e^{\left[\frac{-F(E - E_{fb})}{RT} \right]} \quad (2.35)$$

and

$$p_{sc} = N_A e^{\left[\frac{F(E - E_{fb})}{RT} \right]}. \quad (2.36)$$

In Eqs. (2.35) and (2.36), N_D and N_A represent the donor and acceptor densities, respectively, and $(E - E_{fb})$ is the amount of band-bending (also known as ΔE_{sc}) [20]. The potential dependences of k'_c and k'_a in Eqs. (2.33) and (2.34) are a result of the potential drop $\Delta E'$ across the Helmholtz layer at the semiconductor-electrolyte interface [6]. They follow Butler-Volmer kinetics and can be described by Eqs. (2.18) and (2.19), using $\Delta E'$ instead of E .

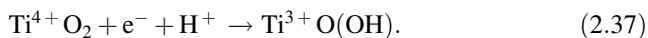
Equations (2.35) and (2.36) allow the quantitative interpretation of the phenomena described in Sect. 2.3.3.1. Under conditions of depletion, i.e. at potentials positive of E_{fb} in n -type semiconductors and negative of E_{fb} in p -type materials, the majority carrier concentrations in each case are lower than the respective density of dopants ($n_{sc} < N_D$ and $p_{sc} < N_A$). Because the potential drop under depletion is distributed across the space-charge region and not the Helmholtz layer, the respective current voltage curves are governed by the carrier concentrations rather than k'_c and k'_a [6]. The currents resulting from applying such a so-called reverse bias are potential independent and remain low, the reason being the lack of minority

carriers in the dark [18, 20].⁴ Under accumulation (forward bias), i.e. $E < E_{\text{fb}}$ in n -type semiconductors and $E > E_{\text{fb}}$ in p -type electrodes, the respective currents are exponentially dependent on the potential until the surface becomes degenerate, when the behaviour becomes similar to that of a metallic electrode [18]. The previous section outlined that a further increase in driving force will cause the potential difference to distribute across the Helmholtz layer rather than the electrode and this can now be rationalised as the further change in potential no longer affecting n_{sc} or p_{sc} significantly, but instead causing changes to $\Delta E'$ and hence k'_c and k'_a (experimentally verifiable by transfer coefficients α different to those arising under depletion) [6].

2.3.3.3 Case Studies: TiO₂ and NiO

This section will reinforce the properties of semiconductor liquid junctions established in the previous two sections by looking at two specific examples: the n -type semiconductor TiO₂ and the p -type material NiO. Both are non-stoichiometric materials (see Sect. 2.3.1) and wide band gap semiconductors, transparent to visible light ($E_g > 3.0$ eV in both materials). Figure 2.12 depicts a cyclic voltammogram of a TiO₂ film electrode.

Due to its inherent non-stoichiometry (oxygen vacancies), TiO₂ is a rather heavily doped n -type semiconductor [25]. In Fig. 2.12 there is virtually no current at potentials above -0.4 V, in agreement with the theoretical assessment in Sect. 2.3.3.2: the TiO₂ flat-band potential lies at approximately -0.5 V vs. SHE at pH 6.0 (measured in Sect. 4.2.3.1) and a depletion layer is formed upon scanning in anodic direction. When E_{fb} is approached in cathodic direction, (trap levels below the conduction band are being populated [26] before) conduction band states become occupied and the current increases exponentially in agreement with Eq. (2.35), showing that the carrier concentration n_s is the dominating factor. In chemical terms, the signature ‘trumpet shape’ of the voltammogram arises from the reversible reduction of Ti(IV) surface centres to Ti(III), which is accompanied by uptake of one proton per site and can be described by the following equation [27]:

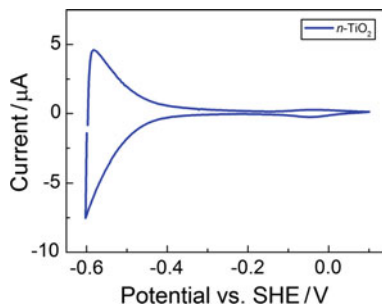


These Ti(III) sites are reoxidised when the potential is raised. The minor peak at ca. -0.1 V corresponds to the population of surface trap states [28, 29] lying about 0.5 eV below the conduction band edge [30].

Figure 2.13 shows a cyclic voltammogram of NiO, which, upon calcination in air, forms a Ni_{1-x}O non-stoichiometry. As expected for a p -type semiconductor, the current-voltage curve displays opposite behaviour compared to n -TiO₂. The material is essentially an insulator at cathodic potentials and conductivity only

⁴Dark currents will arise at very high overpotentials due to breakdown phenomena.

Fig. 2.12 Cyclic voltammogram of a TiO₂ electrode. Conditions: 0.2 M MES buffer (pH 6.0); 20 °C; scan rate: 10 mV s⁻¹; N₂ atmosphere



commences at positive potentials (the flat-band potential of NiO is approximately 0.61 V vs. SHE at pH 6.0 [31]). The increase in current is attributed to the oxidation of surface Ni(II) to Ni(III), coupled with desorption of protons from the surface. It is the presence of these Ni(III) surface sites that is believed to be responsible for the conductivity of NiO [32]. Whereas electron transport in TiO₂ is predominantly conduction band mediated [32], hole conduction in NiO is mainly occurring at the mesoporous NiO/electrolyte interface, most likely by hopping of charges, with holes being present as oxidised Ni(III) atoms [33].

2.3.4 Photoeffects at the Semiconductor/Electrolyte Interface

We now turn our attention to the semiconductor/liquid junction under illumination (i.e. we finally turn the light on⁵). Upon irradiation of sufficient energy to overcome E_g , electrons can be promoted from the semiconductor valence band into the conduction band. If this process occurs within the semiconductor bulk, recombination under release of heat is likely to prevail [18]. However, if excitation takes place in the space-charge region, the electric field can effect *charge-separation*. Consider an *n*-type semiconductor at potentials positive of E_{fb} , where a depletion layer exists and the bands bend upwards (Fig. 2.11a). Light-excitation will cause the excited conduction band electron to move into the semiconductor bulk; holes, in contrast, will migrate to the interface, where they are available for oxidative chemistry. Hence, *n*-type semiconductors behave as dark cathodes and photoanodes.

Figure 2.14 illustrates this behaviour by showing an idealised current-voltage curve of an *n*-type semiconductor both in the dark (a) and under irradiation (b). In the dark, a reductive current arises at potentials below E_{fb} , increasing exponentially with driving force as established in Sect. 2.3.3. An accumulation layer forms and the electrode will display metallic-like behaviour once the surface becomes

⁵The author apologises for this pun.

Fig. 2.13 Cyclic voltammogram of a NiO electrode. Conditions: 0.2 M MES buffer (pH 6.0); 20 °C; scan rate: 30 mV s⁻¹; N₂ atmosphere

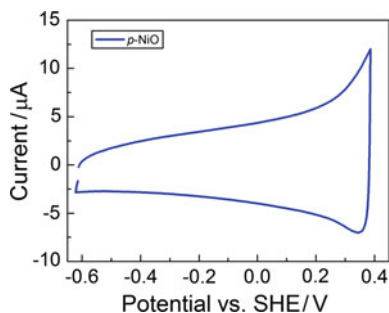
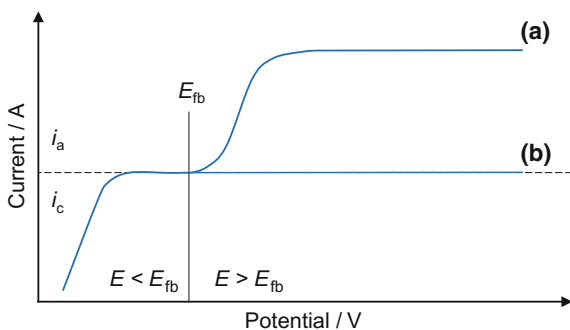


Fig. 2.14 Current-voltage curve showing the ideal behaviour of an *n*-type semiconductor in the dark (a) and under irradiation (b). Adapted from Ref. [18]



degenerate. At potentials positive of the flat-band potential, no oxidative current can be observed due to the formation of a depletion layer.

Upon irradiation, the behaviour at potentials negative of E_{fb} is virtually indistinguishable from the dark-current. Photoeffects are generally not observed at *n*-type materials under accumulation [6]; with the Fermi level being very close, energetically, to the conduction band, no significant current enhancement can be expected under irradiation. In a doped semiconductor, photoeffects are greatest when the minority carriers dominate the electrode response, due to the enormous disparity in the concentrations of the two types of charge carriers [21]. At potentials positive of E_{fb} , the electric field of the space-charge region in the depletion layer assists charge-separation and a photocurrent is observed. Here, the minority carriers (holes) are driving the oxidative chemistry at the semiconductor/electrolyte junction. It is important to note that the photooxidation of the species Red in the redox-electrolyte will occur at potentials less than those required at an inert metal electrode in the dark [6], due to the additional driving force provided by illumination with light energy. The notion of apparent *underpotentials* in photoelectrochemical reactions is of particular importance for Chap. 5 of this thesis. Analogous concepts apply to *p*-type materials, which act as dark anodes and photocathodes.

In quantitative terms, the current-potential curve in Fig. 2.14 can be interpreted by simply adding the photocurrent i_{ph} (minority carrier component) to the dark current component (due to majority carriers) given in Eqs. (2.33) and (2.34),

respectively, noting that the two components are of different sign [20], i.e. they represent opposite directions of flow. Assuming the absence of any recombination in the space-charge layer, that all holes generated within or reaching the depletion layer cause photocurrent (which is not true for potentials close to E_{fb}), and, further, the absence of mass transfer or kinetic limitations, the photocurrent density j_{ph} can be expressed by the Gärtner equation [34] as the product of the incident photon flux I_0 (photons per second per area) and the effective quantum yield Φ [21]:

$$j_{ph} = I_0 \Phi = 1 - \frac{e^{-\alpha W}}{1 + \alpha L}. \quad (2.38)$$

In Eq. (2.38), j_{ph} depends on the absorption coefficient α , the minority carrier diffusion length L (L_p for holes and L_n for electrons), and the width of the depletion layer, W , introduced in Sect. 2.3.2. In regards to the example in Fig. 2.14 of an n -type semiconductor under illumination, the fact that Eq. (2.33) is offset by Eq. (2.38) can be rationalised with the plateau photocurrent being proportional to the photon flux [20]. As long as the depletion layer thickness exceeds the depth of charge carrier generation, the photocurrent quantum efficiencies are independent of the applied potential and the current plateaus. The space-charge layer thickness decreases when the applied potential approaches E_{fb} and recombination rates increase because electrons and holes are no longer being separated by the electric field. The effect is a sharp decrease in photocurrent, which merges with the dark current near E_{fb} [21].

2.3.5 Measurement of the Flat-Band Potential

The flat-band potential is one of the most important parameters in a semiconductor electrode; the concept of E_{fb} is central to Chap. 4 of this thesis and also plays an important role in Chaps. 5 and 6. Knowing E_{fb} , the position of the band edges on the electrochemical scale, the direction of band-bending and, in favourable cases, its magnitude can be derived [21]. The flat-band potential of a semiconductor can be determined by several experimental techniques, most notably by measuring the photocurrent onset potential, the open-circuit photopotential as a function of radiation intensity, or the capacitance of the space-charge region. This section will briefly review the three different methods, emphasising the role of capacitance measurements.

2.3.5.1 Photocurrent Onset Potential

As established in the previous section using the example of an n -type semiconductor, the photocurrent diminishes as E_{fb} is approached. Its total disappearance at the photocurrent onset potential E_{on} should coincide with the flat-band potential

[25, 35].⁶ However, it should be noted that the absolute values obtained by this method are often shifted (anodically in the case of n -type semiconductors and cathodically for p -type materials) as recombination becomes practically complete already at potentials with ca. 0.1–0.3 V from E_{fb} [25]. While E_{on} can be measured relatively easily, the large uncertainty in the measurement and the arbitrariness in deciding at what potentials the photocurrent is perceptible above the dark current constitute significant disadvantages [21].

2.3.5.2 Open-Circuit Photovoltage

Another simple method to determine E_{fb} is to measure the open-circuit photopotential E_{oc} of the electrochemical cell under radiation of varying intensity [18]. Consider again an n -type semiconductor in contact with a redox-electrolyte. As described in Sect. 2.3.2, the two phases will equilibrate at open-circuit under the formation of a depletion layer in the semiconductor. Upon irradiation with light energy $h\nu > E_g$, photogenerated holes move to the surface (where some of them might be captured by reduced molecules in solution) and excited electrons move into the conduction band bulk where they, once having left the depletion layer, have no possible exit [21]. Consequently, the Fermi level⁷ increases, reflecting the change in conduction band occupancy; it is approaching but not exceeding E_{fb} . Hence, under sufficiently high light intensity, E_{oc} becomes constant, attaining a limiting plateau at E_{fb} [18, 25]. Similar to measuring the photocurrent onset potential, a weakness of this method is that surface recombination will decrease the open circuit photovoltage, meaning the experimentally determined flat-band potential is shifted from its true value [21].

2.3.5.3 The Mott-Schottky Plot

The third and most important commonly employed method to determine E_{fb} of a semiconductor is the Mott-Schottky measurement. One of its greatest advantages is that it can be performed in the absence of light, a factor that is of particular importance when the semiconductor of interest undergoes photocorrosion processes that alter its surface. Mott-Schottky measurements are based on the capacitance associated with the space-charge layer.

The different regions around the semiconductor/electrolyte interface (i.e. the space-charge layer, the Helmholtz layer, and also the diffuse layer) have associated capacitances, as they are considered planes of charge separated by distance [21].

⁶More precisely, E_{fb} is the potential at which the dark current and the current component due to illumination are equal.

⁷More precisely, it is now a quasi-Fermi level, since the system is no longer in thermodynamic equilibrium.

The three capacitances are in series with the smallest one dominating the overall capacitance C_{dl} (dl = double layer), as the latter depends on the reciprocals of the separate contributions:

$$\frac{1}{C_{dl}} = \frac{1}{C_{sc}} + \frac{1}{C_H} + \frac{1}{C_{diff}}. \quad (2.39)$$

We already established in Sect. 2.3.2 that the capacitance of the space-charge layer usually dominates over the capacity of the Helmholtz layer. The capacitance of the diffuse layer C_{diff} , omitted in Sect. 2.3.2, is generally so large that it can be completely neglected [21]. Thus, the capacitive properties of the space-charge region govern the total double layer capacitance C_{dl} . Under the conditions of a depletion layer, C_{sc} varies with the width of the space-charge region, which in turn is a function of the potential relative to E_{fb} . The Mott-Schottky equation (derived in Appendix B) incorporates these factors into one equation [21]:

$$C_{sc}^{-2} = \frac{2}{\varepsilon\varepsilon_0e_0N_D} \left(E - E_{fb} - \frac{k_B T}{e_0} \right). \quad (2.40)$$

In Eq. (2.40), ε is the dielectric constant in the direction normal to the surface, ε_0 is the permittivity of free space, e_0 is the electron charge, and the other parameters are as defined earlier. In the depletion region, plotting the reciprocal square of the capacitance against the applied potential should yield a straight line, from which the doping level (slope) and the flat-band potential (intercept) can be determined.

Building upon the excellent introduction by Fisher [7], I will now briefly describe how to experimentally measure the capacitance of the space-charge region, and the capacitance of the electrode/solution interface in general (i.e. including electrodes of metallic conductivity). The capacitance was defined in Eq. (2.4) as the ratio q/E , i.e. the charge ‘stored’ on the capacitor plates upon application of a potential difference E across them. For a simple capacitor where the plates are separated at a fixed distance, the capacitance predicted according to Eq. (2.4) is constant. In an electrochemical cell the problem is more complex as the double layer capacity depends upon the applied potential. Therefore, in electrochemical experiments the differential capacitance C_d characterises the electrode/solution interface and is the variable of interest. For a metal/solution interface with an electrolyte of constant composition, C_d is defined as [7]:

$$C_d = \left(\frac{dq}{dE} \right) = \left(\frac{\partial q^m}{\partial \Delta\phi_{m/s}} \right). \quad (2.41)$$

The differential capacitance is measured by the technique of a.c. impedance spectroscopy, where an oscillating, sinusoidal potential $E(t)$ is applied across the cell:

$$E(t) = E_m \sin(\omega t). \quad (2.42)$$

In Eq. (2.42), E_m represents the maximum amplitude and ω is the angular frequency in rad s^{-1} ($\omega = 2\pi\nu$, with ν being the (ordinary) frequency in Hz). At first, the response of a simple capacitor to an a.c. voltage will be assessed. This will provide the basis for interpreting real electrode/solution interfaces [7]. No Faradaic d.c. current will pass if the electrode potential is insufficient to cause any electrolysis, but the sinusoidal potential in Eq. (2.42) induces an a.c. capacitive current by

$$i(t) = i_m \sin(\omega t + \theta), \quad (2.43)$$

where i_m denotes the maximum current amplitude and θ characterises any phase difference between the applied potential and the detected current. Using Eq. (2.6) that relates current and capacitance, the differential capacitance C_d can be substituted into Eq. (2.43):

$$i(t) = C_d \frac{dE}{dt} = C_d \frac{d(E_m \sin(\omega t))}{dt} = C_d(\omega E_m \cos(\omega t)) = C_d \left(\omega E_m \sin\left(\omega t + \frac{\pi}{2}\right) \right), \quad (2.44)$$

implicating the phase difference $\theta = \pi/2$.

The *impedance* Z is often used to describe the response of an electrical circuit to an applied a.c. voltage:

$$Z(\omega) = \frac{E(t)}{i(t)}. \quad (2.45)$$

Being similar to Ohm's law (where the resistance $R = E/i$), the impedance provides a measure of how a current is 'impeded' by the circuit, i.e. it provides a generalisation of the idea of the 'resistance' of a circuit [7]. As established in Eq. (2.44), for a capacitor the phase difference between current and voltage is $\pi/2$. The conduction is indirect and results from the attraction or repulsion of electrons from the plates as their potential changes [7]. Conversely, for a single resistance the voltage and current are in phase ($\theta = 0$), since charge can flow directly through a resistor. For a real, complex circuit the phase difference can take any value and also change with frequency. The impedance as a function of frequency can then be described, mathematically, by

$$Z(\omega) = Z' \sin(\omega t) - Z'' \cos(\omega t), \quad (2.46)$$

where Z' represents the 'real' component of the impedance ('in-phase') and $-Z''$ the imaginary part ('out-of-phase'). The impedance can be conveniently plotted as $-Z''$ (ordinate) versus Z' (abscissa), a form also known as Nyquist plot (typically, Z at each frequency is plotted as a point with coordinates $[Z', -Z'']$, and the resulting

vector from the origin of the coordinate system to this point represents the impedance, having a magnitude equal to the length of the vector and a phase difference of θ) [7]. In the example of a simple capacitor, the real and imaginary parts of the impedance can be written as

$$Z' = 0 \quad -Z'' = \frac{1}{\omega C_d}. \quad (2.47)$$

This general description of the basic principles that underlie a.c. impedance spectroscopy allows the interpretation of the more complex impedance response of an electrochemical cell. Consider an *n*-type semiconductor/electrolyte junction in the depletion region, where the semiconductor is employed as working electrode in a conventional three-electrode cell and no electrolysis occurs. The aim is to measure the capacitance of the space-charge layer C_{sc} , so as to be able to determine E_{fb} .

For this cell configuration, a simple *equivalent circuit* can be drawn that represents the different cell components. The circuit contains a capacitor that corresponds to the double layer at the electrode according to Eq. (2.39) (in this case the desired variable C_{sc}), connected in series with a resistor that accounts for the solution resistance (Fig. 2.15a). The real and imaginary components of the impedance are:

$$Z' = R_s \quad -Z'' = \frac{1}{\omega C_{sc}}, \quad (2.48)$$

and the capacitance of the space-charge layer can be calculated from the imaginary component of the impedance [18, 25]. The Nyquist plot corresponding to this circuit consists of a vertical line offset from the Z'' axis by the solution resistance R_s (Fig. 2.15b).

Experimentally, modern configurations employ an electrochemical cell coupled to a frequency response analyser, allowing impedance plots to be generated over frequencies in the range of 10^{-2} – 10^5 Hz [7]. The potential dependence of the

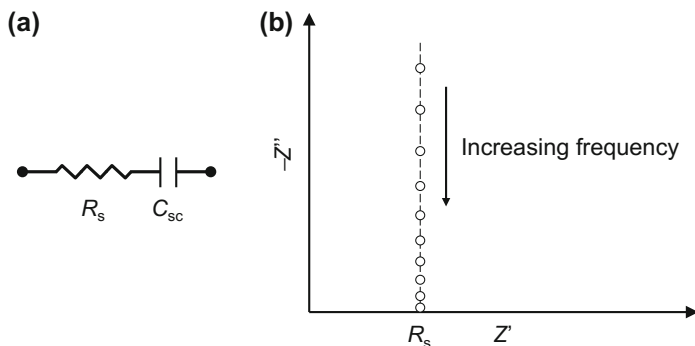


Fig. 2.15 Equivalent circuit (a) and Nyquist plot (b) for the semiconductor solution interface

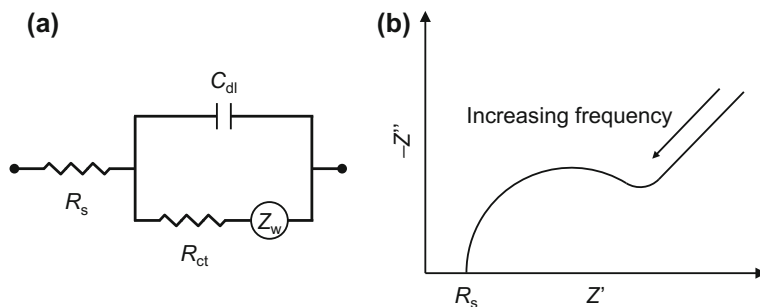


Fig. 2.16 **a** Randles circuit and **b** corresponding Nyquist plot

capacitance can be measured at constant, set frequencies, or, alternatively, the impedance can be recorded over a range of frequencies at different potentials. In the latter case, the capacitance can then be calculated at selected frequencies for each potential, or the equivalent circuit model can be used to fit the experimental data, automatically generating the capacitance values at different frequencies [18]. In this type of analysis, it is common to plot the impedance components against the frequency domain in what is known as a ‘Bode plot’.

To give the reader a more complete picture, I will conclude this section by briefly discussing, qualitatively, the impedance of an electrochemical cell under conditions where electron transfer reactions take place. This general description is not limited to the semiconductor/electrolyte interface and also holds for conductive electrodes. Under conditions where an electrolytic reaction takes place at the electrode, the situation is more complex than in the example above and the simple equivalent circuit needs to be expanded to account for the Faradaic charge transfer reaction and also for diffusion. Figure 2.16a depicts an equivalent circuit known as ‘Randles’ circuit [36] that includes these components.

The charge-transfer resistance R_{ct} , which models Faradaic charge-transfer, is connected in series to the Warburg impedance Z_w , which measures the difficulty of mass transport of the electroactive species [37]. The double layer capacitance C_{dl} [Eq. (2.39)] is connected in parallel to these two elements, meaning the current can either pass through the capacitor, the resistive components, or both at the same time. The subset of these three components, in turn, is connected in series to the solution resistance R_s . A typical Nyquist plot corresponding to electrolytic conditions is depicted in Fig. 2.16b [7]: at high frequencies, no electrolysis takes place and the impedance plot is dominated by the solution resistance. The double layer (C_{dl}) provides a path of negligible resistance to the current. As the frequency is lowered, R_{ct} and C_{dl} will become dominating, giving rise to the characteristic semi-circular part of the plot. At even lower frequencies, significant concentration changes induced by the a.c. current become increasingly difficult to replenish by diffusion and the impedance shows a large rise, modelled by the Warburg impedance element Z_w [7].

Electrodes of porosity and rugosity give rise to a constant phase element CPE, a non-ideal capacitor that is represented by [37]

$$Z_{\text{cpe}} = \frac{1}{b(i\omega C)^\alpha}, \quad (2.49)$$

where b is a proportionality constant, i is the imaginary number, and $0 < \alpha < 1$. In real systems, the CPE is manifested by an impedance spectrum altered from the expected shape, especially in the diffusive part. Typically, $\alpha = 0.5$ for porous electrodes and 1 for a smooth electrode, with rough surfaces giving rise to values between 0.5 and 1 [37].

Before closing this section on semiconductor electrochemistry, it needs to be re-emphasised that all the phenomena discussed in Sect. 2.3 consider the idealised semiconductor/electrolyte interface. Non-idealities can arise due to a number of reasons, notably photodecomposition of the electrode in the depletion region, corrosion (generally oxide layer formation in non-oxide semiconductors [21]), or surface states [18].

2.4 Marcus Theory and Theoretical Treatment of Photoinduced Electron Transfer

Following the review of the underlying principles of PFE and semiconductor electrochemistry, this section will focus on electron transfer theory. Marcus has made seminal contributions to this area and, consequently one might say, was awarded the 1992 Nobel Prize in Chemistry “for his contributions to the theory of electron transfer reactions in chemical systems” [38]. His theories, originally developed for outer-sphere electron transfer problems, are central for understanding electron transfer in biological systems, photosynthesis in particular. Important contributions to the theory of electron transfer reactions were also made by Levich and Dogonadze [39], as well as Hush [40]. This section will briefly convey the key concepts underlying the rate constants and the activation energy requirements of electron transfer reactions (including photoinduced electron transfer), limited to those of relevance to the understanding of this thesis. Instructive, more comprehensive reviews were published by Marcus and Sutin [41–43], as well as Kavarnos [44]. This introductory section broadly follows the structure adopted by the latter.

2.4.1 The Electron Transfer Rate Constant

Consider an electron transfer reaction between a donor molecule D and an acceptor A in solution:



For electron transfer to take place, the two reactant molecules must approach each other closely, forming an *encounter complex*, where they are contained within a solvent cage. We assume the reaction is not diffusion-limited, i.e. the rate of the reaction is controlled by the rate constant of electron transfer k_{et} .

The key to understanding electron transfer reactivity lies in separating the rate-determining factors into nuclear and electronic components, i.e. nuclear motions and electronic interactions [44]. In doing so, the first-order electron transfer rate constant k_{et} can be written as [43]:

$$k_{\text{et}} = \nu_{\text{n}} \kappa_{\text{n}} \kappa_{\text{el}} , \quad (2.51)$$

where ν_{n} is the nuclear frequency, in the range of $\sim 10^{12}$ – 10^{14} s^{-1} , and κ_{n} and κ_{el} represent the nuclear and electronic factors, respectively. Both are dimensionless quantities that range from 0 to 1. The nuclear factor contains the activation energy for electron transfer:

$$\kappa_{\text{n}} = e^{\frac{-\Delta G_{\text{et}}^{\ddagger}}{RT}} . \quad (2.52)$$

Using Eqs. (2.52), (2.51) can be expanded to

$$k_{\text{et}} = \nu_{\text{n}} \kappa_{\text{el}} e^{\frac{-\Delta G_{\text{et}}^{\ddagger}}{RT}} . \quad (2.53)$$

Electronic barriers are usually neglected when applying the classical electron transfer theory of Marcus to reactions in solution, i.e. $\kappa_{\text{el}} \approx 1$ [44]. Such reactions are termed *adiabatic* (see Sect. 2.4.5.1). Quantum mechanical or nonclassical treatments also separate nuclear and electronic factors, but with more emphasis being placed on electronic barriers. The concepts in this section will be established using the classical model and, subsequently, briefly related to the semiclassical expression. First, the different components of Eq. (2.53) will be discussed in more detail.

2.4.2 The Free Energy of Activation

Assume donor and acceptor in Eq. (2.25) are in contact distance and experience a weak electronic interaction, still retaining their individuality. This corresponds to the weakly adiabatic case [44]: $\kappa_{\text{el}} \approx 1$ and the rate-determining factors are assumed to involve nuclear reorganisation. On the kinetic domain, nuclei move much slower than electrons due to their much higher mass (electrons move with frequencies on the order of $\sim 10^{15} \text{ s}^{-1}$; nuclear vibration occurs at $10^{12}\text{--}10^{14} \text{ s}^{-1}$ [44]). In line with the Born-Oppenheimer approximation, electronic and nuclear motions can be treated as separate events occurring on different timescales. According to the Franck-Condon principle, the nuclei do not have time to change either their positions or their momenta during instantaneous electron transfer and remain ‘frozen’ [41].

Importantly, in Marcus theory the encounter complex (precursor state) undergoes a change in nuclear reorganisation *before* electron transfer can take place. Once the transition state is reached, the electron is transferred under conservation of energy. Reorganisation subsequent to electron transfer would violate the first law of thermodynamics (imagine a ‘self-exchange’ reaction $\text{D} + \text{D}^+ \rightarrow \text{D}^+ + \text{D}$ where $\Delta G_{\text{et}} = 0$; without nuclear reorganisation prior to electron transfer, vibrationally excited states of $\text{D}^+ + \text{D}$ would be created before nuclear motions could take place, and their decay would release heat into the solution [44]). The required activation energy $\Delta G_{\text{et}}^\ddagger$ is reached through collisions with solvent molecules. Generally, an electron transfer transition state is determined by the bond changes that take place during its formation and the change in orientations of the surrounding solvent molecules. The free energy of activation can thus be separated into two components:

$$\Delta G_{\text{et}}^\ddagger = \Delta G_{\text{i}}^\ddagger + \Delta G_{\text{o}}^\ddagger. \quad (2.54)$$

In Eq. (2.54), the subscripts i (= inner-sphere) and o (= outer-sphere) represent, respectively, bond distortions and solvent changes in the ionic sphere that surrounds the reactants. Further, according to Marcus [45–47] the activation energy for electron transfer can be expressed as

$$\Delta G_{\text{et}}^\ddagger = \frac{(\lambda + \Delta_{\text{d}}G_{\text{et}}^0)^2}{4\lambda}, \quad (2.55)$$

where $\Delta_{\text{d}}G_{\text{et}}^0$ represents the standard free energy for the electron transfer process (where the reactants are separated by a distance d [43]) and λ denotes the reorganisation energy. This quantity can be separated into two terms:

$$\lambda = \lambda_i + \lambda_o. \quad (2.56)$$

Here, λ_i represents the *inner-sphere* reorganisation energy that accounts for the energy required to effect changes in bond lengths and angles. The *outer-sphere* reorganisation energy λ_o in turn corresponds to energy changes caused by the rearrangement of the solvent shells surrounding the reactants [44].

2.4.3 Reorganisation

Marcus derived the following equation for bond-reorganisation [41, 48]:

$$\lambda_i = \sum_j \frac{f_j^r f_j^p}{f_j^r + f_j^p} (\Delta q_j)^2, \quad (2.57)$$

where f_j^r and f_j^p are the force constants for the respective j th vibration of the reactant and product state. The fraction thus represents the reduced force constant. Δq_j denotes the change in equilibrium bond distance between the reactant and product state corresponding to the j th vibration [44]. Equation (2.57) is a summation over all vibrational modes, which are treated as harmonic oscillators [41]. In principle, using Eq. (2.57) λ_i can be determined from changes in bond lengths. However, if short-lived transients such as excited states are involved, these are often difficult to determine experimentally.

Solvent reorganisation is described by Eq. (2.58) [41], based on the fairly simple physical picture of two spherical reactants being surrounded by a cage of solvent molecules [44].

$$\lambda_o = (\Delta e_0)^2 \left(\frac{1}{2r_D} + \frac{1}{2r_A} - \frac{1}{d_{cc}} \right) \left(\frac{1}{\epsilon_{op}} - \frac{1}{\epsilon_s} \right), \quad (2.58)$$

where r_D and r_A are the (spherical) radii of the donor and acceptor species in Eq. (2.50), d_{cc} is the centre-to-centre separation distance, ϵ_{op} is the optical dielectric constant of the solvent (the square of the refractive index n), and ϵ_s corresponds to the static dielectric constant, sometimes referred to as the relative permittivity. ϵ_s varies greatly between polar and nonpolar solvents (for instance, there is a 40-fold difference between water and benzene [49]), the implication being that the reorganisation energy is greater for polar molecules, which must undergo substantial nuclear changes to adjust to a hypothetical charge in the transition state. According to Eq. (2.58), the outer-reorganisation energy also depends on the size and separation distance of the reactants. The solvent barrier is greater for small spherical molecules and increases with distance. The latter phenomenon can be rationalised by visualising the two reactants positioned at a contact distance within a nonpolar, ellipsoidal cavity that is immersed in the dielectric continuum [44]: at

small separation distances, λ_0 should be small as the reactants ‘feel’ the relatively nonpolar environment of the cavity. With increasing separation, however, the reactants become more sensitive to changes in the more polar dielectric continuum of the solvent.

2.4.4 The Normal and Inverted Regions

2.4.4.1 Implications from the Marcus Equation

Revisiting Eq. (2.55), we note the quadratic dependence between driving force and activation energy. Substituting Eq. (2.55) into Eq. (2.53) yields a direct link between the free energy of the electron transfer reaction and the kinetic rate constant. With $\kappa_{el} \approx 1$ (Sect. 2.4.1),

$$k_{et} = v_n e^{-\frac{(\lambda + \Delta_d G_{et}^0)^2}{4\lambda RT}}. \quad (2.59)$$

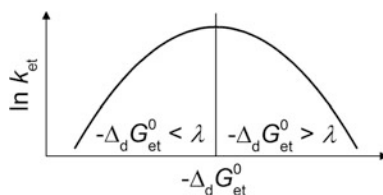
It is well-known that the rate of a chemical reaction generally tends to increase with increasing driving force. The same holds, *initially*, for Eq. (2.59). However, this equation also predicts a maximum rate constant, following which a further increase in exergonicity will cause a *decrease* in rate. This behaviour is schematically illustrated in Fig. 2.17.

In agreement with Fig. 2.17, two kinetic domains can be distinguished. First, in the *normal region*, where $-\Delta_d G_{et}^0 < \lambda$, the electron transfer rate k_{et} increases with increasing driving force until a maximum is reached when $-\Delta_d G_{et}^0 = \lambda$. In this case, $\kappa_n = 1$ and the reaction is termed ‘barrierless’. Moving further along the abscissa in Fig. 2.17, $-\Delta_d G_{et}^0$ will exceed λ and we enter the Marcus *inverted region*. Here, k_{et} decreases with increasing $\Delta_d G_{et}^0$.

2.4.4.2 Pictorial Representations of Electron Transfer Processes

The three different scenarios of electron transfer occurring in the normal region, being barrierless, or taking place in the inverted regime can be visualised graphically. In pictorial representations, electron transfer processes are typically

Fig. 2.17 The relationship between rate constant and driving force in electron transfer reactions predicted by Eq. (2.59)



represented using potential energy surfaces, which are topological depictions of chemical reactions [44]. The energy of the system is plotted as a function of the reaction coordinate, which is often represented as nuclear motion. To reduce complexity, the resulting multidimensional ‘hypersurfaces’ are commonly reduced to two-dimensions: often, one particular nuclear deformation can be used to describe a reaction or, in more complicated cases, a mean or composite of all nuclear changes can be represented as a moving point [44]. As noted in Sect. 2.4.3, nuclear vibrations in classical Marcus theory are treated as harmonic oscillators, the behaviour of which is described by symmetrical one-dimensional parabolic functions. Thus, intersecting parabolic curves are used as idealised energy curves to describe the course of electron transfer from the *precursor state*, immediately prior to electron transfer, to the *successor state* directly following electron transfer [44]. In other words, each of these two supermolecules is described by their own potential energy curve.

Figure 2.18a shows two intersecting parabolic curves representing electron transfer in the normal region. It is worth noting here that the Butler-Volmer model for interfacial electron transfer described in Sect. 2.2.5 is in agreement with the Marcus model, as long as overpotentials are small, i.e. for $\eta < \lambda$ in the normal region [4, 50, 51]. Barrierless electron transfer occurring at maximum rate is depicted in Fig. 2.18b, while Fig. 2.18c depicts electron transfer in the inverted region.

Experimentally verifying Marcus’ prediction of the inverted region proved to be daunting [44]. For electron transfer experiments in solution, experimental plots of $\ln k_{\text{et}}$ vs. $\Delta_{\text{d}}G_{\text{et}}^0$ often show a plateau, one of the reasons being that diffusion becomes rate-limiting at high driving force, ‘masking’ the electron transfer rate constant k_{et} (second order rate constants for diffusion are on the order of $10^9 \text{ M}^{-1} \text{ s}^{-1}$ [44]). Concluding evidence for the existence of the inverted region was provided by Miller et al. in 1984 [52], almost three decades after Marcus’ theoretical prediction. The authors employed pulse radiolysis to study intramolecular electron transfer from a 4-biphenyl electron donor linked to acceptors of different energy via a rigid steroid bridge (Fig. 2.19).

The possibility of exploiting the stark differences in electron transfer kinetics depending upon whether a reaction occurs in the normal or the inverted region sounds attractive, not only from a hypothetical perspective: with respect to light-driven electron transfer reactions, particularly those involved in driving the thermodynamically uphill reactions of artificial photosynthesis, it would be advantageous if forward electron transfer rates were occurring at maximum rate (i.e. being barrierless), but destructive recombination being kinetically retarded through positioning in the Marcus inverted regime. For reactions in solution, control can in principle be exerted via modifications to the polarity of the solvent, provided λ_0 dominates the reorganisation energy [44].⁸

⁸The reader needs to bear in mind, however, that artificial photosynthesis will ultimately have to be carried out in water.

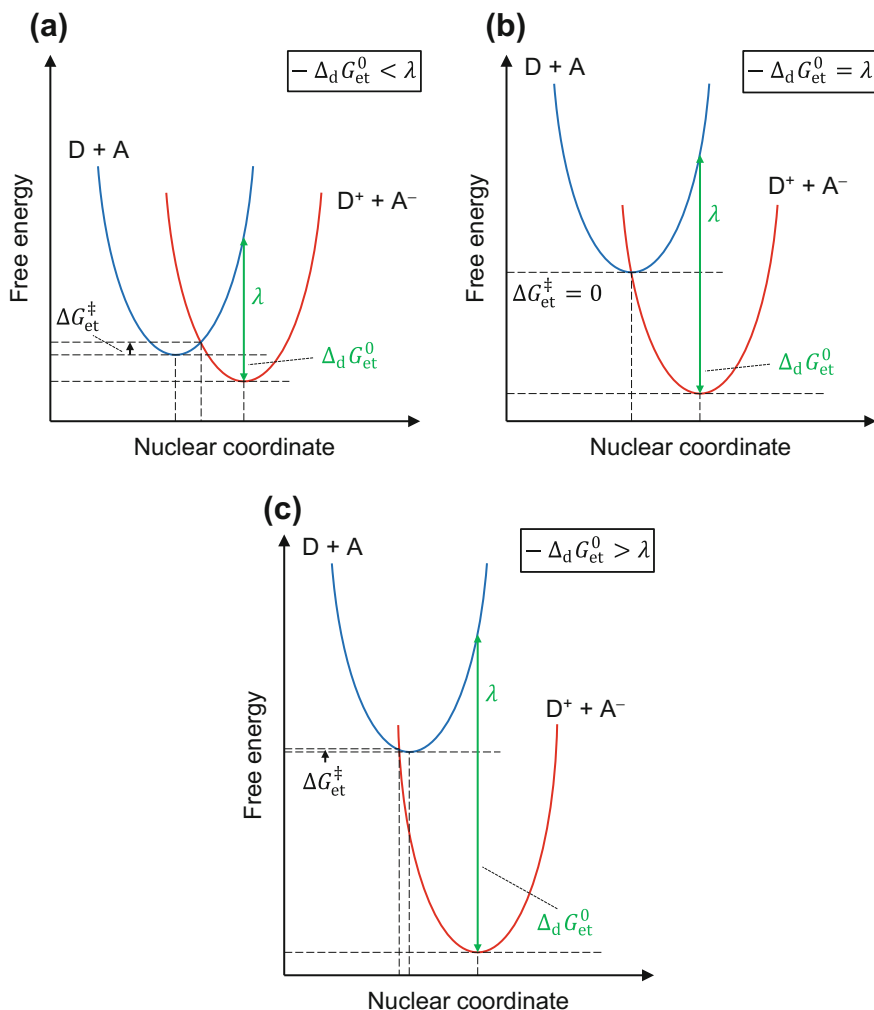
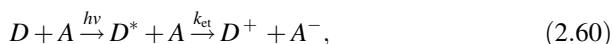
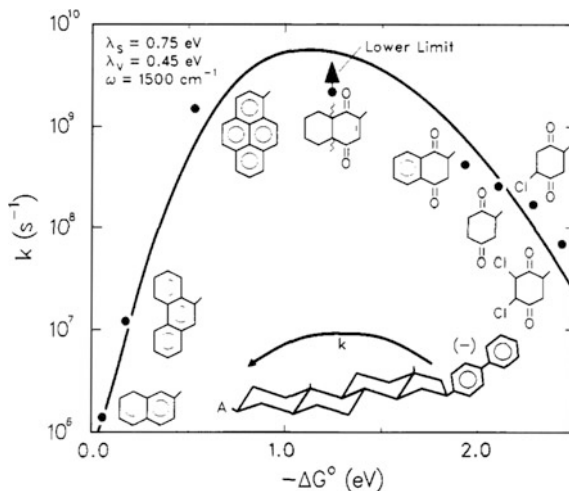


Fig. 2.18 Potential energy curves depicting the electron transfer reaction between D and A according to Eq. (2.50). The surface representing the reactants is shown in *blue*; the product curve is depicted in *red*. **a** Normal region ($-\Delta_d G_{\text{et}}^0 < \lambda$), **b** barrierless electron transfer ($-\Delta_d G_{\text{et}}^0 = \lambda$), **c** inverted region ($-\Delta_d G_{\text{et}}^0 > \lambda$)

2.4.4.3 Photoinduced Electron Transfer

Photoinduced electron transfer events can also be represented by two-dimensional potential energy surfaces, using the principles described in the previous section. In this case Eq. (2.50) is modified and written as

Fig. 2.19 Experimental demonstration of the Marcus inverted region: intramolecular electron transfer rate constants recorded in 2-methyltetrahydrofuran for a series of bi-functional 4-biphenyl steroids, plotted as a function of driving force (free energy change). Reprinted with permission from Ref. [52]. Copyright 1984 American Chemical Society



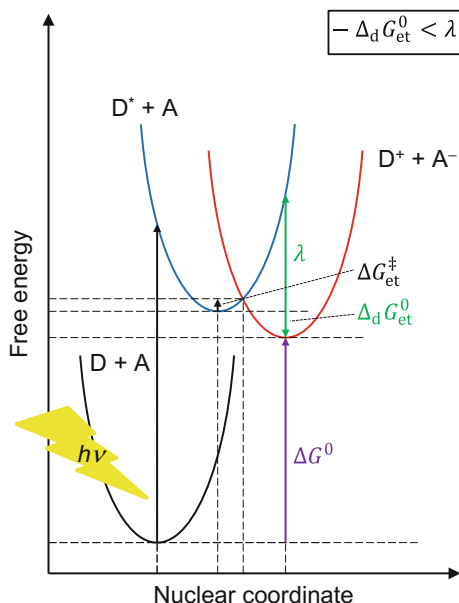
where light-excitation ($h\nu$) generates the excited donor D^* , which reacts with acceptor A . The corresponding changes in free energy as a function of nuclear motion are depicted in Fig. 2.20. According to the Franck-Condon principle, photoexcitation occurs vertically on the reaction coordinate (i.e. the nuclei remain frozen), yielding a vibrational level of the optically excited state. This system will then relax into the vibrational ground state of the electronic excited state by thermal equilibration. The next steps are analogous to the events described in the previous section: formation of the precursor complex is followed by electron transfer and subsequent nuclear relaxation to establish the equilibrated product ions of the successor state [44]. Although the latter steps are downhill in energy, the overall reaction (starting with $D + A$) is endergonic ($\Delta G^0 > 0$); light-energy is stored in the process.

2.4.5 Electronic Coupling

2.4.5.1 Adiabatic and Nonadiabatic Electron Transfer

Despite being very instructive and commonly used throughout the literature, the potential energy curves depicted in Figs. 2.18 and 2.20 are somewhat misleading. When the two reactants D and A in Eq. (2.50) approach one another closely, their frontier orbitals will begin to interact, causing a perturbation of their electronic

Fig. 2.20 Potential energy curves in photoinduced electron transfer according to Eq. (2.60). Vertical excitation of D leads to the formation of the excited state D^* , which, following rapid thermal equilibration, undergoes an electron transfer reaction with A analogously to Fig. 2.18a. Although the electron transfer step is exothermic, energy is stored in the overall process ($\Delta G^0 > 0$). Adapted from Ref. [44]

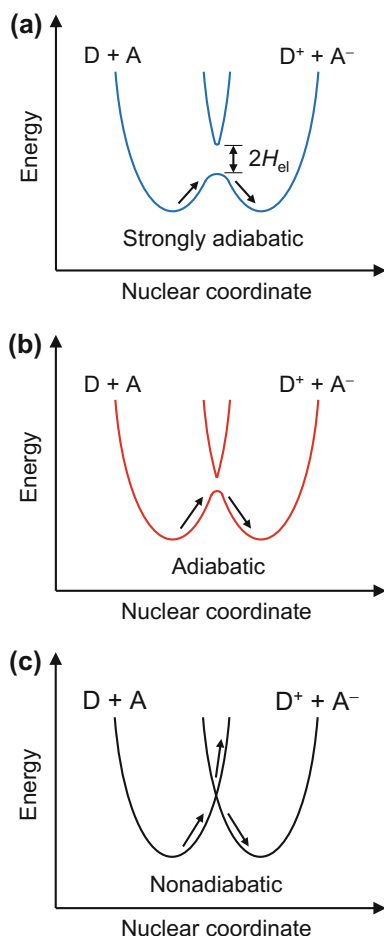


eigenfunctions and the Hamilton operator, which results in a shift in energies [44]. Graphically, a new set of curves emerges as the intersecting potential energy curves representing the precursor and successor complexes interact under perturbation (Fig. 2.21a). The electronic coupling H_{el} between the lower and upper potential energy curve represents the repulsion between the two traces. The term adiabaticity is a measure of the strength of the electronic coupling.

The classical treatment of electron transfer, to which Sect. 2.4 was limited thus far, was developed for weakly adiabatic reactions where $\kappa_{el} \approx 1$ (Fig. 2.21b), meaning that the reaction proceeds on a *single* potential energy surface, with a smooth transition from the precursor complex to the successor state (reactions are considered adiabatic if $H_{el} \geq 0.5 \text{ kcal mol}^{-1}$) [44]. Conversely, non-interacting, intersecting potential energy surfaces, where H_{el} is small, are termed *nonadiabatic* or *diabatic* (Fig. 2.21c). Reactants separated by a large distance constitute an example for a diabatic reaction.

The shape of the potential energy curve (i.e. its steepness) can have a profound influence on the probability of electron transfer [44]: the wavefunction responds more abruptly to nuclear changes in case of a steep slope, rendering electron transfer improbable. Conversely, a smooth transition is allowed if the lower potential energy curve is shallower. The velocity with which reactants and products approach one another also influences the probability of electron transfer: at high nuclear velocities, one can imagine the nuclear point moving back and forth many

Fig. 2.21 Potential energy curves representing adiabatic (a), (b) and nonadiabatic electron transfer (c). In strongly adiabatic electron transfer (a), H_{el} is large enough for the reaction to proceed on one curve. In nonadiabatic electron transfer, the ‘moving point’ oscillates many times on the reactant curve before electron transfer takes place. Adapted from Ref. [44]



times on the reaction curve, the little time spent on the crossing point causes the probability of electron transfer to decrease [44].

2.4.5.2 Distance Dependence of Electron Transfer and the Semiclassical Marcus Equation

The previous section alluded to the fact that H_{el} depends on the separation distance between the reactants. This, by extension, also holds for k_{et} (vide infra). In quantum mechanical terms, the distance dependence of the probability of electron transfer through a potential barrier (i.e. tunnelling) in a nonadiabatic process is expressed as the square of the electronic coupling matrix element H_{el} [53]:

$$H_{\text{el}}^2 = (H_{\text{el}}^0)^2 e^{-\beta(d-d_0)}, \quad (2.61)$$

where d is the separation distance between the two reactants and d_0 represents the separation distance in the case of an encounter complex, determined by the van der Waals radii of the two reactants [44]. H_{el}^0 corresponds to the maximal electronic coupling element when D and A are in contact. An important parameter is the ‘damping factor’ β , also known as attenuation factor or decay coefficient. Being inversely proportional to the orbital overlap between donor and acceptor orbitals [44], β depends on the medium through which the electron travels [53]. In vacuum, for example, β ranges from 2.8 to 3.5 \AA^{-1} [54, 55]. Common values for saturated hydrocarbons bridges are much lower, on the order of 0.8–1.0 \AA^{-1} [56–58], and slightly higher decay constants (1.0–1.4 \AA^{-1}) have been measured in proteins [55, 59, 60]. Remarkably low β -values as low as 0.04 \AA^{-1} have been reported for oligomers of *p*-phenylenevinylene: electron transfer rates constants of 10^{11} s^{-1} have been measured for separation distances of 40 \AA [61]. Consequently, such systems are termed ‘molecular wires’ [62].

Provided no parameters other than distance influence k_{et} , the electron transfer rate constant can be written as [41]

$$k_{\text{et}} = k_{\text{et}}^0 e^{-\beta(d-d_0)} = 10^{13} e^{-\beta(d-d_0)} \text{ s}^{-1}, \quad (2.62)$$

where 10^{13} s^{-1} represents the frequency for nuclear motion along the reaction coordinate, implicitly assuming that the reaction is adiabatic at $d = d_0$.

Comparing Eqs. (2.59) and (2.62) makes apparent that k_{et} shows two exponential dependences, both via the nuclear factor κ_{n} and the electronic factor κ_{el} . The semiclassical Marcus equation [41] combines the two dependences and can be used to predict both adiabatic and nonadiabatic electron transfer

$$k_{\text{et}} = \sqrt{\frac{4\pi^3}{h^2 \lambda k_{\text{B}} T}} H_{\text{el}}^2 e^{-\frac{(\lambda + \Delta_d c_{\text{el}}^0)^2}{4\lambda k_{\text{B}} T}}. \quad (2.63)$$

2.4.6 Electron Transfer in Biological Systems

Marcus theory has been adopted for electron transfer in biological systems [41]. Several researchers made seminal contributions to this field, with Gray being one of the most notable experimentalists (see, for example, Refs. [56, 60, 63–65]).

Equation (2.62) is widely used in the study of biomolecules, where electrons tunnel, often over long distances, between electron transfer relay centres such as the FeS chains in the fuel-forming enzymes that are subject to this thesis. Complex I, the first enzyme of the respiratory chain, constitutes a particular striking example, where the electron transport chain comprises nine iron sulphur clusters that shuttle

charges over a distance of more than 80 Å [66]. The FeS clusters in this and other iron sulphur enzymes such as hydrogenases or CODH have in common that their reorganisation energies are low, and the individual centres are arranged in a near linear fashion and spaced apart at distances short enough to allow efficient electron tunnelling at rates well above the limiting turnover rate [54]. Dutton and co-workers established, empirically, by surveying a wide range of electron transfer proteins with known atomic structure that electrons can travel up to 14 Å between redox centres through the protein medium. Transport over longer distances *always* involves a chain of cofactors [54]. Electron transfer rates on the order of 10^8 – 10^9 s⁻¹ are calculated for the redox enzymes used in this thesis.

Using the principles of electron transfer theory, we can interpret the near-unity efficiency of the initial photosynthetic charge-separation processes described in Sect. 1.2.2.2. Electron transfer from the special pair to the initial pheophytin *a* acceptor is barrierless with a rate constant of ca. 10^{12} s⁻¹, the outer-sphere reorganisation energy inside the hydrophobic protein membrane is low, and bond-length changes are negligible in the rigid porphyrin frameworks [44]. Subsequent electron transfer to plastoquinone Q_A is again barrierless, albeit three orders of magnitude slower, at least in part due to the large separation distance. Yet, destructive recombination is kinetically disfavoured, being placed in the Marcus inverted region owing to its large driving force. Recombination between reduced Q_A and the oxidised special pair P680⁺ is also impeded by strong barriers, notably the poor electronic overlap because of the large separation distance [44].

Long-range electron transfer is still a thriving and actively researched area, and the theoretical concepts described in Sect. 2.4 are powerful tools, not only for describing experimentally observed phenomena, but also for predicting reactivity and hence guiding the experimentalist.

2.5 Electron Paramagnetic Resonance Spectroscopy

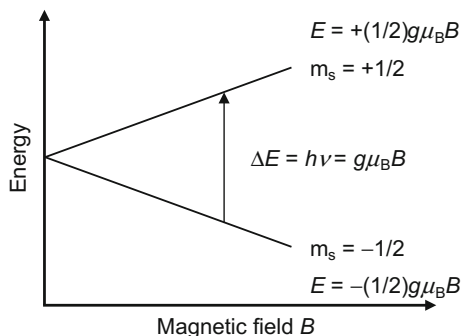
2.5.1 *The Electronic g Value*

This chapter on experimental theory will be concluded with a short, phenomenological discussion of the basic principles behind electron paramagnetic resonance spectroscopy (EPR), focusing on continuous-wave EPR. In a magnetic field *B*, an electron with spin $S = 1/2$ can have two orientations, either parallel to the magnetic field, where $m_s = +1/2$, or antiparallel with $m_s = -1/2$. It is the latter orientation that is lower in energy. The electronic Zeeman energies are given by [67]

$$E = g\mu_B B m_s, \quad (2.64)$$

where μ_B denotes the Bohr magneton and *g* is the property of interest in the experiment (vide infra). Upon absorption of electromagnetic radiation $h\nu$ equal to

Fig. 2.22 Removal of the degeneracy of the electron spin states by a magnetic field. An EPR allowed transition is observed when the resonance condition is fulfilled. Adapted from Ref. [68]



the energy difference ΔE in the two orientations, the electron will change orientation according to the resonance condition

$$h\nu = g\mu_B B. \quad (2.65)$$

This process is schematically depicted in Fig. 2.22.

From Eq. (2.65) follows that there are, in principle, two options for detecting EPR absorption: the frequency can be varied at constant field, or the field can be varied at constant frequency until the resonance condition is met. It is the latter case that finds application in continuous-wave EPR spectroscopy: for practical purposes resonant cavities are used to enhance sensitivity, their use dictates a fixed frequency with a corresponding wavelength that fits the resonator dimensions [67].

The g value of a free electron *in vacuo* $g_e = 2.00232$. However, as a result of spin-orbit coupling, an electron orbiting around one or more nuclei (e.g. a transition metal ion in a metalloenzyme) will experience a second magnetic field δB . In this case, the resonance condition can be expressed as

$$h\nu = g_e\mu_B(B_e + \delta B) \quad (2.66)$$

or, since δB is not known, as

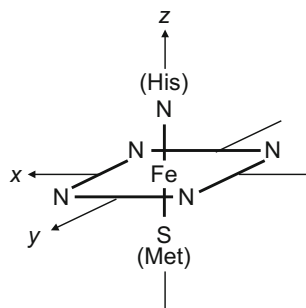
$$h\nu = (g_e + \delta g)\mu_B B. \quad (2.67)$$

The notion of δg lies at the heart of EPR: this quantity not only serves as a ‘fingerprint’ of a given molecule (as $g = g_e + \delta g$), it also contains information about its electronic structure, as well as the nature of electron-nucleus interactions.

2.5.2 The g Value is Anisotropic

Anisotropy is a key concept in EPR spectroscopy: molecular properties such as δg are angular dependent and thus reflect the three-dimensional structure of a

Fig. 2.23 Schematic illustration of axial paramagnetic anisotropy using a simplified representation of a cytochrome *c*-type haem porphyrin with histidine and methionine occupying the axial positions. Adapted from Ref. [67]

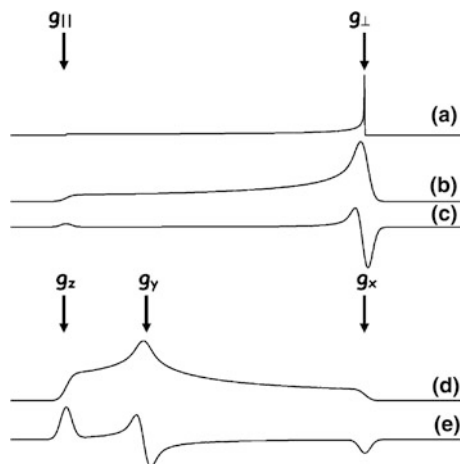


paramagnetic molecule [67]. The principle is illustrated using the following example. Figure 2.23 schematically depicts an oxidised cytochrome *c*-type molecule, having a low-spin ferric haem centre ($S = 1/2$) embedded in a porphyrin plane, with the axial positions being occupied by a histidine and a methionine ligand, respectively. The molecule is depicted spanning a Cartesian coordinate system, such that the tetrapyrrole plane spans the x - and y -plane and the axial ligands are aligned with the z -axis.

Consider this molecule being subjected to an external dipolar magnetic field B with the field vector \mathbf{B} along the x axis: δg in Eq. (2.67) is largely determined by the heteroatomic electrons of the tetrapyrrole plane [67]. Because of the porphyrin plane being symmetric, no change in δg will be observed upon rotation around the z axis so that the y axis is aligned with the magnetic field vector. However, the electronic structure of the His and Met ligands will determine δg if the molecule is rotated so that the z axis is aligned with the magnetic field. The example in Fig. 2.23 is considered to display axial symmetry, with $B_x = B_y \neq B_z$ and thus $g_x = g_y \neq g_z$. In a sample of randomly oriented cytochrome *c* haems, many more molecules will exist with the \mathbf{B} vector anywhere near the xy plane than there will be molecules where \mathbf{B} is parallel to the unique z axis. This discrepancy will impact the intensity distribution of the resulting EPR signals, as (qualitatively) depicted in Fig. 2.24a. A real EPR spectrum is obtained when this stick spectrum is convoluted with a line shape with finite line width (Fig. 2.24b) [67], reflecting the different orientations with respect to the \mathbf{B} vector lying somewhere in between the extreme values that give rise to the sharp, distinct peaks [69]. Figure 2.24c shows the derivative (with respect to the magnetic field) EPR spectrum, which is usually recorded in practice, as standard EPR spectrometers employ field modulation plus phase-sensitive detection to increase sensitivity by filtering out non-resonant noise [67].

Distortion of the axial symmetry (such as in the porphyrin plane in Fig. 2.23) leads to the formation of a rhombic spectrum, where $g_x \neq g_y \neq g_z$. An example of a rhombic absorption spectrum is shown in Fig. 2.24d and the corresponding derivative spectrum is depicted in Fig. 2.24e. The latter shows three different features, the field positions of which correspond closely to the different g_x , g_y , and g_z .

Fig. 2.24 Anisotropy in EPR illustrated for absorption and derivative spectra of axial (a)–(c) and rhombic symmetry (d), (e). (a) axial intensity pattern; (b) axial EPR absorption; (c) axial EPR derivative; (d) rhombic EPR absorption; (e) rhombic EPR derivative. Reprinted with permission from Ref. [67]. Copyright 2006 The Royal Society of Chemistry



For completeness, in the simplest case, termed isotropic system, $g_x = g_y = g_z$.

2.5.3 Multiple Magnetic Interactions

Electronic Zeeman interactions in addition to those between the external magnetic field B and the electron spin S (termed S^*B interactions) give rise to more complicated EPR spectra than those reported in Fig. 2.24. Generically speaking, one can distinguish between electron-electron spin interactions (S^*S interactions) and interactions between electron spins and nuclear spins (S^*I interactions).

Although much weaker than the electronic Zeeman (S^*B) interaction (typically one to several orders of magnitude [67]), S^*I interactions do cause perturbations to the EPR spectrum, they give rise to hyperfine splitting: each of the basic S^*B features (see Fig. 2.24) will be split into $2I + 1$ lines, with the magnitude of the splitting (A) reflecting the strength of the interaction. A is an anisotropic quantity, meaning each g value may show hyperfine splitting of different magnitude. In a rhombic system, for instance, this leads to A_x , A_y , and A_z corresponding to the magnitude of the splitting at g_x , g_y , and g_z , respectively.

Hyperfine splitting arising from interaction with metal ion nuclei is referred to as central hyperfine splitting and allows determination of the isotope of the metal with which the electron is associated. Interaction of electron spin with nuclei from (first) coordination sphere ligands is termed ligand hyperfine or superhyperfine splitting. This type of interaction is important for Chap. 3 of this thesis. The magnitude of ligand hyperfine splitting is typically an order of magnitude less compared to metal hyperfine splitting [67].

Spin systems comprising more than one unpaired electron ($S > 1/2$), e.g. triplet states, give rise to S^*S interactions and cause what is known as zero-field splitting.

Magnetic dipole-dipole interaction between unpaired electrons removes their degeneracy even in the absence of an external field [68].

Nuclear Zeeman interactions (I^*B) and quadrupolar interactions (I^*I) are usually too weak to be detected in a standard continuous-wave EPR experiment; they are, however, amenable to characterisation by some advanced (pulsed-) EPR techniques, notably electron nuclear double resonance (ENDOR) and electron spin echo envelope modulation (ESEEM) [67].

2.5.4 ‘Advanced’ EPR Techniques

The term ‘advanced’ EPR is rather vague. Generally, it refers to so-called double resonance techniques involving two sources of radiation. The common underlying principle involves the partial or full saturation of an EPR absorption, normally using pulsed excitation, and subsequent transfer of spin energy to a different absorption by means of the second radiation, leading to the detection of the difference signal [70]. Contrary to pulsed NMR spectroscopy, pulses in EPR are often not able to excite the entire spectrum of the electron spin.

Electron-nuclear hyperfine interactions that are too small to be resolved within the natural EPR line width can be studied by ESEEM and ENDOR. ESEEM is typically used in the characterisation of ‘more distant’, weakly coupled nuclei with $A \leq 10$ MHz [71]. Weakly coupled nuclear spins cause a modulation of the intensity of the spin echo at the nuclear frequencies of the interacting nucleus. From the modulation depth, it is in principle possible to determine the number of equivalent nuclei of a particular type of coupling with the electron spin; an example is presented in Chap. 3. ESEEM experiments can be carried out as two- or three-pulse experiments, with the latter usually giving better resolution (in the three-pulse experiment, the nuclear coherence decays with the longer nuclear relaxation time T_1 instead of the shorter spin-spin relaxation time T_2) [72]. Hyperfine sublevel correlation spectroscopy (HYSCORE) is a four-pulse variation of the ESEEM experiment.

ENDOR is complementary to ESEEM and generally used for more strongly coupled, ‘closer’ nuclei, with A being in the range of 2–40 MHz [71]. The technique probes the nuclear transitions directly, through coupling of the EPR excitation with an NMR radio frequency pulse. Simply speaking, NMR spectroscopy is detected on an EPR spectrometer.

Because of the highly complicated nature of double-resonance techniques, a theoretical treatment of the above-mentioned pulsed-EPR experiments would be beyond the scope of this introduction. The reader is instead referred to the wealth of literature on advanced EPR spectroscopy. Concise introductions for example are given by Chasteen and Snetsinger [71], and Roessler [72].

References

1. Chen Z, Dinh HN, Miller E (2013) Photoelectrochemical Water Splitting: Standards, Experimental Methods, and Protocols. Springer, Berlin
2. Armstrong FA, Belsey NA, Cracknell JA, Goldet G, Parkin A, Reisner E, Vincent KA, Wait AF (2009) Chem Soc Rev 38:36
3. Blanford CF (2013) Chem Commun 49:11130
4. Vincent KA, Parkin A, Armstrong FA (2007) Chem Rev 107:4366
5. Léger C (2013) In: Louro RRCO (ed) Practical Approaches to Biological Inorganic Chemistry. Elsevier, Oxford, p 179
6. Bard AJ, Faulkner LR (2001) Electrochemical Methods: Fundamentals and Applications, 2nd edn. John Wiley & Sons Inc, New York
7. Fisher AC (1996) Electrode Dynamics. Oxford University Press, Oxford
8. Wedler G (2004) Lehrbuch der Physikalischen Chemie, 5th edn. Wiley-VCH, Weinheim
9. Atkins P, de Paula J (2010) Atkins' Physical Chemistry, 9th edn. Oxford University Press, Oxford
10. Armstrong FA, Hirst J (2011) Proc Natl Acad Sci U S A 108:14049
11. Léger C, Jones AK, Albracht SPJ, Armstrong FA (2002) J Phys Chem B 106:13058
12. Ludwig M, Cracknell JA, Vincent KA, Armstrong FA, Lenz O (2009) J Biol Chem 284:465
13. Brattain WH, Garrett CGB (1955) Bell Syst Tech J 34:129
14. Bockris JOM, Khan SUM (1993) Surface Electrochemistry: A Molecular Level Approach. Plenum Press, New York
15. Fujishima A, Honda K (1972) Nature 238:37
16. O'Regan B, Grätzel M (1991) Nature 353:737
17. Khaselev O, Turner JA (1998) Science 280:425
18. Bott A (1998) Curr Sep 3:87
19. Myamlin VA, Pleskov YV (1967) Electrochemistry of Semiconductors. Plenum Press, New York
20. Rajeshwar K (2002) In: Licht S (ed) Semiconductor Electrodes and Photoelectrochemistry. Wiley-VCH, Weinheim, p 1
21. Finklea HO (1988) In: Finklea HO (ed) Semiconductor Electrodes. Elsevier Science Publishers, Amsterdam, p 1
22. Irebo T, Zhang M-T, Markle TF, Scott AM, Hammarström L (2012) J Am Chem Soc 134:16247
23. Tan MX, Laibinis PE, Nguyen ST, Kesselman JM, Stanton CE, Lewis NS (1994) In: Prog Inorg Chem. John Wiley & Sons, Inc., New York, p 21
24. Gelderman K, Lee L, Donne SW (2007) J Chem Educ 84:685
25. Beranek R (2011) Adv Phys Chem 78:6759
26. Berger T, Anta JA, Morales-Flórez V (2012) J Phys Chem C 116:11444
27. Kavan L, Kratochvilová K, Grätzel M (1995) J Electroanal Chem 394:93
28. Wang H, He J, Boschloo G, Lindström H, Hagfeldt A, Lindquist S-E (2001) J Phys Chem B 105:2529
29. Zhang Q, Celorrio V, Bradley K, Eisner F, Cherns D, Yan W, Fermín DJ (2014) J Phys Chem C 118:18207
30. Boschloo G, Fitzmaurice D (1999) J Phys Chem B 103:2228
31. He J, Lindström H, Hagfeldt A, Lindquist S-E (2000) Sol Energy Mater Sol Cells 62:265
32. Odobel F, Pellegrin Y, Gibson EA, Hagfeldt A, Smeigh AL, Hammarström L (2012) Coord Chem Rev 256:2414
33. Zhu H, Hagfeldt A, Boschloo G (2007) J Phys Chem C 111:17455
34. Gärtner WW (1959) Phys Rev 116:84
35. Sprunken HR, Schumacher R, Schindler RN (1980) Farad Discuss 70:55
36. Randles JEB (1947) Farad Discuss 1:11

37. Brett CMA, Oliveira Brett AM (1993) *Electrochemistry: Principles, Methods, and Applications*. Oxford University Press, Oxford
38. Marcus RA (1993) *Angew Chem Int Ed* 32:1111
39. Levich V, Dogonadze R (1959) *Dokl Akad Nauk SSSR* 124:123
40. Hush NS (1968) *Electrochim Acta* 13:1005
41. Marcus RA, Sutin N (1985) *BBA-Bioenergetics* 811:265
42. Sutin N, Creutz C (1983) *J Chem Educ* 60:809
43. Sutin N (1982) *Acc Chem Res* 15:275
44. Kavarnos GJ (1993) *Fundamentals of Photoinduced Electron Transfer*. Wiley-VCH, Weinheim
45. Marcus RA (1956) *J Phys Chem* 24:966
46. Marcus RA (1960) *Farad Discuss* 29:21
47. Marcus RA (1963) *J Phys Chem* 67:853
48. Marcus RA (1965) *J Phys Chem* 43:679
49. Murov SL, Carmichael I, Hug GL (1993) *Handbook of Photochemistry*, 2nd edn. Marcel Dekker Inc, New York
50. Léger C, Bertrand P (2008) *Chem Rev* 108:2379
51. Compton RG, Banks CE (2011) *Understanding Voltammetry*, 2nd edn. Imperial College Press, London
52. Miller JR, Calcaterra LT, Closs GL (1984) *J Am Chem Soc* 106:3047
53. Atkins PW, de Paula J, Friedman R (2014) *Physical Chemistry: Quanta, Matter, and Change*, 2nd edn. Oxford University Press, Oxford
54. Page CC, Moser CC, Chen X, Dutton PL (1999) *Nature* 402:47
55. Moser CC, Keske JM, Warncke K, Farid RS, Dutton PL (1992) *Nature* 355:796
56. Gray HB, Winkler JR (2005) *Proc Natl Acad Sci U S A* 102:3534
57. Oevering H, Paddon-Row MN, Heppener M, Oliver AM, Cotsaris E, Verhoeven JW, Hush NS (1987) *J Am Chem Soc* 109:3258
58. Johnson MD, Miller JR, Green NS, Closs GL (1989) *J Phys Chem* 93:1173
59. Winkler JR, Gray HB (1992) *Chem Rev* 92:369
60. Gray HB, Winkler JR (2009) *Chem Phys Lett* 483:1
61. Davis WB, Svec WA, Ratner MA, Wasielewski MR (1998) *Nature* 396:60
62. Wielopolski M (2010) *Testing molecular wires: A photophysical and Quantum Chemical Assay*. Springer, Berlin
63. Shih C, Museth AK, Abrahamsson M, Blanco-Rodriguez AM, Di Bilio AJ, Sudhamsu J, Crane BR, Ronayne KL, Towrie M, Vlček A, Richards JH, Winkler JR, Gray HB (2008) *Science* 320:1760
64. Winkler JR, Gray HB (2014) *J Am Chem Soc* 136:2930
65. Winkler JR, Gray HB (2014) *Chem Rev* 114:3369
66. Sazanov LA, Hinchliffe P (2006) *Science* 311:1430
67. Hagen WR (2006) *Dalton Trans* 4415
68. Drago RS (1992) *Physical Methods for Chemists*, 2nd edn. Surfside Scientific Publishers, Gainesville
69. Hexter SV (2014) D Phil Thesis, University of Oxford, Oxford
70. Hagen WR (2008) *Biomolecular EPR Spectroscopy*. CRC Press, Boca Raton
71. Chasteen ND, Snetsinger PA (2000) In: Que L (ed) *Physical Methods in Bioinorganic Chemistry: Spectroscopy and Magnetism*. University Science Books, Sausalito, p 187
72. Roessler MM (2012) D Phil Thesis, University of Oxford, Oxford

Chapter 3

The Mechanism of [FeFe]-Hydrogenases— How Aldehydes Inhibit H₂ Evolution

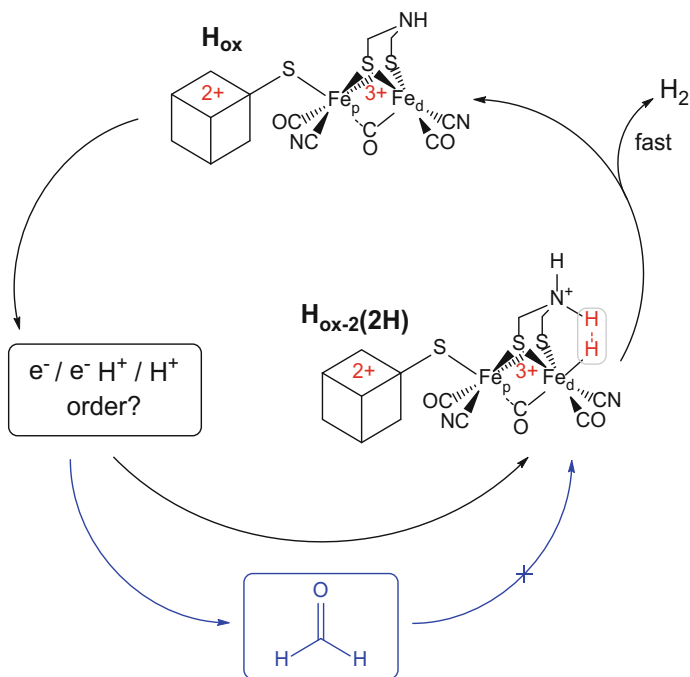
3.1 Introduction

As outlined in Sect. 1.6.2.4, the elementary steps by which [FeFe]-hydrogenases evolve hydrogen so efficiently are still unclear. Scheme 3.1 draws attention to an outstanding question concerning their mechanism. Of the two structures shown, H_{ox} is well characterised; the other structure represents a *transient* state, termed H_{ox-2}(2H), immediately prior to or at the point of H₂ release. To go from H_{ox} to H_{ox-2}(2H) requires two electrons and two protons but it has not been established in a kinetic study in which order these events occur. In the H_{ox-2}(2H) transient, the two additional electrons (with respect to H_{ox}) are stored as a terminal hydride bound to Fe_d; therefore, the oxidation numbers of the H-cluster components [2Fe]_H and [4Fe-4S]_H are already adjusted to the H_{ox} level, which is left behind after H₂ is released from the active site (the individual oxidation numbers of Fe_d and Fe_p (I,II) are not yet established).

The reversible inhibition of [FeFe]-hydrogenases by formaldehyde has recently been established using protein film electrochemistry [1, 2]. The combination of PFE and inhibition by aldehydes provides an interesting new probe for the mechanism of H₂ production: aldehydes almost certainly react at the H-cluster, intercepting highly active reduced states.

Importantly, the activity that is lost very rapidly when formaldehyde is injected into the electrochemical cell is recovered *immediately* when formaldehyde is removed (Fig. 3.1a). Formaldehyde binds rapidly within seconds, the reaction in the potential region where H₂ production occurs is dominated by a fast component with $\tau = 7.89$ s at -0.56 V vs. SHE (Fig. 3.1b). Importantly, the enzymatic activity

Part of the work presented in this chapter has been published: Andreas Bachmeier, Julian Esselborn, Suzannah V. Hexter, Tobias Krämer, Kathrin Klein, Thomas Happe, John E. McGrady, William K. Myers, and Fraser A. Armstrong, *J. Am. Chem. Soc.* **2015**, *137*, 5381.



Scheme 3.1 Pathway to the transient precursor for catalytic H_2 formation at the H-cluster, formation of which is prevented by formaldehyde. As the individual charges on Fe_p and Fe_d are still under debate, the overall oxidation number of $[\text{2Fe}]_H$ is presented, together with the charge of $[\text{4Fe-4S}]_H$. In H_{ox} , $[\text{4Fe-4S}]_H$ is established to have an overall charge of 2+, and both $\text{Fe}_p(\text{I})\text{-Fe}_d(\text{II})$ and $\text{Fe}_p(\text{II})\text{-Fe}_d(\text{I})$ are possible combinations for $[\text{2Fe}]_H$. In $\text{H}_{\text{ox-2(2H)}}$, $[\text{4Fe-4S}]_H$ is also formulated as 2+ [3], implicating that $[\text{2Fe}]_H$ comprises $\text{Fe}_p(\text{I})\text{-Fe}_d(\text{II})$ [4]. Reprinted with permission from Ref. [5]. Copyright 2015 American Chemical Society

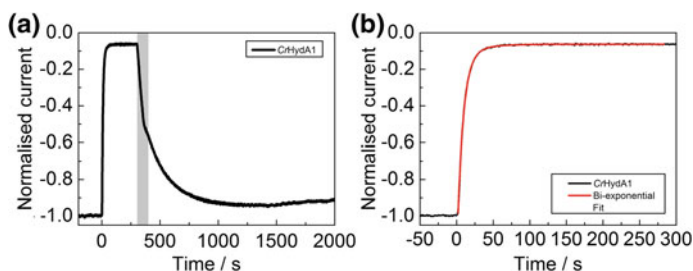


Fig. 3.1 Formaldehyde-inhibition of H^+ reduction by *CrHydA1*, adapted from Ref. [2]. **a** Formaldehyde was injected at $t = 0$ to give a final concentration of 4.5 mM. After 300 s, the cell was rinsed with 50 mL of phosphate buffer (rinsing took approximately 100 s, grey stripe). Other conditions: electrode potential -0.56 V vs. SHE; pH 6.0; 10°C ; 100% H_2 ; $\omega = 2500$ rpm. **b** Represents an expanded section of (a), in which the decay of activity following injection of formaldehyde is fitted to a bi-exponential process by least-square analysis using OriginPro 9.0. Reprinted with permission from Ref. [5]. Copyright 2015 American Chemical Society

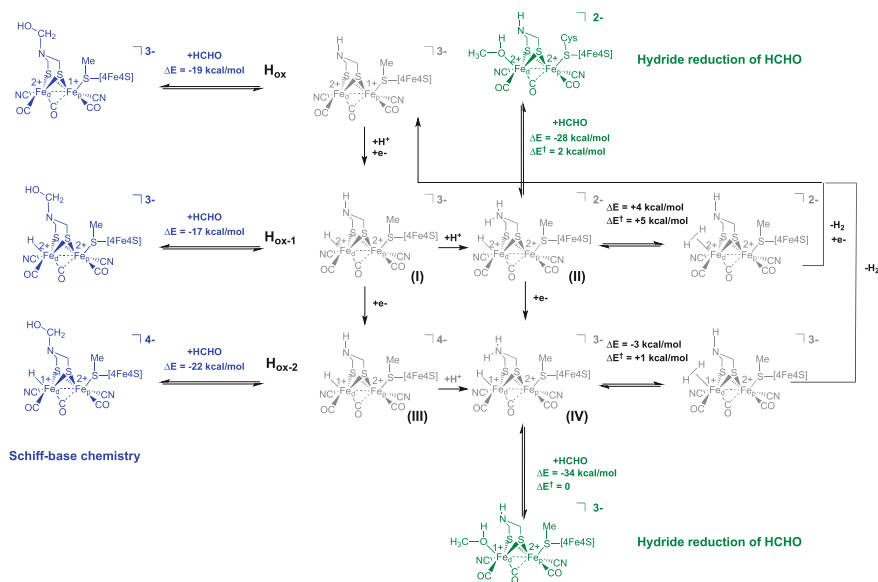
is almost fully recovered when formaldehyde is flushed from the cell after 5 min exposure (Fig. 3.1a).

The fraction of the total current attenuation that is due to rapid, *reversible* interaction with HCHO increases as the electrode potential is lowered [2]: a detailed study with the enzyme from *Clostridium acetobutylicum* showed that the potential dependence spans three zones linked by one-electron Nernst transitions and thus termed H_{ox} , H_{ox-1} , and H_{ox-2} . Allowing for small shifts, the profile complemented that obtained for inhibition by CO, thus implicating the most reduced catalytic intermediate, two electrons below H_{ox} and hence at the level of H_{ox-2} , as the primary target for rapid and reversible inhibition [1]. Formaldehyde thus prevents the formation of the transient species $H_{ox-2}(2H)$ depicted in Scheme 3.1 (blue pathway). A much slower reaction, which is not reversible, is also observed, and becomes dominant as the electrode potential is raised [1, 2]. However, the fact that at negative potentials where H_{ox-2} prevails, the rapidly inhibited fraction is almost quantitatively recovered upon formaldehyde removal after 5 min (Fig. 3.1a) means that the fast binding process offers substantial protection against the slow and irreversible reaction.

Based on earlier evidence from density functional theory (DFT) [3, 6, 7] that in the H_{sred} state (and likely also H_{red}) Fe_d should carry a hydrido-ligand, it has originally been proposed that HCHO inhibition of the H_{ox-1} and H_{ox-2} levels occurs, mechanistically, through electrophilic attack on the respective hydrido complex to form a bound methanol or methoxide species [1]. This process is thermodynamically favourable and resembles Noyori chemistry (catalytic hydrogenation) (Scheme 3.2).

However, subsequent efforts to detect any release of methanol have been unsuccessful [1, 8], implying that HCHO might bind as a true inhibitor and not as an alternative, slow substrate. Further, results from spectroscopic investigations by different groups have led to the proposal that Fe_d neither carries a hydrido ligand in H_{red} [9, 10] (H_{ox-1} level) nor in the spectroscopically accessible form of H_{sred} (H_{ox-2} level) [11]—the implication being that H_2 evolution occurs very rapidly following transfer of two protons upon the transition to or at the H_{ox-2} redox level (compare Scheme 1.1) [4]. These developments place the nature of the reaction with formaldehyde, which contains a potent electrophilic C-atom, in a new context—namely as a probe to investigate *when* the initial H^+ transfer to Fe_d (to form the hydrido complex) occurs during catalysis, as well as the subsequent second protonation of the adt-moiety. The results also convey additional structural information, because known complexes of metals with formaldehyde do not bind only through a single metal-C bond, but involve secondary stabilisation through *di*-hapto (η -C,O) coordination [12–14], a notable example being $Fe(\eta^2-CH_2O)(CO)_2(P(OMe)_3)_2$ reported by Berke et al. [15].

This chapter expands the concept of using the combination of PFE and formaldehyde as probe for the mechanism of H_2 production to longer chain aldehydes, i.e. trifluoroacetaldehyde, acetaldehyde, butyraldehyde, and isovaleraldehyde. Having different electronic and steric properties, these molecules might allow



Scheme 3.2 Theoretical calculations of the mechanism of H₂ formation by the H-cluster (grey). The thermodynamically favourable reaction with formaldehyde is depicted in green. An alternative pathway, Schiff base chemistry at the bridgehead nitrogen atom, is shown in blue. Reprinted with permission from Ref. [1]. Copyright 2012 American Chemical Society

a distinction between different postulated reaction pathways at the H-cluster. Moreover, in addition to intercepting and trapping reactive intermediates such as the super-reduced state H_{red}, extended alkyl chains provide the equivalent of a ‘trail of string’ marking the route taken to and from the active site. These inhibitors could hence shed more light on the gas channels that allow diffusion through the protein towards the active site.

Separately, using the algal enzyme CrHydA1, pulsed-EPR spectroscopy experiments with isotopically enriched formaldehyde (DCDO and H¹³CHO) were undertaken in collaboration with Dr. William Myers (Centre for Advanced Electron Spin Resonance, University of Oxford) to gain insight into the binding mode of formaldehyde (the simplest and most reactive aldehyde inhibitor) to the H-cluster. Use of EPR allows the species formed upon rapid and reversible reaction with formaldehyde to be studied over long periods in frozen samples, avoiding the irreversible degradation that would inevitably result if using techniques such as IR that normally require ambient temperatures. Furthermore, DFT calculations were carried out by Professor John McGrady (Inorganic Chemistry Laboratory, University of Oxford) to provide mechanistic support. Taken together, the results have important implications for the mechanism of [FeFe]-hydrogenases.

3.2 Protein Film Electrochemistry Investigations

Aiming at establishing whether aldehydes can react with the H_{ox-2} redox level and, further, discriminating between the two originally postulated reaction pathways Schiff-base chemistry and hydric carbonyl reduction [1] (see Scheme 3.2), the concept of using formaldehyde as probe for the mechanism of H_2 production was expanded to longer chain aldehydes of different steric demand and electrophilicity. Through chronoamperometry experiments, the potential dependences of the inhibition of *CaHydA* by four different aldehydes have been determined: (i) trifluoroacetaldehyde (CF_3CHO), (ii) acetaldehyde ($MeCHO$), (iii) butyraldehyde ($PrCHO$), and (iv) isovaleraldehyde (*i*-BuCHO) (Fig. 3.2).

To illustrate the general principle, two typical experiments using $MeCHO$ are depicted in Fig. 3.3. In the red trace, the electrode is poised at a low potential in the hydrogen production regime (-0.6 V). Acetaldehyde inhibitor is injected at $t = 0$. The *inhibition kinetics* can be obtained by subsequent monitoring of the decrease in

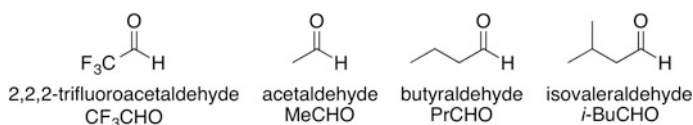


Fig. 3.2 Structures of the different aldehyde molecules studied as inhibitors of [FeFe]-hydrogenases

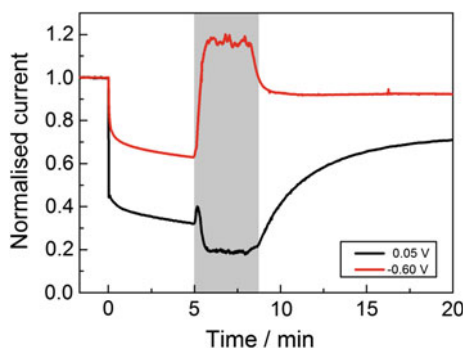


Fig. 3.3 Current vs. time traces depicting the decrease of hydrogen oxidation (*black*) and hydrogen evolution (*red*) activity of *CaHydA* following injection of $168 \mu M$ $MeCHO$ at $t = 0$. The currents are normalised for film loss according to Eq. (2.30). The *grey* area shows Δt in which the buffer solution is exchanged to establish whether activity can be restored after removal of the inhibitor. Experimental conditions: pH 6.0 phosphate buffer; $\omega = 3000$ rpm, dark, $5^\circ C$, 100% H_2 . Due to the volatility of $MeCHO$ (bp $20^\circ C$) H_2 flow was briefly interrupted during inhibition and restored after buffer exchange (see Sect. 3.2.3)

catalytic current. After 300 s, the cell solution is rinsed with fresh, temperature- and gas-equilibrated buffer (ten times the original cell volume, grey area), while maintaining electrical connectivity. The activity that is restored after the rinse determines the *extent of reversibility* the inhibition process displays. Note the initial increase of normalised current immediately after the start of the rinsing process ('current overshoot'); this can most likely be attributed to a slightly higher temperature in the fresh buffer solution, giving higher activity [2]. The black current vs. time trace in Fig. 3.3 shows MeCHO inhibition of hydrogen oxidation by *CaHydA*. Here, the extent of inhibition is higher than in the red trace. However, the process at +0.05 V is less reversible.

3.2.1 Inhibition by Formaldehyde

For comparison, the potential dependence of inhibition of *CaHydA* by formaldehyde, which serves as 'benchmark', is shown in Fig. 3.4. The dependence was established by Foster et al. [1] through chronoamperometry experiments analogous to those shown in Fig. 3.3. The reactivity of formaldehyde towards the enzyme increases as the potential is lowered. The potential dependence follows two one-electron Nernst transitions and maximum inhibition occurs at the H_{ox-2} redox level. Kinetic analysis (see Fig. 3.1 for a sample trace recorded in the H_2 production region) shows that inhibition at low potentials essentially follows a single-exponential time-course. Conversely, at high potentials where formaldehyde inhibition of *CaHydA* is marginal, the kinetics are biphasic, with the slower component being the dominating kinetic process. It needs to be mentioned that

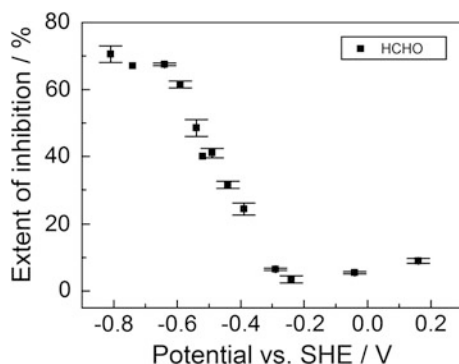


Fig. 3.4 Potential dependence of inhibition of *CaHydA* by formaldehyde. Data taken from Ref. [1]. The extent of inhibition was measured after 100 s of exposure to 4.5 mM HCHO in 100% H_2 , which corresponds to 2.25 μ M non-hydrated HCHO. Conditions: pH 6.0 phosphate buffer, $\omega = 2500$ rpm, 20 $^{\circ}$ C, dark (blacked-out) cell. Error bars represent one standard deviation

formaldehyde is believed to enter the enzyme in its gaseous form, i.e. as free, non-hydrated HCHO [2]. The equilibrium constant for hydration, K_{eq} , is approximately 2000 at 25 °C [16, 17].

3.2.2 Inhibition by Trifluoroacetaldehyde

The potential dependence of CF_3CHO inhibition of CaHydA is depicted in Fig. 3.5. Due to the high K_{eq} for hydrate formation of $\sim 2.9 \times 10^4$ [18] (one order of magnitude larger than $K_{\text{eq,HCHO}}$), the maximum concentration that could be employed in these measurements (restricted by a maximum electrochemical cell volume of 5.0 mL) was 182 mM CF_3CHO , which corresponds to 6.3 μM non-hydrated aldehyde (compared to 2.25 μM HCHO in Sect. 3.2.1). Generally, inhibition studies could not be carried out in the ‘intermediate’ potential region close to the equilibrium potential for H^+/H_2 interconversion (i.e. between -0.4 and -0.15 V, see Fig. 1.33), due to the relatively low catalytic currents in this region that are lowered even further by the exponential ‘film loss’ processes that underlie every experiment (see Sect. 2.2.7).

As shown in Fig. 3.5, in the potential region where hydrogen formation takes place, the extent of CF_3CHO inhibition follows a similar potential dependence profile to that of HCHO inhibition (Fig. 3.4). Even though the magnitude of the extent of inhibition cannot be directly compared, since different concentrations of aldehydes had to be employed, it becomes immediately apparent that CF_3CHO inhibits hydrogen production activity of CaHydA to a much lesser extent than formaldehyde. Interestingly, CF_3CHO shows higher inhibition of H_2 oxidation than proton reduction, which stands in contrast to CaHydA inhibition by formaldehyde, where H_2 oxidation inhibition is marginal.

The kinetics of CF_3CHO inhibition are shown in Fig. 3.6. Similar to formaldehyde inhibition of CaHydA , CF_3CHO inhibition follows bi-exponential kinetics. The rate constants of the fast and slow components of the reaction are depicted in red and blue, respectively. Both increase as the potential is raised, with

Fig. 3.5 Percentage inhibition of CaHydA by CF_3CHO after 100 s of exposure. Conditions: 100% H_2 , 6.3 μM (non-hydrated) CF_3CHO , 20 °C, $\omega = 3000$ rpm, pH 6.0, dark. Error bars represent one standard deviation; all measurements were carried out in triplicate

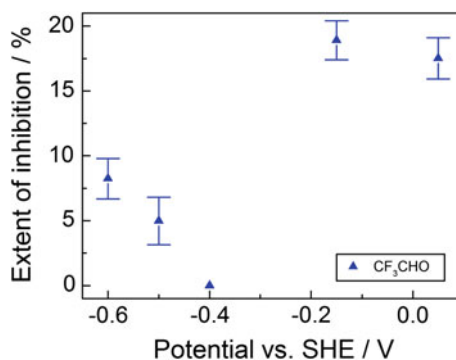
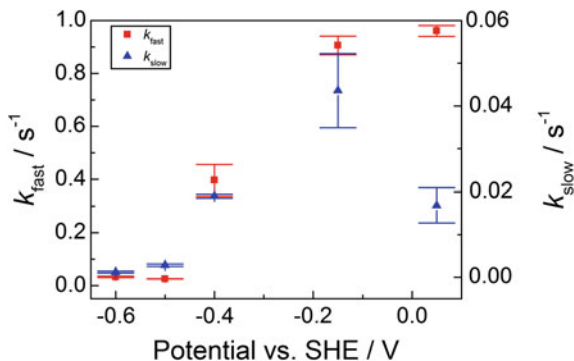


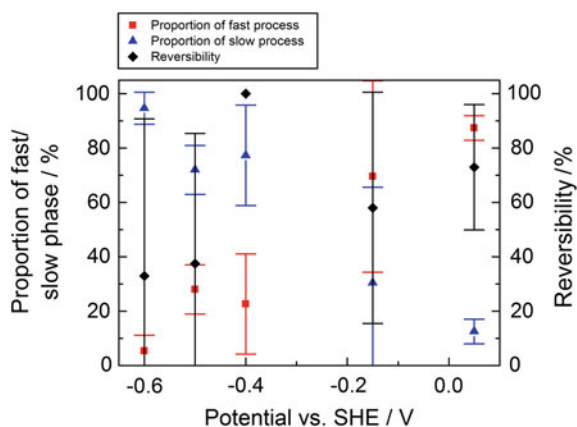
Fig. 3.6 Potential dependences of the average rate constants of the fast (*red*) and slow (*blue*) phase of the biphasic reaction of CF_3CHO with *CaHydA*. Error bars represent one standard deviation of propagated errors from least-square analysis of the inhibition kinetics. All measurements were carried out in triplicate



k_{fast} being about one order of magnitude larger than k_{slow} . In formaldehyde inhibition of *CaHydA*, the rate constant of the fast component also increases as the potential is increased, but k_{slow} is potential independent [8]. In agreement with the faster overall reactivity displayed by HCHO, both the fast and the slow process of HCHO inhibition [8] occur on much faster timescales than CF_3CHO inhibition— $k_{\text{fast,HCHO}} \sim 10^6 \times k_{\text{fast,CF}_3\text{CHO}}$; $k_{\text{slow,HCHO}} \sim 10^4 \times k_{\text{slow,CF}_3\text{CHO}}$.

Figure 3.7 shows the portions of the fast and slow process of the total inhibition (red, blue), compared to the overall reversibility of the inhibition at different potentials (depicted in black). Although caution in interpreting these data has to be taken because of the significant errors, the general trend is that the proportion of the fast phase increases as the potential is raised. This stands in contrast to formaldehyde inhibition, which follows the opposite behaviour [8]. Inhibition of hydrogen oxidation by CF_3CHO shows higher reversibility than inhibition of hydrogen formation and the former is enhanced compared to high potential inhibition by HCHO. Although the amount of fast phase shows the opposite trend with potential depending upon whether HCHO or CF_3CHO is used, in both cases a higher proportion of the fast inhibition process leads to more reversibility.

Fig. 3.7 Comparisons of the potential dependences of the proportions of CF_3CHO inhibition that are due to the fast (*red*) and slow (*blue*) process with the average overall reversibility of the inhibition reaction (*black*). Error bars represent one standard deviation; all measurements were carried out in triplicate



3.2.3 Inhibition by Acetaldehyde

The potential dependence of MeCHO inhibition of *CaHydA* is depicted in Fig. 3.8. In the hydrogen production region at potentials below -0.4 V, MeCHO inhibition shows a trend similar to both HCHO and CF_3CHO inhibition, i.e. increasing inhibition with decreasing potential. Because of the high volatility of MeCHO (bp 20°C), experiments were performed at a lower temperature (5°C) compared to all other aldehydes used in this work (20°C) and the gas flow was interrupted simultaneously to aldehyde injection, until the end of the buffer exchange (rinsing step). The effect of H_2 consumption at high potential during the 5 min of MeCHO exposure was determined in control experiments where buffer was injected in place of aldehyde: less than 5% of activity was lost in these experiments (see Appendix C). Therefore, the impact of the substrate depletion on the activity of *CaHydA* is negligible compared to actual inhibition by acetaldehyde. A relatively high concentration of acetaldehyde was required for significant inhibition to be observable, $168\ \mu\text{M}$ non-hydrated MeCHO was used compared to $2.25\ \mu\text{M}$ non-hydrated formaldehyde and $6.3\ \mu\text{M}$ CF_3CHO .

Although inhibition increases as the potential is lowered, the total extent of inhibition is much lower than for HCHO. Similar to CF_3CHO , but in contrast to HCHO, MeCHO shows higher degrees of inhibition of hydrogen oxidation than proton reduction. The extent of MeCHO inhibition is approximately twice as great as that of CF_3CHO inhibition, although more than 50 times more MeCHO was used. Assuming scalability, this indicates greater reactivity of CF_3CHO compared to MeCHO, in agreement with the former's more electrophilic $\text{C}=\text{O}$ group.

Although acetaldehyde inhibition is at least partially reversible both in the H_2 oxidation and in the H_2 evolution regime (see Fig. 3.3), no clear trend in

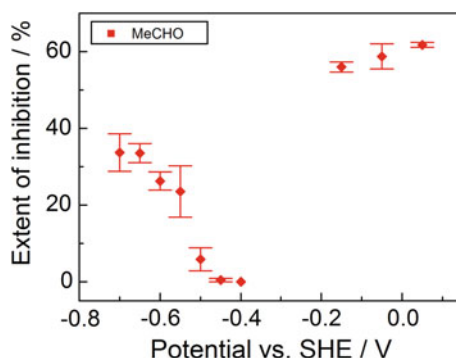


Fig. 3.8 Percentage inhibition of *CaHydA* by acetaldehyde after 100 s of exposure. Conditions: $336\ \mu\text{M}$ MeCHO solution, 5°C , dark, $\omega = 3000$ rpm, pH 6.0 phosphate buffer, 100% H_2 (interrupted during 5 min exposure to MeCHO). MeCHO has an equilibrium constant of 1, i.e. $336\ \mu\text{M}$ MeCHO corresponds to $168\ \mu\text{M}$ of non-hydrated aldehyde. Error bars represent one standard deviation; all measurements were carried out in triplicate

reversibility was observed across the potential window studied. The kinetics of the inhibition could not be determined due to the relatively large errors of the experiments, particularly at low potential, which are due to the complex experimental conditions that had to be employed with MeCHO. Although the interrupted H₂ flow had only marginal effects on H₂ consumption over the course of the experiments (vide supra), simultaneous aldehyde injection and removal of the H₂ gas inlet caused the initial decay in activity to differ slightly between repeats.

3.2.4 Inhibition by Butyraldehyde

Butyraldehyde is significantly less soluble in water than the C1 and C2 analogues described in the previous sections. The maximum aldehyde concentration that could be employed in the experimental set-up was 30 mM. The potential dependence of the inhibition of CaHydA by PrCHO is shown in Fig. 3.9. At potentials below -0.4 V, it is qualitatively similar to the dependences recorded for MeCHO and CF₃CHO, but PrCHO shows much less inhibition.

In the hydrogen production region (below -0.4 V) in Fig. 3.9 the reactivity increases when the potential is lowered. At intermediate and high potentials, no clear trend is apparent. This is also the case for the kinetic rate constants (Fig. 3.10). Two separate processes occur across the whole potential range. The fast process (k_{fast}), is generally approximately 10 times faster than the slow process (k_{slow}), but no correlation between potential and rate constants can be drawn.

Figure 3.11 shows that inhibition by PrCHO is partially reversible, but no clear tendency can be observed across the potential window studied.

Fig. 3.9 Percentage inhibition of PrCHO after 100 s of exposure. Conditions: CaHydA, 100% H₂, 30 mM PrCHO, 20 °C, $\omega = 3000$ rpm, pH 6.0 phosphate buffer, dark. Error bars represent one standard deviation; all measurements were carried out in triplicate

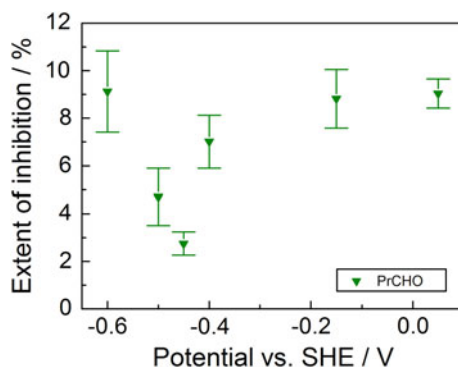


Fig. 3.10 Potential dependences of the average rates constants of the fast (red) and slow (blue) phase of the biphasic reaction of PrCHO with CaHydA. Error bars represent one standard deviation of propagated errors from least-square analysis of the inhibition kinetics. All measurements were carried out in triplicate

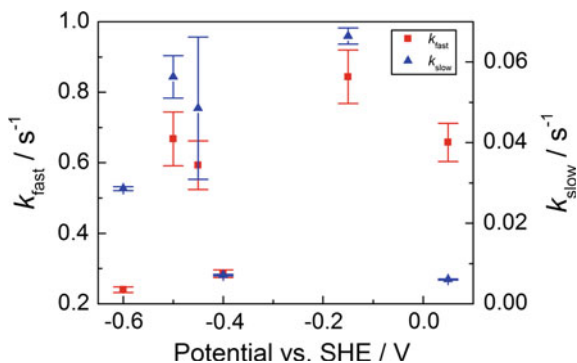
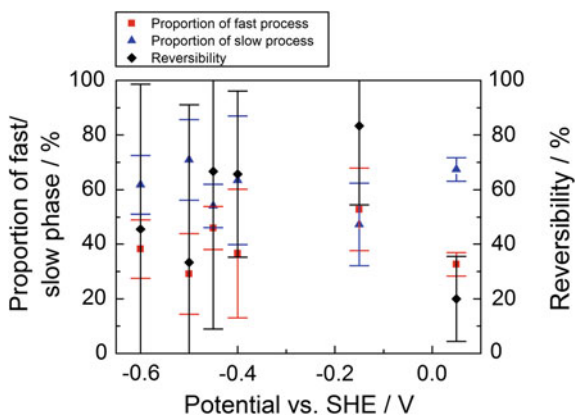


Fig. 3.11 Comparisons of the potential dependences of the proportions of PrCHO inhibition that are due to the fast (red) and slow (blue) process with the average overall reversibility of the inhibition reaction (black). Error bars represent one standard deviation; all measurements were carried out in triplicate



3.2.5 Inhibition by Isovaleraldehyde

The branched aldehyde *i*-BuCHO is the least water-soluble aldehyde used in this work. Its reactivity towards CaHydA is intrinsically low, even at the maximum concentration of 30 mM that could be used in the electrochemical cell. The potential dependence of the extent of inhibition of CaHydA by *i*-BuCHO is depicted in Fig. 3.12. Isovaleraldehyde clearly shows the least inhibition of all the different aldehydes studied.

All recorded current vs. time traces follow bi-exponential decomposition pathways. Similar to inhibition by PrCHO, the obtained rate constants do not follow any trend (Fig. 3.13).

As depicted in Fig. 3.14, the proportion of the fast phase increases as the potential is raised (for potentials > -0.4 V). The inhibition at low potential is irreversible, indicating *i*-BuCHO might not be able to reach the active site of the enzyme.

Fig. 3.12 Percentage inhibition of *i*-BuCHO after 100 s of exposure. Conditions: CaHydA, 100% H₂, 30 mM *i*-BuCHO, 20 °C, $\omega = 3000$ rpm, pH 6.0 phosphate buffer, dark. Error bars represent one standard deviation; all measurements were carried out in triplicate

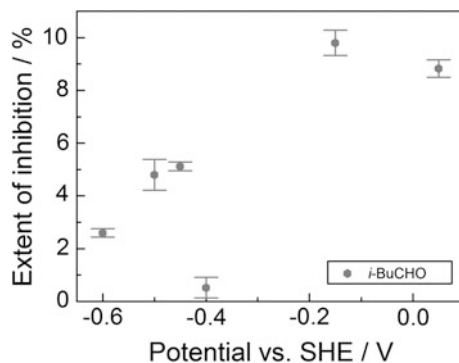


Fig. 3.13 Potential dependences of the average rate constants of the fast (*red*) and slow (*blue*) phase of the biphasic reaction of *i*-BuCHO with CaHydA. Error bars represent one standard deviation of propagated errors from least-square analysis of the inhibition kinetics. All measurements were carried out in triplicate

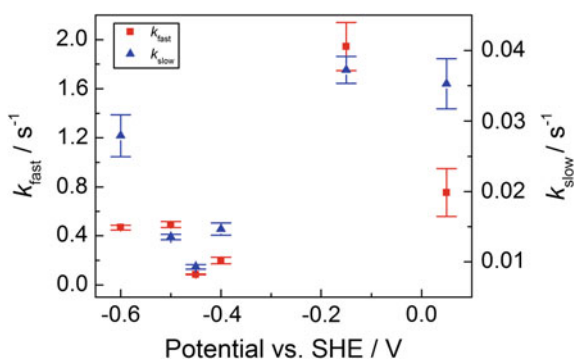
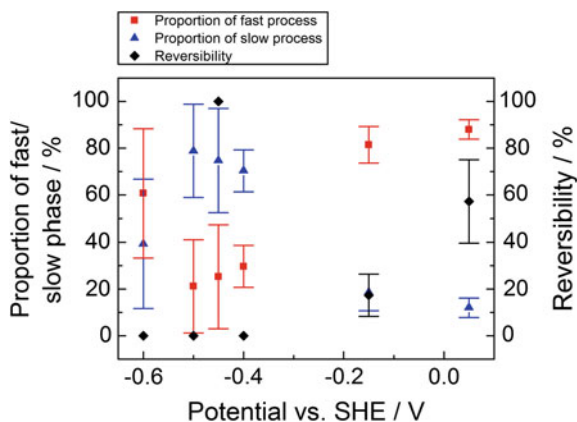


Fig. 3.14 Comparisons of the potential dependences of the proportions of the fast (*red*) and slow (*blue*) process with the average overall reversibility of the inhibition reaction (*black*). Error bars represent one standard deviation; all measurements were carried out in triplicate



3.3 Discussion

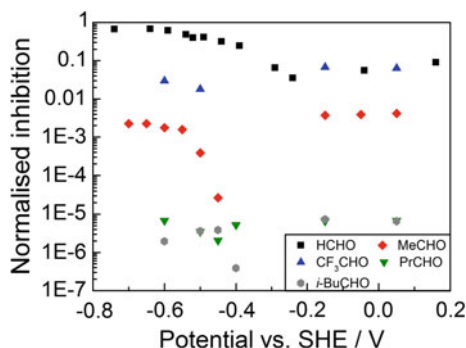
3.3.1 Discussion of the Different Aldehyde Reactivities

If aldehyde inhibition of [FeFe]-hydrogenases takes place at the active site, either at the Fe_d atom or at the pendant amine group (adt-N), the size and electrophilicity of the aldehyde should have a strong influence on its reactivity towards the enzyme. All aldehydes apart from the ‘bulky’ *i*-BuCHO show at least partial reversibility over the entire potential region studied, indicating that these molecules can penetrate into the enzyme, and reaction pathways at the H-cluster similar to those proposed for formaldehyde are feasible.

Both CF₃CHO and MeCHO are similar in steric demand, but the former possesses a more electrophilic C=O group. In the H₂ production regime, both show increased inhibition as the potential is lowered, in agreement with postulated reactivity towards the H_{ox-2} level of the H-cluster. However, both aldehydes also show reversible inhibition at high potential, in contrast to HCHO. Concentrations significantly higher than those used for experiments involving HCHO had to be employed to observe measurable inhibition. At low potential, the potential dependence of inhibition by PrCHO is qualitatively similar to CF₃CHO and MeCHO, but PrCHO shows much less reactivity. *i*-BuCHO shows the least inhibition of all aldehydes employed in this work and reacts irreversibly with *CaHydA* at low potentials.

Figure 3.15 shows a comparison between the normalised potential dependences of all four aldehydes, revealing orders of magnitude differences in (concentration corrected) reactivity. One has to be cautious and avoid a quantitative interpretation of this comparison, due to normalisation over a large concentration range, but qualitative trends become apparent: the order of reactivity HCHO > CF₃CHO > MeCHO > PrCHO > *i*-BuCHO suggests that the less electrophilic and sterically accessible the carbonyl C-atom (the former because of positive inductive effects of the different alkyl substituents and the latter due to increasing steric hindrance caused by the alkyl groups), the lower the reactivity at

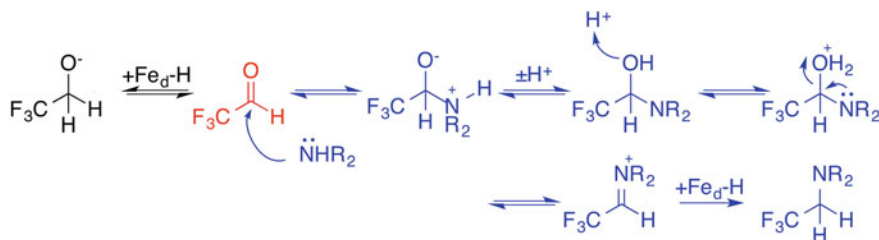
Fig. 3.15 Comparison of the normalised (i.e. concentration corrected) extent of inhibition as a function of potential for the four different aldehydes studied in this work, measured after 100 s of exposure. Data for formaldehyde inhibition were taken from Ref. [1]



low potentials where the H_{Ox-2} level prevails and the enzyme is most active for H_2 formation. The correlation suggests that these aforementioned properties of the aldehydes modulate their reactivities at the enzyme active site, corroborating the hypothesis of aldehyde inhibition occurring at the H-cluster, preferably targeting the H_{Ox-2} level, as proposed for HCHO [1].

Kinetic analyses of the inhibition reactions of the different aldehydes were carried out with the aim of gaining more insight into the possible reaction pathways. All aldehydes display biphasic inhibition kinetics, but no direct correlations between fast/slow reaction and reversibility (as is the case for HCHO [1, 2, 8, 19]) could be determined. Instead, the picture is more complex. Whereas formaldehyde shows relatively ‘clean’ reactivity, with the proportion of the dominating, fully reversible rapid reaction increasing as the potential is lowered, aldehydes of larger size are more likely to react with nucleophilic groups at the protein periphery or in the gas channels (blocking substrate delivery and product removal to and from the active site) since access to the H-cluster is likely to be restricted. Furthermore, different reactivities towards the *adt-N* moiety of the H-cluster have to be taken into account. For example, HCHO and CF_3CHO cannot form enamines due to the lack of α -carbonyl protons. Although formation of enamines is theoretically a reversible reaction, these are expected to be thermodynamically (*meta*-) stable products. Possible reaction pathways of CF_3CHO and the H-cluster are depicted in Scheme 3.3, specifically reduction by Fe_d -hydrido species (black) and nucleophilic attack by *adt-N* (blue). Since α -protons in CF_3CHO are replaced with fluorine substituents, the only likely fate of an iminium ion formed by Schiff base chemistry, other than the reverse reaction, is irreversible reduction with an iron hydride to form a fluorinated alkylamine.

The higher irreversibility of CF_3CHO inhibition at low potentials compared to HCHO (see Fig. 3.7) can in principle be rationalised by equilibration to the iminium ion and its subsequent reduction (blue pathway in Scheme 3.3) being the dominant pathway over direct Fe_d -H reduction of the carbonyl bond. This would be in agreement with the more bulky nature of CF_3CHO compared to HCHO; greater steric demand might likely favour reaction at the more easily accessible *adt-N*. The greater reversibility of the inhibition at high potentials could be explained by the fact that Schiff base chemistry cannot proceed beyond reversible equilibration to the

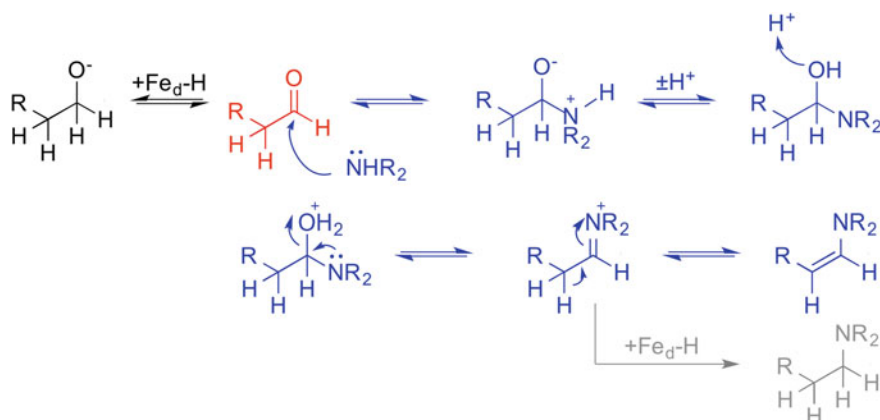


Scheme 3.3 Possible reactions of CF_3CHO (red) with the H-cluster. Alkoxide formation through hydride transfer from Fe_d is depicted in black. Iminium chemistry is shown in blue

iminium ion, since neither highly reducing metal-hydrido species nor α -protons required for enamine formation are available.

In contrast to CF_3CHO , MeCHO , PrCHO , and $i\text{-BuCHO}$ do possess α -protons, and reversible enamine formation is possible, in addition to the interception of Fe-H species that occur transiently at the H-cluster. The different reaction pathways are outlined in Scheme 3.4. For acetaldehyde, direct reduction of the carbonyl carbon by a metal-hydrido bond formed in a reduced H-cluster state (black pathway) would be in agreement with the observed potential dependence (Fig. 3.8), since the reactivity of the H-cluster increases as the potential is lowered. Electrophilic attack of MeCHO on adt-N is projected to yield, initially, the iminium ion (via the aminol). Subsequently, two different routes have to be considered: irreversible hydride transfer to form a tertiary amine (grey pathway) and reversible enamine formation (depicted in blue). Although iminium ions are considerably easier to reduce than carbonyl bonds, under strong reducing conditions (i.e. low potentials), direct reaction with the aldehyde is still expected to be the kinetically dominant pathway, since the former species are only accessible through a multistep equilibrium.

Acetaldehyde inhibition at potentials where CaHydA catalyses H_2 oxidation (> -0.3 V) displays a different potential dependence to inhibition by formaldehyde. CaHydA shows very little formaldehyde inhibition ($< 15\%$, irrespective of the applied potential in this region; Fig. 3.4), whereas $\sim 60\%$ of activity is inhibited by acetaldehyde (Fig. 3.8). Since inhibition of H_2 oxidation at high potentials is, due to the absence of reducing species such as metal-hydrides, less likely to stem from direct hydride transfer, the potential independent iminium chemistry can be expected to prevail, leading to enamine formation. Conversely, formaldehyde *cannot* form enamines due to the lack of α -protons, a fact that might contribute to the observed difference in reactivity between these two



Scheme 3.4 Possible reaction pathways of MeCHO , PrCHO , and $i\text{-BuCHO}$ with the H-cluster. Hydride transfer to the carbonyl bond is depicted in *black*, Schiff base chemistry at the bridgehead N atom of the H-cluster is shown in *blue*, and formation of a tertiary amine is shown in *grey*. $\text{R} = -\text{H}$ (MeCHO), $-\text{CH}_2\text{CH}_3$ (PrCHO), or $-\text{CH}(\text{CH}_3)_2$ ($i\text{-BuCHO}$)

aldehydes. The greater extent of acetaldehyde inhibition at high potentials compared to formaldehyde indicates that nucleophilic attack by the adt-N moiety might be more favoured for acetaldehyde. This may be related to the greater steric demand of acetaldehyde, possibly limiting access to Fe_d compared to the pendant amine group.

Nucleophilic attack by adt-N on the carbonyl carbon proceeds via the hemiaminal (Schemes 3.3 and 3.4). Although it is an intermediate in the equilibrium towards formation of the iminium ion (and further products), the hemiaminal *itself* can be stabilised through secondary ligation (by its $-\text{O}^-$ group) to Fe_d , which has a vacant coordination site in the H_{ox} state. Figure 3.16 depicts the resulting species, which can, principally, account for reversible inhibition of the H-cluster (by all four aldehydes studied in this work) at oxidising potentials.

In principle, both PrCHO and *i*-BuCHO should follow the same reaction pathways as acetaldehyde (Scheme 3.4 or Fig. 3.16). In PrCHO, even though free rotation is allowed in the two additional σ -bonds compared to MeCHO/CF₃CHO, the increased chain length seems to have a profound effect on the extent of inhibition, which is significantly lower compared to its smaller analogues. The increase in inhibition with added driving force in the hydrogen production region shown in Fig. 3.9 (between -0.45 and -0.6 V) might indicate that this aldehyde can, to some extent, reach and react with the H-cluster. However, inhibition is only partially reversible, no coherent reactivity pattern is observable at intermediate to high potentials, and there is no correlation between potentials, rate constants, and reversibility (Figs. 3.10 and 3.11). Thus, processes other than reaction at the active site must be taken into account, including reaction at nucleophilic residues surrounding the active site or at the periphery of the protein, possibly blocking H₂ binding sites or disturbing the proton transfer chain.

The low inhibition observed with *i*-BuCHO suggests that this relatively bulky molecule can hardly, if at all, reach the enzyme active site (Fig. 3.12). Inhibition in the hydrogen oxidation region could stem from reaction at the periphery of the protein (*vide supra*). These reactions have not been explicitly taken into account for the other aldehydes apart from PrCHO, as they do not explain the potential dependences observed for these molecules. The fact that inhibition by *i*-BuCHO at

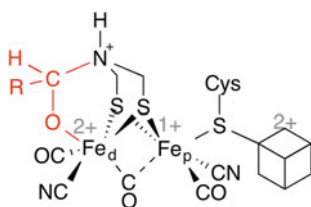


Fig. 3.16 Possible aldehyde adduct to the H-cluster in the H_{ox} state, formed upon hemiaminal formation following electrophilic attack of the aldehyde carbonyl-C on adt-N of the enzyme active site. R = $-\text{H}$ (HCHO), $-\text{CH}_3$ (MeCHO), $-\text{CF}_3$ (CF₃CHO), $-(\text{CH}_2)_2\text{CH}_3$ (PrCHO), or $-\text{CH}_2\text{CH}(\text{CH}_3)_2$ (*i*-BuCHO)

low potential is irreversible (Fig. 3.13) supports the hypothesis that this branched aldehyde cannot reach the active site.

In general, the observed reactivity trends of the four different aldehydes investigated by PFE (Fig. 3.15) seem to support previous mechanistic hypotheses [1] and suggest that aldehydes can target and inhibit the active site of [FeFe]-hydrogenases. However, the complex kinetic patterns the different aldehydes displayed over the examined potential window stand in stark contrast to inhibition by formaldehyde, where a fast, fully reversible process dominates inhibition of H₂ formation and a slower, potential independent process is responsible for (marginal) inhibition of H₂ oxidation [8, 19]. Further, the fact that only partial reversibility was observed for these ‘longer chain’ aldehydes strongly suggests a more complex picture than with formaldehyde, i.e. additional, different processes occur. Aldehydes are highly reactive electrophiles that can target many nucleophilic residues and positions in the complex and intricate structures of [FeFe]-hydrogenases.

An inherent disadvantage of PFE is that it does not provide any structural information. Hence, the mechanistic proposals put forward in this chapter, as attractive or unattractive as they may be, have in common that they lack structural evidence and therefore remain speculative. In order to determine the *mode* of binding and the *mechanism* of inhibition, one has to utilise other, structure-specific techniques, such as EPR spectroscopy. Implications from investigations of HCHO inhibition by advanced EPR-techniques, supported by density functional theory, are presented in the following sections.

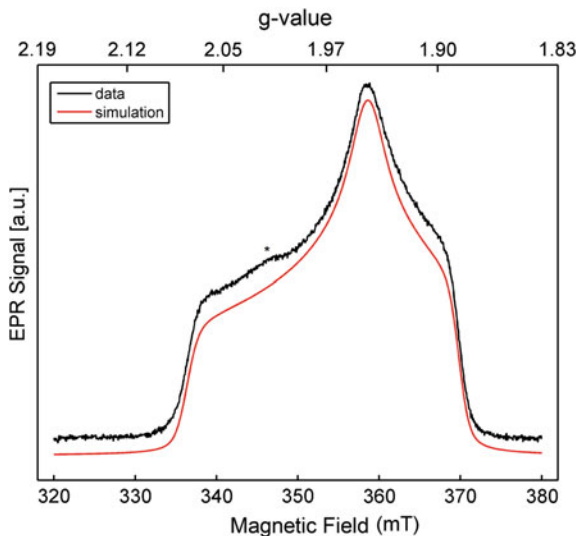
3.3.2 *Implications from the Investigation of Formaldehyde Inhibition of the H-Cluster by Pulsed-EPR Techniques*

3.3.2.1 **Formaldehyde Inhibition of the H-Cluster Detected by ENDOR and ESEEM**

Pulsed-EPR experiments were undertaken with the aim of directly determining the binding mode of formaldehyde to the H-cluster, using the enzyme *CrHydA1* (instead of *CaHydA*) because of its lack of F-clusters, which would give rise to complicated EPR-signatures. The experiments were conducted in collaboration with Dr. William Myers (Centre for Advanced Electron Spin Resonance, University of Oxford), who developed the mathematical model for analysis of the pulsed-EPR spectra, analysed and simulated the data, and prepared the figures presented in this section.

Figure 3.17 shows the integrated free-induction decay (FID) X-band EPR spectrum of H₂-reduced *CrHydA1* in the presence of HCHO. I equilibrated the sample in an anaerobic glove box under H₂ flow for 3.5 h before injecting formaldehyde into the enzyme solution to give a final concentration of free, (i.e. non-hydrated) HCHO equal to the concentration of *CrHydA1* (see Sect. 8.2.4). The spectrum features a rhombic system consistent with a reduced cubane cluster

Fig. 3.17 X-band FID-detected EPR spectrum, recorded at 10 K (black), and a simulation (red) of formaldehyde-inhibited *CrHydA1*, at a spin concentration of 830 μM . The $\pi/2$ pulse length was 320 ns. Simulation values were $g_x = 2.074$, $g_y = 1.946$, $g_z = 1.886$. A degradation product at $g = 2.025$ is indicated (*). Reprinted with permission from Ref. [5]. Copyright 2015 American Chemical Society



($[\text{4Fe-4S}]^{1+}$) [20], meaning that the great majority of spin density resides on $[\text{4Fe-4S}]_{\text{H}}$. EPR simulation yields g values of 2.074, 1.946, and 1.886, in agreement with those observed previously for $\text{H}_{\text{ox-2}}$ [11, 21]. The minor signal at $g = 2.025$ most likely corresponds to a slowly formed decay product following HCHO inhibition of *CrHydA1*. This observation is consistent with PFE results, where small proportions of slow, irreversible inhibition are observed when *CrHydA1* is subjected to HCHO at negative potentials (even though fast, reversible inhibition is the dominant pathway) [8]. For comparison, the derivative continuous-wave (CW) spectrum of the same sample, also obtained at X-band, is shown in Appendix D.

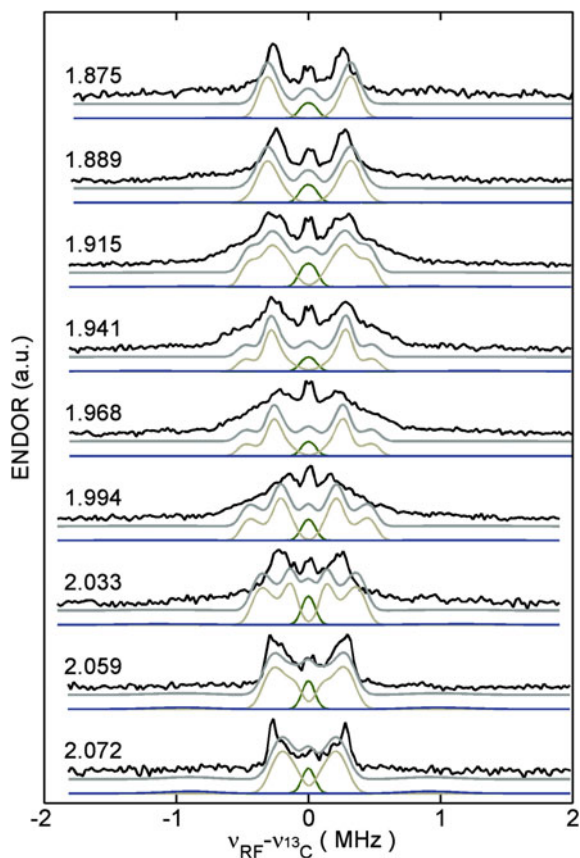
To characterise the interaction of formaldehyde with the H-cluster in the $\text{H}_{\text{ox-2}}$ level, pulsed-ENDOR spectra of ^{13}C -labelled HCHO were recorded at Q-band¹ for several g values, as shown in Fig. 3.18 (at the extreme g values, the single-crystal-like spectra provide the highest resolution of different classes of ^{13}C [22]). The observed ENDOR frequencies for the hyperfine interaction (A) of $A/2$ less than the nuclear Larmor frequency are

$$\nu_{\text{ENDOR}}^{\pm}(^{13}\text{C}) = \nu(^{13}\text{C}) \pm |A(^{13}\text{C})|/2. \quad (3.1)$$

Here, $\nu(^{13}\text{C})$ is the nuclear Larmor frequency and $A(^{13}\text{C})$ corresponds to the hyperfine interaction value for an arbitrary orientation of the electron-nucleus vector in the magnetic field. The ENDOR data were analysed using the following equation:

¹ENDOR measurements performed at Q-band afford increased orientation selection and separate the ^{13}C Larmor frequency from overlapping ^{14}N frequencies that are of concern at X-band.

Fig. 3.18 Q-band Mims ENDOR spectra (black) and simulations of H^{13}CHO inhibited CrHydA1 recorded at several g values, as indicated. For all traces the temperature was 8 K, with a τ value of 250 ns, $\pi(\text{RF}) = 80 \mu\text{s}$, repetition time of 20.4 ms; the microwave frequency was 33.7704 GHz [5]. Reprinted with permission from Ref. [5]. Copyright 2015 American Chemical Society



$$\mathbf{A} = a_{\text{iso}}\mathbf{1} + g\mathbf{T}/g_e, \quad (3.2)$$

where \mathbf{A} is the full hyperfine tensor, a_{iso} is the isotropic value of \mathbf{A} , defined as its mean, $\mathbf{1}$ is the identity matrix, and \mathbf{T} is the dipolar component for the nucleus which is scaled by the effective g value, g/g_e . In the principle axis of a point-dipole interaction \mathbf{T} is defined as

$$\mathbf{T} = \frac{\mu_0}{4\pi h} \frac{g_e \mu_B g_n \mu_n}{r^3} \rho_{\text{Fe}} \begin{bmatrix} -1 & -1 & 2 \end{bmatrix} = \begin{bmatrix} -T & -T & 2T \end{bmatrix}. \quad (3.3)$$

Importantly, Eq. (3.3) shows that the dipolar interaction is proportional to the spin density of the Fe centre, ρ_{Fe} (but also dependent on the distance, r), and this could be appropriate for coordination at the distal Fe, more than 8 Å away from the spin-bearing $[\text{4Fe-4S}]_{\text{H}}^{1+}$ subdomain. However, since for a mixed-valence metal cluster \mathbf{T} is a summation of dipolar interactions of *all* spin densities with a given nucleus, an approximate local spin model was developed (by Dr. William Myers)

that is sufficiently accurate to test trial locations for the coordination of HCHO in the presence of the $[4\text{Fe-4S}]_{\text{H}}^{1+}$ and $[2\text{Fe}]_{\text{H}}$ domains of the H-cluster [5]. In addition to Fe_{d} , other sites that are able to undergo nucleophilic attack at the HCHO carbonyl carbon also constitute points of interest, including adt-N and the bridging CO position between Fe_{p} and Fe_{d} , which has recently been suggested to be occupied by a μ -hydrido ligand in the $\text{H}_{\text{ox-2}}$ level, most likely separate from the catalytic H_{Sred} state (vide infra) [10].

In Fig. 3.18, ^{13}C hyperfine interaction with formaldehyde that is remote from Fe_{d} is seen in the centre of the spectrum as a small peak that is somewhat suppressed (with a τ value of 250 ns). This signal does not stem from naturally occurring ^{13}C atoms in the protein close to the active site (as, for example, observed in ^{13}C ENDOR studies on CO inhibited nitrogenase [23]), as ENDOR experiments using unlabelled H^{12}CHO show no such signal contributions (Appendix E).

The splitting of about 0.6 MHz at both extreme g values in Fig. 3.18 changes over the EPR envelope, to approximately 1.2 MHz in width for broad shoulders, with the maximum intensity narrowing to 0.3 MHz at intermediate fields. These variations suggest that the dipolar component is larger than the isotropic component [5]. Simulation using $A_{\text{iso}} = 0.12$, and $T = 0.55$ represents the field dependent pattern, but cannot account for the orientational distributions that give rise to the low resolution shoulders in Fig. 3.18. Simulations using the approximate local spin model show that dipolar components required to fit the shoulders in intermediate fields in Fig. 3.18 (i.e. $A_{\text{max}} \approx 1.2$ MHz) could arise only through positions of formaldehyde that either bisect the azadithiolate bridge or positions lying on the side of adt-bridge closer to the $[4\text{Fe-4S}]_{\text{H}}^{1+}$ subcluster [5].

A third class of ^{13}C contributes to the ENDOR data in Fig. 3.18 with very low intensity as shoulders at ± 0.5 MHz at $g = 2.072$ and as slight peaks near ± 0.9 MHz at $g = 1.875$. X-band HYSORE data recorded on the same H^{13}CHO -inhibited *CrHydA1* sample suggest these signals are largely isotropic rather than dipolar in character, but the intensity is insufficient for detailed analysis [5]. In short, while ^{13}C hyperfine interactions detected in ENDOR experiments on H^{13}CHO -inhibited *CrHydA1*, poised in the $\text{H}_{\text{ox-2}}$ level, unambiguously show that formaldehyde can access the H-cluster, the complicated nature of these interactions also reveals a complex picture where binding takes place in multiple orientations.

As it is possible to determine the number of equivalent nuclei of a particular type of coupling with the electron spin from the ESEEM modulation depth (Sect. 2.5.4), 3-pulse ESEEM experiments were carried out (using deuterated formaldehyde, DCDO) to gain insight into the relative amounts of the different formaldehyde-bound species suggested by the aforementioned ENDOR experiments. The modulation depth in the ESEEM data presented in Fig. 3.19a is primarily due to weakly coupled formaldehyde [24] and simulations suggest *six* weak ^2H hyperfine interactions that are randomly oriented [5].

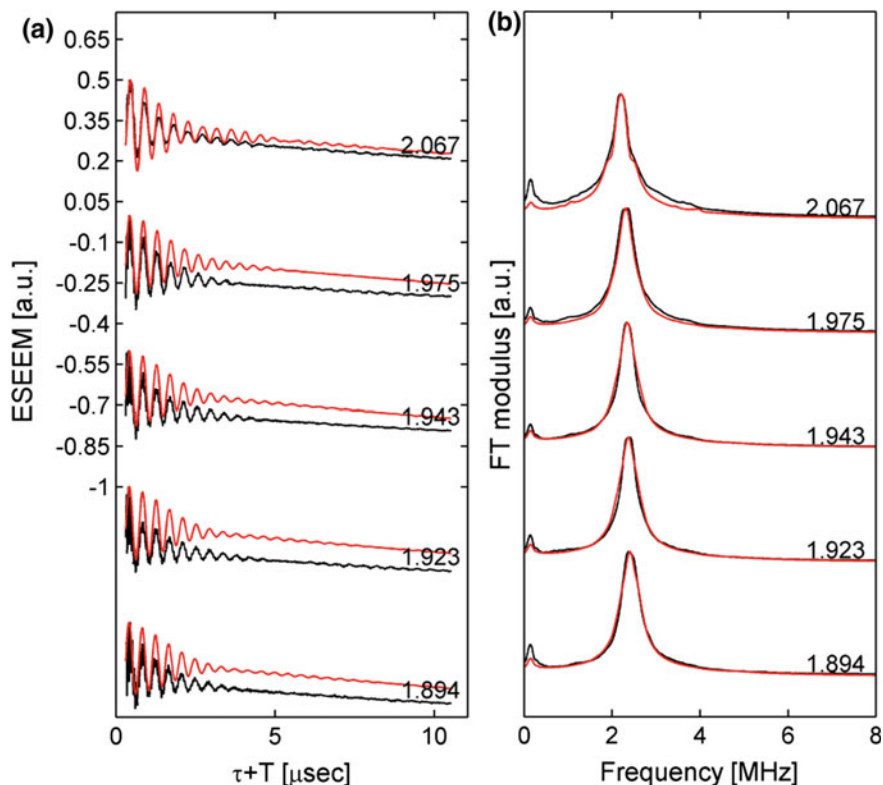


Fig. 3.19 X-band 3-pulse ESEEM of DCDO inhibited CrHyA1 (*black*) and simulations (*red*) at several g values as listed for **a** time domain and **b** frequency domain. The temperature was 12 K, microwave frequency of 9.7491 GHz, at a field of 337.2 mT. For ESEEM, $\tau = 212$ ns, with an initial T of 100 ns, a time step of 20 ns, and a shot repetition time of 1.36 ms [5]. Reprinted with permission from Ref. [5]. Copyright 2015 American Chemical Society

3.3.2.2 Implications

The pulsed-EPR experiments presented above establish that formaldehyde can access the active site of the H-cluster and simulations indicate *several* possible binding sites. When evaluating these from a mechanistic perspective, one needs to take into account a recent study that suggests, based on observations by site-selective XAE spectroscopy, a bridging μ -hydrido ligand between Fe_p and Fe_d might be formed and accumulate in the $\text{H}_{\text{ox}-2}$ level under conditions similar to the way EPR samples were prepared in this work, i.e. under H_2 flow without the presence of an external redox partner [10]. Although the ENDOR results cannot rule out the existence of such a species, it is unlikely that it can be a catalytic intermediate of *mechanistic* relevance, given the recently established requirement for the organic bridging ligand to be *adt* [25–27], an observation that is rationalised by the bridgehead N-atom acting as the pendant base, lying in close proximity to

Fe_d to cleave H₂ in the manner of a frustrated Lewis pair mechanism (Scheme 1.1). Further, although it would be thermodynamically more stable than its terminal analogue, formation of a bridging hydride seems to be kinetically hindered, as it would require rearrangement of surrounding amino acids at a significant energetic cost. In the [FeFe]-hydrogenase from *Clostridium pasteurianum* the salt bridge that holds Lys358 in place (Lys358 is conserved in other [FeFe]-hydrogenases) to form a hydrogen bond to the Fe_d ligated CN⁻ is stabilised by a binding energy of 99 kcal mol⁻¹ [28].

To help understand how formaldehyde inhibits the *mechanism* of hydrogen formation by [FeFe]-hydrogenases, i.e. the catalytic cycle, the EPR results presented above need to be evaluated in the context of other experimental and theoretical observations, thus placing realistic chemical constraints on possible binding modes. PFE experiments [1, 2] established that the *rapid* binding of formaldehyde under catalytic turnover occurs with $\tau = 7.89$ s at -0.56 V (Fig. 3.1) and is *fully reversible*, and the formaldehyde-inhibited state is fully recovered after 300 s, a timescale similar to the EPR sample preparations. Further, as depicted in Fig. 3.4, this reversible process exhibits a strong potential dependence, with the most reduced level H_{ox-2} showing the highest degree of inhibition. Taken together with the EPR results that firmly establish the presence of formaldehyde in the vicinity of the H-cluster, these observations strongly suggest that HCHO reacts at a mechanistically important site in the H-cluster, i.e. Fe_d, the likely site of H₂ binding, as inferred from CO inhibition studies [29]. If formaldehyde were to react with a hydrido-ligand bound to Fe_d (or bridging between Fe_d and Fe_p) as originally proposed (Scheme 3.2) [1], a methoxide species would be formed. However, release of methanol is not detected [8], and it has recently been suggested that hydride formation only occurs upon reduction of H_{ox-1} [4, 11], indicating that formaldehyde is very likely to intercept the H-cluster *before* formation of a Fe-hydride in the most reduced state of the enzyme. In light of these arguments, DFT calculations were conducted by Professor John McGrady (Inorganic Chemistry Laboratory, University of Oxford) on a likely candidate that may form during turnover and is consistent with the aforementioned restraints.

3.3.3 *Insight from Density Functional Theory*

Scheme 3.1 highlighted the fact that the precise order of protonation and electronation steps that ultimately lead to release of H₂ is uncertain. The combination of the EPR results presented in the previous section and the lack of methanol detection [1, 8] suggests that formaldehyde might intercept the H_{ox-2} level *before* hydride formation at Fe_d rather than afterwards, as assumed previously [1], since hydride transfer to the carbonyl-C should produce methoxide. Based on DFT calculations, Bruschi and colleagues proposed a number of possible intermediates that link H_{ox} and hydrido-forms of the H_{ox-2} level including one, ‘H_{ox-2}(H⁻)’ (denoted H_{sred}-H⁻ in Scheme 1.1), where Fe_d carries a terminal hydride and adt-N is unprotonated.

This species bears a strong consistency with one of the species responsible for the ^{13}C ENDOR signal and the strong potential dependence of inhibition observed in PFE experiments. $\text{H}_{\text{ox-2}}(\text{H}^-)$ is in the $\text{H}_{\text{ox-2}}$ electronation level and Fe_d is coordinatively saturated, with a small amount of spin density delocalised onto Fe_d [3]. Density functional theory was therefore used to explore potential modes for formaldehyde binding to Fe_d in the $\text{H}_{\text{ox-2}}$ level *in place* of a proton. The computational protocol followed closely that established by Bruschi et al. [3] in that the protein active site from the H-cluster of *Desulfovibrio desulfuricans* was taken and truncated as shown in Fig. 3.20, with four methyl carbons frozen at their crystallographic positions. Total energies and Mulliken spin densities for the various stationary points are summarised in Table 3.1.

Introduction of a HCHO molecule in the vicinity of Fe_d yields a rather weakly bound intermediate **I** with Fe–C and Fe–O distances of 2.86 and 3.56 Å, respectively (**I** in Fig. 3.20 and Table 3.1). In **I**, formaldehyde is stabilised by a hydrogen bond to the proton on adt-N, but is otherwise not strongly bound. The spin density on $[\text{2Fe}]_{\text{H}}$ is negligible in **I** (< 0.03 electrons in total) which, consistent with the spectroscopically characterised (H_{Sred}) form of $\text{H}_{\text{ox-2}}$ [11], is formulated as a $[\text{4Fe-4S}]^{1+}$ species. The net spin densities and values of $\langle S^2 \rangle$ suggest that the electronic structure of **I** is well described as an exchange-coupled $[\text{4Fe-4S}]^{1+}$ cluster.

Protonation of adt-N, i.e. addition of a proton to the system, leads to formation of a *direct Fe–C covalent bond* (Fe–C = 2.11 Å), accompanied by transfer of a proton from adt-N to the O atom of HCHO (structure **II** in Fig. 3.20—note the ‘mirror

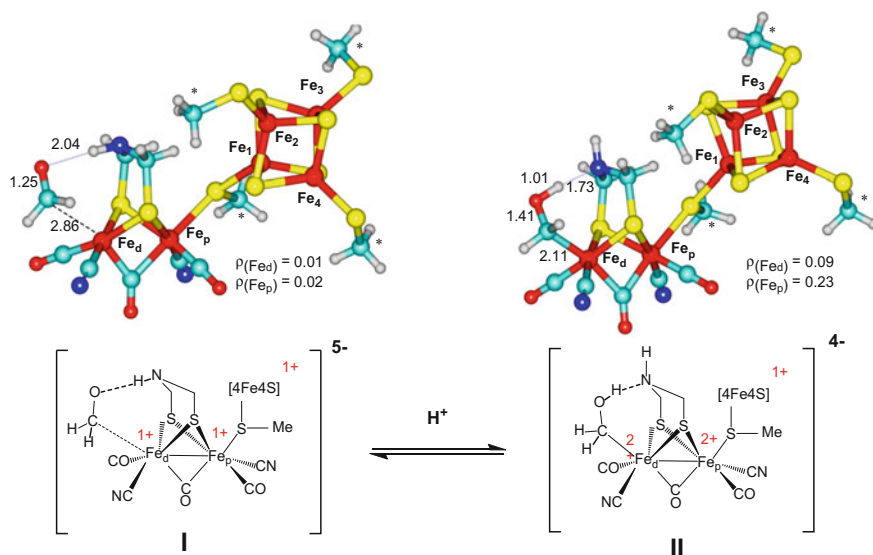


Fig. 3.20 DFT-computed structures for possible adducts of $\text{H}_{\text{ox-2}}$ and HCHO. Asterisks indicate methyl carbons that are frozen during the geometry optimisation process [5]. Reprinted with permission from Ref. [5]. Copyright 2015 American Chemical Society

Table 3.1 Total energies and Mulliken spin densities for the formaldehyde adducts I and II depicted in Fig. 3.20 [5]

Functional	HCHO (I)	$\bar{\text{C}}\text{H}_2\text{OH}$ (II)	
	BP86	BP86	B3LYP
Energy / au	-12,501.3804	-12,501.9462	-12,500.4320
$\langle S^2 \rangle$	6.53	6.68	8.01
$\rho(\text{Fe}_1)$	3.16	3.11	3.51
$\rho(\text{Fe}_2)$	3.12	3.05	3.60
$\rho(\text{Fe}_3)$	-2.97	-3.04	-3.44
$\rho(\text{Fe}_4)$	-2.69	-2.69	-3.28
$\rho(\text{Fe}_p)$	0.02	0.23	0.03
$\rho(\text{Fe}_d)$	0.01	0.09	0.01
$\rho(\text{S}_{\text{br}})$	0.05	0.01	0.04

image'-like similarity to the proposed H_{ox} adduct depicted in Fig. 3.16). This formation of an $\text{Fe}_d\text{-C}$ bond, following (the first) protonation of adt-N , leads to a formal 2-electron oxidation of the $[\text{2Fe}]_{\text{H}}$ subdomain. The result is the accumulation of a small amount of spin density on Fe_d , consistent with the ENDOR results. The precise value of this spin density however is extremely dependent on the computational details, and in particular on the exchange functional (Table 3.1). A larger spin moment on the high-spin Fe centres of the cubane together with a concomitant decrease at the $[\text{2Fe}]_{\text{H}}$ subsite is obtained upon switching from the BP86 functional to the hybrid B3LYP [5]. While the uncertainty in the absolute magnitude of the spin density precluded a study of the hyperfine coupling, the computational investigation establishes that binding of HCHO via a *covalent Fe-C bond* is *favourable* at the highly reduced oxidation levels of interest in this system, but only when a proton is also present at adt-N .

3.3.4 Comparative Analysis and Discussion

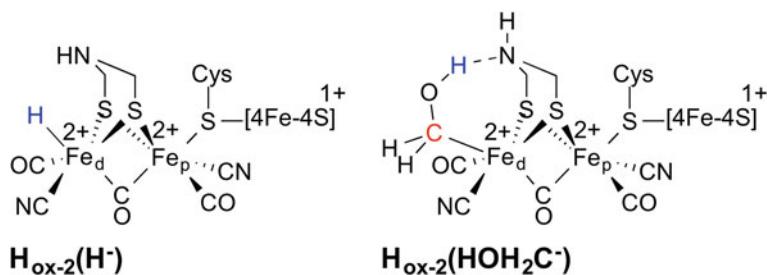
Taking into consideration all the observations and data obtained on the formaldehyde inhibition reaction, along with evidence from investigations of others, a new hypothesis can be proposed to arrive at a consistent model. Comparing the structural information obtained from the X-band ^2D ESEEM experiments (Fig. 3.19) to the ^{13}C ENDOR results depicted in Fig. 3.18, it becomes apparent that although there is a *specific* interaction of formaldehyde with the H-cluster that is responsible for the isotropic component of the hyperfine interaction and can, amongst other possibilities, be attributed to direct Fe-C coordination, the whole picture is more complex. The large ^2D ESEEM modulation depth suggests that much more 'matrix' formaldehyde is present in the vicinity of the active site than is specifically bound. This is not surprising: anhydrous HCHO molecules, being neutral and of similar

size to other small molecules such as CO or O₂ that are known to diffuse freely into hydrogenases [30], should be able to occupy many different sites within the protein.

Structure **I** can be interpreted as being the ‘limiting case’ of a single ‘matrix’ HCHO, i.e. a single formaldehyde molecule approaching Fe_d closely, but not yet being bound. As depicted in Fig. 3.20, protonation of adt-N is required to shift the equilibrium towards **II**. The precise values of the spin density at Fe_d in **II** are to some extent dependent on the details of computational methodology, but lie in the range of 0–0.10 electron (Table 3.1), consistent with the EPR data that require the great majority of spins to be localised on [4Fe-4S]_H (Fig. 3.17). The results reported by Bruschi et al. for the hydrido complex H_{ox-2}(H⁻) show very similar trends and very similar absolute values of $\rho(\text{Fe}_{\text{p/d}})$ [3]. The computational results presented in Sect. 3.3.3 therefore give rise to the hypothesis that HCHO coordination to *un*protonated Fe_d is favourable provided it is accompanied by protonation at the bridgehead adt-N (the first proton transfer, in this case). The results suggest that binding of HCHO as in structure **II** results in a state that is equivalent to the hydrido complex H_{ox-2}(H⁻) that exists just before H–H bond formation (Scheme 3.5).

In essence, HCHO has intercepted the catalytic cycle at the point of the first H⁺ transfer from adt-N to Fe_d. This proton, transferring from quaternised adt-N, is abstracted instead by HCHO during formation of the covalent Fe_d–C bond. Structure **II** is best expressed as a carbanionic complex H_{ox-2}(HOH₂C⁻), in which HOH₂C⁻ is a hydride analogue. The stable adduct may also offer protection against more permanent inactivation, if the latter involved attack by formaldehyde on the bridgehead amine-N.

There are the strong links to existing models for the catalytic cycle where a bridging [10] or, most-likely, terminal hydride (at Fe_d) [28] is formed upon reduction of H_{ox-1} and transfer of the first proton required for H₂ formation from the bridgehead adt-N [3, 4]: the subsequent second protonation of adt-N leads to electron transfer from [4Fe-4S]_H to [2Fe]_H. This through-bond reoxidation of [4Fe-4S]_H¹⁺ [3] results in the formation of H_{ox-2}(2H) (Scheme 3.1), which is immediately followed by facile formation and release of H₂. Structure **II**, which requires only minimal reorganisation of the H-cluster, accounts for the rapid and reversible inhibition by formaldehyde. The main mechanistic difference between



Scheme 3.5 Comparison of the hydrido species H_{ox-2}(H⁻) [3] with the formaldehyde adduct **II**

formaldehyde inhibition and H₂ formation is that the second protonation of **II** at adt-N is not achievable, as the amine group is stabilised through hydrogen bonding with the adjacent hydroxyl group. This aspect explains why in **II**, similar to H_{ox-2}(H⁻) but in contrast to H_{ox-2}(2H), the majority of unpaired electron density still resides on [4Fe-4S]_H [3].

In Fig. 3.20 all that is required to release HCHO from the active site is the transfer of the hydroxyl proton back to the bridgehead adt-N. This proposed mode of inhibition accounts not only for the PFE results but also the subsequent failure to detect any release of methanol. Moreover, direct reaction with unprotonated Fe_d in H_{ox-2}, i.e. Fe_d having a vacant coordination site (as opposed to hydride transfer from H_{ox-2}(H⁻) [1]), is also fully consistent with recent experimental evidence for H_{ox-1} being unprotonated at Fe_d [9, 10].

Previous PFE experiments carried out under turnover conditions established that formaldehyde shows a weak affinity for the H_{ox-1} level and a much stronger affinity for H_{ox-2} (Fig. 3.4). This observation strongly indicates that, while the second electronation step to form H_{ox-2} might not be necessary for some minor degree of HCHO inhibition to occur (e.g. through formation of an H_{ox-1} analogue of **I**), significant inhibition by Fe–C bond formation occurs only in the H_{ox-2} level. A large population of the H_{ox-1} level can be excluded since the EPR-sample preparation method that I employed, i.e. prolonged H₂ incubation, produces clean H_{ox-2} samples, as established by Lubitz and co-workers using FTIR spectroscopy [11].

The possibility that the *state* on the H_{ox-2} overall redox level that is inhibited by formaldehyde (leading to structure **II**) measured by EPR differs from the transient state on the same redox level that is formed under catalytic turnover (inhibition of which has been demonstrated by PFE experiments [1, 2]) cannot be excluded. However, while this general restriction applies to all spectroscopic states identified and characterised by various methods (see Refs. [10, 11, 21] for the H_{ox-2} level), the combination of experimental and theoretical evidence presented in this chapter provides compelling evidence that, under catalytic turnover, formaldehyde inhibits H₂ formation by binding to a highly reduced H-cluster having a vacant coordination site at Fe_d.

To summarise, the combination of results supports a model in which Fe–C bond formation in the most reduced state of the H-cluster can only occur if a Fe–H bond has not yet formed, a conclusion that has important mechanistic implications. The requirement for secondary stabilisation through interaction with the O atom, as seen in simple formaldehyde complexes [12–15], is satisfied by use of the pendant adt-N...H. A new link, both structural and conceptual, is now made between the pendant adt-N and the catalytic Fe_d. Whereas free formaldehyde is a proton mimic, the *bound* protonated formaldehyde anion, as illustrated in Scheme 3.5, mimics a terminal hydride just before the point at which a second proton binds to adt-N, ultimately transferring to form H₂.

3.4 Conclusions and Perspectives

Using protein film electrochemistry, the kinetics of the (partially reversible) inhibition of the [FeFe]-hydrogenase *CaHydA* by different aldehyde molecules with varying steric and electronic properties have been determined (Sect. 3.2). Despite these new findings, evidence for the *mechanism* of inhibition of the H-cluster could not be provided. In agreement with the observed potential dependences, the initial working hypothesis was that reversible aldehyde inhibition occurs, mechanistically, by electrophilic attack on a reducing Fe_d -hydrido species (Scheme 3.2). However, previous attempts to ascertain the methanol/methoxide product of formaldehyde inhibition via NMR spectroscopy have been unsuccessful [8] and recent studies [10, 11] suggest hydride formation *only* takes place when the enzyme is in the super-reduced oxidation level. On the basis of these findings, which indicate that formaldehyde might react *before* a metal-hydrido species is formed, pulsed-EPR and DFT calculations have been conducted to gain *structural insight* into the binding mode. The EPR observations firmly establish that formaldehyde can access the H-cluster, but reveal a complex picture. The relatively large modulation depth observed in ^2D ESSEM experiments (Fig. 3.19) suggests that several aldehyde molecules surround the H-cluster, and Q-Band ENDOR spectra of *CrHydA1* inhibited by H^{13}CHO can be fitted with the ^{13}C nucleus being in several positions in the vicinity of the enzyme active site [5]. Further, the protonation state of the spectroscopically accessible ‘resting-form’ of $\text{H}_{\text{ox}-2}$ is yet to be definitively established. Whereas earlier studies suggested the $[\text{2Fe}]_{\text{H}}$ subdomain is unprotonated [4, 11], recent XAE observations suggest the existence of a bridging hydride between Fe_p and Fe_d [10]. The presence/absence of such a hydrido complex has a profound impact on the possible reaction pathways of the H-cluster with formaldehyde.

However, despite this complex picture obtained under ‘static’ (frozen) equilibrium conditions, formaldehyde inhibition under catalytic turnover, i.e. *in operando*, is likely very different. While not giving structural insight, formaldehyde inhibition measured by PFE not only shows a strong potential dependence, inhibition is rapid, fully reversible, and dominated by a single-exponential process, indicating that a single reaction pathway prevails (Fig. 3.1). Based on the above-mentioned observations, DFT calculations show that formaldehyde, acting as a proton-mimic, is likely to intercept the reduced H-cluster before formation of a Fe_d -hydride can take place, with bound formaldehyde acting as a hydride-mimic (Scheme 3.5).

While the experiments discussed in Sect. 3.3.2 seem to have reached the limit in terms of the information EPR spectroscopy can provide on the reaction of formaldehyde with the H-cluster, other physical techniques might yield more conclusive structural evidence. Co-crystallisation of [FeFe]-hydrogenase in the presence of formaldehyde is one possibility: following the principles established by Dobbek and colleagues in the co-crystallisation of CODH with *n*-butyl isocyanide [31], crystals of [FeFe]-hydrogenase would have to be chemically reduced to the $\text{H}_{\text{ox}-2}$ level and then exposed to formaldehyde. However, the highly reactive

electrophile is likely to cause irreversible degradation of the enzyme upon prolonged exposure. Despite this limitation, preliminary experiments are currently being carried out in the laboratory of Professor Thomas Happe at the Ruhr-Universität Bochum, Germany.

A recently developed technique known as protein film infrared electrochemistry (PFIRE) [32] has the potential to provide structural information under catalytic conditions: here, protein film electrochemistry is coupled to infrared spectroscopy, allowing the investigator to simultaneously gain information from both techniques. PFIRE has thus far only been applied to [NiFe]-hydrogenases [32, 33], but could become a valuable tool for elucidating the remaining ambiguities concerning the mechanism of [FeFe]-hydrogenases, Nature's most proficient hydrogen cycling catalysts.

References

1. Foster CE, Krämer T, Wait AF, Parkin A, Jennings DP, Happe T, McGrady JE, Armstrong FA (2012) *J Am Chem Soc* 134:7553
2. Wait AF, Brandmayr C, Stripp ST, Cavazza C, Fontecilla-Camps JC, Happe T, Armstrong FA (2011) *J Am Chem Soc* 133:1282
3. Bruschi M, Greco C, Kaukonen M, Fantucci P, Ryde U, De Gioia L (2009) *Angew Chem Int Ed* 48:3503
4. Lubitz W, Ogata H, Rüdiger O, Reijerse E (2014) *Chem Rev* 114:4081
5. Bachmeier A, Esselborn J, Hexter SV, Krämer T, Klein K, Happe T, McGrady JE, Myers WK, Armstrong FA (2015) *J Am Chem Soc* 137:5381
6. Greco C, Bruschi M, De Gioia L, Ryde U (2007) *Inorg Chem* 46:5911
7. Greco C, Bruschi M, Fantucci P, Ryde U, De Gioia L (2011) *ChemPhysChem* 12:3376
8. Foster CE (2012) D Phil Thesis, University of Oxford, Oxford
9. Lambertz C, Chernev P, Klingan K, Leidel N, Sigfridsson KGV, Happe T, Haumann M (2014) *Chem Sci* 5:1187
10. Chernev P, Lambertz C, Brünje A, Leidel N, Sigfridsson KGV, Kositzki R, Hsieh C-H, Yao S, Schiwon R, Driess M, Limberg C, Happe T, Haumann M (2014) *Inorg Chem* 53:12164
11. Adamska A, Silakov A, Lambertz C, Rüdiger O, Happe T, Reijerse E, Lubitz W (2012) *Angew Chem Int Ed* 51:11458
12. Brown KL, Clark GR, Headford CEL, Marsden K, Roper WR (1979) *J Am Chem Soc* 101:503
13. Green MLH, Parkin G, Moynihan KJ, Prout K (1984) *J Chem Soc, Chem Commun* 1540
14. Gambarotta S, Floriani C, Chiesi-Villa A, Guastini C (1986) *Organometallics* 5:2425
15. Berke H, Bankhardt W, Huttner G, v. Seyerl J, Zsolnai L (1981) *Chem Ber* 114:2754
16. Bell RP (1966) In: Gold V (ed) *Adv Phys Org Chem*. Academic Press, USA, vol 4, p 1
17. Hilal SH, Bormander LL, Carreira LA (2005) *QSAR Comb Sci* 24:631
18. Guthrie JP (1975) *Can J Chem* 53:898
19. Wait AF (2011) D Phil Thesis, University of Oxford, Oxford
20. Guigliarelli B, Bertrand P (1999) In: Sykes AG (ed) *Adv Inorg Chem*. Academic Press, USA, vol 47, p 421
21. Mulder DW, Ratzloff MW, Shepard EM, Byer AS, Noone SM, Peters JW, Broderick JB, King PW (2013) *J Am Chem Soc* 135:6921

22. Chasteen ND, Snetsinger PA (2000) In: Que L (ed) *Physical Methods in Bioinorganic Chemistry: Spectroscopy and Magnetism*. University Science Books, Sausalito, p 187
23. Pollock RC, Lee H-I, Cameron LM, DeRose VJ, Hales BJ, Orme-Johnson WH, Hoffman BM (1995) *J Am Chem Soc* 117:8686
24. Hoffman BM, De Rose VJ, Doan PE, Gurbiel RJ, Houseman ALP, Telser J (1993) *Biol Magn Reson* 13:151
25. Berggren G, Adamska A, Lambertz C, Simmons TR, Esselborn J, Atta M, Gambarelli S, Mouesca JM, Reijerse E, Lubitz W, Happe T, Artero V, Fontecave M (2013) *Nature* 499:66
26. Esselborn J, Lambertz C, Adamska-Venkatesh A, Simmons T, Berggren G, Noth J, Siebel J, Hemschemeier A, Artero V, Reijerse E, Fontecave M, Lubitz W, Happe T (2013) *Nat Chem Biol* 9:607
27. Siebel JF, Adamska-Venkatesh A, Weber K, Rumpel S, Reijerse E, Lubitz W (2015) *Biochemistry* 54:1474
28. Finkelmann AR, Stiebritz MT, Reiher M (2014) *Chem Sci* 5:215
29. Lemon BJ, Peters JW (1999) *Biochemistry* 38:12969
30. Cohen J, Kim K, King P, Seibert M, Schulten K (2005) *Structure* 13:1321
31. Jeoung J-H, Dobbek H (2012) *J Biol Inorg Chem* 17:167
32. Hidalgo R, Ash PA, Healy AJ, Vincent KA (2015) *Angew Chem Int Ed* 54:7110
33. Murphy BJ, Hidalgo R, Roessler MM, Evans RM, Ash PA, Myers WK, Vincent KA, Armstrong FA (2015) *J Am Chem Soc* 137:8484

Chapter 4

The Direct Electrochemistry of Fuel-Forming Enzymes on Semiconducting Electrodes: How Light-Harvesting Semiconductors Can Alter the Bias of Reversible Electrocatalysts in Favour of H₂ Production and CO₂ Reduction

4.1 Introduction

In artificial photosynthesis, both the fuel- and O₂-forming catalysts can be regarded as electrocatalysts, as they catalyse the respective electrochemical half-cell reaction. Ideal artificial photosynthetic catalysts exhibit high activities and do not rely on large, wasteful overpotentials to drive the reaction; a minimal overpotential requirement corresponds most closely to reversibility. However, it is beneficial to render the reaction as unidirectional as possible, thus trapping the electrons or holes and opposing recombination [1]. Under the condition of very low overpotential that is beneficial for efficiency, it is interesting and important to consider how the relative rates of catalysis for the forward and reverse reactions can be biased in favour of the desired direction. Photocatalytic fuel-formation by enzymes immobilised on semiconductor particles is now well established (Sect. 1.5.3.4), but the processes at the enzyme-semiconductor interface that are likely to govern efficiencies are still relatively poorly understood. Protein film electrochemistry techniques are valuable tools that can be of help in improving the understanding of the enzyme-semiconductor interface.

To briefly recapitulate, electrochemical kinetics at semiconductors depend on the density of charge carriers in the space-charge region adjacent to the solution interface (see Sect. 2.3) [2, 3]. In principle, control over the relative rates of oxidation and reduction catalysis can be provided if the carrier density of the semiconductor material changes greatly in a potential region close to the reduction

Part of the work presented in this chapter has been published: Andreas Bachmeier, Vincent C.-C. Wang, Thomas W. Woolerton, Sophie Bell, Juan C. Fontecilla-Camps, Mehmet Can, Stephen W. Ragsdale, Yatendra S. Chaudhary, and Fraser A. Armstrong, *J. Am. Chem. Soc.* **2013**, *135*, 15026.

potential of the reaction of interest. A useful physical characteristic of a semiconductor, unrestricted by its chemical nature, but of general relevance, is the flat-band potential (E_{fb}). For an n -type semiconductor, the electron density at the surface increases as the applied potential becomes more negative than E_{fb} , giving rise to an accumulation layer. The conduction and valence bands bend downward and the semiconductor approaches metallic-like electrochemistry when the Fermi level contacts the conduction band edge at the semiconductor-catalyst/electrolyte interface [3]. Conversely, when the applied potential is increased relative to E_{fb} , a depletion layer forms and the bands bend upwards, resulting in a barrier for electron transfer from the catalyst/electrolyte to the semiconductor. At E_{fb} there is no band-bending. The space-charge region can extend well into the material, with values in the range from 10 nm to 1 μ m being reported [2].

Several reports have described the electrochemistry of proteins on semiconductor electrodes. Durrant et al. reported a series of studies dealing with the electrochemistry of cytochrome c and haemoglobin immobilised on TiO_2 film electrodes [4, 5]. The authors found irreversible reduction of the proteins' active sites at potentials substantially more negative than the solution-based redox potentials, similar to observations with simple redox couples such as potassium ferricyanide $K_3[Fe(CN)_6]$ [5]. The TiO_2 electrode thus exerts a rectifying effect. However, these electrochemical reductions are not catalytic.

This chapter explores the directionality that can be imposed on electrocatalytic behaviour when certain enzymes (i.e. [NiFeSe]-hydrogenase and CODH) and, by extension, any *reversible* electrocatalyst, are attached to a semiconductor. Although materials will differ considerably in their chemical properties, the concept of E_{fb} provides the means to explore some generalisations because changes in carrier density ought to be particularly influential in biasing the direction if they occur in the potential region of the reduction potential for the redox reaction being catalysed. Therefore, the reversibility of H^+/H_2 and CO_2/CO interconversion by [NiFeSe]-hydrogenase (see Sect. 1.6.3) and CODH (Sect. 1.6.4) is compared at a metallic-like graphite electrode (PGE) and at TiO_2 and CdS electrodes (both n -type semiconductors) by analysing the electrocatalytic voltammograms recorded under H_2 or CO_2/CO mixtures.

Both types of FeS enzyme are excellent examples of reversible electrocatalysts when attached to a metallic electrode (including 'semi-metallic' PGE) [6–10]. Voltammograms recorded with the enzyme-modified electrode being immersed in a solution containing both oxidised and reduced forms of the substrate (i.e. the redox-active molecules in solution) intersect the zero current axis at the equilibrium potential with little or no inflection.

The n -type semiconductors CdS and TiO_2 (anatase) have conduction band potentials (E_{cb} at pH 6.0 ca. -0.87 and ca. -0.52 V vs. SHE, respectively [11]) more negative than the equilibrium potentials for H^+/H_2 (-0.36 V vs. SHE) and CO_2/CO (-0.46 V), and nanoparticles of CdS and dye-sensitised TiO_2 (anatase or P25, a commercially available mixed rutile-anatase phase) modified with hydrogenases or CODH are excellent model-systems for photoreducing H_2O and CO_2 [12–16] (compare Sect. 1.5.3.4).

4.2 Results

4.2.1 Characteristics of Porous CdS and TiO₂ Electrodes and Enzyme Immobilisation

Protein film electrochemistry has been pioneered using PGE electrodes [17]. The roughness of the ‘edge’ plane (see SEM image depicted in Fig. 4.1a) compared to the basal plane, as well as its hydrophilicity and richness in acidic oxides [18] make it particularly suitable for electroactive enzyme immobilisation—it enables the irregularly shaped macromolecules to make multiple polar contacts with the electrode [17]. Dispersion of interfacial electron transfer kinetics, a result of protein molecules adopting a distribution of orientations on the electrode, is minimised, as the rough surface allows for efficient electron transfer with a multitude of different enzyme orientations. Protein film electrochemistry on semiconductor electrodes in turn is not well established yet and, to my knowledge, only few preliminary studies exist [12, 19, 20], none of which having the focus on the underlying principles of enzyme semiconductor interaction. In a broader context, little is known about electron transfer between semiconductors and *reversible* electrocatalysts.

Figure 4.1 also depicts SEM images of porous TiO₂ (b, prepared from Degussa P25) and CdS electrode films (c). The TiO₂ thin film exhibits porous structures consisting of nanoparticles (on the order of 20 nm, the average particle diameter of P25) which have formed aggregates, as expected upon calcination at 450 °C (see Sect. 8.3.2.1). The CdS film consists of a highly porous 3-dimensional network of CdS nanoflakes/sheets. These nanosheets are typically 20 ± 5 nm in width and the pore size of CdS varies from 700 nm to approximately 1 μ m. The porous nature of these two electrode materials somewhat resembles the surface characteristics of PGE and should therefore allow electroactive enzyme immobilisation.

The surface charge of a semiconductor is an important quantity that can be used to facilitate ‘directed’ enzyme adsorption by exploiting attractive electrostatic interactions. The point of zero charge (PZC) of P25 TiO₂ is 6.2 [21]. With the isoelectric points of CODH being 5.5 [22] and of [NiFeSe]-hydrogenase being 5.4 [13], stable attachment of both enzymes at TiO₂ nanoparticles has been achieved for photocatalytic CO₂ and H⁺ reduction at pH 6, where the net surface charge of the enzymes is negative and TiO₂ is positively charged [12–14]. In the case of [NiFeSe]-hydrogenase, the presence of a negatively charged surface patch around the distal FeS cluster indicates that the interaction between enzyme(s) and TiO₂ particles is likely to be controlled by localised polar interactions between side-chain carboxylates and a number of Ti-O(H) sites rather than by overall electrostatic interactions [4, 13]. In aqueous solution, CdS has a PZC of 7.5 [23]. Hence, attractive electrostatic interactions similar to those observed with TiO₂ and CODH or [NiFeSe]-hydrogenase can be expected. Indeed, CODH immobilised on CdS nanocrystals shows activity towards light-driven CO₂ reduction in aqueous media at pH 6 [16].

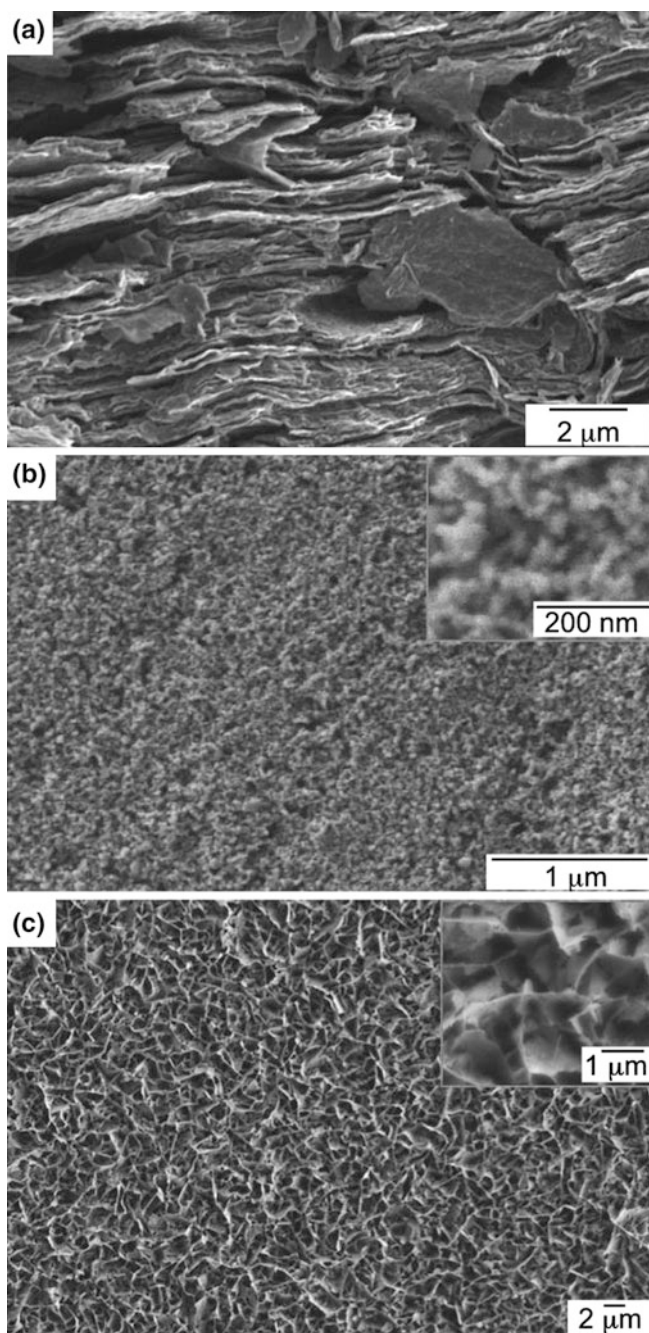


Fig. 4.1 SEM images of **a** PGE, **b** TiO_2 , and **c** CdS film electrodes used in this thesis

To assess the stability of both enzymes for electrochemical CO_2/H^+ reduction, chronoamperometry experiments of CODH-TiO₂, CODH-CdS, [NiFeSe]-TiO₂, and [NiFeSe]-CdS were performed over a period of 4 h (Fig. 4.2). The enzymes show excellent stability on both TiO₂ and CdS; catalytic currents persist up to the 4 h mark (cyclic voltammograms were recorded after these experiments to verify the catalytic nature of the current vs. time curves and confirm that the enzymes had

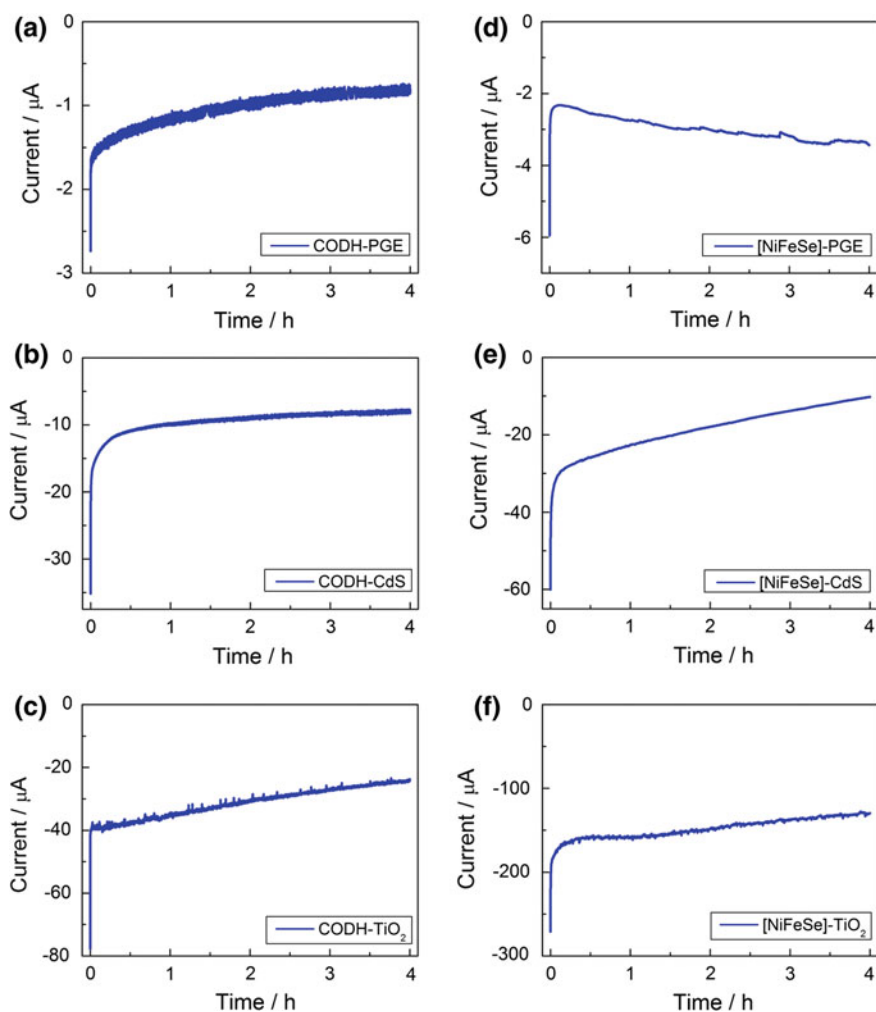


Fig. 4.2 Chronoamperometry experiments recorded at -0.65 V vs. SHE on PGE, CdS and TiO₂ electrodes modified with CODH (*left panel*, recorded under 100% CO₂ flow) or [NiFeSe]-hydrogenase (*right panel*, recorded under 100% N₂ flow). All experiments were carried out at 20 °C, the buffer solution was 0.2 M MES (pH 6.0), and the cell solutions were sparged with the respective gas close to the stationary working electrode surface throughout the experiment

remained intact throughout the experiments). For CODH this stability is indeed remarkable: this enzyme is relatively unstable on PGE electrodes, where the presence of poly-ionic co-adsorbates such as the cationic polymyxin B sulphate is normally required to allow PFE experiments to be carried out [24, 25] (particularly for rotating disk experiments).

4.2.2 Direct Electrochemistry of CODH and [NiFeSe]-Hydrogenase on TiO_2 and CdS

Panel (a) of Fig. 4.3 shows cyclic voltammograms of CODH attached to PGE (CODH-PGE), CdS (CODH-CdS), and TiO_2 (CODH- TiO_2) electrodes in separate experiments with 100% CO_2 or a mixture of 50% CO_2 /50% CO gently bubbling through the cell solution. Protein film electrochemistry provides precise and continuous measurement of the relative catalytic rates in either direction. The shapes of the cyclic voltammograms on PGE in the presence of both oxidised and reduced substrates reveal the inherent catalytic bias of the enzymes to function more effectively in one particular direction, and reaffirm that on metallic-like electrodes, catalysis is controlled by the redox properties of the enzyme [26, 27]. A dominant factor in determining the bias of an enzyme is the reduction potential ($E_{\text{Ox/Red}}^0$) of the relay centre that serves as the electron entry/exit point for transfer to the buried catalytic centre [26, 28].

In contrast to CODH adsorbed on PGE, the voltammograms recorded on CODH-CdS and CODH- TiO_2 are dominated by CO_2 reduction, i.e. the bias appears *reversed* (with respect to the bias observed at PGE) to favour instead the formation of CO. In fact, CO oxidation is negligible at CdS and extremely sluggish at TiO_2 . The effect is all the more pronounced if one considers that CO is a natural inhibitor of CO_2 reduction by CODH (a phenomenon known as product inhibition) [25], i.e. the exponentially increasing reductive current is suppressed when both oxidised and reduced substrate are present (red traces in Fig. 4.3a). Voltammograms recorded under 100% CO_2 (blue traces) reveal the further increase in current that is obtained when CO is not introduced.

Panel (b) of Fig. 4.3 shows analogous experiments for [NiFeSe]-hydrogenase immobilised on PGE, CdS, and TiO_2 carried out under H_2 flow through the cell solution. Once again, the effect of product inhibition is clearly visible in the case of [NiFeSe]-PGE [7]. Electrocatalysis in the reduction direction is strongly inhibited by H_2 and cyclic voltammograms recorded in the absence of H_2 reveal the higher rate of H^+ reduction by uninhibited enzyme. As with CODH, comparison with PGE shows that the H_2 oxidation currents at CdS or TiO_2 are greatly suppressed relative to the rates of H^+ reduction.

With regard to the voltammetric reduction waves observed on CODH-CdS and CODH- TiO_2 (panel (a) of Fig. 4.3), experimental verification for these to correspond to catalytic conversion of CO_2 into CO was needed. In previous work by our

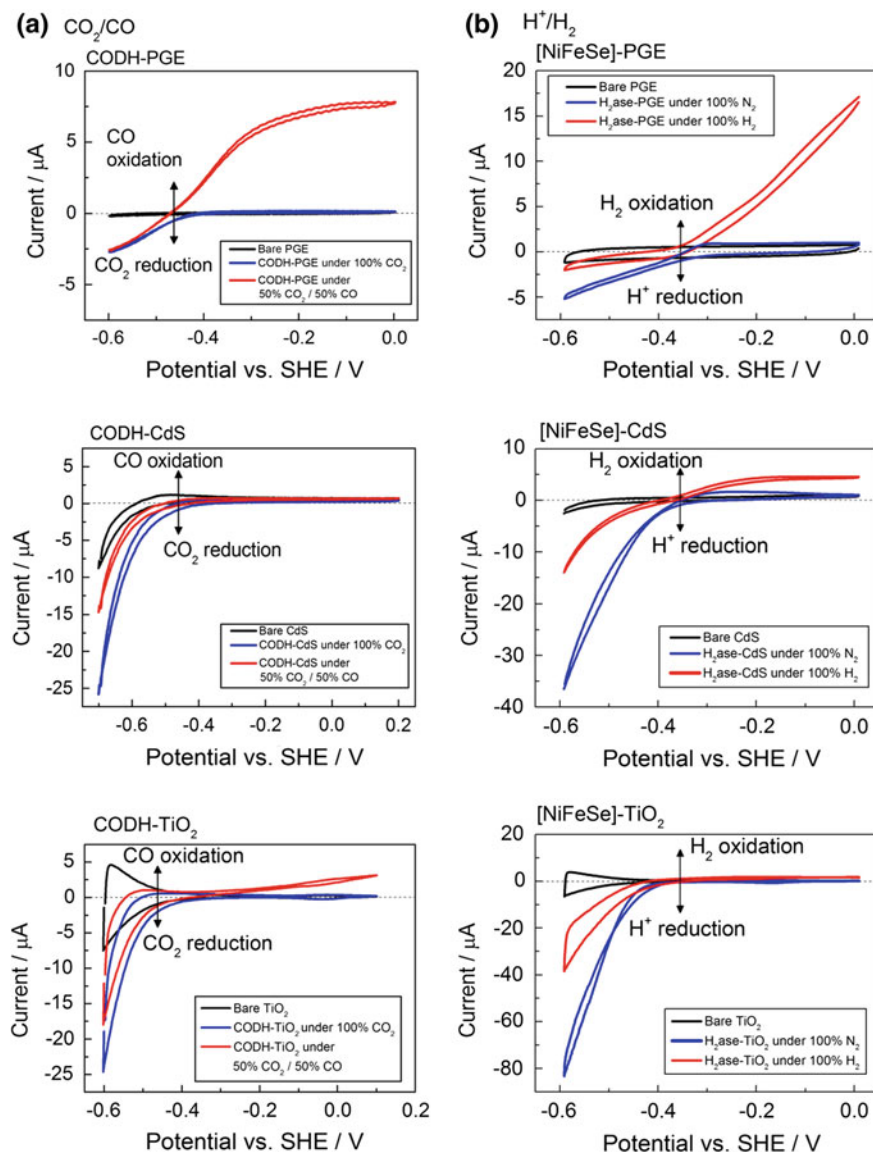


Fig. 4.3 Cyclic voltammograms (10 mV s^{-1}) of unmodified (*black*) and enzyme-modified electrodes (*red, blue*), recorded in 0.2 M MES , $\text{pH } 6.0$, at $20 \text{ }^\circ\text{C}$. Voltammograms recorded under $100\% \text{ CO}_2$ (CODH-PGE, CODH-CdS, and CODH-TiO₂) or $100\% \text{ N}_2$ ([NiFeSe]-PGE, [NiFeSe]-CdS, and [NiFeSe]-TiO₂) are depicted in *blue*. Experiments with a $50\% \text{ CO}_2/50\% \text{ CO}$ gas mixture (CODH-PGE, CODH-CdS, and CODH-TiO₂) or with $100\% \text{ H}_2$ ([NiFeSe]-PGE, [NiFeSe]-CdS, and [NiFeSe]-TiO₂) bubbling through the cell are shown in *red*

laboratory on photocatalytic CO_2 reduction using CODH- TiO_2 and CODH-CdS nano-assemblies, catalytic CO_2 reduction was monitored by gas chromatography [14, 15]. This approach is not feasible herein because of the minute quantities of enzyme used in protein film electrochemistry experiments (on the order of pmol). A selective inhibitor of CODH was used instead to prove that the reduction currents at each semiconductor electrode correspond to CO_2 reduction to CO. Cyanate (NCO^-), which is isoelectronic to the substrate CO_2 , targets the active site of CODH and selectively blocks CO_2 reduction by intercepting the reduced $\text{C}_{\text{red}2}$ level of the enzyme [25]. NCO^- is released as the potential is raised and does not significantly inhibit CO oxidation.

The selective inhibition of CO_2 reduction on CODH-modified TiO_2 and CdS electrodes after addition of KOCN is depicted in Fig. 4.4. Quantitative inhibition was achieved with a final concentration of 20 mM KOCN in the case of CODH- TiO_2 (Fig. 4.4a) and 60 mM KOCN at CODH-CdS (Fig. 4.4b). Upon KOCN injection (red current-voltage curves), the portions of the cathodic currents due to CO_2 reduction before introducing the inhibitor (blue traces) are quenched. Instead, the voltammogram for CODH- TiO_2 resembles the characteristic shape of a TiO_2 electrode at low potential (see Sect. 2.3.3.3). In the CODH-CdS system, the voltammogram also closely resembles the shape of the bare electrode after introduction of the inhibitor. Thus, it is established that the reductive catalytic currents stem specifically from CO_2 reduction.

The potential dependences of the low-level CO and H_2 oxidation currents at CdS and TiO_2 depicted in Fig. 4.3 vary slightly between different experiments and residual oxidation currents differ in magnitude at both electrodes. These non-idealities can be ascribed to several complex phenomena including direct contact between some enzyme molecules and the conducting oxide support (due to pinholes in the semiconductor film), dispersion in enzyme orientation on the semiconductor surface and variations in semiconductor film thickness, electron

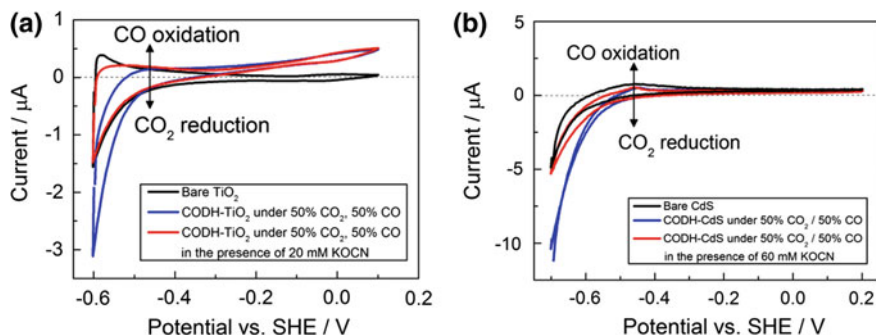


Fig. 4.4 Cyclic voltammograms showing selective inhibition of CO_2 reduction on CODH-modified TiO_2 (a) and CdS (b) electrodes in the presence of 20 and 60 mM KOCN, respectively, under a mixture of 50% CO_2 /50% CO bubbling through the cell. The solutions contained 0.2 M MES (pH 6.0) buffer; temperature: 20 °C; scan rate: 10 mV s^{-1}

tunnelling through the interfacial potential barrier (depletion region) near the surface (mainly via surface states/semiconductor defects), and electrons surmounting this barrier.

These non-idealities however do not change the general effect of catalytic rectification, which becomes even more prominent when ‘background-subtracted’ voltammograms are taken into account. When first observing the effect of catalytic rectification in preliminary experiments on CODH-modified TiO_2 electrodes, Woolerton [20] suggested comparing the ratios of background-corrected reduction/oxidation currents at a fixed value either side of the equilibrium potential for CO_2 reduction. Figure 4.5 depicts typical ratios of reduction vs. oxidation currents at ± 0.15 V either side of the thermodynamic potential for CO_2/CO and H^+/H_2 interconversion, clearly revealing the changes in catalytic bias for each enzyme. For [NiFeSe]-hydrogenase, the background-corrected current ratio (H_2 oxidation/ H^+ reduction) drops from 8.1 on PGE, to 0.81 on CdS and 0.11 on TiO_2 , i.e. attenuation factors of approximately 10- and 80-fold, respectively. For CODH the current ratio (CO oxidation/ CO_2 reduction) drops from 2.2 on PGE to 0.04 on CdS and 0.05 on TiO_2 , i.e. an attenuation factor of approximately 50-fold in each case. These results demonstrate that although the residual oxidising currents for both enzymes differ at TiO_2 and CdS, the fuel-forming reactions are essentially rendered irreversible.

4.2.3 Mott-Schottky Measurements

4.2.3.1 The Flat-Band Potential of TiO_2 and CdS Electrodes

In the case of enzyme-modified TiO_2 electrodes (Figs. 4.3 and 4.4a), the exponential increase in reductive current for both H^+ and CO_2 reduction coincides closely with the characteristic increase in capacitive current of the bare TiO_2 electrode [29, 30]. In chemical terms, the reversible reduction of Ti(IV) sites (accompanied by uptake of one proton per centre) is responsible for this effect, increasing the carrier density as the potential is lowered (see Sect. 2.3.3.3) [29]. An analogous observation is not immediately apparent for CdS, apart from reduction and stripping of Cd(II) centres at potentials below ca. -0.65 V vs. SHE [31].

Electrical impedance spectroscopy (EIS, Sect. 2.3.5.3) is a suite of techniques that can help resolve the effects that conductivity changes near the flat-band potential impose on the properties of immobilised catalysts, and probe interfacial interactions between enzyme and electrode. The initial task at hand was to measure how the capacitance of TiO_2 and CdS electrodes changes with applied potential, as it allows extracting the respective E_{fb} through Mott-Schottky analysis according to Eq. (2.40):

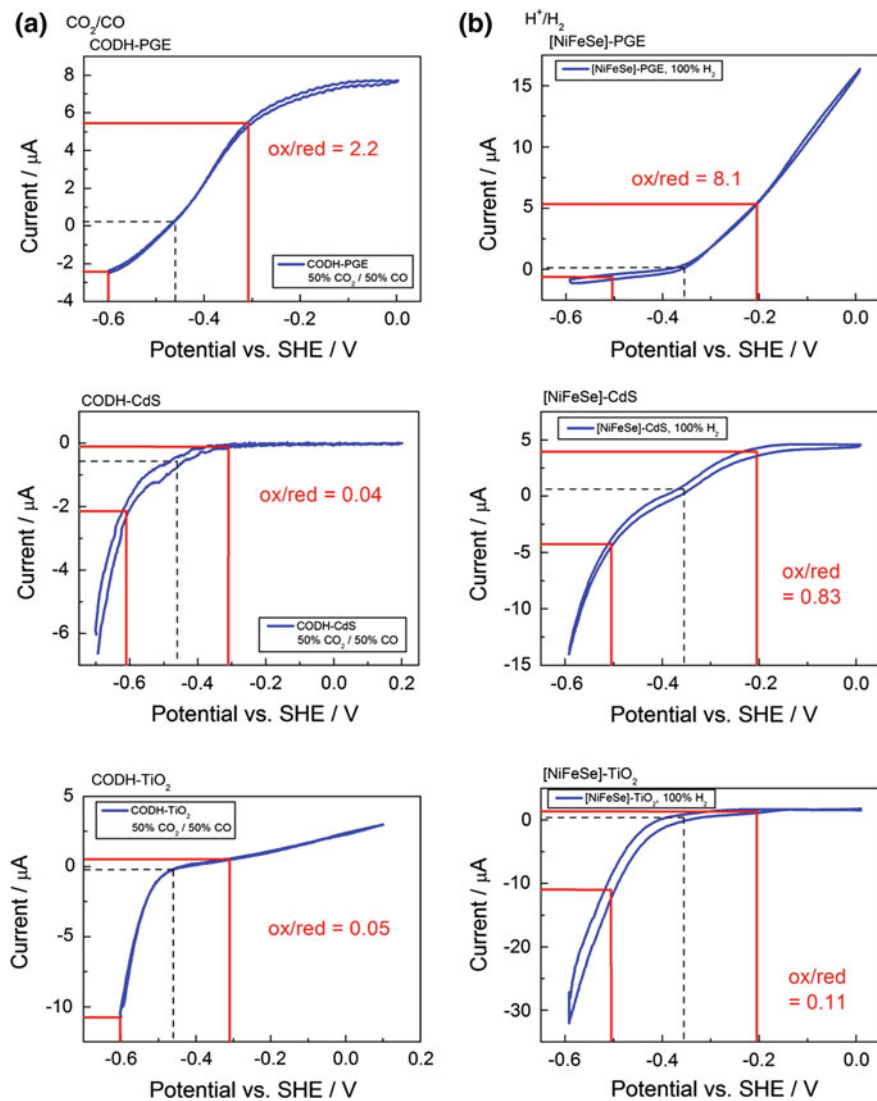


Fig. 4.5 ‘Background-corrected’ current-voltage curves, obtained after subtracting the current vs. voltage traces of the bare electrodes of the voltammograms depicted in Fig. 4.3 (i.e. *red traces* minus *black traces*). Vertical dotted lines mark the thermodynamic equilibrium potentials for CO_2/CO and H^+/H_2 interconversion at pH 6.0; horizontal red lines mark the current recorded 150 mV either side of the equilibrium potential, from which the ratio of oxidation current to reduction current (‘*ox/red*’) is calculated (using the arithmetic average of the respective forward and backward scan)

$$C_{sc}^{-2} = \frac{2}{\varepsilon\varepsilon_0e_0N_D} \left(E - E_{fb} - \frac{k_B T}{e_0} \right).$$

Linear extrapolation of the 1 kHz plots depicted in Fig. 4.6 yields flat-band potentials of approximately -0.50 V vs. SHE for TiO_2 and ca. -0.61 V vs. SHE for CdS; both values were obtained in 0.2 M MES buffer (2-(*N*-morpholino)ethanesulfonic acid) at pH 6.0 at 20 °C.

It must be noted that the electrodes prepared in this work are made up of particles that are interconnected and partly fused together, making the materials thick enough to support a space-charge region (see SEM images in Fig. 4.1), in contrast to semiconductor nanoparticles where formation of a space-charge layer is improbable because of the very small crystallite sizes [32] and the concepts of band-bending and formation of accumulation and depletion layers do no longer apply. Investigations by others on TiO_2 electrodes similar in structure to those used in this thesis [33] further suggest that the aggregates exhibit bulk properties to some extent rather than being completely dominated by the individual particles. Thin ‘compact’ TiO_2 films behave similarly to conventional macroscopic semiconductor electrodes, formation of a space-charge layer is feasible, and the Schottky-formalism can be applied to measure E_{fb} [32].

The E_{fb} value of ca. -0.50 V measured for TiO_2 at pH 6.0/20 °C agrees well with the value of -0.52 V vs. SHE predicted by a model for nanostructured TiO_2 electrodes in aqueous solution developed by Fitzmaurice [34] (using the correction 0.2445 V for the conversion of SCE to SHE at 20 °C [35]):

$$E_{fb}(\text{V, SCE}) = -0.40 - (0.06 \times \text{pH}). \quad (4.1)$$

The relationship described by Eq. (4.1) has also been observed experimentally [36].

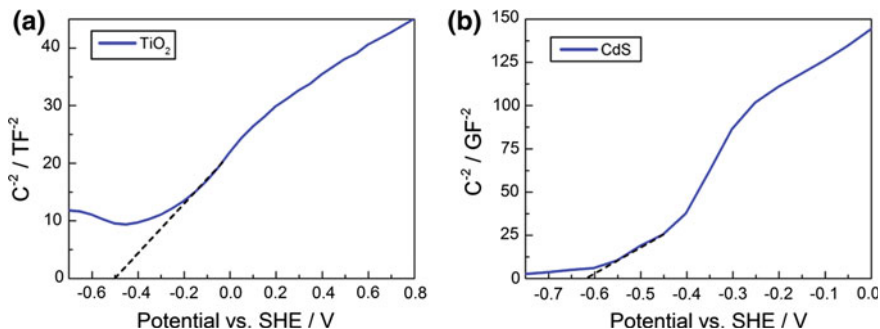


Fig. 4.6 Mott-Schottky plots ($1/C^2$ vs. E) recorded in the presence of CO_2 at 20 °C, 1 kHz for **a** TiO_2 and **b** CdS. The cell buffer solution was 0.2 M MES (pH 6.0) in both cases

In principle, E_{fb} should be independent of the applied frequency. However, the impedance response of the probed systems often contains non-idealities such as back contact capacitance (from the transparent conducting oxide), sample resistance, electrolyte resistance, and capacitance and resistance of Helmholtz layer and surface states [32]. These effects show different contributions depending on the applied frequency. In the particular case of TiO_2 adsorbed on ITO, similar E_{fb} values have reproducibly been obtained in different studies using frequencies in the range of 0.1–2 kHz [32, 36, 37]. Hence, impedance studies in this thesis were carried out in this low-to-mid frequency range.

Mott-Schottky measurements on TiO_2 electrodes carried out in a different protic electrolyte (LiClO_4 , Fig. 4.7) confirm that the flat-band potential is independent of the electrolyte [34], i.e. the capacitance of the Helmholtz layer C_H at the semiconductor-electrolyte interface is negligible compared to the capacitance of the space-charge region C_{SC} [32] (compare Sect. 2.3.2).

4.2.3.2 The Flat-Band Potential of CODH- TiO_2 in the Absence of Substrate

Having measured the flat-band potentials of TiO_2 and CdS electrodes, I sought to investigate the influence of CODH. In contrast to [NiFeSe]-hydrogenase, where the solvent (buffer) constitutes the substrate for the fuel-forming reaction (protons), surface-immobilised CODH can be studied both under turnover (in the presence of CO_2/CO) and non-turnover conditions (under an inert atmosphere). Figure 4.8 shows a Mott-Schottky experiment carried out with CODH immobilised on TiO_2 under 100% N_2 without the presence of substrate (an analogous experiment on CODH-CdS is depicted in Appendix F). Importantly, when CODH was employed in impedance spectroscopy experiments, cyclic voltammograms were recorded prior to and after every impedance measurement to ensure that the catalytic activity of the enzyme had remained steady throughout the experiment.

The experiment depicted in Fig. 4.8 shows that the presence of enzyme alone has a considerable effect on the shape of the Mott-Schottky plots. Independent of

Fig. 4.7 Mott-Schottky plot ($1/C^2$ vs. E) recorded for a TiO_2 electrode at 0.5 kHz, 20 °C, under an atmosphere of N_2 . The cell buffer solution was 0.1 M LiClO_4 (pH 6.0)

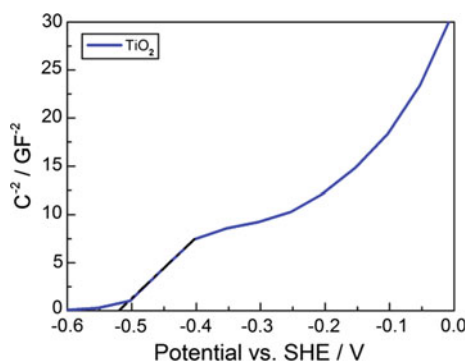
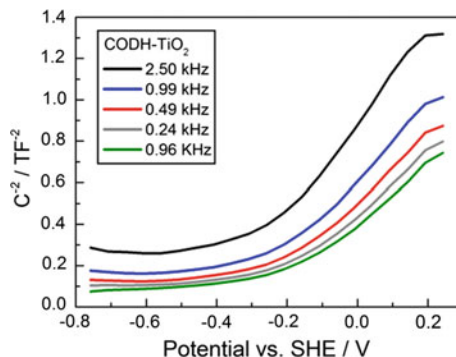


Fig. 4.8 Mott-Schottky plots ($1/C^2$ vs. E) recorded at 20 °C for CODH-TiO₂. Each experiment was performed under 100% N₂ in a 0.2 M MES (pH 6.0) cell buffer solution



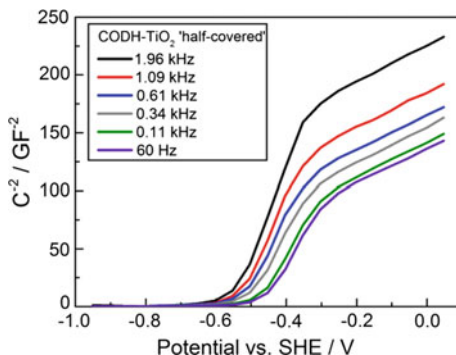
the applied frequency, each trace is characterised by an unfeatured shape and sensible E_{fb} values can no longer be extrapolated because of the absence of defined linear gradients.

Although the SEM images in Fig. 4.1 show the pores in the TiO₂ and CdS films to be of approximately the same size as the dimensions of CODH (approximately $88 \times 63 \times 60$ Å), these observations suggest the enzyme adsorbs mainly on the outer (geometric) surfaces and acts mostly as a ‘resistive’ film, blocking the inner surface area created by the porous electrode structure from contact with the solution. This effect can be rationalised by the relatively short enzyme adsorption times employed in PFE experiments, where minute quantities of protein (μ L volumes) are spotted onto the respective electrode and dried within minutes. A study by Durrant and co-workers supports this hypothesis; it was measured that haemoglobin takes up to 15 days to fully penetrate into nanostructured pores of TiO₂ electrodes similar to those employed in this work [4].¹

The aforementioned hypothesis was investigated in more detail using well established TiO₂ electrodes as test-system. First, Mott-Schottky experiments were carried out on electrodes where CODH was only applied to half of the exposed geometric TiO₂ surface area, creating a system that comprises both ‘bare’ and CODH-modified zones on the solution-exposed TiO₂ surface. The C^{-2} vs. potential traces in Fig. 4.9 are similar to the capacitive behaviour exhibited by unmodified TiO₂ (shown in Fig. 4.6a) and comparable E_{fb} values can be obtained through extrapolation in the frequency range of 0.5–2 kHz. This observation implies that sites on the unmodified part of the TiO₂ electrode dominate the capacitance of the surface. As indicated by the porosity of the TiO₂ electrodes (Fig. 4.1b), the intrinsic (i.e. real) surface area is much greater than the ‘outer’ geometric area. Leaving half of the latter uncovered allows the electrolyte to access the larger inner surface.

¹This approach is entirely impractical in PFE experiments with hydrogenase or CODH enzymes due to the low yields of the enzyme preparations, where typically only μ L of enzyme are obtained from 10+ L batches.

Fig. 4.9 Mott-Schottky experiments (C^{-2} vs. potential) for a TiO_2 electrode half-covered with CODH, recorded at various frequencies as indicated. Experimental conditions: 100% N_2 , 0.2 M MES buffer (pH 6.0), 20 °C



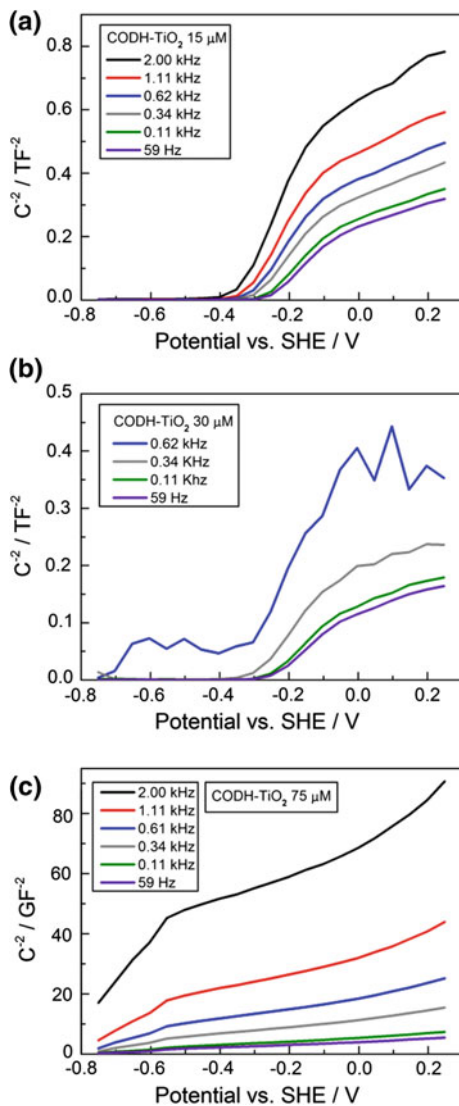
Second, a series of dilution experiments was conducted in which each TiO_2 electrode was modified with the same volume of CODH solution (4 μL), but with different concentrations being employed. Figure 4.10 shows flat-band potential measurements carried out using (a) 15 μM CODH, i.e. 1/10th the concentration of the normally employed enzyme ‘stock’ solution of 0.15 mM; (b) 30 μM , i.e. 1/5th the concentration of the original stock solution; and (c) 75 μM , i.e. 1/2 the initial CODH concentration. The stock solution was diluted to the respective concentration using 0.2 M MES buffer (pH 6.0) before the enzyme was applied to the TiO_2 electrodes of 0.25 cm^{-2} geometric surface area each. Assuming all enzyme molecules bind to the surface, 0.15 mM CODH corresponds to a ‘geometric surface concentration’ of 1.44×10^{15} molecules cm^{-2} .

In Fig. 4.10, properties consistent with TiO_2 dominating the capacitance are observed with diluted CODH concentrations of 15 μM (a, 1.44×10^{14} molecules cm^{-2}) and, at lower frequencies, 30 μM (b, 2.89×10^{14} molecules cm^{-2}). In contrast, Fig. 4.10c suggests that at a concentration increased to 75 μM (7.22×10^{14} CODH molecules cm^{-2}) enough surface sites are covered so that, independent of the applied frequency, the measured capacitance is no longer dominated by TiO_2 and an extrapolation to yield E_{fb} can no longer be made. The effects shown in Figs. 4.9 and 4.10 both seem to corroborate the hypothesis that CODH mainly adsorbs as a dense film when immobilised on TiO_2 electrodes, blocking charge-transfer between electrode and solution.

4.2.3.3 The Flat-Band Potential of CODH-Modified TiO_2 Under Turnover Conditions

Compared to the observations made with CODH- TiO_2 electrodes under non-turnover conditions, an interesting effect is revealed when substrate is added: a much sharper plot is obtained in the presence of CO_2 (Fig. 4.11), but becomes ‘flattened’ as the frequency is raised. This finding suggests that when CO_2 is

Fig. 4.10 Mott-Schottky measurements on TiO_2 electrodes modified with **a** 4 μL of 15 μM CODH solution, **b** 4 μL of 30 μM CODH, and **c** 4 μL of 75 μM CODH. All experiments were carried out under a 100% N_2 atmosphere at 20 $^\circ\text{C}$ in 0.2 M MES buffer (pH 6.0). In **(b)**, frequencies above 0.6 kHz are omitted because no defined gradients were observed



introduced, a charge-transport pathway becomes available and E_{fb} can be measured at frequencies low enough for interfacial electron transfer to occur between the semiconductor surface and CODH. At higher frequencies, in contrast, charge-transfer seems to be slower than the potential modulation applied in the experiment and E_{fb} can no longer be obtained.

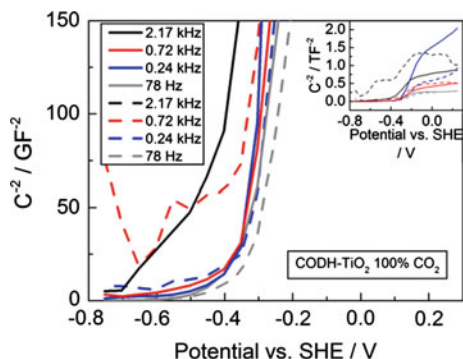


Fig. 4.11 Mott-Schottky plots ($1/C^2$ vs. potential) recorded on CODH-TiO₂ under 100% CO₂ at 20 °C in 0.2 M MES buffer (pH 6.0). Two sets of experiments carried out at several frequencies are shown. The main figure shows a magnification to highlight the linear gradients from which E_{fb} can be obtained; the inset depicts a larger C^{-2} range, showing the change in curvature when the frequency is increased to 2.17 kHz

4.2.4 Photoelectrochemistry

Visible-light-driven photoelectrochemical H₂ production at the [NiFeSe]-hydrogenase-CdS electrode was also studied (Fig. 4.12). Cadmium sulphide, having a band gap of around 2.3 eV (540 nm), allows for visible-light excitation. Cyclic voltammograms were first recorded on an unmodified (bare CdS) electrode, both in the dark and under illumination ($\lambda > 420$ nm, 16 mW cm⁻²). To eliminate heating effects, the water bath temperature was monitored throughout the experiments; no light-dependent variation was noted. Upon irradiation, the unmodified CdS electrode exhibits an anodic photocurrent at potentials above -0.4 V (as expected for an n -type semiconductor at a potential positive of E_{fb} ; Fig. 4.12a). In the presence of [NiFeSe]-hydrogenase, the anodic photocurrent is of the same magnitude as that of the bare CdS electrode. Because of the transparency of ITO toward visible-light irradiation, possible direct contact of enzyme and the underlying transparent conducting oxide support-layer (mediated by pinholes in the semiconductor surface) does not contribute to the observed photooxidation current under light exposure.

Regarding the cathodic currents, no difference can be observed for the bare CdS electrode in the dark and under illumination, as expected for an n -type semiconductor with high majority carrier density at potentials close to E_{fb} . Conversely, when [NiFeSe]-hydrogenase is introduced, catalytic H₂ reduction can be observed in the dark, analogous to the experiments described in Sect. 4.2.2. When the [NiFeSe]-CdS electrode is illuminated with visible-light, a two-fold enhancement of H₂ evolution current is observed, accompanied by a small but noticeable shift in onset potential towards less cathodic potentials. This cathodic photocurrent remains

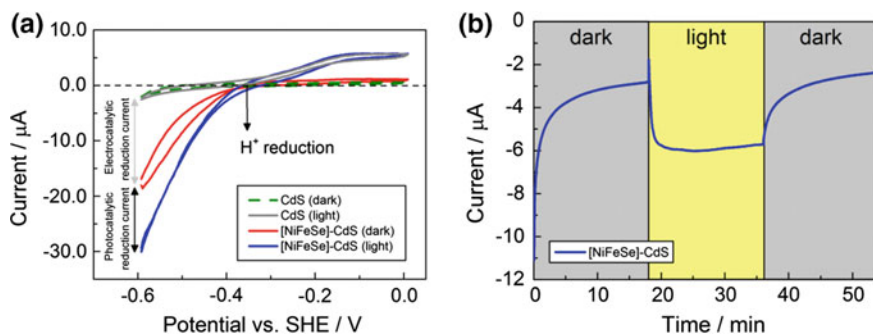


Fig. 4.12 **a** Cyclic voltammograms recorded both under dark conditions and under visible-light irradiation for an unmodified CdS electrode, and following modification with [NiFeSe]-hydrogenase. Scan rate: 10 mV s^{-1} . **b** Chronoamperometry experiments comparing the catalytic H_2 evolution current of [NiFeSe]-CdS at -0.65 V vs. SHE in the dark and under irradiation. Both experiments were carried out under an inert atmosphere in 0.2 M MES solution ($\text{pH } 6.0$) at $20 \text{ }^\circ\text{C}$. Visible-light irradiation was carried out with $\lambda > 420 \text{ nm}$ at 16 mW cm^{-2}

steadily over prolonged light exposure, illustrated in the chronoamperometry experiment depicted in Fig. 4.12b. These observations, unusual for an n -type semiconductor, will be discussed in the following section.

4.3 Discussion

When measured at TiO_2 and CdS electrodes instead of PGE, the cyclic voltammograms depicted in Fig. 4.3 clearly display a pronounced rectification of the otherwise reversible electrocatalysis of H^+/H_2 and CO_2/CO interconversion by [NiFeSe]-hydrogenase and CODH enzymes. According to established models, the surface concentration of electrons (the majority carriers for an n -type semiconductor) increases exponentially as the potential is scanned towards more negative values: according to Eq. (2.35) it is controlled, through a Boltzmann-like relationship, by the difference between E_{FB} and the applied potential [38]. As the electrode potential is lowered beyond E_{fb} there is a transformation to metallic-like character as an accumulation layer forms (Fig. 4.13). The increase in electron density at the semiconductor-catalyst interface favours efficient electron transfer from the semiconductor to the enzyme to drive fuel-formation.

In contrast, raising the applied potential E above E_{fb} results in the formation of a depletion layer that poses a barrier for electron transfer from the enzyme to the semiconductor. This reasoning explains the resistive effect observed for the oxidation reactions when each enzyme is coupled to CdS and TiO_2 surfaces. The E_{fb} values broadly lie within 0.25 V of the reduction potentials for CO_2/CO and H^+/H_2 under the experimental conditions used: this is important because the catalysts are operating in a nearly reversible manner and the respective currents change direction

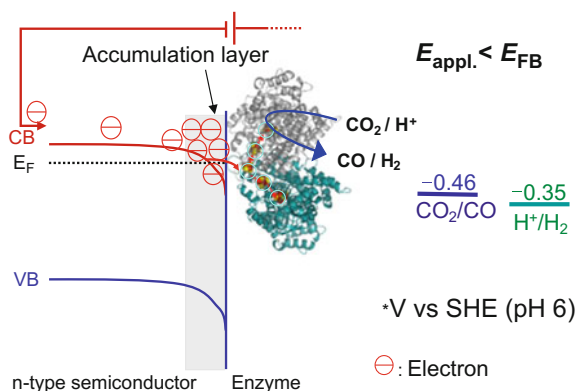


Fig. 4.13 Schematic representation of the formation of an accumulation layer at the surface of CdS or TiO₂ electrodes due to the increased electron density at the semiconductor surface when E is lowered relative to E_{fb} . The increased electron density and subsequent downward band-bending facilitate efficient electron transfer to the enzyme active site via FeS clusters to catalyse H₂ production or CO₂ reduction. Reprinted with permission from Ref. [39]. Copyright 2013 American Chemical Society

(oxidation \leftrightarrow reduction) across the same limited potential region. The apparent catalytic bias of each enzyme is thus shifted to favour fuel-formation when coupled to CdS and TiO₂ electrode surfaces, which is catalysed, efficiently, at very low overpotentials. The destructive back reaction (oxidation) in turn is greatly suppressed.

Investigations by EIS have revealed some insight into the binding of CODH on TiO₂ electrodes. Although these electrodes possess pore sizes large enough to accommodate enzyme molecules, these are now rationalised to adsorb mainly on the outer geometric surface, presumably at least partly due to the short adsorption times employed in PFE experiments. Mott-Schottky experiments on CODH-TiO₂ carried out under an inert atmosphere show that the properties greatly depend on the surface concentration of enzyme: behaviour consistent with bare TiO₂ surfaces (albeit with small shifts of the intercepts of the linear gradients to more positive values) is observed only when part of the geometric area is left uncovered or when diluted CODH solutions are employed. Taken together, these results imply that CODH adsorbs as a ‘resistive’ film, blocking charge-transfer between semiconductor and electrolyte. This description is corroborated by the change in shape of the Mott-Schottky traces upon introduction of substrate (CO₂) and the observed frequency dependence (compare Figs. 4.11 to 4.8), suggesting that a charge-transfer pathway becomes available only in the presence of CO₂.

Although these phenomena are far from being fully understood, there are implications on systems for photocatalytic CO₂ reduction that use CODH as catalyst [14–16]. In cases where small ruthenium polypyridyl dye molecules are employed as visible-light sensitisers, these are thought to penetrate more deeply into TiO₂ films/aggregates, generating excited conduction band electrons

throughout the TiO₂ electrode film/particle aggregate. These electrons must migrate to the outer surface, at which interfacial electron injection into CODH occurs. The limited carrier mobility and lifetime of the transient conduction band electrons in TiO₂ thus favour charge recombination even *before* interfacial electron transfer can occur. This notion is one explanation for the turnover frequencies of photocatalytic CO₂ reduction catalysed by CODH (the record being 1.23 s⁻¹ [16]) being orders of magnitude lower than values obtained from PFE experiments conducted under controlled potentials or from conventional solution assays.

The photoelectrochemistry experiments on [NiFeSe]-hydrogenase-modified CdS electrodes are interesting and unusual in that a two-fold enhancement of H⁺ reduction current is observed under illumination of [NiFeSe]-CdS as a result of an only modest increase in free carrier concentration. For an *n*-type semiconductor at potentials close to E_{fb} , illumination should only have a marginal effect on the magnitude of the reductive current due to the already high density of free carriers. Typically, E_F lies within 50 mV of the conduction band edge [3], consistent with the only small shift in onset potential observed for [NiFeSe]-CdS under irradiation (Fig. 4.12a). Yet, H₂ evolution is significantly enhanced by photoexcitation of electrons from the CdS valence band into the conduction band, from where they transfer to the hydrogenase enzyme. This significant amplification in catalytic current highlights the importance of the enzyme as a reversible catalyst: the enzyme is so proficient that the current is controlled more by the charge carrier availability in the semiconductor than by the properties of the hydrogenase, and the availability (concentration) of electrons can be at least as important as the overpotential driving the reaction.

However, the results in depicted in Fig. 4.12 also underline that electrode assemblies such as [NiFeSe]-CdS are not ideal photoelectrodes in a classical sense: generally, a photoelectrode should be able to lift the thermodynamic restrictions that apply to dark reactions to potentials well above the thermodynamic equilibrium. However, as *minority* carriers drive the reactions in a typical photoelectrode, an *n*-type semiconductor would be employed to drive photooxidation reactions. Still, different geometries can be used as light-absorbing and charge-separating units in artificial photosynthesis. In PV-PEC configurations for instance, the minority carriers recombine in buried junctions inside the materials, whereas the majority carriers are injected into the catalysts [38]. Demonstrating visible-light enhanced fuel-forming catalysis carried out by reversible catalysts that are driven by majority carriers, as observed in Fig. 4.12, is thus very important.

4.4 Conclusions and Perspectives

Although the enzymes used in this thesis are wholly unsuited for long-term, large-scale systems, the results presented in this chapter provide valuable insight for developing integrated artificial systems where getting as close as possible to reversible catalysis is important for efficiency. Semiconducting electrodes can be used to impose directionality on reversible catalysts that operate in the region of the

semiconductor flat-band potential: the catalytic direction shifts in response to the exponential increase in surface electron concentration as the applied potential approaches E_{fb} . In the n -type semiconductors studied in this chapter, the reduction reaction is then favoured over (destructive) oxidation.

The fact that in impedance spectroscopy experiments a frequency-dependent charge-transfer pathway becomes available when substrate is introduced (Fig. 4.11) suggests that the kinetics of electron transfer between semiconductor and enzyme could in principle be determined from the frequency dependence of the changes in capacitance vs. applied potential. However, more detailed impedance experiments and further analysis are needed to characterise the complex behaviour of the enzyme-electrode assemblies used in this thesis and construct appropriate equivalent circuits in order to fit the respective Bode and Nyquist plots (Sect. 2.3.5.3). Preliminary experiments conducted in our laboratory by Katherine Lee suggest that uniform electrodes (particularly in terms of semiconductor film-thickness) are needed to be able to determine reproducible equivalent circuits across the applied potential range. These cannot be obtained via the ‘Doctor blading’ method [40] by which TiO_2 electrodes are prepared in our laboratory (i.e. by spreading a TiO_2 slurry on the underlying transparent conducting oxide substrate using a microscope glass slide, see Sect. 8.3.2). Instead, more elaborate deposition techniques such as spin coating are required.

The photoelectrochemistry results are intriguing and important in that they establish that even under limited carrier-enhancement, significantly amplified catalysis (i.e. by a factor of two) can be observed, highlighting the proficiency of the enzyme. In reduction catalysis, p -type materials would be required to maximise the enhancement of free carrier generation by illumination and achieve catalysis at significant *under* potentials. Accordingly, having established the principles of PFE on semiconductor electrodes in this chapter, the next chapter deals with the construction of a true, ‘minority carrier utilising’ photocathode for light-driven fuel-formation.

References

1. Soo HS, Agiral A, Bachmeier A, Frei H (2012) *J Am Chem Soc* 134:17104
2. Bott A (1998) *Curr Sep* 3:87
3. Gelderman K, Lee L, Donne SW (2007) *J Chem Educ* 84:685
4. Topoglidis E, Campbell C, Cass AG, Durrant JR (2001) *Langmuir* 17:7899
5. Topoglidis E, Lutz T, Durrant JR, Palomares E (2008) *Bioelectrochemistry* 74:142
6. Jones AK, Sillery E, Albracht SPJ, Armstrong FA (2002) *Chem Commun* 866
7. Parkin A, Goldet G, Cavazza C, Fontecilla-Camps JC, Armstrong FA (2008) *J Am Chem Soc* 130:13410
8. Armstrong FA, Hirst J (2011) *Proc Natl Acad Sci U S A* 108:14049
9. Frey M (2002) *ChemBioChem* 3:153
10. Parkin A, Seravalli J, Vincent KA, Ragsdale SW, Armstrong FA (2007) *J Am Chem Soc* 129:10328
11. Grätzel M (2001) *Nature* 414:338

12. Reisner E, Fontecilla-Camps JC, Armstrong FA (2009) *Chem Commun* 550
13. Reisner E, Powell DJ, Cavazza C, Fontecilla-Camps JC, Armstrong FA (2009) *J Am Chem Soc* 131:18457
14. Woolerton TW, Sheard S, Reisner E, Pierce E, Ragsdale SW, Armstrong FA (2010) *J Am Chem Soc* 132:2132
15. Woolerton TW, Sheard S, Pierce E, Ragsdale SW, Armstrong FA (2011) *Energy Environ Sci* 4:2393
16. Chaudhary YS, Woolerton TW, Allen CS, Warner JH, Pierce E, Ragsdale SW, Armstrong FA (2012) *Chem Commun* 48:58
17. Armstrong FA, Heering HA, Hirst J (1997) *Chem Soc Rev* 26:169
18. Armstrong FA (1990) In: *Bioinorganic Chemistry*, vol 72. Springer, Berlin, p 137
19. Morra S, Valetti F, Sadeghi SJ, King PW, Meyer T, Gilardi G (2011) *Chem Commun* 47:10566
20. Woolerton TW (2012) D Phil Thesis. University of Oxford, Oxford
21. Bacsa RR, Kiwi J (1998) *Appl Catal B* 16:19
22. Svetlitchnyi V, Peschel C, Acker G, Meyer O (2001) *J Bacteriol* 183:5134
23. Park SW, Huang CP (1987) *J Colloid Interf Sci* 117:431
24. Wang VC-C, Ragsdale SW, Armstrong FA (2013) *ChemBioChem* 1845:14
25. Wang VC-C, Can M, Pierce E, Ragsdale SW, Armstrong FA (2013) *J Am Chem Soc* 135:2198
26. Hexter SV, Grey F, Happe T, Climent V, Armstrong FA (2012) *Proc Natl Acad Sci U S A* 109:11516
27. Murphy BJ, Sargent F, Armstrong FA (2014) *Energy Environ Sci* 7:1426
28. Hexter SV, Esterle TF, Armstrong FA (2014) *Phys Chem Chem Phys* 16:11822
29. Kavan L, Grätzel M, Rathouský J, Zukalb A (1996) *J Electrochem Soc* 143:394
30. Fabregat-Santiago F, Mora-Seró I, Garcia-Belmonte G, Bisquert J (2003) *J Phys Chem B* 107:758
31. Meissner D, Memming R, Kastening B (1988) *J Phys Chem* 92:3476
32. Beranek R (2011) *Adv Phys Chem* 786759
33. Lee MS, Cheon IC, Kim YI (2003) *Bull Korean Chem Soc* 24:1155
34. Boschloo G, Fitzmaurice D (2000) *J Electrochem Soc* 147:1117
35. Bard AJ, Faulkner LR (2001) *Electrochemical Methods: Fundamentals and Applications*, 2nd edn. John Wiley & Sons Inc., New York
36. Kavan L, Grätzel M, Gilbert SE, Klemenz C, Scheel HJ (1996) *J Am Chem Soc* 118:6716
37. Spadavecchia F, Cappelletti G, Ardizzone S, Ceotto M, Falciola L (2011) *J Phys Chem C* 115:6381
38. Walter MG, Warren EL, McKone JR, Boettcher SW, Mi Q, Santori EA, Lewis NS (2010) *Chem Rev* 110:6446
39. Bachmeier A, Wang VC-C, Woolerton TW, Bell S, Fontecilla-Camps JC, Can M, Ragsdale SW, Chaudhary YS, Armstrong FA (2013) *J Am Chem Soc* 135:15026
40. Barbé CJ, Arendse F, Comte P, Jirousek M, Lenzmann F, Shklover V, Grätzel M (1997) *J Am Ceram Soc* 80:3157

Chapter 5

Selective Visible-Light-Driven CO₂ Reduction on a *p*-Type Dye-Sensitised NiO Photocathode

5.1 Introduction

As a general rule, fuels derived from artificial photosynthesis fuels can either be H₂, the immediate product of water splitting, or carbon-based compounds such as methanol. Most obviously, carbon fuels can be formed indirectly by ‘hydrogenation’ of CO₂, similar to the processes occurring in photosynthetic dark reactions. However, direct reduction of CO₂ is also an attractive possibility that could lead to CO₂ replacing petrochemicals as the feedstock for value-added organic chemicals. Like natural photosynthesis, artificial photosynthesis can be broken down into four essential processes: harvesting of visible-light, charge (electron-hole) separation, fuel formation, and water oxidation to O₂. The last two processes require an efficient and selective catalyst (see Sect. 1.2). It is difficult to integrate all of these processes, so researchers have streamlined efforts by focusing on individual aspects.

This chapter addresses the direct reduction of CO₂ to CO using a photoelectrochemical cell comprising a dye-sensitised *p*-type NiO photocathode functionalised by spontaneous adsorption of CODH (Fig. 5.1). Reductive CO₂ activation is a fundamentally challenging process and only CODH and formate dehydrogenase are known to selectively and reversibly achieve synchronous, proton-coupled two-electron reduction of CO₂ to CO or formate, avoiding the highly unfavourable one-electron reduced intermediate CO₂^{•-} [Eq. (1.4)].

Despite its low majority carrier (i.e. hole) mobility, values between 10⁻⁸ and 10⁻⁹ cm² S⁻¹ have been reported—two orders of magnitude lower than the electron diffusion coefficient in *n*-TiO₂ [2], NiO is the most widely studied semiconductor material in *p*-type DSSCs [3, 4]. Having a band gap of 3.55 eV [5], NiO is transparent to visible light (apart from a phenomenon known as ‘parasitic absorption’, vide infra) and requires sensitisation to extend the absorbance into the visible

Part of the work presented in this chapter has been published: Andreas Bachmeier, Samuel Hall, Stephen W. Ragsdale, and Fraser A. Armstrong, *J. Am. Chem. Soc.* **2014**, *136*, 13518.

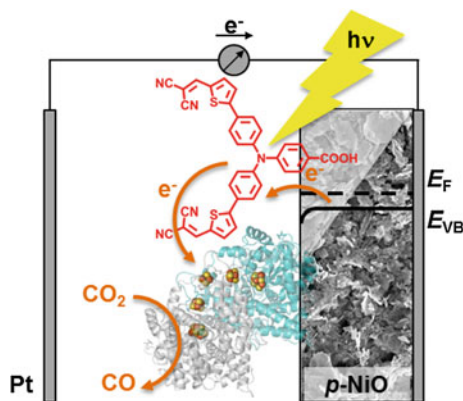


Fig. 5.1 Schematic representation of a photoelectrochemical cell for the selective reduction of CO₂ to CO at *p*-type NiO. Light-absorption by the organic dye P1 (red) is followed by electron transfer to CODH, which is co-adsorbed on the NiO surface and carries out CO₂ reduction, while hole injection into the NiO valence band regenerates the P1 ground state. The porous nature of the NiO surface is indicated by the SEM image (full image in Fig. 5.2). The Fermi level and valence band potentials of NiO are denoted as E_F and E_{VB} . Reprinted with permission from Ref. [1]. Copyright 2014 American Chemical Society

region of the electromagnetic spectrum. To this end, Sun and co-workers developed the organic pigment P1 (Fig. 5.1) as photosensitiser for *p*-type dye-sensitised solar cells [6]. Being one of the most efficient sensitisers to date (maximum IPCE = 63%, open-circuit voltage $V_{oc} = 84$ mV, short-circuit current density $j_{sc} = 5.48$ mA cm⁻², fill factor $ff = 33\%$, resulting in a photoconversion efficiency of 0.15% [2]), this ‘push-pull’ dye uses a triphenylamine moiety as electron donor component and two malononitrile groups as acceptors. The different components are connected by a conjugated chain comprising a thiophene unit. Light excitation is associated with spatial intramolecular charge separation through electron transfer from the donor part of the dye to the acceptor [6]. Being partly localised on the triphenylamine unit and hence close to the –COOH anchoring group/NiO surface and having its energy level (1.38 V vs. NHE) below the valence band of NiO, the HOMO of P1 allows for efficient hole injection into NiO. The LUMO, in turn, is spatially separated from the HOMO and localised on the acceptor (i.e. malononitrile) moieties.

Recently, Sun et al. achieved light-driven H₂ evolution by co-adsorbing P1 and a molecular cobalt cobaloxime catalyst on NiO [7]. Taking their lead, the work described in this chapter adapted the concept for light-driven CO₂ reduction. The mechanistic principle being exploited is that each excitation of P1 results in an electron being transferred to its co-adsorbed partner CODH, passing through a relay of FeS clusters to the [Ni₄Fe-4S]-active site at which CO₂ is converted to CO in a proton-coupled two-electron reaction according to Scheme 1.4. Unlike simple molecular catalysts, the additional FeS centres enable redox enzymes such as CODH to capture irreversibly [8] all the electrons required to complete the catalytic

Table 5.1 Reduction potentials of the individual components of the CO₂ reducing photocathode assembly depicted in Fig. 5.1

	$E(\text{CO}_2/\text{CO})$	$E(\text{P1}/\text{P1}^-)$	$E_{\text{vb}}, E_{\text{cb}}$
CODH	-0.46 [9]		
P1		-1.13 [6, 10]	
NiO			0.60, -3.00 [11]

All values in V vs. SHE at pH 6.0

cycle when supplied to a highly efficient active site. The P1 ground state is regenerated through hole injection into the NiO valence band. The relevant electrochemical potentials of the individual components are given in Table 5.1.

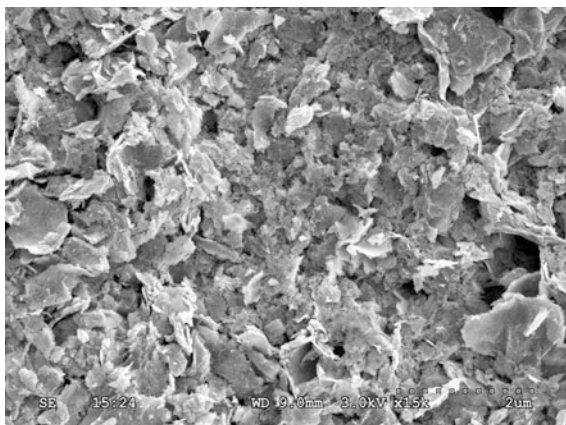
5.2 Results and Discussion

5.2.1 *Electrocatalytic Activity of Carbon Monoxide Dehydrogenase Adsorbed on a p-Type NiO Electrode*

First, the dark electrocatalytic activity of CODH adsorbed on a *p*-type NiO electrode was studied using PFE. Figure 5.2 depicts an SEM image of a typical NiO film electrode used in this work. Being similar in porosity to the TiO₂ and CdS films depicted in Fig. 4.3, the surface possesses sites for electroactive enzyme adsorption in a variety of orientations. With the point of zero charge between 8.3 and 8.5, depending on the experimental method employed in its determination [12], at pH 6.0 the NiO surface gives rise to attractive electrostatic interactions with CODH similar to those observed for TiO₂ and CdS (Sect. 4.2.1).

To remind the reader, CODH displays catalytic activity for both CO₂ reduction and CO oxidation when adsorbed on a PGE electrode and both CO₂ and CO are

Fig. 5.2 SEM image of a NiO film deposited on ITO. Reprinted with permission from Ref. [1]. Copyright 2014 American Chemical Society

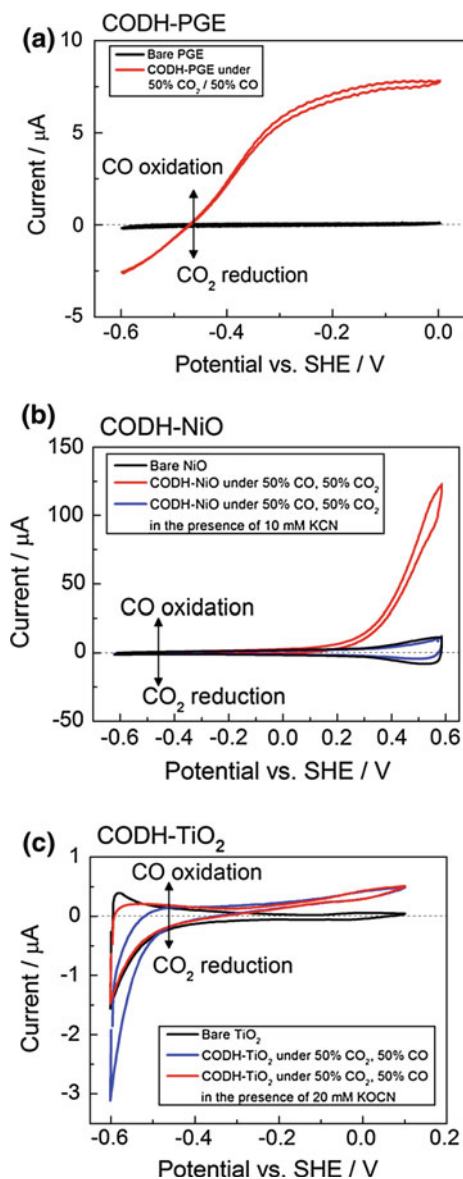


present in the solution, as shown in Fig. 5.3a (which displays the same data as Fig.4.3a). Importantly, the voltammogram cuts sharply through the zero-current axis at the thermodynamic potential and catalysis is controlled by the inherent properties of the enzyme [13–15]. The catalytic bias prevails, and it is largely controlled by the potential of the electron entry/exit point of the enzyme [13, 16]. As described in Sect. 1.6.4.2, the active site of CODH alternates between the two

Fig. 5.3 Cyclic voltammograms of CODH adsorbed on **a** PGE, **b** NiO, and **c** TiO₂ electrodes.

Current-voltage curves of the bare electrodes are depicted in *black*, experiments with adsorbed CODH (recorded in a 50% CO/50% CO₂ gas mixture bubbling through the cell) are shown in *red*. The *blue* CVs in **b** and **c** were recorded in the presence of 10 mM KCN in the presence of 20 mM KOCN (c). Other conditions: 20 °C, 0.2 M MES buffer (pH 6.0), scan rate: 10 mV s⁻¹.

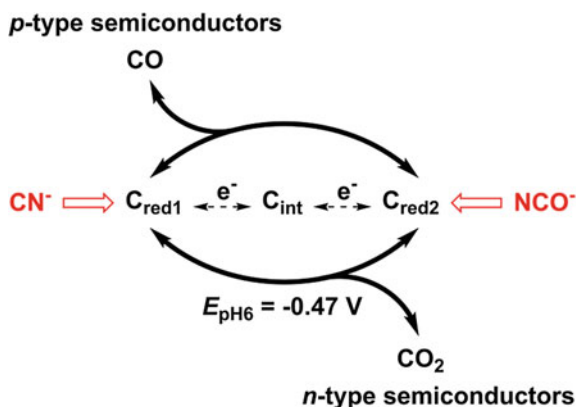
a and **c** adapted from Fig. 4.3



catalytically active states C_{red1} and C_{red2} , separated by two electrons (Scheme 1.4), with C_{int} as an intermediate formed during long-range electron transfers from the FeS clusters.

In contrast to the reversible catalytic interconversion of CO_2 and CO observed on the metallic-type PGE electrode, CODH behaves as a *unidirectional* CO oxidiser when attached to NiO (Fig. 5.3b, red trace); in other words, the otherwise bidirectional catalysis is rectified. A catalytic oxidation current in Fig. 5.3b is observed only upon applying an overpotential of approximately 0.6 V (oxidising conditions under which CODH converts slowly to the inactive C_{ox} state [17]). To prove that the oxidation current indeed stems from catalytic turnover, KCN was injected into the electrochemical cell (to a final concentration of 10 mM; blue voltammogram in Fig. 5.3b). Being isoelectronic with CO, cyanide targets the C_{red1} state of CODH (Scheme 5.1), thereby selectively inhibiting CO oxidation [17]. The voltammogram thus obtained resembles the baseline (bare NiO). These results mirror the observations with CODH adsorbed on the *n*-type materials TiO_2 and CdS described in Sect. 4.2.2 [15]. Figure 5.3c (adapted from Fig. 4.3a) illustrates this effect for TiO_2 and shows cyclic voltammograms of CODH adsorbed on TiO_2 recorded under identical conditions to the voltammograms displayed in Fig. 5.3a,b. In contrast to *p*-NiO, CO oxidation at *n*- TiO_2 is barely detectable whereas a strong reduction current is observed, which is established to be CO_2 reduction by introducing cyanate (NCO^- , isoelectronic with CO_2) which targets the C_{red2} state and blocks CO_2 reduction (see Scheme 5.1 and blue trace in Fig. 5.3c).

The results presented in this section highlight that, when attached to semiconducting electrodes such as TiO_2 , CdS, and NiO, the activity of an electrocatalyst depends greatly on the properties of the semiconductor, in particular the carrier



Scheme 5.1 Redox states involved in catalytic CO_2 interconversion at the active site of CODH and how *p*-type and *n*-type semiconductors rectify catalytic electron flow. The small molecule inhibitors CN^- and NCO^- selectively intercept the C_{red1} and C_{red2} states and inhibit CO oxidation (CN^-) and CO_2 reduction (NCO^-) [17]. Reprinted with permission from Ref. [1]. Copyright 2014 American Chemical Society

availability at the semiconductor/enzyme interface. The resulting rectification in either direction, depending on the choice of semiconductor, is evident only when an electrocatalyst that otherwise behaves reversibly is used [15]. According to Eqs. (2.35) and (2.36), the surface concentration of majority carriers in a semiconductor depends exponentially on the difference between the applied potential E and the flat-band potential E_{fb} [18]. The catalytic directionality enforced on *n*-type TiO₂ (i.e. the inversion of the apparent catalytic bias) coincides with a change in carrier availability around the flat-band potential of the semiconductor ($E_{\text{fb}}(\text{TiO}_2) \approx -0.50$ V vs. SHE at pH 6.0; see Sect. 4.2.3.1). In chemical terms, some Ti⁴⁺ sites are reduced to Ti³⁺. In contrast, *p*-type NiO ($E_{\text{fb}}(\text{NiO}) \approx 0.61$ V vs. SHE at pH 6.0 [11]) forms a depletion layer at potentials negative of E_{fb} , which acts as a barrier for electron transfer from the semiconductor to the catalyst, blocking CO₂ reduction. As E_{fb} is approached, the conductivity of NiO increases exponentially, allowing CO oxidation catalysis to occur. In chemical terms, some Ni²⁺ sites are oxidised to Ni³⁺ (see Sect. 2.3.3.3). This effect is reflected in a steep increase in the catalytic oxidation current in Fig. 5.3b positive of ca. 0.3 V vs. SHE, i.e. relatively close to E_{fb} .

5.3 Photoelectrocatalytic CO₂ Reduction

Having established the electroactivity of CODH on NiO, the semiconductor electrodes have been sensitised with the visible-light-absorbing dye P1 [6] (Fig. 5.1), by soaking the electrodes in a 300 mM solution of P1 in ethanol overnight. Figure 5.4 shows linear sweep voltammograms recorded under chopped illumination in CO₂-saturated buffer (cyclic voltammograms of NiO–P1 are depicted in Fig. 5.5).¹ Bare NiO shows very little photocurrent because of its large band gap of 3.55 eV [5] (black current-potential curve). It has to be noted that despite its large band gap, non-stoichiometric NiO is a material of dark colour. Whereas ideal, stoichiometric NiO is pale-green (owing its colour to intra-3d transitions in octahedral Ni²⁺ sites [19]), calcination in air yields a dark-coloured material. Originally, this dark hue in mesoporous NiO films has been ascribed to the presence of Ni³⁺ species at the surface, which are produced as some Ni²⁺ is oxidised during the heat treatment in air [20]. These species give rise to brown or black coloration, and, importantly, excitation of which does not result in photocurrent [5, 21]. However, this explanation now seems to be oversimplistic because Renaud et al. recently established that black elemental Ni is also formed in the calcination process, and is a major source of the dark colour [19]. These Ni(0) impurities do also not

¹Current densities, normalised to the respective geometric surface area, are reported in photoelectrochemistry experiments where this seems advantageous from a viewpoint of allowing general comparability across different (literature) systems. However, the reader should bear in mind that the intrinsic surface areas of porous semiconductor electrodes are much greater than the outer, geometric values suggest.

Fig. 5.4 Linear sweep voltammograms of NiO (black), NiO-P1 (red), and NiO-P1-CODH (blue) recorded under chopped illumination (0.5 Hz, 45 mW cm⁻²) and CO₂ flow. Conditions: 0.2 M MES buffer (pH 6.0), $T = 32\text{ }^{\circ}\text{C}$, scan rate = 10 mV s⁻¹

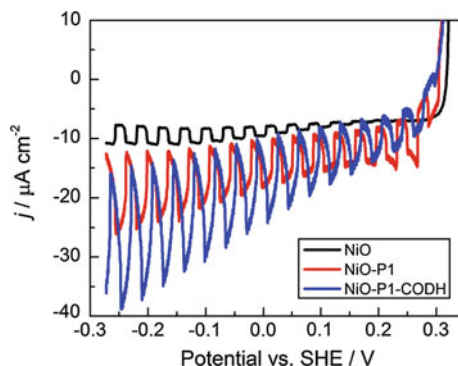
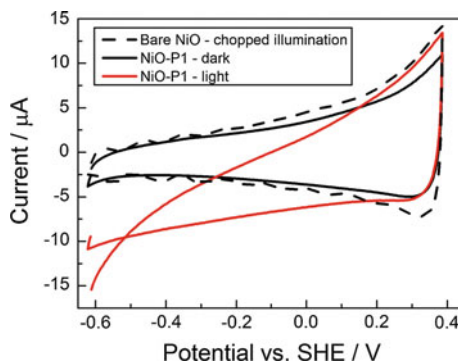


Fig. 5.5 Cyclic voltammograms of a bare NiO electrode (dashed line) and NiO-P1 in the dark (black) and under illumination (45 mW cm⁻², red). Scan rate: 30 mV s⁻¹, 0.2 M MES buffer (pH 6.0), 25 °C



contribute to the photocurrent. Commonly, these phenomena of ‘non-current-producing’ absorption are known as ‘parasitic optical absorption’ [22]. Upon sensitisation with P1, the photocurrent increases since P1 is capable of absorbing visible light ($\lambda_{\text{max}} = 550\text{ nm}$ in solution and 500 nm when adsorbed on NiO [6]).

Modification with CODH results in a further photocurrent enhancement, which can be ascribed to the light-driven reduction of CO₂. Photoexcited P1 provides sufficient driving force to effect CO₂ reduction catalysed by CODH (see Table 5.1) but does not reduce CO₂ itself. The LUMO of P1 lies approximately 0.7 V lower in energy than the CO₂/CO₂⁻ redox couple: importantly, as a single-electron transfer dye that is not capable of accumulating a second electron, P1 cannot undergo the PCET reactions that are required to lower the activation barrier for CO₂ activation, in contrast to CODH (which easily accumulates the two electrons needed).

The hypothesis that the photocurrent enhancement observed upon adsorption of CODH on NiO-P1 is due to catalytic conversion of CO₂ to CO had to be verified experimentally. Once again NCO⁻ was used as a selective inhibitor of CO₂ reduction, as even prolonged illumination over several hours did not produce enough CO to allow detection by gas chromatography (Fig. 5.6). This was due to the minute quantities of enzymes on the electrode surface (nmol)—in contrast to the much larger amounts of substance used in the photocatalysis experiments our laboratory has carried out previously [23–25].

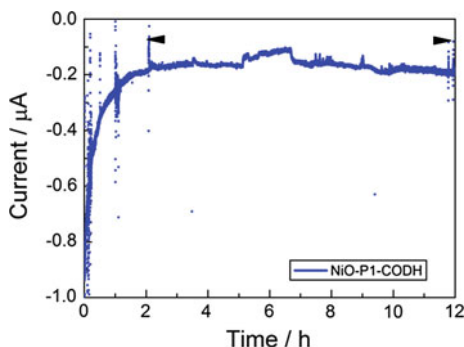


Fig. 5.6 Typical long-term chronoamperometry experiment of NiO-P1-CODH under illumination (45 mW cm^{-2}) at -0.3 V vs. SHE; 0.2 M MES buffer (pH 6.0), $10 \text{ }^\circ\text{C}$. The cell solution (7.5 mL buffer) and headspace were saturated with a mixture of $98\% \text{ CO}_2$ and $2\% \text{ CH}_4$ prior to the experiment (CH_4 served as internal standard in post-experimental gas chromatographic analysis). The *black arrows* indicate the capacitive dark current. No CO could be detected after the experiment. A total charge of 5.05 mC (after subtraction of the electrode capacitance) was passed through the system, which would, assuming 100% Faradaic efficiency for CO_2 reduction as the upper limit, correspond to the formation of a maximum of 26.2 nmol CO . Such a small amount could not be detected by GC, as it would still be dissolved in the cell solution and furthermore lie below the detection limit of the employed gas chromatograph

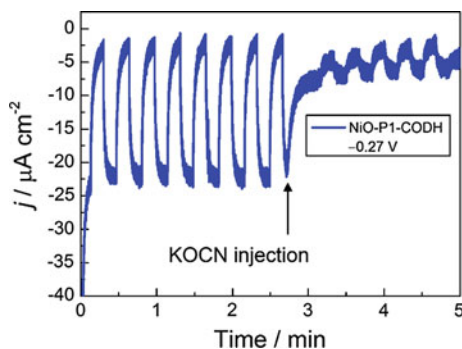


Fig. 5.7 Chronoamperometry experiment showing transient photocurrents under chopped illumination of NiO-P1-CODH under a flow of CO_2 with the potential being held at -0.27 V vs. SHE. NCO^- was injected to a final concentration of 60 mM as indicated. Experimental conditions: white-light illumination (45 mW cm^{-2}); 0.2 M MES buffer (pH 6.0), $T = 32 \text{ }^\circ\text{C}$

Figure 5.7 depicts transient photocurrents of NiO-P1-CODH recorded at -0.27 V vs. SHE (pH 6.0), which represents a 0.2 V *under* potential with respect to CO_2 reduction in the dark.

The photocurrent decreases significantly upon introduction of 60 mM KOCN, which establishes that the major proportion of the observed photocurrent stems from CO_2 reduction. Control experiments in the absence of CODH, i.e. NiO-P1 only, show that injecting KOCN has no effect on the photocurrent (Fig. 5.8).

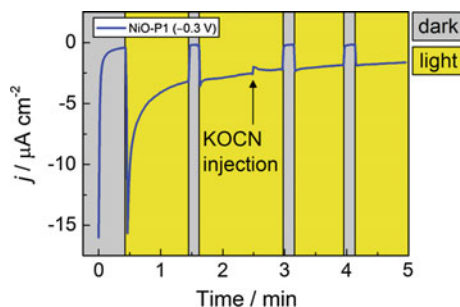


Fig. 5.8 Chronoamperometry experiment of NiO–P1 (control experiment *without* CODH) under illumination (45 mW cm^{-2}) at -0.3 V vs. SHE; 0.2 M MES buffer (pH 6.0), $25 \text{ }^\circ\text{C}$, 50 s/min CO₂ flow. At $t = 2.5 \text{ min}$ KOCN solution was injected into the cell to a final concentration of 60 mM . KOCN did not affect the photocurrent, in contrast to NiO–P1–CODH shown in Fig. 5.7

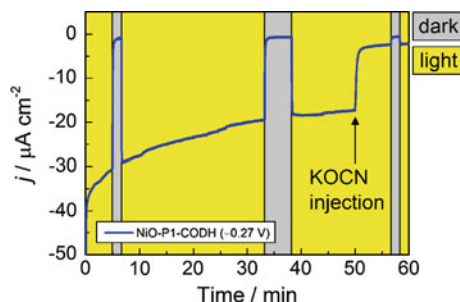


Fig. 5.9 Continuous illumination of NiO–P1–CODH to assess the stability of the photocathode-assembly under turnover conditions. Experimental conditions: white-light illumination (45 mW cm^{-2}); $E = -0.27 \text{ V}$ vs. SHE; CO₂ flow; 0.2 M MES buffer (pH 6.0); $T = 32 \text{ }^\circ\text{C}$. NCO⁻ was injected to a final concentration of 60 mM at $t = 50 \text{ min}$

Having identified the nature of the photocurrent, the stability of CO₂ reduction was assessed. Figure 5.9 depicts the temporal behaviour of the catalytic current produced by NiO–P1–CODH during prolonged illumination. The assembly shows good stability until cyanate is injected, analogous to the experiment depicted in Fig. 5.7, again demonstrating the catalytic turnover of the photocathode-catalyst system. Both Figs. 5.4 and 5.7 strongly support a mechanism similar to that described by Sun and co-workers for H₂ production [7]. In the system described in this work, P1 acts as a visible-light-responsive sensitizer that generates excited-state electrons, transfers these to CODH for catalysis, and is regenerated via hole injection into NiO.

Concerning the kinetic order of the elementary steps, the current understanding of these complex multi-site photoinduced reactions is scant. Hole injection into the NiO valence band is usually fast (ps-timescale), but, in contrast to dye-sensitised

n-type TiO₂, geminate recombination is also a very fast process (ns-regime) [2]. Reasons for the fast back electron transfer processes are not fully understood, but it has recently been shown that, in contrast to most TiO₂-based DSSCs that have a large driving force for recombination [26], for NiO this reaction lies in the normal Marcus regime, as experimentally verified for a series of perylene imide sensitiser attached to NiO surfaces [27]. Rapid recombination in dye-NiO assemblies may arise, in part, due to the Ni(III) sites being located on the semiconductor surface (in contrast to the behaviour of TiO₂, see Sect. 2.3.3.3), in close proximity to the photoreduced dye [3]. Hence, efficient charge separation *within* the dye, as for example in push-pull architectures such as P1, is crucial to suppress geminate recombination.

Among the few examples in the literature, Hammarström and co-workers recently showed that electron injection from an excited dye immobilised on NiO into a co-adsorbed H⁺ reduction catalyst significantly retards destructive geminate recombination between NiO and the dye, in their case coumarin [28]. Based on these observations, it is plausible to assume a mechanism in which visible-light excitation of P1 is followed, kinetically, by hole injection into the NiO valence band, forming the P1 anion. Then, electron transfer from the LUMO of P1 to CODH (presumably to the D-cluster) takes place. Time-resolved studies of photoinduced electron transfer by transient absorption spectroscopy would, in principle, be insightful and might establish the charge transfer kinetics. However, a major problem is that electron injection into FeS enzymes such as CODH is not accompanied by a distinct change in absorbance, due to the broad absorption bands of FeS clusters [8].

5.4 Conclusions and Perspectives

In conclusion, catalytic electron flow through the CO₂-reducing enzyme CODH, which behaves as a reversible catalyst on a metallic-like electrode, is rectified when CODH is attached to *n*-type or *p*-type semiconductors, leading to unidirectional CO₂ reduction and CO oxidation, respectively. When NiO is sensitised with the visible-light sensitiser P1, a photocathode is produced that selectively reduces CO₂ to CO under visible-light illumination and application of a mildly reducing potential. To the best of my knowledge, these results provide the first demonstration of visible-light-driven clean and efficient CO₂ reduction at a *p*-type photocathode—a reaction intrinsically more difficult than proton reduction. While the photocurrent densities observed are too small to allow for scale-up, they are of the same magnitude as similar systems for H₂ evolution [7, 29]. Both CODH and P1 are co-adsorbed on NiO without specific coupling, similar to work by Hammarström [28], Mozer [29], and Sun [7]. Specific covalent linkage of CODH and P1 would be an attractive strategy to improve the efficiency of electron transfer, but is not straightforward as it requires genetic modification of the enzyme to introduce binding sites for the sensitiser.

The assembly depicted in Fig. 5.1 shows good stability under turnover conditions, indicating that it could, in principle, be coupled with a photoanode for water oxidation in a tandem-photoelectrochemical cell in order to close the photosynthetic cycle. Preliminary experiments have been carried out based on a procedure employed by Mozer et al. [29]. A wired photoelectrochemical tandem cell (similar to the schematic in Fig. 1.21) was created by connecting the NiO-P1-CODH electrode as working electrode to a W-BiVO₄ photoanode serving as counter electrode [30] (see Sect. 6.2.3) for light-driven unassisted CO₂ reduction coupled to water oxidation. The two electrodes were placed in different compartments of an electrochemical cell separated by a Nafion 117 membrane and illuminated separately, using two visible-light sources. Figure 5.10 depicts a typical experiment under no externally applied bias. Although illumination does generate a photocurrent, this cannot be attributed to CO₂ reduction as injection of KOCN does not result in photocurrent attenuation. The temporal behaviour of the photocurrent after KOCN was introduced was similar to the control experiment carried out in the absence of CODH depicted in Fig. 5.8.

Although these initial attempts were unsuccessful, they serve to illustrate the importance of the different components not only being active individually, but also when coupled to form an integrated device. Possible reasons for the inactivity of this ‘integrated system’ include instability of the NiO-P1-CODH electrode under the experimental conditions used (for example, P1 desorption in phosphate buffer [7]), as well as enhanced carrier recombination *before* catalysis can occur [31], due to the transient nature of the charge carriers when no external bias is applied (in contrast to the potential-controlled experiments depicted in Figs. 5.7 and 5.9).

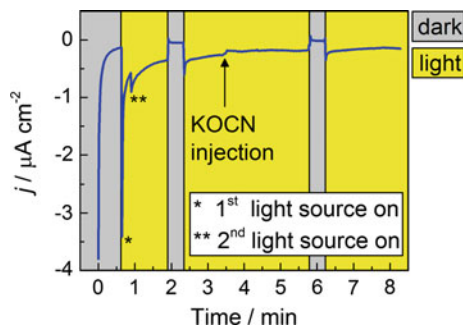


Fig. 5.10 Photocurrent profile of a photoelectrochemical cell comprising a NiO-P1-CODH photocathode (working electrode) and a W-BiVO₄ photoanode (counter electrode). The electrodes were placed in two compartments of an electrochemical cell, separated by a Nafion 117 membrane, and illuminated separately with $P_{\text{in}} = 45 \text{ mW cm}^{-2}$ in each case. The cell solution was 0.1 M potassium phosphate buffer (pH 6.0 at 25 °C, see Sect. 8.5.1.1) in both compartments. The CE compartment was purged with Ar (50 scc min⁻¹) and the WE was sparged with CO₂ over the course of the experiment (50 scc min⁻¹). At $t = 45 \text{ s}$, the CE compartment was illuminated (*) through the ITO back contact, illumination of the WE compartment commenced shortly afterwards at $t = 60 \text{ s}$ (**). KOCN was injected to a final concentration of 60 mM at $t = 210 \text{ s}$, to no effect on the photocurrent

Other limiting factors of the NiO–P1–CODH cathode-component are the intrinsically low conductivity of NiO, fast geminate charge recombination within the cathode-assembly, and the low surface concentration of CODH due to its large ‘footprint’.

Based on the limited knowledge that is available on the electron transfer kinetics in dye-sensitised NiO films, a mechanism of light-driven photoelectrocatalytic CO₂ reduction by NiO–P1–CODH is proposed, but the precise order of electron transfer steps still remains unclear. The next chapter deals with solar-to-chemical conversion using flavocytochrome *c*₃, an enzyme containing an electron transfer relay which comprises four coloured haem moieties with distinct absorption bands that change upon oxidation/reduction [32]. Thus, this enzyme should be amenable to future time-resolved optical studies.

Although they are not suitable for large-scale applications, this chapter again highlights that reversible and highly selective electrocatalysts such as CODH are valuable model catalysts for artificial photosynthesis. Only using a catalyst that is otherwise reversible reveals rectification of catalytic electron transport at a semiconductor. Multi-centred enzymes, which have well-defined and stable active sites, have a special ability to accumulate electrons, a property that is less likely for simple catalysts but likely to be very important in competing with recombination.

References

1. Bachmeier A, Hall S, Ragsdale SW, Armstrong FA (2014) *J Am Chem Soc* 136:13518
2. Odobel F, Pellegrin Y (2013) *J Phys Chem Lett* 4:2551
3. Odobel F, Pellegrin Y, Gibson EA, Hagfeldt A, Smeigh AL, Hammarström L (2012) *Coord Chem Rev* 256:2414
4. Odobel F, Le Pleux L, Pellegrin Y, Blart E (2010) *Acc Chem Res* 1063:43
5. Boschloo G, Hagfeldt A (2001) *J Phys Chem B* 105:3039
6. Qin P, Zhu H, Edvinsson T, Boschloo G, Hagfeldt A, Sun L (2008) *J Am Chem Soc* 130:8570
7. Li L, Duan L, Wen F, Li C, Wang M, Hagfeldt A, Sun L (2012) *Chem Commun* 48:988
8. Wilker MB, Shinopoulos KE, Brown KA, Mulder DW, King PW, Dukovic G (2014) *J Am Chem Soc* 136:4316
9. Benson EE, Kubiak CP, Sathrum AJ, Smieja JM (2009) *Chem Soc Rev* 38:89
10. Qin P, Wiberg J, Gibson EA, Linder M, Li L, Brinck T, Hagfeldt A, Albinsson B, Sun L (2010) *J Phys Chem C* 114:4738
11. He J, Lindström H, Hagfeldt A, Lindquist S-E (2000) *Sol Energy Mater Sol Cells* 62:265
12. Mahmood T, Saddique MT, Naeem A, Westerhoff P, Mustafa S, Alum A (2011) *Ind Eng Chem Res* 50:10017
13. Hexter SV, Grey F, Happe T, Climent V, Armstrong FA (2012) *Proc Natl Acad Sci U S A* 109:11516
14. Murphy BJ, Sargent F, Armstrong FA (2014) *Energy Environ Sci* 7:1426
15. Bachmeier A, Wang VC-C, Woolerton TW, Bell S, Fontecilla-Camps JC, Can M, Ragsdale SW, Chaudhary YS, Armstrong FA (2013) *J Am Chem Soc* 135:15026
16. Hexter SV, Esterle TF, Armstrong FA (2014) *Phys Chem Chem Phys* 16:11822
17. Wang VC-C, Can M, Pierce E, Ragsdale SW, Armstrong FA (2013) *J Am Chem Soc* 135:2198

18. Bard AJ, Faulkner LR (2001) *Electrochemical Methods: Fundamentals and Applications*, 2nd edn. John Wiley & Sons Inc, New York
19. Renaud A, Chavillon B, Cario L, Pleux LL, Szuwarski N, Pellegrin Y, Blart E, Gautron E, Odobel F, Jobic S (2013) *J Phys Chem C* 117:22478
20. Gonzalez-Elipe AR, Holgado JP, Alvarez R, Munuera G (1992) *J Phys Chem* 96:3080
21. Zhu H, Hagfeldt A, Boschloo G (2007) *J Phys Chem C* 111:17455
22. Powar S, Wu Q, Weidener M, Nattestad A, Hu Z, Mishra A, Bauerle P, Spiccia L, Cheng Y-B, Bach U (2012) *Energy Environ Sci* 5:8896
23. Woolerton TW, Sheard S, Reisner E, Pierce E, Ragsdale SW, Armstrong FA (2010) *J Am Chem Soc* 132:2132
24. Woolerton TW, Sheard S, Pierce E, Ragsdale SW, Armstrong FA (2011) *Energy Environ Sci* 4:2393
25. Chaudhary YS, Woolerton TW, Allen CS, Warner JH, Pierce E, Ragsdale SW, Armstrong FA (2012) *Chem Commun* 48:58
26. Kuciauskas D, Freund MS, Gray HB, Winkler JR, Lewis NS (2001) *J Phys Chem B* 105:392
27. Smeigh AL, Pleux LL, Fortage J, Pellegrin Y, Blart E, Odobel F, Hammarstrom L (2012) *Chem Commun* 48:678
28. Gardner JM, Beyler M, Karnahl M, Tschierlei S, Ott S, Hammarström L (2012) *J Am Chem Soc* 134:19322
29. Tong L, Iwase A, Nattestad A, Bach U, Weidener M, Gotz G, Mishra A, Bauerle P, Amal R, Wallace GG, Mozer AJ (2012) *Energy Environ Sci* 5:9472
30. Ye H, Park HS, Bard AJ (2011) *J Phys Chem C* 115:12464
31. Youngblood WJ, Lee S-HA, Kobayashi Y, Hernandez-Pagan EA, Hoertz PG, Moore TA, Moore AL, Gust D, Mallouk TE (2009) *J Am Chem Soc* 131:926
32. Morris CJ, Black AC, Pealing SL, Manson FD, Chapman SK, Reid GA, Gibson DM, Ward FB (1994) *Biochem J* 302:587

Chapter 6

A Multi-haem Flavoenzyme as a Solar Conversion Catalyst

6.1 Introduction

Artificial photosynthesis seeks to convert sunlight to storable chemical energy, i.e. fuels. Such ‘solar-fuels’ have the potential to address both the world’s growing energy demand and reduce greenhouse gas emissions caused by the combustion of fossil fuels [1]. Building on the principles of natural photosynthesis, light harvesting and charge separation are coupled by electron transfers to fuel formation and O₂ evolution at efficient and specific catalysts. For ultimate commercial viability and scale-up, an artificial photosynthetic system must not only be intrinsically simpler in design than the complex photosynthetic enzymes, but should also be efficient, stable, and comprise earth-abundant, inexpensive materials. Despite major research efforts and significant progress being made [2–7] (compare Sect. 1.3), the search for ‘champions’ is slow and major scientific breakthroughs are needed to fulfil all the above-mentioned criteria. Currently, artificial photosynthesis research is focused on H₂ production or reduction of CO₂, but the low-value products have little immediate opportunity to compete with fossil fuels. One way to bridge the gap is to identify reactions that could be driven by an artificial photosynthetic system, especially the synthesis of high-value organic chemicals [8–12]. Such a diversion from conventional paths is intellectually desirable and could attract more immediate commercial interest.

This chapter concerns initial experiments to expand the repertoire of fuel-forming reactions to include reductions of organic molecules. To this end, an enzyme-based photocatalytic system is presented that helps to level the aforementioned hurdles at the bench scale. Catalytic reduction of fumarate to succinate [Eq. (6.1)] is equivalent to hydrogenation across a C=C bond, with each olefinic carbon changing oxidation number from –1 to –2. Used in an artificial

Part of the work presented in this chapter has been published: Andreas Bachmeier, Bonnie J. Murphy, and Fraser A. Armstrong, *J. Am. Chem. Soc.* **2014**, 136, 12876.

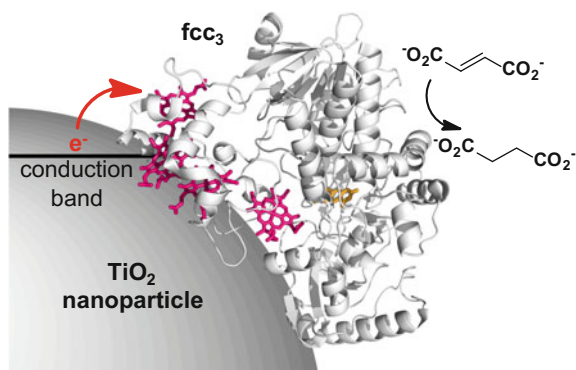
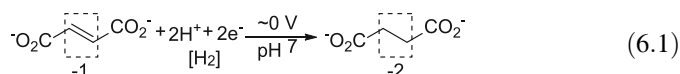


Fig. 6.1 Cartoon showing flavocytochrome c_3 (PDB structure 1QJD [14]) adsorbed onto a TiO_2 surface. Intramolecular electron transfer to and from the flavin active site (orange) occurs over a distance of up to ca. 40 Å via four visible-light absorbing haem groups (pink) that are close to the enzyme surface. Reprinted with permission from Ref. [15]. Copyright 2014 American Chemical Society

photosynthetic system, it exemplifies direct conversion of hydrogen into storable organic molecules, not unlike photosynthetic hydrogen fixation as NADPH [13].



This reaction is catalysed by flavocytochrome c_3 (fcc_3) from *Shewanella frigidimarina* NCIMB400 (Fig. 6.1). Although succinate itself is not a high-value chemical, a demonstration of its ‘photo-synthesis’ may stimulate new directions and possibilities for enzymes in the light-driven transformation of organic chemicals. Enzymes are highly selective catalysts, which are already used in the chemical industry; vast libraries are available, and the development of suitable examples for artificial photosynthesis may further increase their commercial usage.

Figure 6.1 shows a pictorial depiction of fcc_3 adsorbed on a TiO_2 surface. The enzyme has four haem groups that collect and relay electrons to the flavin (FAD) active site. A further important feature of fcc_3 is that both FAD and the haem centres strongly absorb visible light [16]: the kinetics of the entire electron transfer process, from the excited light-absorber to catalytic conversion at active site, are thus amenable to time-resolved optical techniques.

6.2 Results and Discussion

6.2.1 Protein Film Electrochemistry

To establish if fcc_3 can be incorporated into an artificial photosynthetic system, the initial task at hand was to study its electroactivity when immobilised on electrodes

and light-harvesting components. The interaction of fcc_3 with different electrodes was explored using protein film electrochemistry. Figure 6.2 compares the electrocatalytic reduction of fumarate by fcc_3 adsorbed on the n -type semiconductor electrodes TiO_2 and CdS with results obtained using PGE and mesoporous indium tin oxide (*meso*-ITO, 10% Sn(IV)-doped In_2O_3 [17, 18]). Cyclic voltammograms recorded on a rotating-disc PGE electrode and a stationary ITO electrode are shown in Fig. 6.2a,b, where the peak-like Faradaic current observed for the latter is due to substrate depletion, as expected under these conditions. The two catalytic reduction waves display a similar onset potential (ca. -0.05 V vs. SHE at pH 7.0) reflecting the fact that this parameter is controlled by the redox properties of the enzyme, provided the electrode behaves like a metal [19–21]. The results for PGE agree well with previous reports [22].

The electrocatalytic behaviour of fcc_3 on TiO_2 and CdS electrodes is shown in Fig. 6.2c,d. In contrast to PGE and ITO, the onset of the catalytic current

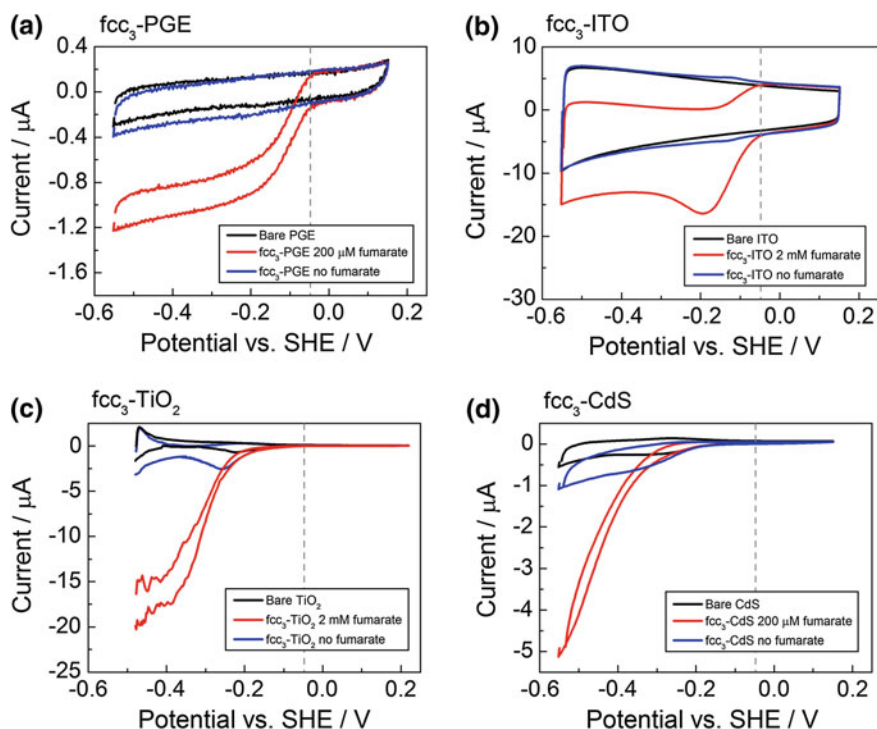
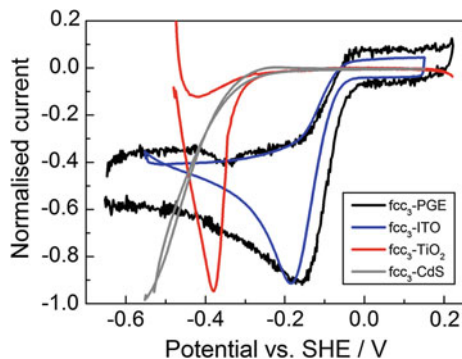


Fig. 6.2 a–d Cyclic voltammograms (20 mV s^{-1}) of unmodified (*black*, recorded in the presence of fumarate) and fcc_3 -modified electrodes (*red*, *blue*) in a mixed buffer system (pH 7.0) at 5°C in the presence of fumarate (*red*), and after removal of substrate (*blue*), recorded (a) under rotation ($\omega = 2500$ rpm) and b–d with a stationary electrode with no gas flow (a), (b) and sparging of the solution with argon close to the working electrode surface (c), (d). The dashed grey lines indicate the onset potential for fumarate reduction on PGE and ITO

Fig. 6.3 A comparison of the onset potentials of fumarate reduction on different electrode materials. These current-voltage curves correspond to normalised, background-subtracted traces of the voltammograms shown in Fig. 6.2



commences at much higher overpotentials on both semiconductor materials. The negative shift in onset potential reflects the limited surface electron availability at the semiconductor/catalyst interface when the applied potential is well away from the semiconductor flat-band potential E_{fb} . The majority carrier (i.e. electron in n -type semiconductors) availability increases exponentially according to Eq. (2.35) as E_{fb} is approached [23]. Figure 6.3 makes this feature even more prominent by directly comparing the normalised background-subtracted cyclic voltammograms obtained on all four electrodes at pH 7.0.

The catalytic onset potentials for fumarate reduction on TiO₂ and CdS are similar, which can be ascribed, at least in part, to their relatively similar E_{fb} [21] (see Sect. 4.2.3.1). These observations reaffirm that the carrier availability and E_{fb} have a profound impact on electrocatalytic activity, effects that are discussed in Chaps. 4 and 5 for [NiFeSe]-hydrogenase and CODH adsorbed on TiO₂, CdS, and NiO [21, 24].

6.2.2 Photocatalytic Fumarate Formation

Having established the electroactivity of fcc₃ on the semiconducting electrode materials CdS and TiO₂, a photocatalytic system to check for visible-light-driven fumarate reduction based on dye-sensitised TiO₂ nanoparticles was assembled. The enzyme shows good stability when adsorbed on TiO₂ electrodes: cyclic voltammograms recorded 24 h after enzyme immobilisation are shown in Fig. 6.4.

The TiO₂ nanoparticles (anatase, 15 nm) were modified with fcc₃ and then sensitised with the visible-light-absorbing chromophore RuP ([Ru^{II}(bpy)₂(4,4'-(PO₃H₂)₂bpy)]Br₂; bpy = 2,2'-bipyridine) as used in previous studies [25, 26] to assemble the complete photocatalytic system. Uptake of both RuP and enzyme on the TiO₂ nanoparticles was quantified by analysing the supernatant of the particle suspension by UV/vis spectroscopy after centrifugation. Quantitative adsorption was obtained for 56 nmol RuP and 1.95 nmol fcc₃ on 5 mg TiO₂, corresponding to a surface coverage of up to 86% fcc₃ (depending on enzyme orientation, see

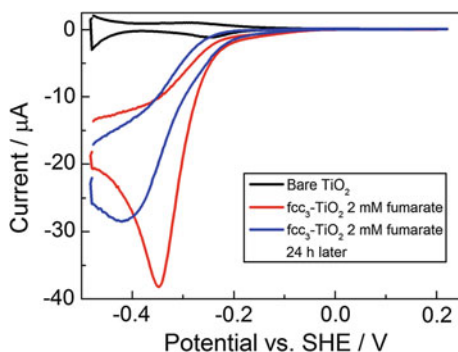


Fig. 6.4 Stability of fcc_3 adsorbed on a stationary TiO_2 electrode. The *blue* voltammogram was recorded approximately 24 h after the current-voltage *curve* displayed in *red*. Conditions: 20 mV s^{-1} , mixed buffer (pH 7.0), 5°C , Ar flow. In the time between the two experiments, the electrode was stored in buffer solution at 5°C

Sect. 8.5.5.1) and 25% RuP. Figure 6.5a shows a photograph of TiO_2 nanoparticles modified with fcc_3 ; the pink colour of the enzyme is clearly observable. UV/vis spectra of an fcc_3 solution taken before and after adsorption on TiO_2 are presented in Fig. 6.5b. No features due to fcc_3 are observed after 20 min stirring with TiO_2 , confirming quantitative uptake. More details are provided in Sect. 8.5.5.

Photochemical fumarate reduction was carried out as follows: 1.95 nmol fcc_3 and 56 nmol RuP were co-adsorbed on 5 mg TiO_2 , which was suspended in 5 mL of deuterated 0.2 M pH 6.0 MES buffer containing 6 mM disodium fumarate. MES also acts as sacrificial electron donor. The stirred suspension was irradiated by a W-halogen lamp fitted with a 420 nm UV-filter ($P_{\text{in}} = 45 \text{ mW cm}^{-2}$). Catalytic turnover was monitored by ^1H NMR spectroscopy. Spectra recorded after visible-light illumination of TiO_2 nanoparticles modified with RuP and fcc_3 are

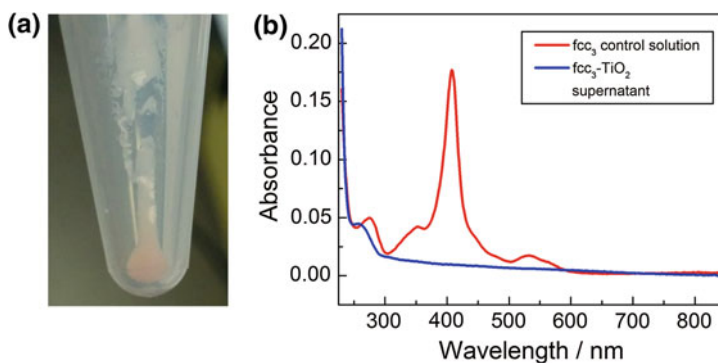


Fig. 6.5 **a** Photograph of fcc_3 -modified TiO_2 nanoparticles after centrifugation. The *pink colour* is due to immobilised fcc_3 . Reprinted with permission from Ref. [15]. Copyright 2014 American Chemical Society. **b** Absorption spectra recorded before and after modification of TiO_2 with fcc_3 show quantitative enzyme adsorption

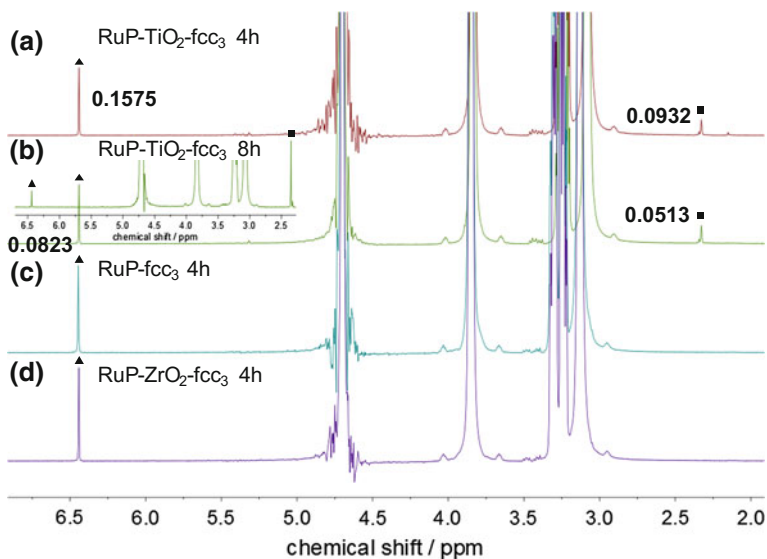


Fig. 6.6 **a,b** ^1H NMR spectra showing visible-light-driven photocatalytic conversion of fumarate to succinate. The olefinic fumarate protons are highlighted by *black triangles* and give rise to a singlet at 6.44 ppm. The aliphatic succinate protons (indicated by *black squares*) resonate at 2.33 ppm. The product conversion is calculated from the ratio of the fumarate/succinate integrals provided in **a,b**. The H_2O signal appears at 4.70 ppm, and the signals at 3.85, 3.29, 3.26, and 3.13 ppm stem from MES buffer. The *inset* in **b** shows a spectrum recorded after adding additional succinate. Photochemistry experiments in the absence of TiO_2 (**c**) or with ZrO_2 instead of TiO_2 (**d**) show no signals corresponding to succinate formation. The original NMR spectra are presented in Sect. 8.5.5

shown in Fig. 6.6 (NMR spectra were recorded after centrifuging the reaction mixture). Succinate formation was confirmed by the ^1H NMR signal at 2.33 ppm, which increased when more succinate was added (see Fig. 6.6b inset). The succinate/fumarate ratio calculated after 4 h of irradiation (Fig. 6.6a) corresponds to a TON of 5800 and an average TOF of 0.4 s^{-1} (both on a per enzyme basis). The derivation of these values is presented in Sect. 8.5.5.

Illumination over 8 h (Fig. 6.6b) gave no significant enhancement in fumarate reduction, indicating that the maximum TON had already been reached after approximately 4 h. The average TOF of 0.4 s^{-1} is therefore a lower limit for what must be achievable under these reaction conditions. Under catalytic turnover, the reaction mixture changed colour from colourless to orange, indicating dissociation of the non-covalently bound flavin active site and/or the haem moieties (see Figs. 6.7 and 6.8). This instability is discussed below.

Mechanistically, visible-light excitation of RuP (giving RuP*) injects electrons into the TiO_2 conduction band; these CB-electrons can then transfer to fcc_3 . This ‘through-particle’ pathway [27] was established by the following experiments. No succinate was formed after illumination for 4 h in the absence of TiO_2 , i.e. RuP and

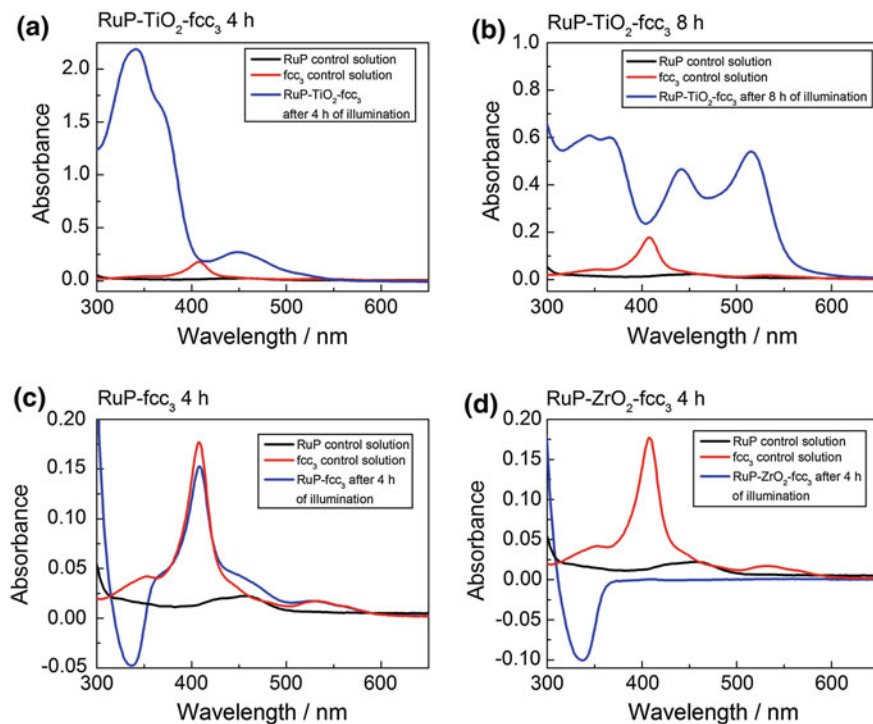


Fig. 6.7 UV/Vis spectra of the supernatants of the reaction mixtures recorded after centrifugation following photocatalytic fumarate reduction on RuP–TiO₂–fcc₃ (a), (b), and ‘control’ experiments using RuP–fcc₃ (c) and RuP–ZrO₂–fcc₃ (d)

fcc₃ co-dissolved in MES/fumarate buffer (Fig. 6.6c). A bimolecular reaction pathway between RuP* and fcc₃ in solution is thus ruled out. Illumination of RuP and fcc₃ co-adsorbed on ZrO₂ nanoparticles instead of TiO₂ also yielded no detectable amounts of succinate after 4 h (see Fig. 6.6d). The conduction band energy of colloidal ZrO₂ in water is about 0.4 V negative of the value for colloidal TiO₂ [28] and therefore too negative to accept electrons from RuP* [27]. Instead, this experimental configuration would only allow direct electron transfer from surface-bound RuP* to co-adsorbed fcc₃, which evidently does not occur. The reaction mixtures remained colourless in both types of ‘control’ experiments and the sensitised ZrO₂ particles retained their pink colour after illumination, indicating that fcc₃ remained undamaged (see Figs. 6.7, 6.8 and 6.9).

Taken together, these observations suggest strongly that enzyme degradation occurs only under photochemical turnover. A possible degradation route involves the powerfully oxidising species RuP⁺ ($E = 1.26$ V vs. NHE [29]), formation of which requires TiO₂ as support. RuP⁺ is not formed when RuP is adsorbed on ZrO₂.

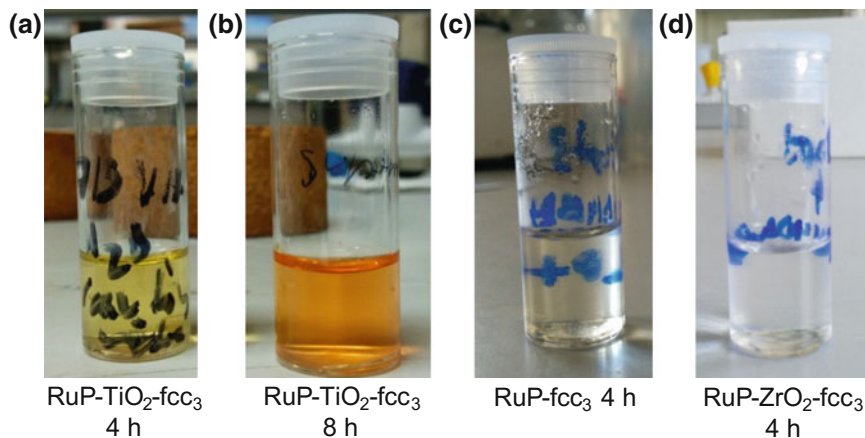
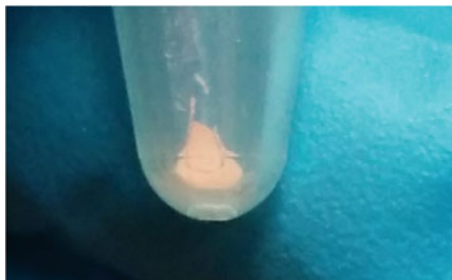


Fig. 6.8 Photographs of the supernatants of the reaction mixtures recorded after photocatalytic fumarate reduction by RuP-TiO₂-fcc₃ (a), (b), and ‘control’ experiments using RuP-fcc₃ (c) and RuP-ZrO₂-fcc₃ (d)

Fig. 6.9 Photograph of fcc₃ adsorbed on ZrO₂ nanopowder, recorded after centrifugation. Reprinted with permission from Ref. [15]. Copyright 2014 American Chemical Society



6.2.3 Closing the Photosynthetic Cycle

A full photosynthetic cycle using water as the electron donor was achieved using a photoelectrochemical cell in which a visible-light-responsive *n*-type W-BiVO₄ photoanode [30] was used as counter electrode in a two-electrode configuration (Fig. 6.10). The BiVO₄ conduction band potential (−0.39 V vs. SHE at pH 7.0 [31]) provides sufficient driving force to reduce fumarate at neutral pH without an externally applied bias.

To enhance the water oxidation rate, the electrode was coated with a cobalt phosphate (Co-Pi) surface electrocatalyst [32] via bias-assisted photodeposition [33] (see Fig. 6.11, and Sect. 1.3.2 for an introduction of the Co-Pi catalyst). In a separate cell compartment (separated by a porous frit), a *meso*-ITO electrode modified with fcc₃ was used as the working electrode as the reductive chemistry

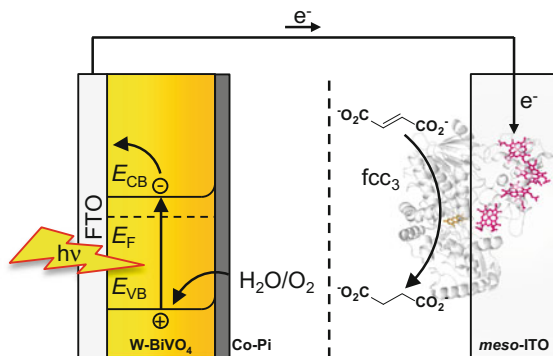


Fig. 6.10 Schematic of a photoelectrochemical cell comprising an fcc_3 -modified *meso*-ITO cathode (working electrode) and a Co-Pi-modified W-BiVO₄ photoanode (counter electrode) in a two-electrode configuration, separated by a porous frit. Reprinted with permission from Ref. [15]. Copyright 2014 American Chemical Society

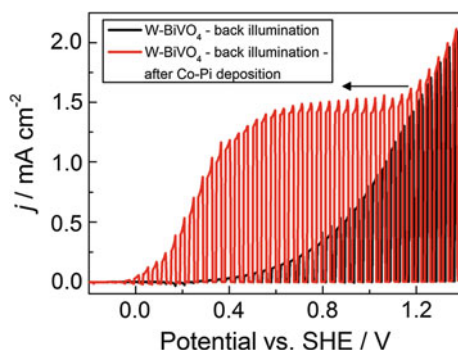


Fig. 6.11 Linear sweep voltammograms of a W-BiVO₄ electrode before (*black*) and after bias-assisted Co-Pi photodeposition (*red*). Scan rate: 10 mV s⁻¹, chopped irradiation (back illumination, 0.5 Hz), 25 °C, 0.1 M KPi buffer (pH 7.0). The *black arrow* indicates the scan direction

constitutes the reaction of interest here (analogous experiments with inverse connections, i.e. Co-Pi-modified W-BiVO₄ as the working electrode and fcc_3 -ITO as counter are depicted in Appendix G). The photoanode was irradiated through the FTO support (back illumination), meaning the charge carriers are generated close to the transparent conducting oxide back contact, since previous studies have shown that ‘regular’ front illumination (through the electrolyte, where electron-hole separation occurs close the semiconductor/electrolyte interface) gives lower photocurrents, implying that electron transport is the performance-limiting factor in bismuth vanadate photoelectrodes [34–36]. Various strategies of tungsten

(gradient-) doping have shown to alleviate the problem of poor electron conductivity in this material [6, 34, 37].

Figure 6.11 depicts current-voltage curves recorded under chopped illumination for the bare W-BiVO₄ photoanode (black) and following surface-modification with the cobaltate electrocatalyst film (red). The effect of Co-Pi becomes immediately apparent: in agreement with the extensive literature available on this catalyst (compare Sect. 1.3.2), there is a significant cathodic shift in onset for the water oxidation photocurrent, i.e. the overpotential requirement for this process is lowered considerably. It is worth noting that this effect has very recently been attributed to Co-Pi not playing a catalytic role when immobilised on BiVO₄, but, rather, providing a means to retard destructive electron-hole recombination within the semiconductor [38], not unlike the effects proposed for Co-Pi-modified haematite [39] but in contrast to the dark electrocatalysis observed on conducting substrates. While further studies are needed to clarify the precise role of Co-Pi when immobilised on semiconductor surfaces, the important aspect for this work is that, independent of the particular physico-chemical mechanism involved, the desired effect of overpotential-relief is achieved.

Figure 6.12 shows the photocurrent profile for the integrated system illustrated in Fig. 6.10, at neutral pH under zero external bias. In the absence of fumarate, only a small, rapidly decaying photocurrent is observed ($\Delta t = 0.7\text{--}2.5$ min; note that the assembly does not provide enough driving force for H⁺ reduction), not unlike the bare ITO electrode (Fig. 6.13; the enzyme-modified ITO electrode in Fig. 6.12 has a capacitance different to the bare ITO surface, compare Chap. 4). Injection of fumarate into the working electrode compartment at $t = 2.5$ min in Fig. 6.12 (final concentration 2 mM) causes an immediate steep increase in photocurrent as the charge-transport pathway becomes available and fumarate reduction takes place.

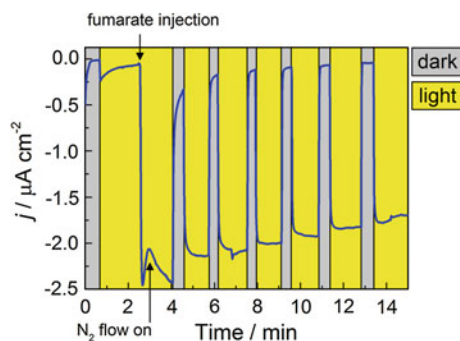


Fig. 6.12 Photocurrent profile for visible-light-driven fumarate reduction in the photoelectrochemical cell illustrated in Fig. 6.10. The cell solution was 0.1 M potassium phosphate (pH 7.0) at 25 °C. The working electrode compartment was sparged with N₂, but the gas flow was briefly stopped during injection of fumarate (to a final concentration of 2 mM) at $t = 2.5$ min

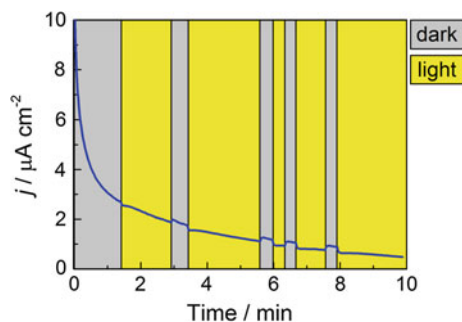


Fig. 6.13 Chronoamperometry experiment showing the temporal behaviour of a *meso*-ITO electrode (WE) connected to a Co-Pi-modified W-BiVO₄ photoelectrode (CE) in a two-compartment photoelectrochemical cell at zero external bias. Conditions: no gas flow, 25 °C, 0.1 M KPi buffer (pH 7.0)

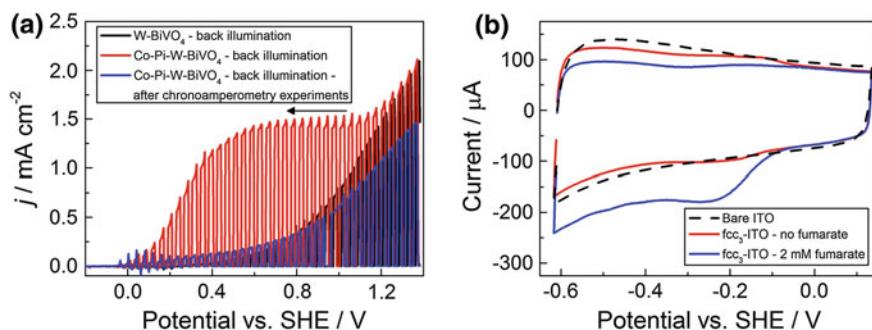


Fig. 6.14 **a** Linear sweep voltammogram of a Co-Pi-W-BiVO₄ electrode recorded after the chronoamperometry experiments depicted in Figs. 6.12 and 6.13 (*blue trace*). The voltammogram indicates detachment of the Co-Pi catalyst from the electrode surface (compared with the *red trace*) and resembles the current-voltage curve of the bare W-BiVO₄ electrode (*black curve*). Experimental conditions: 10 mV s⁻¹, chopped illumination (0.5 Hz, back illumination), 25 °C, 0.1 M KPi buffer (pH 7.0). The *black arrow* indicates the scan direction. **b** Cyclic voltammogram of fcc₃-ITO recorded after the chronoamperometry experiment depicted in Fig. 6.12; 30 mV s⁻¹, 25 °C, 0.1 M KPi buffer (pH 7.0), N₂ flow. The trace corresponding to the bare ITO electrode was measured before the chronoamperometry experiment was carried out. The *blue trace*, recorded after introducing fumarate to the solution (to a final concentration of 2 mM), shows that the enzyme retained catalytic activity for fumarate reduction

Importantly, as shown in Fig. 6.14, voltammograms of each electrode were recorded (separately) after the experiment depicted in Fig. 6.12 to verify the activities of the individual components.

The overall ‘solar-to-succinate’ efficiency (η_{STS}) can be determined according to Eq. (6.2), which is based on Eq. (2.2) [40] that describes the efficiency of H₂O photoelectrolysis:

$$\eta_{\text{STS}} = j_{\text{ph}} \eta_{\text{F}} 0.79 \text{ V } P_{\text{in}}^{-1} \quad (6.2)$$

To remind the reader, in Eq. (6.2) j_{ph} is the photocurrent density, η_{F} is the Faradaic efficiency for fumarate reduction, 0.79 V is the potential that is theoretically required to achieve both fumarate reduction and water oxidation (at pH 7.0, the fumarate/succinate potential is +0.03 V vs. SHE [22] and the H₂O/O₂ potential is +0.82 V), and $P_{\text{in}} = 45 \text{ mW cm}^{-2}$ refers to the incident light intensity. With $\eta_{\text{F}} = 100\%$ for fcc₃-catalysed fumarate reduction as the upper limit (no significant photocurrent could be observed before introducing fumarate), $\eta_{\text{STS}} = 0.03\%$ at $t = 15 \text{ min}$. The estimated TOF per enzyme molecule is 0.01 s^{-1} (see Sect. 8.5.6.3 for the derivation of this value), one order of magnitude lower than the value obtained in photocatalytic conversion with RuP–TiO₂, where a sacrificial electron donor was used to drive the reaction.

Efficiency limitations in these proof-of-principle experiments include irradiation with only the visible spectral region and delamination of the Co–Pi catalyst from the W–BiVO₄ surface (Fig. 6.14a), similar to observations made by Sivula and co-workers [41]: under no external bias, the Co–Pi layer detaches within minutes from the photoanode surface, fundamentally limiting the performance of the system. Most likely, it is the ‘bare’ W–BiVO₄ surface that drives water oxidation during much of the chronoamperometry experiments for overall solar-to-succinate conversion using water as the oxidant depicted in Fig. 6.12.

Comparing the photoelectrochemical cell presented in this section to a similar BiVO₄-based system for H₂ evolution developed by Kudo et al. ($\eta_{\text{STH}} = 0.014\%$) [42] shows that photoconversion efficiencies are similarly low (these authors apply an external bias of 0.8 V, meaning that both their system and the photoelectrochemical cell described herein provide a comparable driving force for the respective overall reaction). This observation and the order of magnitude decrease in turnover frequency observed when going from photocatalytic fumarate reduction driven by a sacrificial electron donor to photoelectrochemical conditions under no applied bias again highlight that the transient nature of charge carriers and resulting destructive, thermodynamically preferred recombination processes remain a grand challenge to artificial photosynthesis research. Yet, despite the low overall efficiency in photoelectrochemical succinate formation, the proof of principle is established, and there is large scope for improvement.

6.3 Conclusions and Perspectives

In conclusion, this chapter describes the use of an enzyme that catalyses C=C bond hydrogenation in two types of artificial photosynthetic systems, the implication being that artificial photosynthesis building upon water oxidation can be extended to other enzymes/catalysts performing reductive transformations having greater value than bulk fuel-formation.

Photocatalytic experiments with fcc_3 adsorbed on RuP-sensitised anatase nanoparticles show efficient solar-to-succinate conversion with an average per-enzyme turnover frequency of 0.4 s^{-1} over 4 h, using MES as a sacrificial electron donor. Further, an integrated artificial photosynthetic system is presented, where fumarate reduction is coupled to water oxidation by a Co–Pi-modified W– BiVO_4 photoanode in a photoelectrochemical cell. An estimated TOF for fumarate reduction of 0.01 s^{-1} per molecule of fcc_3 was achieved in this architecture. The one order of magnitude drop in TOF is not unexpected when moving to an integrated system without using an externally applied bias. The performance of the photoanode seems, to a great extent, responsible for the low overall efficiency η_{STS} of 0.03%. Recently developed nanoporous BiVO_4 photoanodes modified with dual-layer (FeOOH/NiOOH) oxygen evolving catalysts that show high stability under low external bias [43] are one possible route to increase both stability and efficiency.

From a mechanistic perspective, an important factor is that enzymes like fcc_3 , possessing intense chromophores, may be exploited to elucidate electron transfer kinetics by time-resolved optical spectroscopy. The results presented in this chapter help highlight new directions for artificial photosynthesis, away from the traditional solar-to-fuels paradigm to more advanced solar-to-chemical conversions, also using water as the electron source.

References

1. Lewis NS, Nocera DG (2006) *Proc Natl Acad Sci U S A* 103:15729
2. Khaselev O, Turner JA (1998) *Science* 280:425
3. Jacobsson TJ, Fjallstrom V, Sahlberg M, Edoff M, Edvinsson T (2013) *Energy Environ Sci* 6:3676
4. Luo J, Im J-H, Mayer MT, Schreier M, Nazeeruddin MK, Park N-G, Tilley SD, Fan HJ, Grätzel M (2014) *Science* 345:1593
5. Cox CR, Lee JZ, Nocera DG, Buonassisi T (2014) *Proc Natl Acad Sci U S A* 111:14057
6. Abdi FF, Han L, Smets AHM, Zeman M, Dam B, van de Krol R (2013) *Nat Commun* 4:2195
7. Reece SY, Hamel JA, Sung K, Jarvi TD, Esswein AJ, Pijpers JJH, Nocera DG (2011) *Science* 334:645
8. Cuendet P, Grätzel M (1984) *Photochem Photobiol* 39:609
9. Kim Y, Ikebukuro K, Murguruma H, Karube I (1998) *J Biotechnol* 59:213
10. Jiang Z, Lü C, Wu H (2005) *Ind Eng Chem Res* 44:4165
11. Lu J, Li H, Cui D, Zhang Y, Liu S (2014) *Anal Chem* 86:8003
12. Song W, Vannucci AK, Farnum BH, Lapidus AM, Brennaman MK, Kalanyan B, Alibabaei L, Concepcion JJ, Losego MD, Parsons GN, Meyer TJ (2014) *J Am Chem Soc* 136:9773
13. Archer MD, Barber J (2004) In: Archer MD, Barber J (eds) *Molecular to Global Photosynthesis*. Imperial College Press, London, p 1
14. Taylor P, Pealing SL, Reid GA, Chapman SK, Walkinshaw MD (1999) *Nat Struct Mol Biol* 6:1108
15. Bachmeier A, Murphy BJ, Armstrong FA (2014) A Multi-Heme Flavoenzyme as a Solar Conversion Catalyst. *J Am Chem Soc* 136:12876

16. Morris CJ, Black AC, Pealing SL, Manson FD, Chapman SK, Reid GA, Gibson DM, Ward FB (1994) *Biochem J* 302:587
17. Kato M, Cardona T, Rutherford AW, Reisner E (2012) *J Am Chem Soc* 134:8332
18. Hoertz PG, Chen Z, Kent CA, Meyer T (2010) *J Inorg Chem* 49:8179
19. Hexter SV, Grey F, Happe T, Climent V, Armstrong FA (2012) *Proc Natl Acad Sci U S A* 109:11516
20. Murphy BJ, Sargent F, Armstrong FA (2014) *Energy Environ Sci* 7:1426
21. Bachmeier A, Wang VC-C, Woolerton TW, Bell S, Fontecilla-Camps JC, Can M, Ragsdale SW, Chaudhary YS, Armstrong FA (2013) *J Am Chem Soc* 135:15026
22. Turner KL, Doherty MK, Heering HA, Armstrong FA, Reid GA, Chapman SK (1999) *Biochemistry* 38:3302
23. Walter MG, Warren EL, McKone JR, Boettcher SW, Mi Q, Santori EA, Lewis NS (2010) *Chem Rev* 110:6446
24. Bachmeier A, Hall S, Ragsdale SW, Armstrong FA (2014) *J Am Chem Soc* 136:13518
25. Reisner E, Fontecilla-Camps JC, Armstrong FA (2009) *Chem Commun* 550
26. Woolerton TW, Sheard S, Reisner E, Pierce E, Ragsdale SW, Armstrong FA (2010) *J Am Chem Soc* 132:2132
27. Gross MA, Reynal A, Durrant JR, Reisner E (2014) *J Am Chem Soc* 136:356
28. Lemon BI, Liu F, Hupp JT (2004) *Coord Chem Rev* 248:1225
29. Park H, Bae E, Lee J-J, Park J, Choi W (2006) *J Phys Chem B* 110:8740
30. Ye H, Park HS, Bard AJ (2011) *J Phys Chem C* 115:12464
31. Hong SJ, Lee S, Jang JS, Lee JS (2011) *Energy Environ Sci* 4:1781
32. Kanan MW, Nocera DG (2008) *Science* 321:1072
33. Zhong DK, Cornuz M, Sivula K, Grätzel M, Gamelin DR (2011) *Energy Environ Sci* 4:1759
34. Abdi FF, Firet N van de Krol R (2013) *ChemCatChem* 5:490
35. Liang Y, Tsubota T, Mooij LPA, van de Krol R (2011) *J Phys Chem C* 115:17594
36. Abdi FF, van de Krol R (2012) *J Phys Chem C* 116:9398
37. Han L, Abdi FF, van de Krol R, Liu R, Huang Z, Lewerenz H-J, Dam B, Zeman M, Smets AHM (2014) *ChemSusChem* 7:2832
38. Pendlebury SR (2015) In: ISF-1 Young, Uppsala
39. Barroso M, Mesa CA, Pendlebury SR, Cowan AJ, Hisatomi T, Sivula K, Grätzel M, Klug DR, Durrant JR (2012) *Proc Natl Acad Sci U S A* 109:15640
40. Chen Z, Dinh HN, Miller E (2013) *Photoelectrochemical Water Splitting: Standards, Experimental Methods, and Protocols*. Springer
41. Bornozy P, Abdi FF, Tilley SD, Dam B, van de Krol R, Grätzel M, Sivula K (2014) *J Phys Chem C* 118:16959
42. Iwase A, Kudo A (2010) *J Mater Chem* 20:7536
43. Kim TW, Choi K-S (2014) *Science* 343:990

Chapter 7

Conclusions and Perspectives

7.1 Conclusions

The work presented in this thesis spans a wide range, from the mechanism of H₂ formation at the H-cluster, the superbly efficient H₂ evolution catalyst, to the interaction between fuel-forming enzymes with semiconductor surfaces, and, finally, towards an integrated model system for solar-to-chemical conversion. To briefly recapitulate:

Chapter 3 describes how aldehydes of different steric nature and electrophilicity react with [FeFe]-hydrogenases. Using advanced EPR techniques, possible binding modes of formaldehyde at the H-cluster were determined. DFT calculations suggest that under catalytic turnover, HCHO coordinates to Fe_d by forming an Fe–C bond that can only occur before Fe–H bond formation, suggesting adt-N protonation and terminal hydride formation only occur at the super-reduced redox level of the enzyme. In short, Chap. 3 highlights the importance of precisely tuning electron and proton transfer steps in multi-electron catalysis.

Chapter 4 deals with the direct electrochemistry of [NiFeSe]-hydrogenase and CODH on the *n*-type semiconductor materials TiO₂ and CdS. Compared to the behaviour on metallic-like PGE electrodes, catalytic rectification arises on the semiconductor electrodes, favouring the fuel-forming reaction over oxidation. The results demonstrate that semiconducting electrodes can be used to impose directionality on reversible catalysts that operate in the region of the semiconductor flat-band potential. Photoelectrochemistry experiments show that the enzymes are so proficient that the current is controlled more by the charge carrier availability in the semiconductor than by properties of the catalyst.

Chapter 5 reaffirms the principles established in Chap. 4 by demonstrating that catalysis is also rectified when CODH is attached to a *p*-type semiconductor: catalytic rectification turns the enzyme into a unidirectional CO oxidiser when immobilised on NiO. When CODH-modified NiO is sensitised with the visible-light-absorbing dye P1, a photocathode-assembly is produced that

selectively reduces CO_2 to CO under visible-light illumination and application of a mildly reducing potential that is lower than the thermodynamic potential in the dark, a further evolutionary step compared to photocatalytic reduction in aqueous suspension.

Chapter 6 describes enzyme (fcc_3) catalysed $\text{C}=\text{C}$ bond hydrogenation in two types of artificial photosynthetic systems, photocatalytic reduction using fcc_3 immobilised on dye-sensitised TiO_2 nanoparticles, and photoelectrocatalytic hydrogenation coupled to water oxidation in a photoelectrochemical cell. The results represent a significant advance in the development of artificial photosynthesis [1] and open up the door to a new research area: the solar-driven, enzyme catalysed synthesis of organic chemicals of greater value than bulk fuel formation, ideally coupled to water oxidation.

7.2 Perspectives

Throughout this thesis, we learned that fuel-forming enzymes such as [FeFe]-hydrogenase, [NiFeSe]-hydrogenase, and CODH are excellent model catalysts for artificial photosynthesis. Enzymes set the benchmark for both light-driven H_2 formation and CO_2 reduction: on a per-site basis, the activities for photocatalytic fuel-formation portrayed in Table 1.1 in the introduction of this thesis are unmatched by even the most efficient synthetic catalysts [2]. Despite the considerable ‘footprint’ of the individual protein molecules, enzyme systems also appear remarkably lean, compared with the substantial molar quantities of catalysts used in the purely inorganic world, such as the Rh compounds that are deposited on (oxy) nitride photocatalyst particles developed by Domen and co-workers [3].

Yet, an equally relevant point is that the photo- and photoelectrocatalytic enzyme rates fall far short of those measured in other types of kinetic studies, where TOFs for enzyme-catalysed H_2 and CO evolution exceed 10^3 per second. This observation holds in particular for CO_2 reduction, where the highest photocatalytic TOF obtained so far (on a per catalytic unit basis) stems from using CODH adsorbed on CdS nanorods [4]: the value of only 1.23 s^{-1} (three orders of magnitude slower than the theoretical maximum) emphasises the need for improvement in photodriven CO_2 reduction and to understand why there is such a difference compared to electrocatalytic rates.

Reduction of CO_2 to CO is thermodynamically more demanding than H^+ reduction. Further to the obvious problem of only a small driving force being available at semiconductor nanoparticles including TiO_2 (which provides a marginal overpotential with E_{cb} (anatase) at ca. -0.52 V vs. SHE at pH 6.0) and CdS (where the driving force is shallow, E_{cb} being approximately -0.35 V more negative than that of TiO_2 [5]), this work has provided some insight. Chapter 4 showed that the best catalysts will ultimately be limited by electron availability (Fig. 4.12). This problem is much more severe when electrons are available only transiently, as in the integrated artificial system depicted in Fig. 6.12, because there is

unfavourable competition with destructive charge carrier recombination. Mott-Schottky experiments in Sect. 4.2.3 indicate that, although enzyme molecules could be accommodated within the sizeable pores of TiO_2 (and other porous materials; CdS and NiO possess similar pore sizes), they mainly adsorb instead on the outer surface, suggesting that due to the limited carrier mobility and lifetime of the transient conduction band electrons in TiO_2 and, by extension, other systems studied throughout this thesis, destructive charge recombination is likely to take place even *before* interfacial electron injection into the enzyme can occur.

Little is known about the actual charge-transfer *dynamics* between excited semiconductor conduction band electrons and fuel-forming enzymes. An assembly comprising the [FeFe]-hydrogenase *CaHydA* immobilised on CdS nanorods (Fig. 7.1) constitutes one of the few examples where the elementary kinetic processes of light-driven hydrogen evolution have been investigated. Initial findings revealed that H_2 generation rates scale linearly with light intensity, consistent with the system being limited by availability of photogenerated electrons rather than catalysis [6].

In a follow-up paper, King and Dukovic then investigated the interfacial electron transfer kinetics of the *CaHydA*–CdS system using transient absorption spectroscopy [7]. The decay of the absorbance of the excited semiconductor conduction band electron should coincide exactly with the arrival of the electron in the enzyme. However, because *CaHydA* does not have absorptive features with intensities comparable to the strength of the CdS band gap absorption [8], no transient features corresponding to excited electrons in the enzyme are found in transient absorption

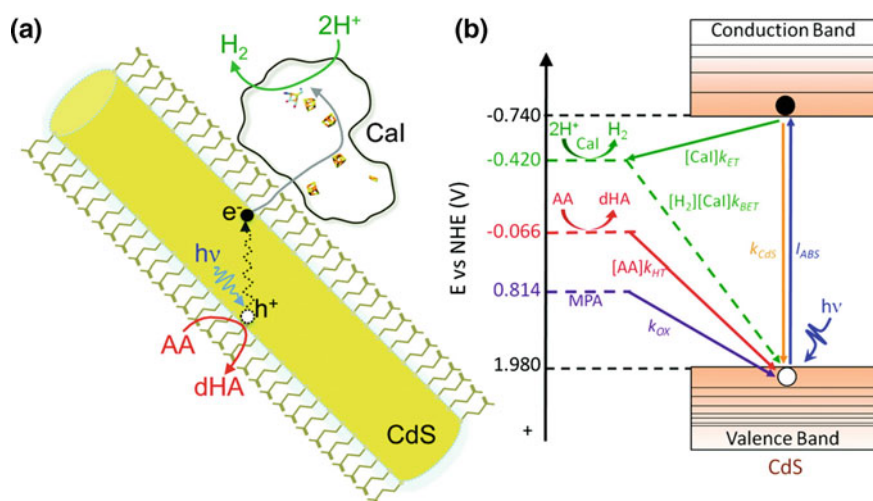


Fig. 7.1 **a** Cartoon showing a *CaHydA*–CdS nanorod assembly for photocatalytic H_2 formation (*CaHydA* is referred to as *CaI* in this figure). **b** Energy diagram of *CaHydA*–CdS and photochemical processes. Reprinted with permission from Ref. [6]. Copyright 2012 American Chemical Society

spectra recorded on *CaHydA*–CdS [7]. The broad absorption bands of the FeS clusters in the electron transfer relay do not give rise to sharp, distinct changes upon excitation.

Electron injection from CdS to *CaHydA* (involving the distal [4Fe-4S] cluster as the first acceptor site, well ahead of catalysis itself), occurs with $k_{\text{et}} \approx 10^7 \text{ s}^{-1}$, similar to the excited state decay rate constant for CdS, but very slow when compared with electron transfer to platinum deposited on CdS ($k_{\text{et}} > 10^{11} \text{ s}^{-1}$). The fraction of photoexcited electrons available for catalysis is therefore much higher in Pt–CdS than in *CaHydA*–CdS. However, the quantum yields for H₂ formation are much higher in the enzymatic system (20%) than with Pt (1–4%), an observation that highlights the proficiency of the enzyme. Given that a limiting factor seems to be slow interfacial electron transfer *to* enzymes, the question is thus raised—how good is an enzyme at trapping electrons once they are transferred?

The properties of the electron transfer relay provide insight. First, electron transfer rates within the enzyme are fast, on the order of 10^8 – 10^9 s^{-1} through the chain of FeS clusters—a distance of nearly 30 Å. Hence, once transferred to the enzyme, electrons move efficiently, under a small driving force, away from the CdS surface and accumulate to feed the catalytic process at the active site. The large spatial separation distance retards back electron transfer. Second, buried FeS clusters have low reorganisation energies, and counterproductive electron transfer into the semiconductor valence band (driving force $\sim 1.5 \text{ eV}$) probably falls well into the Marcus inverted region, making it kinetically disfavoured. The situation is similar to the initial charge separation events occurring in PSII in biological photosynthesis [9]. In Pt–CdS assemblies, in contrast, the bare catalytic sites cannot provide such a trap: the catalyst is located at the nanocrystal surface and reorganisation energies are higher. Therefore, recombination with a valence band hole is potentially more likely. Similar restrictions may hold generally for small molecular catalysts [10].

In short, electron injection into the enzyme seems to be the rate-limiting step. However, it is essentially irreversible because FeS enzymes such as hydrogenase and CODH enzymes are very efficient in charge separation and transport, shuttling electrons away from the interface into the enzyme and placing destructive recombination in the Marcus inverted regime. The work by Dukovic et al. highlights how enzymes employed in artificial photosynthetic systems outperform even the best available synthetic catalysts.

Other spectroscopic techniques have yet to be developed for use with enzymes. Time-resolved infrared measurements could potentially be employed to monitor catalysis under steady-state conditions. The CO and CN[−] ligands of the H-cluster, for instance, show very characteristic IR bands. A general advantage of IR spectroscopy over optical techniques is its structure-specificity, i.e. signals corresponding to transient species can be correlated with distinct chemical groups. Another potentially useful technique is time resolved X-ray absorption

spectroscopy (XAS). Transient XAS may be able to give precise information about bond-length and oxidation state changes during the catalytic cycle, while leading to less radiation damage than crystallography.

7.3 New Directions in Artificial Photosynthesis—Where Do We Go from Here and How Enzymes May Lead the Way

Current artificial photosynthesis research is focused on H₂ production or reduction of CO₂, but the low-value products have little immediate opportunity to compete with fossil fuels. One way to break this deadlock is to identify other reactions that could be driven by artificial photosynthesis, especially the synthesis of high-value organic chemicals [11]. Here lie possibilities for enzymes that can perform highly selective redox transformations.

Solar-driven asymmetric reduction of acetophenones, using a commercially available alcohol dehydrogenase [12], establishes this new direction, but relies on multistep NADPH regeneration. Asymmetric, enzymatic C=C bond reduction (ketoisophorone to (*R*)-levodione) by an ‘old yellow enzyme’ homologue has been coupled with photocatalytic water oxidation by Au:TiO₂ nanoparticles [13]. However, this system also relies on cofactor regeneration. Conversely, an intrinsically simpler system that couples light-driven water oxidation with enzymatic C=C reduction in a photoelectrochemical cell was presented in Chap. 6. Building on these few examples, enzymes may lead the way towards new directions in artificial photosynthesis research, away from simple solar-fuels to more advanced solar-chemicals. Synthetic biology provides the platform to engineer enzymes to perform myriad transformations that may ultimately be driven by sunlight.

For the conversion of sunlight to fuels, the reader needs to bear in mind that although some enzymatic artificial photosynthetic systems show remarkable stability under illumination [2], the fuel-forming enzymes used therein are wholly unsuited for long-term, large-scale systems. Nonetheless, the redox enzymes used in this thesis provide valuable insight for developing integrated artificial systems where both rates and efficiency are essential. Enzymes are relatively easy to deposit on materials (albeit not necessarily with ideal connections) and, as opposed to molecular catalysts, their active site structures remain unperturbed by the support-surface and therefore intact during catalysis. The benchmark per-active site efficiencies for both H₂ evolution and CO₂ reduction achieved by hydrogenases and CODH show that artificial photosynthesis based on highly abundant first-row transition metals has a future. Ultimately, integrated, commercially viable artificial photosynthetic devices need to be based upon robust materials and scalable, earth-abundant, and inexpensive components. Therefore, one of the major scientific challenges in artificial photosynthesis research is ‘how can we design synthetic materials to make them work like enzymes?’

References

1. Gordon EJ (2014) *J Am Chem Soc* 136:13469
2. Caputo CA, Gross MA, Lau VW, Cavazza C, Lotsch BV, Reisner E (2014) *Angew Chem Int Ed* 53:11538
3. Moriya Y, Takata T, Domen K (2013) *Coord Chem Rev* 257:1957
4. Chaudhary YS, Woolerton TW, Allen CS, Warner JH, Pierce E, Ragsdale SW, Armstrong FA (2012) *Chem Commun* 48:58
5. Woolerton TW, Sheard S, Chaudhary YS, Armstrong FA (2012) *Energy Environ Sci* 5:7470
6. Brown KA, Wilker MB, Boehm M, Dukovic G, King PW (2012) *J Am Chem Soc* 134:5627
7. Wilker MB, Shinopoulos KE, Brown KA, Mulder DW, King PW, Dukovic G (2014) *J Am Chem Soc* 136:4316
8. Adams MW, Mortenson LE (1984) *J Biol Chem* 259:7045
9. Kavarnos GJ (1993) *Fundamentals of Photoinduced Electron Transfer*. Wiley-VCH, Weinheim
10. Reynal A, Willkomm J, Muresan NM, Lakadamyali F, Planells M, Reisner E, Durrant JR (2014) *Chem Commun* 50:12768
11. Kim JH, Nam DH, Park CB (2014) *Curr Opin Biotechnol* 28:1
12. Choudhury S, Baeg J-O, Park N-J, Yadav RK (2012) *Angew Chem Int Ed* 51:11624
13. Mifsud M, Gargiulo S, Iborra S, Arends IWCE, Hollmann F, Corma A (2014) *Nat Commun* 5

Chapter 8

Experimental Section

8.1 General Considerations

Unless otherwise noted, all protein film electrochemistry experiments presented in this thesis were carried out inside an anaerobic glove box (Belle Technologies, $O_2 < 3$ ppm, or MBraun, $O_2 < 1$ ppm). Precise gas mixtures (BOC gases) were created using mass flow controllers (Sierra Instruments), and the headspace of the electrochemical cell was, unless otherwise mentioned, constantly purged with the gas mixture throughout the experiments. Pyrolytic graphite edge electrodes of geometric surface area 0.03 cm^2 were constructed in house as described previously [1]. The electrodes were abraded using P400 Tufbak Durite sandpaper and sonicated to remove carbon debris before attachment of enzyme. Unless otherwise noted, the direction of scan in CV experiments was from negative to positive potentials, linear sweep voltammetry experiments were carried out with the potential being swept in cathodic direction.

8.2 The Mechanism of [FeFe]-Hydrogenases—How Aldehydes Inhibit H_2 Evolution

8.2.1 General Considerations

All chemicals were used as purchased without further purification. Phosphate buffer was made up of NaCl, NaH_2PO_4 and Na_2HPO_4 (all analytical reagent grade, Sigma-Aldrich) and titrated to pH 6.0 with HCl or NaOH (both Sigma-Aldrich). For EPR measurements, 10% (v/v) glycerol was added to the phosphate buffer. All aldehydes used in this work were purchased from Sigma-Aldrich: formaldehyde (ACS reagent, 37 wt% in H_2O), acetaldehyde (ACS reagent, $\geq 99.5\%$), trifluoroacetaldehyde monohydrate (technical, $\sim 75\%$ in H_2O), butyraldehyde

($\geq 98\%$), isovaleraldehyde ($\geq 97\%$), and, for EPR experiments, formaldehyde- d_2 solution (~ 20 wt% in D_2O , 98 atom % D) and formaldehyde- ^{13}C solution (20 wt% in H_2O , 99 atom % ^{13}C).

8.2.2 Enzyme Preparation

Electrochemistry experiments were carried out using the [FeFe]-hydrogenase *CaHydA* from the fermentive, strictly anaerobic bacterium *Clostridium acetobutylicum* [2]. EPR experiments were conducted on *CrHydA1* from the green alga *Chlamydomonas reinhardtii* [3, 4]. Both enzymes were prepared and provided by Julian Esselborn (laboratory of Professor Thomas Happe, Ruhr-Universität Bochum, Germany): “*CaHydA* was isolated as described previously [5] and showed a hydrogen evolution activity of $130 \mu\text{mol } H_2 \text{ min}^{-1} \text{ mg}^{-1}$. *CrHydA1* was isolated as apo-protein lacking the $[2Fe]_H$ subcluster via strep-tactin affinity chromatography from heterologous expression in *E. coli* as described previously [5–7]. The protein was matured in vitro with the complex $[Fe_2(\mu\text{-SCH}_2)_2\text{NH}(\text{CN})_2(\text{CO})_4]^{2-}$ and subsequently purified using a NAPTM 5 gel filtration column (GE Healthcare) and concentrated using Amicon Ultra centrifugal 10 K filters (Millipore) as shown before [8]. The total protein concentration (2.4 mM) was estimated spectroscopically using the method of Bradford [9], with bovine serum albumin (Sigma-Aldrich) as the protein standard; protein purity was assessed by SDS-PAGE. The H_2 evolution activity of *CrHydA1* was determined to be $1.37 \text{ mmol } H_2 \text{ min}^{-1} \text{ mg}^{-1}$ in a well established assay with methyl viologen as electron mediator and detection of H_2 via GC [10].” Isolation, handling and storage of both enzymes were conducted under strictly anaerobic conditions. Protein samples were stored at -80 °C before use in protein film electrochemistry experiments or preparation for EPR.

8.2.3 Protein Film Electrochemistry

In PFE experiments, aliquots of enzyme samples ($\sim 1.5 \mu\text{L}$ of 0.1 g L^{-1} *CaHydA*) were drop cast onto the PGE electrode and left for one minute until partially dry. The electrode was then connected to an electrode rotator (EcoChemie) and fitted into a gastight electrochemical cell similar to the one shown in Fig. 2.1. The cell was covered with electrical tape to prevent light-induced deactivation of the enzyme (‘self-cannibalisation’ [11, 12]) and the temperature was controlled via a water jacket surrounding the main cell compartment. Unless otherwise noted, all experiments were carried out at 20 °C. A platinum wire, placed in the main compartment, was used as counter electrode. The saturated calomel reference electrode (SCE) was placed in a side-arm containing 100 mM NaCl electrolyte that was connected to the main cell via a Luggin capillary. All potentials are quoted vs. the standard hydrogen electrode (SHE) using the correction $E_{\text{SHE}} = E_{\text{SCE}} + 242 \text{ mV}$ at 20 °C [13]. The electrolyte

was 50 mM phosphate buffer containing 100 mM NaCl in purified water (Millipore, 18 M Ω cm). Electrochemical measurements were made with an Autolab potentiostat (PGSTAT30) controlled by Nova software (EcoChemie). To ensure non-rate-limiting substrate supply, rapid removal of product, and fast gas-solution equilibration, the electrode was rotated at a constant high rate (> 2500 rpm) in all experiments. Chronoamperometry experiments were normalised for film loss according to Eq. (2.30). In aldehyde inhibition experiments, 1 mL of the respective aldehyde inhibitor solution was injected into the electrochemical cell containing 4 mL buffer solution. The inhibition kinetics, i.e. the current decay over time following injection of the inhibitor, were determined over 300 s. Generally, inhibition studies could not be carried out in the ‘intermediate’ potential region close to the equilibrium potential for H⁺/H₂ interconversion (between -0.4 and -0.15 V) due to the relatively low current densities in this region, which are further lowered by the exponential ‘film loss’ processes that underlie every experiment. Rate constants for inhibition k_{obs} and corresponding errors were obtained by ‘least square fits’ of current vs. time traces recorded at different potentials. Fits were attained using OriginPro 9 software. Average values represent the mean value of three different experiments.

8.2.4 Electron Paramagnetic Resonance

All EPR samples were prepared in an anaerobic glove box (O₂ < 3 ppm) in 50 mM phosphate buffer containing 0.1 M NaCl and 10% (v/v) glycerol, adjusted to pH 6.0 at 20 °C. All samples were prepared in 3.0 mm high-precision EPR tubes (WilmaD 706-PQ-9.50) to ensure accurate spin quantification. EPR-samples were prepared by reducing approximately 70 μ L of as-isolated enzyme using 100% H₂ at 20 °C under zero-current flow until the potential of the solution equilibrated, typically after 3.5 h. Formaldehyde (DCDO or H¹³CHO) was then injected to give a final concentration of free, non-hydrated aldehyde (the equilibrium constant for hydration $K_{\text{eq}} \approx 2000$ at 25 °C [14, 15]) equal to the concentration of CrHydA1. Aliquots (ca. 70–90 μ L) of the resulting solution were transferred as quickly as possible to WilmaD EPR tubes and frozen in liquid nitrogen, i.e. within 5 min after injection, a timescale after which almost all enzymatic activity was noted to be recovered in PFE experiments (Fig. 3.1a). Spin quantification was carried out using copper perchlorate samples (50 μ M CuSO₄ in 2 M NaClO₄ (aq) adjusted to pH 1.22 with HCl) measured under non-saturating conditions [16].

Continuous wave EPR experiments were performed using an X-band (ca. 9.4 GHz) Bruker EMX^{micro} Premium spectrometer (Bruker BioSpin GmbH, Germany) with an X-band SHQE-W cylindrical TE₀₁₁-mode resonator (Bruker). Background spectra of the empty resonator were recorded under identical conditions and subtracted from the EPR spectrum of the enzyme sample. Pulse measurements were carried out on an X-/W-band Bruker Elexsys 680 spectrometer and a Q-band Bruker Elexsys 580 spectrometer.

Spectroscopic simulations were performed by Dr. William Myers (Centre for Advanced Electron Spin Resonance, University of Oxford) in MATLAB 2013a with the EasySpin 4.5 toolbox [17]: “Simulation of the FID-detected EPR signal employed matrix diagonalisation with the *pepper* function using a *g*-strain model for linewidth, as is characteristic for simulations of FeS cluster EPR signals. The EPR fit was then converted to an equivalent linewidth defined by hyperfine broadening, ‘H-Strain’, and this set of EPR simulation parameter values acted as a basis for Mims ENDOR simulations making use of the *saffron* function with explicit use of the experimental parameter values.”

8.2.5 Density Functional Theory

All DFT calculations presented in Chap. 4 were performed by Professor John McGrady (Inorganic Chemistry Laboratory, University of Oxford), using the Gaussian 09 suite: “The basic structure of the H-cluster was extracted from the reported crystal structure of *Desulfovibrio desulfuricans* (PDB code 1HFE [18]) following the procedure set out by Bruschi et al. [19]. The active site was extracted from the protein matrix, and the oxygen atom originally assigned in the bridging position was replaced with a CO unit. The H-cluster is attached to the protein via four cysteine units (cys179, cys234, cys378 and cys382); all four were modelled as CH₃S units, with the carbon atoms frozen at the positions found in the matrix. All other structural parameters were freely optimised. Given the uncertainty in the position of the bridging CO ligand, optimisations were initialised from a number of starting geometries where the CO is bridging, semi-bridging, or terminal. In all cases the CO reverts to the bridging position in the optimised structure. At the H_{ox-2} oxidation level the total charge on the cluster is -5, decreasing to -4 when the system is protonated, as in the [tH-dtma]⁴⁻ structure reported by Bruschi et al. [19]. The stabilising influence of the wider protein matrix was introduced through a polarised continuum model with dielectric constant $\epsilon = 4.0$. The majority of the calculations were performed with the BP86 functional [20, 21] along with a triple- ζ quality basis set (Ahlrich’s TZVP [22]) on all atoms. The dependence of the spin density distribution on methodology was also explored, using the B3LYP [23] functional. These latter calculations were done as single points using the geometries optimised at the BP86/TZVP level. The exchange coupling within the [4Fe-4S]_H cluster (and also, in principle, within the [2Fe]_H subdomain) was treated using the broken-symmetry approach, wherein opposing spin moments are imposed on the initial (guess) spin density, such that the system converges to a predominantly antiferromagnetic state. In all cases here, the antiferromagnetic species has an $M_S = \frac{1}{2}$ ground state, which can be formulated to a first approximation in terms of a reduced [4Fe-4S]¹⁺ cluster. Appropriately spin-polarised initial guesses were constructed using the ‘guess = fragment’ keyword available in Gaussian 09 [24]. Calculations were initialised using a wide range of initial spin densities corresponding to ferro/antiferromagnetic coupling within the [4Fe-4S]_H cubane and also

to ferro/antiferromagnetic coupling of the spin densities on the [2Fe]_H unit. A range of initial guesses was constructed in which the extra electron starts (a) on the [4Fe-4S]_H unit and (b) on the [2Fe]_H subdomain. The converged wavefunction for the one-electron oxidised case (where the oxidation states are unambiguous) was also used as an initial guess. In no case did the initial guess have a significant impact on the converged results; the self-consistent density is essentially identical. Moreover, no evidence for antiferromagnetic coupling (i.e. opposing spin densities) on the [2Fe]_H subsite in the converged self-consistent solution was found: Mulliken spin densities on Fe_d and Fe_p are always small (< 0.25 electrons) and of the same sign.”

8.3 The Direct Electrochemistry of Fuel-Forming Enzymes on Semiconducting Electrodes

8.3.1 General Considerations

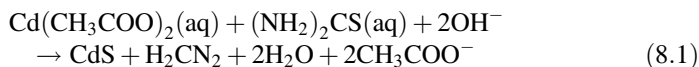
All chemicals were of the highest available quality and used as received without any further purification. Cadmium acetate, thiourea and ammonia solution (28–30%) for the synthesis of CdS thin film electrodes were procured from Sigma-Aldrich. For the preparation of TiO₂ thin film electrodes, nitric acid was purchased from Fisher Scientific, and the TiO₂ particles were Degussa P25 (80% anatase, 20% rutile, average diameter 21 nm). Indium tin oxide coated glass slides (1.1 mm thick, 8–12 Ω), used as substrates for the semiconductor thin films, were purchased from SPI Supplies, USA. 2-(*N*-morpholino)ethanesulfonic acid (MES) was obtained from Melford, and aqueous buffer solutions containing MES were titrated to the correct pH using NaOH (Sigma-Aldrich). KOCN was obtained from Sigma-Aldrich. In experiments under gas flow, the electrochemical cell was constantly purged with the respective gas mixture throughout the experiments.

8.3.2 Semiconductor Electrodes

8.3.2.1 Synthesis of Semiconductor Thin Films

CdS: ITO slides of approximate dimensions 1 × 2 cm² were cleaned by sonication for 15 min each in ethanol, followed by acetone, and deionised H₂O. The cleaned and degreased slides were activated in a solution containing 1.9 mg KMnO₄ (Sigma-Aldrich ACS reagent, ≥ 99%), 30 μL butanol (Alfa Aesar, 99%) and 20 mL water for 30 min at 93 °C. These activated substrates were washed thoroughly with H₂O and dried. To grow CdS thin films, 0.66 g cadmium acetate was dissolved in 2.5 mL deionised H₂O. Subsequently, ammonia solution was added dropwise until a clear solution was obtained. An aqueous solution (2.5 mL) containing 0.19 g

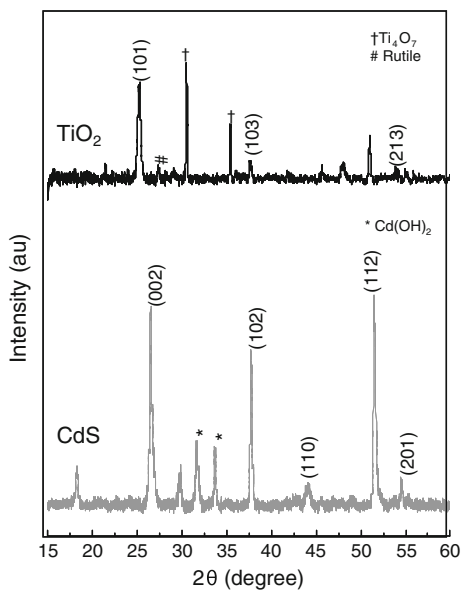
thiourea was then added to the cadmium acetate containing reaction mixture. The activated ITO substrate was placed in a vial containing the reaction mixture, ensuring that a portion of the substrate remained out of solution, and this mixture was then heated at ca. 90 °C for 30 min. Upon heating, thiourea releases sulphide ions which then form CdS by metathesis with the hydrolysed Cd(II) species. The overall reaction of CdS formation from cadmium acetate and thiourea is described by the following equation [25]:



Following CdS deposition, the thin film was washed thoroughly with deionised H₂O to remove unadsorbed CdS particles, and dried at room temperature. The appearance of diffraction peaks [(002), (102), (110), (112) and (201)] in the XRD pattern indicates predominant formation of the hexagonal phase of CdS (Fig. 8.1 lower). However, few peaks corresponding to Cd(OH)₂ were also observed.

TiO₂: A suspension was prepared by dispersing 50 mg TiO₂ (P25) in 70 μL of 0.1 M HNO₃, followed by sonication for 30 min. The ITO substrate was cleaned by sonication for 15 min each in acetone, ethanol, and water. TiO₂ thin films were then deposited onto a cleaned conducting glass substrate by the ‘Doctor blading’ technique [27]. An area of approximately 10 mm × 10 mm was covered, with the TiO₂ film thickness being controlled by a layer of Scotch tape. The TiO₂ films were then

Fig. 8.1 X-ray diffraction patterns of TiO₂ (*top*) and CdS (*bottom*) deposited on ITO substrates. Reprinted with permission from Ref. [26]. Copyright 2013 American Chemical Society



subjected to heat treatment at 450 °C for 30 min (ramp rate 5 °C min⁻¹). The TiO₂ XRD pattern, recorded after calcination, shows the presence of both rutile and anatase phases (Fig. 8.1 upper).

8.3.2.2 Electrode Fabrication

The semiconductor films deposited on ITO were converted into electrodes by making ohmic contact with copper wire using silver paint (Agar Scientific G3691) at an uncoated area of the transparent conducting oxide [28]. The copper wire was insulated with a glass tube, which was connected to the electrode assembly by epoxy resin (Loctite Hysol 9462). The contact edges of the films were then also covered by Hysol epoxy, leaving only parts of the thin semiconductor films exposed. Typical geometric surface areas were 0.1–0.4 cm².

8.3.3 Enzyme Preparation

Isolation, purification and activity measurements of CODH I from *Carboxydotherrmus hydrogenoformans* were carried out by Dr. Mehmet Can (laboratory of Professor Stephen Ragsdale, University of Michigan, USA) according to previously described procedures [29]. The activity for CO oxidation was 1.30 mmol min⁻¹ mg⁻¹ at 20 °C. The [NiFeSe]-hydrogenase sample from *Desulfomicrobium baculatum*, provided by Professor Juan Fontecilla-Camps (CEA/CNRS Grenoble, France), was obtained according to previously published methods [30, 31]. The specific H₂ oxidation activity of [NiFeSe]-hydrogenase was determined as 1.70 mmol min⁻¹ mg⁻¹, using conventional room temperature assays after a few minutes under H₂ to fully activate the enzyme.

8.3.4 Protein Film Electrochemistry

To study the electrocatalytic behaviour of the enzymes on CdS, TiO₂, and PGE, aliquots of enzyme samples (either CODH or H₂ase, < 100 pmol) were drop cast onto the electrode and left for a few minutes until partially dry. The electrode was then placed in an electrochemical cell and connected as the working electrode in conjunction with an Ag/AgCl (1 M KCl) reference electrode and a Pt wire as counter. All potentials are quoted vs. the standard hydrogen electrode (SHE) using the conversion $E_{\text{SHE}} = E_{\text{Ag/AgCl}} + 234 \text{ mV}$ at 20 °C. The electrolyte was 0.2 M MES at pH 6.0, and all solutions were prepared using purified water (Millipore, 18 MΩ cm). Electrochemical measurements were made with an Autolab potentiostat (PGSTAT30) controlled by Nova software (EcoChemie). Impedance measurements were conducted using an Ivium Technologies COMPACTSTAT.e

portable electrochemical interface and impedance analyser, controlled by IviumSoft software. Cyclic voltammograms were recorded prior to and after impedance and chronoamperometry experiments with enzyme-modified electrodes, in order to ensure that the catalytic activity of the enzyme had remained steady throughout the measurements.

A Kodak light source (Kodak Carousel S-AV 1010 projector) fitted with a 250 W tungsten-halogen bulb and a 420 nm long-pass filter (UQG Optics) was used in the photoelectrochemistry experiments. At the position of the electrochemical cell, the light intensity was 16 mW cm^{-2} , measured using a Melles Griot Broadband Power/Energy Meter (13PEM001). All electrochemistry experiments were repeated at least twice.

8.4 Selective Visible-Light-Driven CO_2 Reduction on a *p*-Type Dye-Sensitised NiO Photocathode

8.4.1 General Considerations

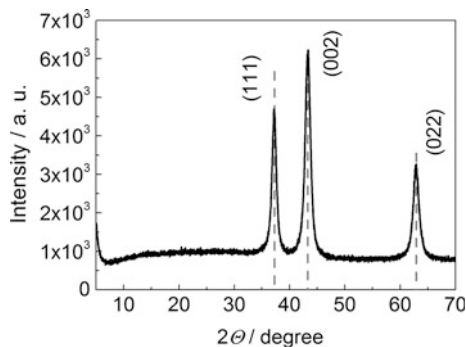
All chemicals were of the highest available quality and used as received without any further purification. All PFE experiments were carried out in 0.2 M MES buffer (pH 6.0 at 20 °C), which was prepared by dissolving 2-(*N*-morpholino)ethanesulfonic acid (Melford) in purified H_2O (Milli-Q, 18 M Ω cm). The pH was adjusted to the correct value using NaOH (Sigma-Aldrich). In experiments under gas flow, the electrochemical cell was constantly purged with the respective gas mixture throughout the experiments.

8.4.2 Fabrication of NiO Electrodes

8.4.2.1 Synthesis of NiO Particles

Nanocrystalline NiO particles were synthesised according to a previously published procedure [32]. Solutions of 4 mM oxalic acid (Sigma-Aldrich, 99+%), 20 mM hexamethylenetetramine (Sigma-Aldrich, ACS reagent, $\geq 99\%$) and 20 mM Ni (NO_3)₂ (BDH Laboratory Supplies) were mixed and refluxed at 100 °C for 5 h. The resulting green precipitate was then filtered and washed with ethanol and water before being dried under vacuum overnight and heated to 400 °C for 2 h. The powder XRD pattern obtained after heating in air is depicted in Fig. 8.2.

Fig. 8.2 X-ray diffraction pattern of synthesised NiO powder



8.4.2.2 Fabrication of Electrodes from NiO Particles

First, ITO slides (see Sect. 8.3.2) were degreased and activated as described in Sect. 8.3.2.1-‘CdS’. In parallel, NiO powder (2.0 g) was suspended in a mixture of 10 μ L acetylacetone (Sigma-Aldrich, ReagentPlus, \geq 99%), 25 μ L Triton X100 surfactant (Fisher Scientific), and 12 mL H₂O. The suspension was sonicated for 30 min and then centrifuged for 20 s at 4000 rpm to create an aggregate-free NiO suspension. This suspension was applied to the activated ITO sheets by the Doctor’s blade technique [27], with the electrode film thickness being controlled by a layer of Scotch tape (compare Sect. 8.3.2.1-‘TiO₂’). The resulting films were then calcined at 550 °C for 10 min (an SEM image recorded after calcination is depicted in Fig. 5.2). The synthesised NiO films were converted into electrodes according to the procedure described in Sect. 8.3.2.2. Typical geometric surface areas were 0.1–0.4 cm². Surface areas were determined with the freely available program ‘Image J’ by counting the number of pixels on a digital picture of the electrode, which included a ruler to set the scale [28].

8.4.2.3 Synthesis of P1 and Sensitisation of NiO Electrodes

4-[Bis(4-{5-[2,2-dicyanovinyl]-thiophene-2-yl}]phenyl)amino]benzoic acid (P1) was synthesised by Samuel Hall under my supervision as previously described by Qin et al. [33] and characterised accordingly. ¹H NMR and ¹³C NMR spectra of P1 are shown in Figs. 8.3 and 8.4, respectively. NiO electrodes were sensitised with P1 by soaking the electrodes in a 300 μ M solution of P1 in ethanol overnight.

8.4.3 Enzyme Preparation

Preparation and activity parameters of CODH I from *Carboxydotherrnus hydrogenoformans* are described in Sect. 8.3.3.

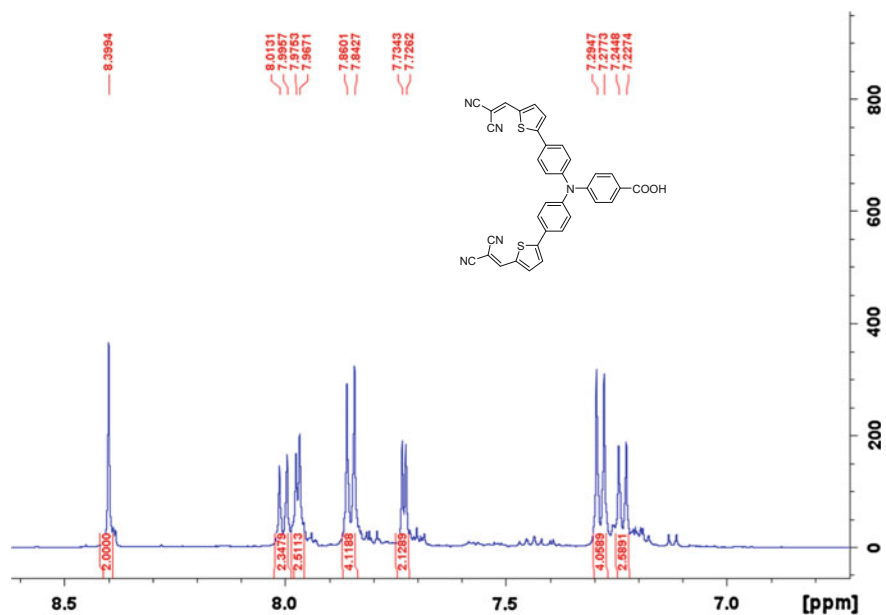


Fig. 8.3 ^1H NMR spectrum of P1. δ_{H} (500 MHz, acetone- d_6) 7.23 (2H, d, J 8.72), 7.28 (4H, d, J 8.71), 7.73 (2H, d, J 4.10), 7.85 (4H, d, J 8.69), 7.97 (2H, d, J 4.10), 8.00 (2H, d, 8.70), 8.40 (2H, s). Reprinted with permission from Ref. [34]. Copyright 2014 American Chemical Society

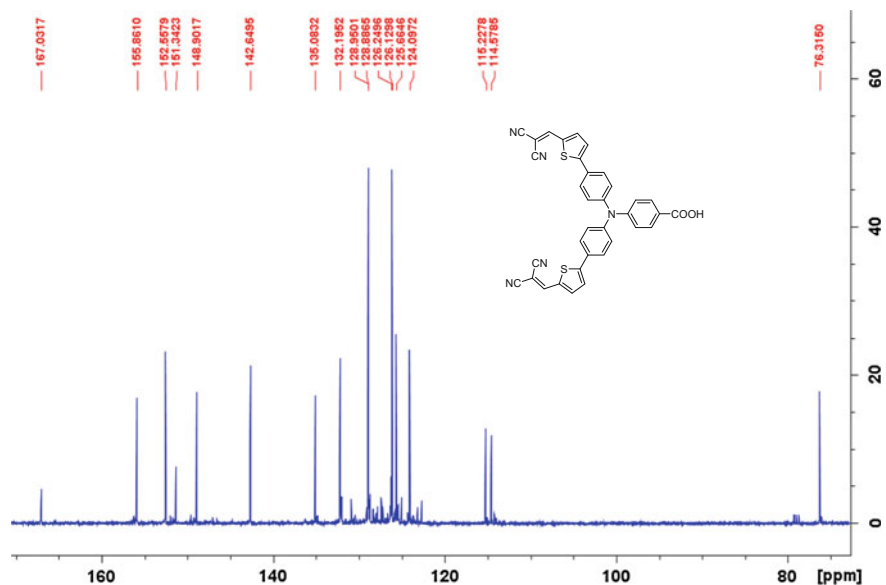


Fig. 8.4 ^{13}C NMR spectrum of P1. δ_{C} (125 MHz, acetone- d_6) 76.3, 114.6, 115.2, 124.1, 125.7, 126.1, 126.2, 128.9, 129.0, 132.2, 135.1, 142.6, 148.9, 151.3, 152.6, 155.9, 167.0. Reprinted with permission from Ref. [34]. Copyright 2014 American Chemical Society

8.4.4 Protein Film Electrochemistry

To study the electrochemistry of CODH on PGE, aliquots of enzyme (< 100 pmol) were drop cast onto the electrode and left for a few minutes until partially dry. In the case of NiO and NiO–P1 electrodes, in a typical experiment, 4 μL of 0.12 mM enzyme was applied to a NiO electrode of 0.4 cm² geometric surface area. The total coverage is therefore 1.2 nmol cm⁻². The electrodes prepared according to the above-mentioned protocols were used as working electrodes in a single-compartment electrochemical cell, with a Pt (wire) counter electrode and a Ag/AgCl 3.5 M KCL reference electrode. All potentials in Chap. 5 are quoted vs. the standard hydrogen electrode (SHE) using the conversion $E_{\text{SHE}} = E_{\text{Ag/AgCl}} + 205 \text{ mV}$ at 25 °C. The electrolyte was 0.2 M MES at pH 6.0, and all solutions were prepared using purified water (Millipore, 18 MΩ cm). Electrochemical measurements were made with an Autolab potentiostat (PGSTAT30) controlled by Nova software (EcoChemie). The Kodak light source and the 420 nm long-pass filter described in Sect. 8.3.4 were used in the photoelectrochemistry experiments. At the position of the electrochemical cell, the light intensity was 45 mW cm⁻². An optical chopper, built in house, was used to measure transient photocurrents.

Inhibition experiments to establish the activity of CODH for CO₂ and CO reduction using the selective inhibitors KOCN (Sigma-Aldrich) and KCN (Fisher-Scientific) were conducted as follows: 1.0 mL of a stock solution of the respective inhibitor (dissolved in 0.2 M MES buffer, pH 6.0, and pre-saturated with the gas-mixture present in the electrochemical cell) was injected into the electrochemical cell containing 9.0 mL buffer.

8.5 A Multi-haem Flavoenzyme as a Solar Conversion Catalyst

8.5.1 General Considerations

All chemicals were of the highest available quality and were used as received without further purification.

8.5.1.1 Buffer Solutions

All electrochemistry experiments were carried in one of the following buffer solutions, which were prepared using purified H₂O (Millipore, 18 MΩ cm):

- 0.2 M MES buffer (pH 6.0 at 20 °C), which was prepared by dissolving MES (Melford > 99.5%) in purified H₂O;

- ‘Mixed buffer system’ (pH 7.0 at 20 °C) containing 50 mM TAPS (3-[[tris (hydroxymethyl)methyl]amino]propanesulfonic acid, Melford > 99.5%), HEPES (*N*-(2-hydroxy-ethyl)piperazine-*N'*-2-ethanesulfonic acid, Melford > 99.5%), MES, PIPES (1,4-piperazinediethanesulfonic acid, Sigma-Aldrich > 99%), and an additional supporting electrolyte of 0.1 M NaCl (Fisher Scientific, 99.9+%);
- 0.1 M Potassium phosphate buffer, ‘KPi’, (pH 7.0 at 25 °C), made up of K_2HPO_4 and KH_2PO_4 (both Fisher Scientific, 99+%).

Sodium fumarate dibasic (Sigma-Aldrich, $\geq 99\%$) was dissolved in or injected into the buffer at various concentrations, depending on the experiment. For each buffer solution, the pH was adjusted to the desired value at the working temperature for the experiment in question using NaOH or HCl (Sigma-Aldrich).

8.5.1.2 RuP Synthesis

$[\text{Ru}(\text{bpy})_2(4,4'-(\text{PO}_3\text{H}_2)_2\text{bpy})]\text{Br}_2$ (RuP), prepared as reported previously [35], was kindly provided by Dr. Thomas Woolerton.

8.5.2 Protein Purification

Samples of flavocytochrome c_3 from *Shewanella frigidimarina* NCIMB400 were provided by Professors Graeme A. Reid (Institute of Cell and Molecular Biology, University of Edinburgh) and Stephen K. Chapman (Department of Chemistry, University of Edinburgh) and purified as described previously [36]. The total protein concentration (4.13 mg mL^{-1}) was estimated spectroscopically using the method of Bradford [9], with bovine serum albumin (Sigma-Aldrich) as the protein standard.

8.5.3 Preparation of Thin Film Electrodes

8.5.3.1 Cadmium Sulphide and Titanium Dioxide

Thin films of CdS and TiO_2 on ITO slides (SPI Supplies USA, 1.1 mm thick, 8–12 Ω) were synthesised and characterised as described in Sect. 8.3.2.1.

8.5.3.2 Meso-Indium Tin Oxide

meso-ITO was prepared according to the procedure reported by Kato et al. [37] using indium tin oxide nanopowder (Sigma-Aldrich): $1 \times 2 \text{ cm}^2$ ITO slides were sonicated for 20 min each in *iso*-propanol and then acetone. Subsequently, the cleaned and degreased sheets were dried in air. A dispersion of ITO was created by sonicating a mixture of ITO nanopowder (20 wt%) in 5 M acetic acid solution in ethanol. The mixture was applied onto the ITO sheets using the Doctor's blade technique [27], following a 30 min calcination step at 450 °C (ramp rate 4 °C min⁻¹).

8.5.3.3 Tungsten-Doped Bismuth Vanadate

W–BiVO₄ electrodes were deposited on FTO slides (Sigma-Aldrich, 2.2 mm thickness, $\sim 7 \text{ } \Omega/\text{sq}$, 80% transmittance) according to a method described by Bard and co-workers [38]. A premixed solution of Bi(NO₃)₃·5H₂O, VCl₃ (both Sigma-Aldrich), and (NH₄)₁₀(H₂W₁₂O₄₂)·4H₂O (Alfa Aesar) in ethylene glycol (Sigma-Aldrich) with a molar ratio of Bi:V:W = 4.5:5:0.5 at 10 mM concentration (total of the three elements) was pipetted onto the FTO substrates followed by annealing at 500 °C for 3 h (ramp rate 1 °C min⁻¹).

8.5.3.4 Electrode Fabrication

Semiconductor and *meso*-ITO films were converted into electrodes using the procedure described in Sect. 8.3.2.2. Geometric surface areas were again determined using the program 'Image J' [28], geometric areas were 0.1–0.4 cm².

8.5.4 Protein Film Electrochemistry Experiments

To study the (photo-)electrochemistry of fcc₃ on PGE, TiO₂, CdS, and *meso*-ITO electrodes, aliquots of enzyme (< 1 nmol) were pipetted onto the respective electrode and left for a few minutes until partially dry. Electrochemistry experiments were carried out as described in Sect. 8.4.4, using an Ag/AgCl 3.5 M KCl reference electrode, the conversion factor (to SHE) of which is $E_{\text{SHE}} = E_{\text{Ag/AgCl}} + 205 \text{ mV}$ at 25 °C. In experiments with PGE electrodes, the working electrode was controlled by an electrode rotator (EcoChemie or EG&G) and rotated at a constant speed. All electrochemistry experiments were repeated at least twice.

8.5.5 Photocatalysis Experiments

8.5.5.1 Adsorption of fcc₃ on TiO₂ Nanoparticles

5 mg TiO₂ nanoparticles (anatase, average particle diameter 15 nm) were dispersed at room temperature in 5 mL MES buffer (0.2 M, pH 6.0). Following sonication for 20 min, 1.95 nmol fcc₃ (as a 30 μ L stock solution) was added to the suspension and the mixture was stirred for 20 min. After centrifugation (8000 rpm for 12 min), a UV/Vis spectrum of the supernatant was recorded (Fig. 6.5b).

The unit cell dimensions of fcc₃ are $a = 77.7 \text{ \AA}$, $b = 86.7 \text{ \AA}$, $c = 211.2 \text{ \AA}$ [39], resulting in a maximum 'footprint' per enzyme molecule of $b \times c = 1.83 \times 10^{-16} \text{ m}^2$. With the surface area of anatase nanoparticles being $50 \text{ m}^2 \text{ g}^{-1}$, the total surface area of 5 mg TiO₂ particles is 0.25 m^2 . The upper limit for monolayer coverage of fcc₃ = $0.25 \text{ m}^2 / 1.83 \times 10^{-16} \text{ m}^2 \text{ molecule}^{-1} = 1.37 \times 10^{15}$ molecules, which equal 2.27 nmol. Hence, 1.95 nmol fcc₃ cover up to 86% of the TiO₂ surface.

8.5.5.2 Adsorption of RuP on TiO₂ Nanoparticles

Verification of RuP adsorption on TiO₂ was carried out previously, similarly to adsorption of fcc₃. It was established that 213 nmol RuP is required to completely cover the surface of 5 mg nanoparticle [40]. Thus, 56 nmol is expected to cover approximately 25% of the TiO₂ surface.

8.5.5.3 Photocatalysis by RuP–TiO₂–fcc₃

Photocatalytic fumarate conversion was carried out as follows. In an anaerobic glove box, 5 mg TiO₂ nanoparticles were suspended in 5 mL of 0.2 M MES buffer solution (pH 6.0, D₂O, containing 6.0 mM fumarate) by sonication in a Pyrex pressure vessel at room temperature for 20 min. Then, 1.95 nmol of fcc₃ (as a solution of 30 μ L) was added to the nanoparticles and the suspension was stirred for 20 min to allow adsorption. Next, attachment of RuP was carried out by adding 100 μ L of 0.56 mM RuP (56 nmol) in 0.2 M MES (pH 6.0, D₂O) to the suspension, and stirring the mixture for 20 min. The pressure vessel was tightly sealed with a rubber septum, removed from the glove box, and clamped in a water bath connected to a thermostated water circulator with the temperature maintained at 5 °C, and exposed to visible light ($\lambda > 420 \text{ nm}$) provided by a Kodak Carousel S-AV 1010 projector fitted with a 250 W tungsten-halogen bulb and a 420 nm long-pass filter ($P_{\text{in}} = 45 \text{ mW cm}^{-2}$ at the position of the reaction vessel, see Sect. 8.3.4). After illumination, the reaction mixture was centrifuged for 12 min at 8000 rpm and analysed by ¹H NMR and UV/vis spectroscopy. NMR spectra of typical experiments, recorded after 4 h and 8 h of illumination, are depicted in

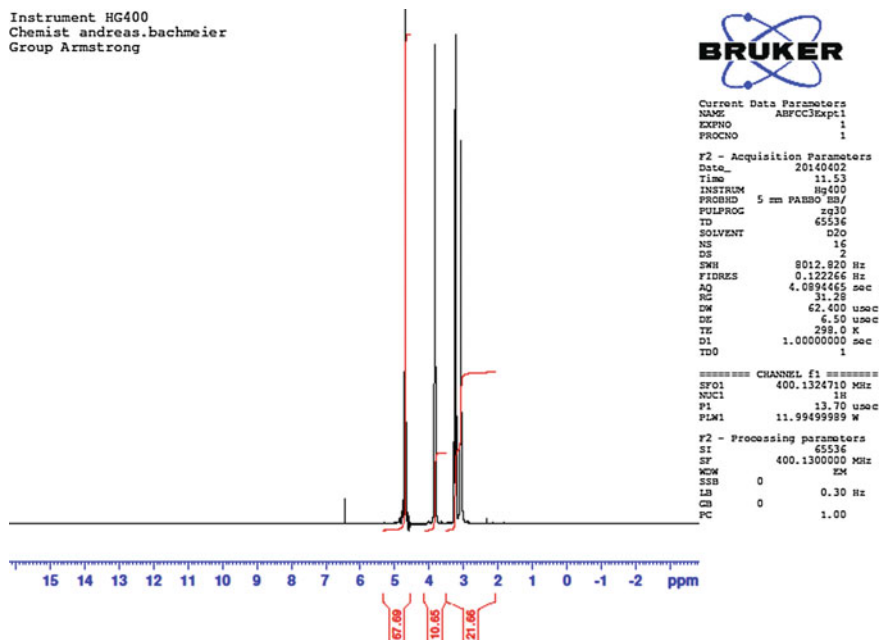


Fig. 8.5 ^1H NMR spectrum recorded after 4 h of illumination of RuP–TiO₂–fcc₃ in the presence of 6 mM fumarate. Reprinted with permission from Ref. [41]. Copyright 2014 American Chemical Society

Fig. 6.6 (comparison) and Figs. 8.5 and 8.6 (original spectra). In Fig. 6.6, the olefinic fumarate protons are highlighted by black triangles and give rise to a singlet at 6.44 ppm. The aliphatic succinate protons (indicated by black squares) resonate at 2.33 ppm. This peak increased after addition of further succinate, providing additional evidence for the nature of the product (see Fig. 6.6 inlay, original NMR spectrum depicted in Fig. 8.7). The product conversion can be calculated from the ratio of the integrals of the fumarate and succinate peaks (see Fig. 6.6). It is important to note that, as the experiments were carried in D₂O, each succinate molecule that is produced contains two aliphatic protons (from the original fumarate molecule) and two aliphatic deuterons (from D₂O) in the central unit, i.e. CH(D)–CH(D).

The fumarate/succinate ratio of 0.6 in Fig. 6.6a corresponds to a succinate concentration of 2.25 mM, indicating 37.5% conversion of the initial fumarate concentration of 6 mM after 4 h of illumination. With $n_{\text{fcc}3} = 1.95$ nmol, this gives a TON of 5800 and an average TOF of 0.4 s^{-1} per enzyme molecule, assuming all enzyme contributed to catalytic turnover. After 8 h of illumination (Fig. 6.6b), the fumarate/succinate ratio was 0.62, corresponding to a slightly higher TON of 5900 and an average TOF of 0.2 s^{-1} .

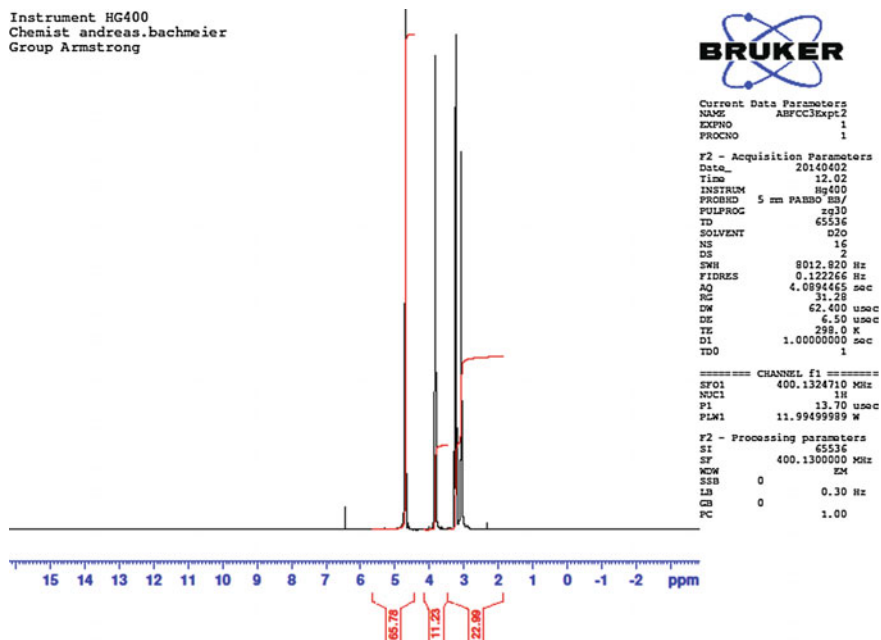


Fig. 8.6 ^1H NMR spectrum recorded after 8 h of illumination of RuP–TiO₂–fcc₃ in the presence of 6 mM fumarate. Reprinted with permission from Ref. [41]. Copyright 2014 American Chemical Society

Figure 6.7 depicts UV/vis spectra recorded after 4 h and 8 h of illumination and shows the photodegradation of the enzyme under turnover conditions. The different peaks in Fig. 6.7a,b indicate multiple decomposition pathways. Photographs of the solutions corresponding to the UV/vis spectra depicted in Fig. 6.7 are shown in Fig. 6.8.

8.5.5.4 Photochemistry Experiment—RuP–fcc₃ in Solution

This type of experiment was carried out analogously to the RuP–TiO₂–fcc₃ experiment, but without TiO₂ being added to the reaction mixture. 1.95 nmol fcc₃ and 56 nmol RuP were dissolved in 5 mL 0.2 M MES buffer (pH 6.0, D₂O) containing 6.0 mM fumarate. The pressure vessel was sealed and illuminated at 5 °C as described above. No fumarate was formed after 4 h of illumination (Figs. 6.6c and 8.8). UV/vis spectra and a photograph of the reaction mixture taken after the experiment are depicted in Figs. 6.7c and 6.8c.

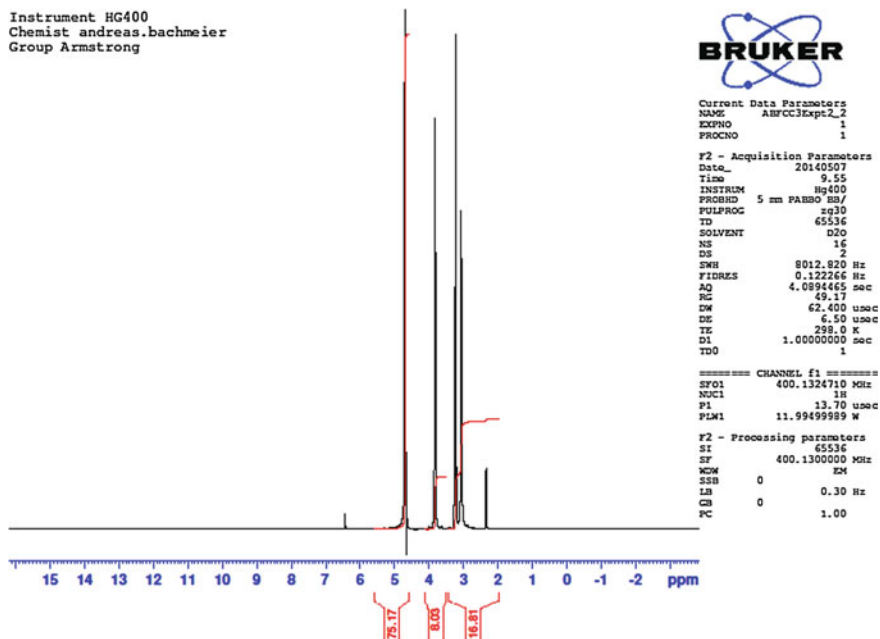


Fig. 8.7 ^1H NMR spectrum recorded after 8 h of illumination of $\text{RuP-TiO}_2\text{-fcc}_3$ in the presence of 6 mM fumarate. 0.5 mL of 6 mM disodium succinate was added to 0.5 mL of the centrifuged reaction mixture, leading to a change in fumarate/succinate ratio compared to Fig. 8.6. Reprinted with permission from Ref. [41]. Copyright 2014 American Chemical Society

8.5.5.5 Photochemistry Experiment— $\text{RuP-ZrO}_2\text{-fcc}_3$

This experiment was carried out analogously to the $\text{RuP-TiO}_2\text{-fcc}_3$ experiment, except that ZrO_2 was used instead of TiO_2 . 5 mg ZrO_2 nanopowder (Sigma-Aldrich) were dispersed in 5 mL 0.2 M MES buffer (pH 6.0, D_2O) containing 6.0 mM fumarate, and sonicated for 20 min. 1.95 nmol fcc_3 and 56 nmol RuP were added to the reaction mixture and stirred for 20 min. The reaction vessel was sealed and illuminated at 5 °C as described above. No fumarate was formed after 4 h of illumination (Figs. 6.6d and 8.9). UV/vis spectra and a photograph of the supernatant taken after post-experimental centrifugation are depicted in Figs. 6.7d and 6.8d. A photograph of the precipitate taken after centrifugation, i.e. fcc_3 adsorbed on ZrO_2 nanopowder, is shown in Fig. 6.9.

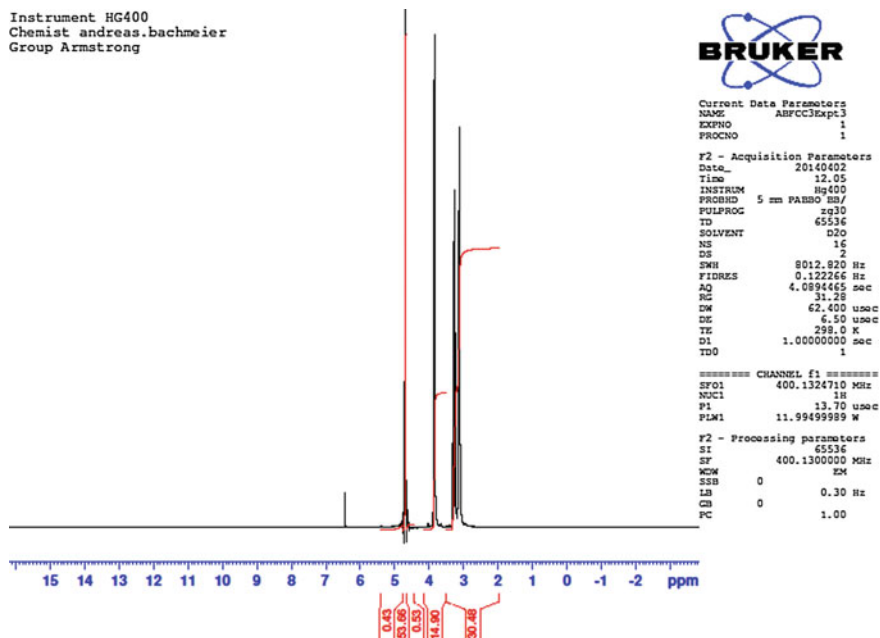


Fig. 8.8 ^1H NMR spectrum recorded after 4 h of illumination of RuP-fcc₃ in the presence of 6 mM fumarate. Reprinted with permission from Ref. [41]. Copyright 2014 American Chemical Society

8.5.6 Photoelectrochemistry Experiments

8.5.6.1 Experimental Procedures

Generally, photoelectrochemistry experiments were carried out as described in Sect. 8.5.4, either in a thermostated one-compartment electrochemistry cell, or a two-compartment cell, separated by a porous glass frit. The Kodak light source was employed as described above, using a 420 nm long-pass UV filter. An optical chopper, built in house, was used to measure transient photocurrents. For two-electrode measurements, the reference electrode lead of the potentiostat was connected to the counter electrode. Current densities were calculated with respect to the geometric surface area of the working electrode.

8.5.6.2 Catalyst Deposition on W-BiVO₄ Electrodes

The Co-Pi electrocatalyst was photodeposited (bias-assisted) on W-BiVO₄ from a solution of 0.5 mM Co(NO₃)₂ (Sigma-Aldrich, ACS reagent) dissolved in 0.1 M KPi buffer (pH 7.0) according to a method by Zhong et al. [42]. The catalyst film

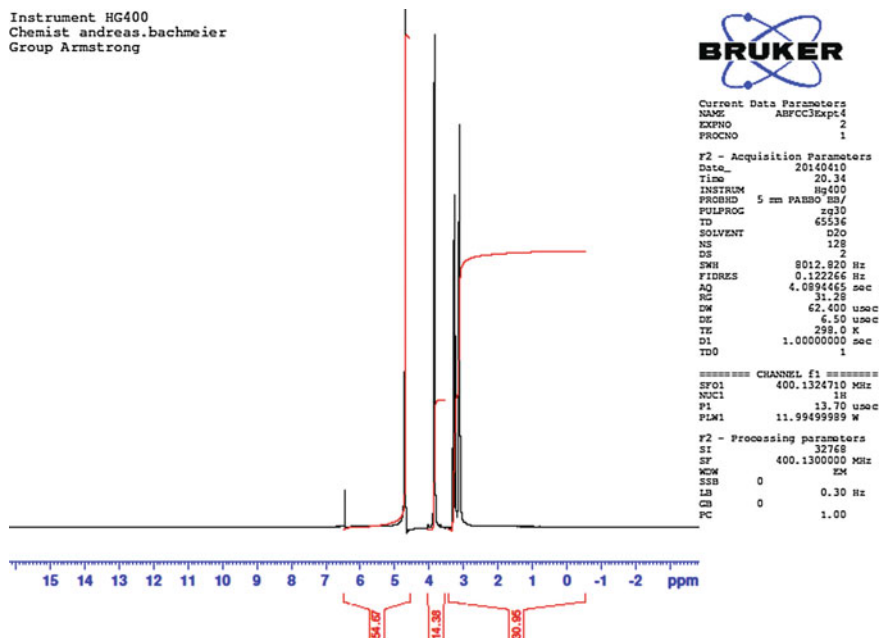


Fig. 8.9 ^1H NMR spectrum recorded after 4 h of illumination of $\text{RuP-ZrO}_2\text{-fcc}_3$ in the presence of 6 mM fumarate. Reprinted with permission from Ref. [41]. Copyright 2014 American Chemical Society

was deposited over a period of 5 min at 0.24 V vs. RHE under constant illumination through the FTO support (back illumination). Figure 6.11 depicts a comparison of the current-voltage curves obtained before and after Co-Pi deposition.

8.5.6.3 Photoelectrocatalysis Experiments

Figure 6.13 shows the temporal behaviour of a bare *meso*-ITO electrode (WE) connected to a Co-Pi modified W-BiVO_4 photoelectrode (CE) in a two-compartment photoelectrochemical cell at zero external bias. The systems displays a rapidly decaying capacitive current and the current shows little response to illumination, as the energy levels of the illuminated Co-Pi- W-BiVO_4 electrode do not permit overall water splitting.

Photoelectrocatalysis experiments including fcc_3 were carried out in the same two-electrode configuration, with the electrode compartment containing the fcc_3 -*meso*-ITO working electrode being sparged with N_2 to allow rapid substrate/product transport to and from the electrode. During the experiments, 1.0 mL 20 mM fumarate solution (in pH 7.0 KPi buffer) was injected into 9.0 mL buffer solution to a final concentration of 2.0 mM. Gas flow was briefly interrupted during the introduction of fumarate.

An *estimate* of the turnover frequency on a per enzyme basis was obtained from the overall charge passed through the photoelectrochemical cell under catalytic turnover. In the experiment depicted in Fig. 6.12, a total charge of 6.3×10^{-4} C was passed through the system between $\Delta t = 153\text{--}900$ s (i.e. after fumarate was injected into the solution). The capacitive charge during this period, estimated from the dark currents, was 1.7×10^{-5} C. With $F = 96,485$ C mol $^{-1}$, the ‘turnover’-charge (i.e. the total charge minus the capacitive charge) corresponds to 6.4 nmol electrons. Assuming $\eta_F = 100$ % as the upper limit, 3.2 nmol succinate was formed over the course of the reaction, since 2 e $^{-}$ are required to reduce one equivalent of fumarate, corresponding to 5.6 pmol s $^{-1}$ (under illumination). Assuming all fcc $_3$ molecules immobilised on *meso*-ITO (0.4 nmol) were adsorbed in an electroactive configuration, a TOF (on a per enzyme basis) of 0.01 $_4$ s $^{-1}$ is obtained. An analogous photoelectrocatalysis experiment carried out with reversed connections, i.e. Co-Pi-W-BiVO $_4$ employed as WE and fcc $_3$ -ITO as the counter is depicted in Appendix G.

References

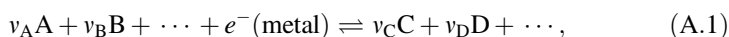
1. Sucheta A, Cammack R, Weiner J, Armstrong FA (1993) *Biochemistry* 32:5455
2. Girbal L, von Abendroth G, Winkler M, Benton PMC, Meynial-Salles I, Croux C, Peters JW, Happe T, Soucaille P (2005) *Appl Environ Microbiol* 71:2777
3. Lubitz W, Ogata H, Rüdiger O, Reijerse E (2014) *Chem Rev* 114:4081
4. Happe T, Naber JD (1993) *Eur J Biochem* 214:475
5. von Abendroth G, Stripp ST, Silakov A, Croux C, Soucaille P, Girbal L, Happe T (2008) *Int J Hydrogen Energy* 33:6076
6. Kuchenreuther JM, Grady-Smith CS, Bingham AS, George SJ, Cramer SP, Swartz JR (2010) *PLoS ONE* 5
7. Akhtar MK, Jones PR (2008) *Appl Microbiol Biotechnol* 78:853
8. Esselborn J, Lambert C, Adamska-Venkatesh A, Simmons T, Berggren G, Noth J, Siebel J, Hemschemeier A, Artero V, Reijerse E, Fontecave M, Lubitz W, Happe T (2013) *Nat Chem Biol* 9:607
9. Bradford MM (1976) *Anal Biochem* 72:248
10. Hemschemeier A, Melis A, Happe T (2009) *Photosynth Res* 102:523
11. Roseboom W, De Lacey AL, Fernández VM, Hatchikian EC, Albracht S (2006) *J Biol Inorg Chem* 11:102
12. Albracht SJ, Roseboom W, Hatchikian EC (2006) *J Biol Inorg Chem* 11:88
13. Bard AJ, Faulkner LR (2001) *Electrochemical Methods: Fundamentals and Applications*, 2nd edn. John Wiley & Sons Inc, New York
14. Bell RP (1966) In: Gold V (ed) *Adv Phys Org Chem*, vol 4. Academic Press, p 1
15. Hilal SH, Bornander LL, Carreira LA (2005) *QSAR Comb Sci* 24:631
16. Roessler MM (2012) D Phil Thesis, University of Oxford, Oxford
17. Stoll S, Schweiger A (2006) *J Magn Reson* 178:42
18. Nicolet Y, Piras C, Legrand P, Hatchikian EC, Fontecilla-Camps JC (1999) *Structure* 7:13
19. Bruschi M, Greco C, Kaukonen M, Fantucci P, Ryde U, De Gioia L (2009) *Angew Chem Int Ed* 48:3503
20. Becke AD (1988) *Phys Rev A* 38:3098
21. Perdew J (1986) *Phys Rev B* 33:8822
22. Schäfer A, Huber C, Ahlrichs R (1994) *J Phys Chem* 100:5829

23. Becke AD (1993) *J Phys Chem* 98:5648
24. Frisch MJT, Trucks GW, Schlegel HB, Scuseria GE, Robb MA, Cheeseman JR, Scalmani G, Barone V, Mennucci B, Petersson GA, Nakatsuji H, Caricato M, Li X, Hratchian HP, Izmaylov AF, Bloino J, Zheng G, Sonnenberg JL, Hada M, Ehara M, Toyota K, Fukuda R, Hasegawa J, Ishida M, Nakajima T, Honda Y, Kitao O, Nakai H, Vreven T, Montgomery JA Jr, Peralta JE, Ogliaro F, Bearpark M, Heyd JJ, Brothers E, Kudin KN, Staroverov VN, Kobayashi R, Normand J, Raghavachari K, Rendell A, Burant JC, Iyengar SS, Tomasi J, Cossi M, Rega N, Millam MJ, Klene M, Knox JE, Cross JB, Bakken V, Adamo C, Jaramillo J, Gomperts R, Stratmann RE, Yazyev O, Austin AJ, Cammi R, Pomelli C, Ochterski JW, Martin RL, Morokuma K, Zakrzewski VG, Voth GA, Salvador P, Dannenberg JJ, Dapprich S, Daniels AD, Farkas Ö, Foresman JB, Ortiz JV, Cioslowski J, Fox DJ (2009) *Gaussian 09*, Revision A. 02, Gaussian, Inc, Wallingford CT
25. Kaur I, Pandya DK, Chopra KL (1980) *J Electrochem Soc* 127:943
26. Bachmeier A, Wang VC-C, Woolerton TW, Bell S, Fontecilla-Camps JC, Can M, Ragsdale SW, Chaudhary YS, Armstrong FA (2013) *J Am Chem Soc* 135:15026
27. Barbé CJ, Arendse F, Comte P, Jirousek M, Lenzmann F, Shklover V, Grätzel M (1997) *J Am Ceram Soc* 80:3157
28. Chen Z, Dinh HN, Miller E (2013) *Photoelectrochemical Water Splitting: Standards, Experimental Methods, and Protocols*. Springer
29. Seravalli J, Ragsdale SW (2008) *Biochemistry* 47:6770
30. Parkin A, Goldet G, Cavazza C, Fontecilla-Camps JC, Armstrong FA (2008) *J Am Chem Soc* 130:13410
31. Hatchikian EC, Bruschi M, Le Gall J (1978) *Biochem Biophys Res Commun* 82:451
32. Powar S, Wu Q, Weidelener M, Nattestad A, Hu Z, Mishra A, Bauerle P, Spiccia L, Cheng Y-B, Bach U (2012) *Energy Environ Sci* 5:8896
33. Qin P, Zhu H, Edvinsson T, Boschloo G, Hagfeldt A, Sun L (2008) *J Am Chem Soc* 130:8570
34. Bachmeier A, Hall S, Ragsdale SW, Armstrong FA (2014) *J Am Chem Soc* 136:13518
35. Trammell SA, Moss JA, Yang JC, Nakhle BM, Slate CA, Odobel F, Sykora M, Erickson BW, Meyer T (1999) *J Inorg Chem* 38:3665
36. Pealing SL, Cheesman MR, Reid GA, Thomson AJ, Ward FB, Chapman SK (1995) *Biochemistry* 34:6153
37. Kato M, Cardona T, Rutherford AW, Reisner E (2012) *J Am Chem Soc* 134:8332
38. Ye H, Park HS, Bard AJ (2011) *J Phys Chem C* 115:12464
39. Turner KL, Doherty MK, Heering HA, Armstrong FA, Reid GA, Chapman SK (1999) *Biochemistry* 38:3302
40. Woolerton TW (2012) D Phil Thesis, University of Oxford, Oxford
41. Bachmeier A, Murphy BJ, Armstrong FA (2014) A Multi-Heme Flavoenzyme as a Solar Conversion Catalyst. *J Am Chem Soc* 136:12876
42. Zhong DK, Cornuz M, Sivula K, Gratzel M, Gamelin DR (2011) *Energy Environ Sci* 4:1759

Appendix A

Derivation of the Nernst equation

Consider the general reaction [1, 2]



where v_i are the stoichiometric coefficients of the individual components i . With the *electrochemical potential* $\tilde{\mu}_i$ of component i being related to its chemical potential μ_i by

$$\tilde{\mu}_i = \mu_i + z_i F \phi, \quad (\text{A.2})$$

where $z_i F \phi$ is the electrical energy of species i (z_i is the charge carried by i , F is Faraday's constant, and ϕ is the potential of the particular phase (electrode or solution) in which i resides), the electrochemical potentials of the reactants and products in the equilibrium described by Eq. (A.1) can be expressed as

$$v_A \tilde{\mu}_A + v_B \tilde{\mu}_B + \dots + \tilde{\mu}_{e^-} = v_C \tilde{\mu}_C + v_D \tilde{\mu}_D + \dots \quad (\text{A.3})$$

The different $\tilde{\mu}_i$ can be substituted according to Eq. (A.2):

$$\begin{aligned} v_A (\mu_A + z_A F \phi_s) + v_B (\mu_B + z_B F \phi_s) + \dots + (\mu_{e^-} - F \phi_m) \\ = v_C (\mu_C + z_C F \phi_s) + v_D (\mu_D + z_D F \phi_s) + \dots \end{aligned} \quad (\text{A.4})$$

Conservation of electrical charge requires that

$$v_A z_A + v_B z_B + \dots - 1 = v_C z_C + v_D z_D + \dots \quad (\text{A.5})$$

Rearrangement of Eq. (A.4), substitution into Eq. (A.5), and solving for $F(\phi_m - \phi_s)$ leads to

$$F(\phi_m - \phi_s) = v_A \mu_A + v_B \mu_B + \cdots + \mu_{e^-} - v_C \mu_C - v_D \mu_D. \quad (\text{A.6})$$

With

$$\mu_i = \mu_i^0 + RT \ln a_i. \quad (\text{A.7})$$

follows

$$F(\phi_m - \phi_s) = v_A(\mu_A^0 + RT \ln a_A) + v_B(\mu_B^0 + RT \ln a_B) + \cdots + \mu_{e^-} - v_C(\mu_C^0 + RT \ln a_C) - v_D(\mu_D^0 + RT \ln a_D). \quad (\text{A.8})$$

Substitution of the term

$$F\Delta\phi^0 = (v_A \mu_A^0 + v_B \mu_B^0 + \cdots) - (v_C \mu_C^0 + v_D \mu_D^0 + \cdots) + \mu_{e^-}, \quad (\text{A.9})$$

which is constant at a fixed temperature and pressure, into Eq. (A.8), and rearrangement lead to a general statement of the Nernst equation:

$$\phi_m - \phi_s = \Delta\phi^0 + \frac{RT}{F} \ln \left\{ \frac{a_A^{v_A} a_B^{v_B} \cdots}{a_C^{v_C} a_D^{v_D} \cdots} \right\}. \quad (\text{A.10})$$

For ‘ideally’ behaving solutions activities can be approximated to concentrations. With $E = \phi_m - \phi_s$ and $E^0 = \Delta\phi^0$, and by introducing z for the number of electrons transferred in the process (as a means of generalisation to account for processes with $z > 1$), Eq. (A.9) can be rewritten as

$$E = E^0 + \frac{RT}{zF} \ln \frac{[\text{Ox}]}{[\text{Red}]}, \quad (\text{A.11})$$

which, when at equilibrium ($E = E_{\text{eq}}$), equates Eq. (2.7) in Sect. 2.2.4.

With the change in free energy ΔG being defined as the sum of the products of the stoichiometric coefficients v_i and the chemical potentials μ_i of the individual components i

$$\Delta G = \sum v_i \mu_i, \quad (\text{A.12})$$

the relationship between the Nernst equation and ΔG becomes apparent:

$$\Delta G = \sum v_i \mu_i^0 + RT \sum v_i \ln a_i \quad (\text{A.13})$$

or, rearranged:

$$\Delta G = \Delta G^0 + RT \ln \prod_i [a_i]^{v_i}. \quad (\text{A.14})$$

Hence,

$$\Delta G = -zFE. \quad (\text{A.15})$$

Appendix B

Derivation of the Mott-Schottky Equation

Consider an n -type semiconductor under depletion [3]. The density of electrons and holes at the surface, n_s and p_s , respectively, is related to their constant bulk values by

$$n(x) = n_b e^{\frac{e_0 \Delta \phi}{k_B T}} \quad \text{and} \quad p(x) = p_b e^{-\frac{e_0 \Delta \phi}{k_B T}}, \quad (\text{B.1})$$

where $\Delta \phi = \phi_x - \phi_b$ represents the surface-bulk potential difference, i.e. the band-bending, and n_b and p_b are the electron and hole concentrations in the bulk of the semiconductor. The potential, the charge density (ρ), and the number of carriers (n and p) all depend on the distance (x) away from the interface into the semiconductor bulk. The charge density in an n -type semiconductor can be expressed as [4]

$$\rho(x) = e_0(-n(x) + p(x) - N_A + N_D) \quad (\text{B.2})$$

and $n \gg p$, $N_D \gg N_A$. Further, the density of electrons in the bulk principally equals the donor density, i.e. $n_b \approx N_D$. Using these simplifications, Eq. (B.2) can be rewritten as follows:

$$\rho(x) = e_0 N_D \left(1 - e^{\frac{e_0 \Delta \phi}{k_B T}} \right). \quad (\text{B.3})$$

The charge density is related to the potential by the Poisson equation [5]:

$$\frac{d^2 \phi(x)}{dx^2} = \frac{-\rho(x)}{\epsilon_r \epsilon_0}. \quad (\text{B.4})$$

Using the substitution

$$v = -\Delta\phi = -(\phi_x - \phi_b) \quad (\text{B.5})$$

Equation (B.4) can be expressed as

$$-\frac{d^2v}{dx^2} = -\frac{\rho(x)}{\varepsilon_r\varepsilon_0} \quad (\text{B.6})$$

and substituted in Eq. (B.3):

$$\frac{d^2v}{dx^2} = \frac{e_0N_D}{\varepsilon_r\varepsilon_0} \left(1 - e^{\frac{-e_0v}{k_B T}}\right). \quad (\text{B.7})$$

With the property of derivatives [5]

$$\frac{d^2v}{dx^2} = \frac{1}{2} \frac{d}{dv} \left(\frac{dv}{dx}\right)^2 \quad (\text{B.8})$$

Equation (B.7) transforms into

$$d\left(\frac{dv}{dx}\right)^2 = \frac{2e_0N_D}{\varepsilon_r\varepsilon_0} \left(1 - e^{\frac{-e_0v}{k_B T}}\right) dv. \quad (\text{B.9})$$

Integration gives

$$\left(\frac{dv}{dx}\right)^2 = \frac{2e_0N_D}{\varepsilon_r\varepsilon_0} \left(v + \frac{k_B T}{e_0} e^{\frac{-e_0v}{k_B T}}\right) + \text{const.} \quad (\text{B.10})$$

Taking into account that in the bulk of the semiconductor ($x \rightarrow \infty$) $\phi_x = \phi_b$, i.e. there is no potential difference between two points ($v = 0$) and $\frac{dv}{dx} = 0$,

$$\left(\frac{dv}{dx}\right)^2 = \frac{2e_0N_D}{\varepsilon_r\varepsilon_0} \left(v - \frac{k_B T}{e_0} \left(1 - e^{\frac{-e_0v}{k_B T}}\right)\right). \quad (\text{B.11})$$

At the surface with $x = 0$; $v = v_s$, the following approximation can be used for the depletion layer of the semiconductor:

$$v_s \gg \frac{k_B T}{e_0}. \quad (\text{B.12})$$

Then, Eq. (B.11) simplifies to

$$\left(\frac{dv}{dx}\right)_{x=0} = \left(\frac{2e_0N_D}{\varepsilon_r\varepsilon_0}\left(v_s - \frac{k_B T}{e_0}\right)\right)^{1/2}. \quad (\text{B.13})$$

Using Gauss' law to express the total charge Q [4] as

$$Q = \varepsilon_r\varepsilon_0\left(\frac{dv}{dx}\right), \quad (\text{B.14})$$

and combining Eqs. (B.13) and (B.14), Eq. (B.15) is obtained:

$$Q = \left(2\varepsilon_r\varepsilon_0e_0N_D\left(v_s - \frac{k_B T}{e_0}\right)\right)^{1/2}. \quad (\text{B.15})$$

The interfacial capacitance of the space-charge layer C_{sc} is given as

$$C_{sc} = \frac{dQ}{dv_s}. \quad (\text{B.16})$$

Substitution of Eq. (B.15) into Eq. (B.16) and differentiation yields

$$C_{sc} = \frac{\varepsilon_r\varepsilon_0e_0N_D}{\sqrt{2}\sqrt{\varepsilon_r\varepsilon_0e_0N_D\left(v_s - \frac{k_B T}{e_0}\right)}} = \left(\frac{2}{\varepsilon_r\varepsilon_0e_0N_D}\left(v_s - \frac{k_B T}{e_0}\right)\right)^{-1/2}. \quad (\text{B.17})$$

With $v_s = 0$ at $E = E_{fb}$

$$v_s = E - E_{fb}, \quad (\text{B.18})$$

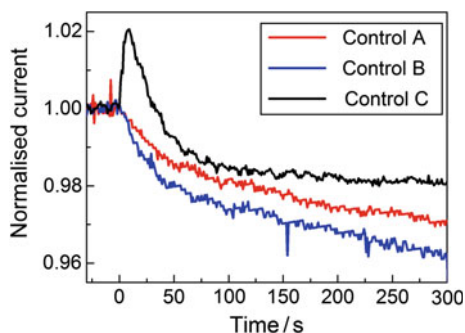
and Eq. (B.17) transforms into the Mott-Schottky equation Eq. (2.40) [3]:

$$C_{sc}^{-2} = \frac{2}{\varepsilon_r\varepsilon_0e_0N_D}\left(E - E_{fb} - \frac{k_B T}{e_0}\right). \quad (\text{B.19})$$

Appendix C

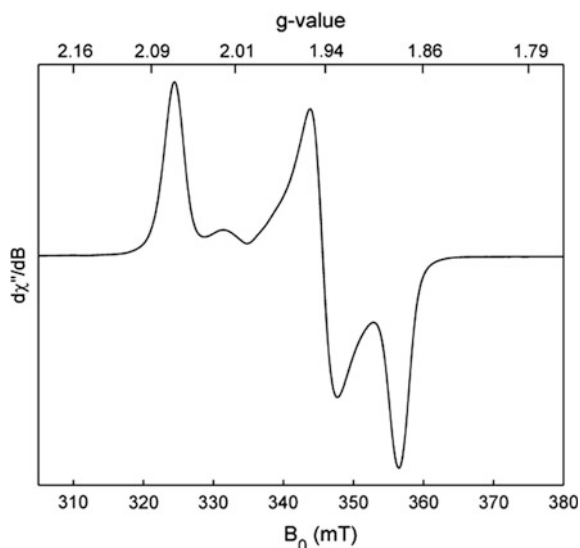
The Effect of H₂ Consumption by CaHydA at High Potential

The effect of H₂ consumption by *CaHydA* at oxidising potentials was determined by chronoamperometry, since in inhibition studies using acetaldehyde (described in Sect. 3.2.3) the gas flow had to be interrupted simultaneously to aldehyde injection, because of the high volatility of MeCHO (bp 20 °C). The figure below depicts three control experiments carried out analogously to the inhibition studies described in Sect. 3.2.3, apart from buffer solution being injected into the electrochemical cell at $t = 0$ instead of acetaldehyde (H₂ flow was turned off simultaneously to buffer injection; the electrode was poised at 0.0 V vs. SHE; $\omega = 3000$ rpm; pH 6.0 phosphate buffer; dark). In all three cases, less than 5% activity is lost during 5 min, the typical time-course of an actual inhibition experiment.



Appendix D

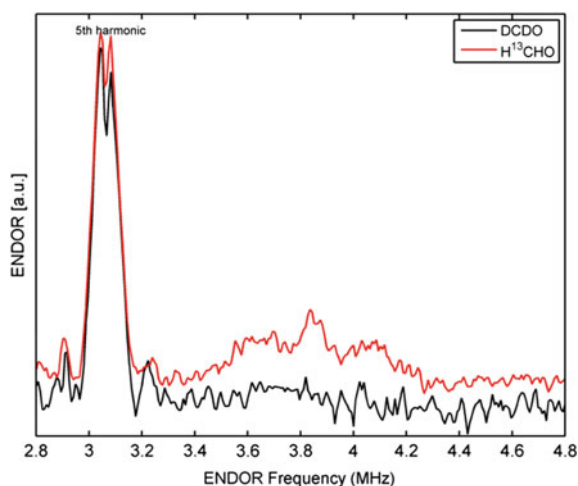
Continuous-Wave EPR Spectrum of Formaldehyde-Inhibited CrHydA1



X-band EPR spectrum of formaldehyde-inhibited *CrHydA1* collected at 11 K, 9.3902 GHz, with a total spin concentration of 830 μM . Non-saturating conditions were employed, i.e. microwave power of 1 mW, modulation amplitude of 1 Gauss, and digital smoothing of 10 points of 1 point per Gauss in a sweep of 1500 G in 10 s. The minor signal at 330 mT ($g = 2.025$) most likely corresponds to a decay product following HCHO inhibition of *CrHydA1*.

Appendix E

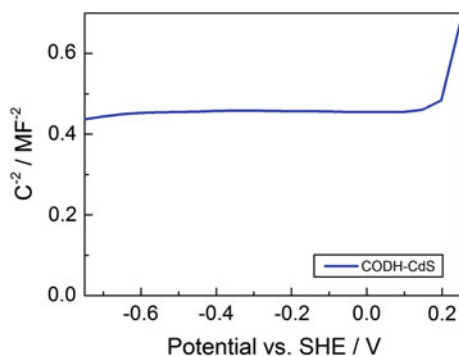
X-Band ENDOR Natural Abundance Carbon Control



X-band ENDOR spectrum of a ^2H control, DCDO, with natural abundance carbon (i.e. approximately 99% ^{12}C), compared to formaldehyde isotopically labelled with ^{13}C . The two spectra are scaled to the 5th harmonic of the ^1H -ENDOR signal (as indicated in the figure). Data was collected at $g = 1.944$, under the same conditions as in Fig. 3.18. Reprinted with permission from [6]. Copyright 2016 American Chemical Society

Appendix F

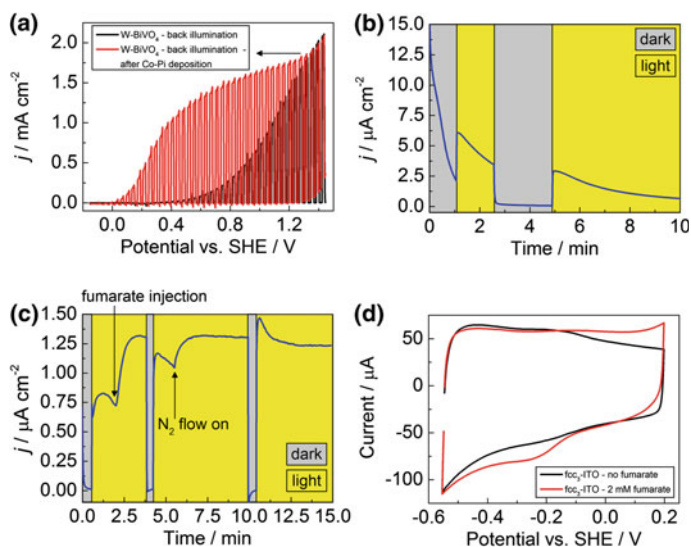
Mott-Schottky Experiment on CODH-CdS



Mott-Schottky plot ($1/C^2$ vs. E) recorded at 20 °C, 1 kHz for CODH-CdS under 100% N_2 in a 0.2 M MES (pH 6.0) cell buffer solution.

Appendix G

Photoelectrocatalytic Fumarate Reduction Under Inverse Connections



Photoelectrocatalysis experiment carried out with reversed connections, i.e. Co-Pi-W-BiVO₄ as the working electrode and fcc₃-ITO as counter. (a) Linear sweep voltammograms recorded before and after Co-Pi deposition on W-BiVO₄; 10 mV s⁻¹, chopped illumination (0.5 Hz, back illumination), 25 °C, 0.1 M KPi buffer (pH 7.0). (b) Current vs. time trace of the Co-Pi-W-BiVO₄ WE connected to the bare *meso*-ITO electrode (CE) in a two-compartment photoelectrochemical cell at zero external bias. Conditions: no gas flow, 25 °C, 0.1 M KPi buffer (pH 7.0). (c) Chronoamperometry experiment depicting photocurrent densities corresponding to visible-light-driven fumarate reduction; 25 °C, 0.1 M KPi buffer (pH 7.0). The

reduction compartment was sparged with N_2 to allow efficient substrate transport to the electrode, gas flow was turned off during injection of fumarate (final concentration 2 mM) into the reduction compartment at $t = 2.0$ min. (d) Cyclic voltammogram of fcc_3 -ITO recorded after chronoamperometry experiments depicted in (c); 30 mV s^{-1} , $25 \text{ }^\circ\text{C}$, 0.1 M KPi buffer (pH 7.0), N_2 flow. The red trace, recorded after introducing fumarate (final concentration 2 mM) into the solution, shows that the enzyme is still catalytically active towards fumarate reduction.

References

1. Compton RG, Banks CE (2011) *Understanding Voltammetry*, 2nd edn. Imperial College Press, London
2. Compton RG, Sanders GHW (1996) *Electrode Potentials*. Oxford University Press, Oxford
3. Gelderman K, Lee L, Donne SW (2007) *J Chem Educ* 84:685
4. Bockris JOM, Khan SUM (1993) *Surface Electrochemistry: A Molecular Level Approach*. Plenum Press, New York
5. Brett CMA, Oliveira Brett AM (1993) *Electrochemistry: Principles, Methods, and Applications*. Oxford University Press, Oxford
6. Bachmeier A, Esselborn J, Hexter SV, Krämer T, Klein K, Happe T, McGrady JE, Myers WK, Armstrong FA (2015) *J Am Chem Soc* 137:5381